

**Investigation of the role of dipole moments
in supramolecular crystals of benzene-1,3,5-
triamides by NMR crystallography and total
X-ray scattering**

Dissertation

zur Erlangung des akademischen Grades

Doktor der Naturwissenschaften

(Dr. rer. nat)

im Promotionsprogramm „Materialchemie und Katalyse“ der
Graduiertenschule für Mathematik und Naturwissenschaften
(BayNAT) an der Universität Bayreuth

Christoph Zehe

geboren in Bamberg

Bayreuth 2016

FÜR MEINE FAMILIE.

Die vorliegende Arbeit wurde unter der Betreuung von Prof. Dr. Jürgen Senker an der Universität Bayreuth zwischen Oktober 2012 und Juli 2016 an der Universität Bayreuth erstellt.

Vollständiger Abdruck der von der Bayreuther Graduiertenschule für Mathematik und Naturwissenschaften (BayNAT) der Universität Bayreuth genehmigten Dissertation zur Erlangung des akademischen Grades eines Doktors der Naturwissenschaften (Dr. rer. nat.).

Dissertation eingereicht am: 09.09.2016

Zulassung durch das Leitungsgremium: 29.09.2016

Wissenschaftliches Kolloquium: 06.03.2017

Amtierender Direktor: Prof. Dr. Stephan Kümmel

Prüfungsausschuss:

Prof. Dr. Jürgen Senker
Prof. Dr. Josef Breu
Prof. Dr. Markus Retsch

Erstgutachter
Zweitgutachter

Prof. Dr. Hans-Werner Schmidt

Vorsitz

THE IMPORTANT THING IS NOT TO STOP QUESTIONING.
CURIOSITY HAS ITS OWN REASON FOR EXISTING. ONE
CANNOT HELP BUT BE IN AWE WHEN HE CONTEMPLATES
THE MYSTERIES OF ETERNITY, OF LIFE, OF THE MARVELOUS
STRUCTURE OF REALITY. IT IS ENOUGH IF ONE TRIES
MERELY TO COMPREHEND A LITTLE OF THIS MYSTERY
EVERY DAY. NEVER LOSE A HOLY CURIOSITY.

ALBERT EINSTEIN

Danksagung

Zuerst möchte ich Herrn Prof. Dr. Jürgen Senker danken: Dafür, dass deine Tür immer offen für unsere Probleme ist, egal um welche Uhrzeit und wie viel Arbeit du gerade hast. Danke für die interessanten und spannenden Themen und Diskussionen und danke für deine buddhistische Gelassenheit, egal wie nahe (vor oder hinter uns) die nächste Deadline war!

Für die produktive Zusammenarbeit (inklusive Bier & Pizza) und die vielen inspirierenden Gespräche möchte ich mich auch bei Prof. Dr. Hanns-Werner Schmidt, Dr. Klaus Kreger sowie Dr. Reiner Giesa vom Lehrstuhl für Makromolekulare Chemie I der Universität Bayreuth bedanken.

I also want to thank Prof. Dr. Andrew Goodwin from the University of Oxford for the great opportunity of working in his brilliant group and for the numerous inspiring discussions! Thanks to Josh and Nick for all the support and to Ali, Joe, Matt, Paul, Peter, Sam and Will for the great atmosphere and for showing me many nice places in Oxford!

Besonders danken möchte ich der Hanns-Seidel-Stiftung für die langjährige finanzielle und besonders für die bereichernde ideelle Förderung im Rahmen meines Studien- und Promotionsstipendiums. Auch dem Elitenetzwerk Bayern möchte ich für die Unterstützung im Rahmen des Elitestudienganges Macromolecular Science in Form vieler abwechslungsreicher Seminare und finanzieller Unterstützung danken.

Dankbar bin ich auch Dr. Renée Siegel für die Hilfe zu jeder noch so späten Zeit und die viele Schokolade sowie Kilian und Carsten für die vielen motivierenden wissenschaftlichen (und nicht-wissenschaftlichen) Dialoge und die lustige Zeit im und außerhalb des Büros. Mein Dank geht auch an alle anderen Mitarbeiter und Praktikanten am Lehrstuhl für Anorganische Chemie III für viele interessante Diskussionen und die lustige Zeit.

Besonderer Dank geht an meine (große) Familie und insbesondere an meine Eltern, für die viele Unterstützung und die vielen schönen und lustigen Momente. Danke auch an meinen Freund und Sparringspartner Michael für den notwendigen Ausgleich zur Arbeit in Form von zahlreichen Badminton-Trainingseinheiten, Grillabenden und (Bürger-)Festen.

Contents

Zusammenfassung	xiii
Abstract	xv
1 Introduction	1
1.1 Investigation of correlated disorder by analysis of diffuse scattering	3
1.2 Structure solution by NMR crystallography	6
2 Synopsis	9
2.1 Investigations of macrodipole ordering in the bulk structures of benzene-1,3,5-trisamides by total X-ray scattering	10
2.2 Structure elucidation of microcrystalline BTAs by NMR crystallography: beyond the limits of X-ray diffraction	14
2.2.1 Implementation of ^{19}F DQ experiments at high magic angle spinning rates for distance measurements	16
2.2.2 Structure elucidation in a fluorinated BTA: the impact of fluorine on the supramolecular interactions	19
2.3 Structure elucidation of 2D self-assembling low-molecular mass organic compounds <i>via</i> NMR crystallography	23
Bibliography	27
3 Index of Publications	41
4 Publications	43
4.1 NMR-crystallographic study of two-dimensionally self-assembled cyclohexane-based low-molecular-mass organic compounds	43
4.2 Influence of Fluorine Side-Group Substitution on the Crystal Structure Formation of Benzene-1,3,5-trisamides	67
4.3 Influence of proton coupling on symmetry-based homonuclear ^{19}F dipolar recoupling experiments	105
4.4 Mesoscale Polarisation <i>via</i> Geometric Frustration in Supramolecular Crystals	129
4.5 Solid State NMR Spectroscopy	159

Zusammenfassung

Ziel dieser Arbeit ist die Strukturaufklärung von fehlgeordneten oder mikrokristallinen Benzol-1,3,5-trisamide (BTAs) mittels NMR Kristallographie und totaler Röntgenstreuung, um die Rolle von Dipolmomenten in ausgedehnten supramolekularen Kristallen zu verstehen.

Ausgewählte BTAs, die mittels dreifach-helikalen Wasserstoffbrückenbindungen zu kolumnaren Stapeln assemblieren und dadurch große Makrodipole entlang der Kolumnenachse ausbilden, zeigen ausgeprägte Fehlordnung, die sich in diffuser Röntgenstreuung an Einkristallen manifestiert. Dies wird verursacht durch geometrische Frustration der Makrodipolwechselwirkung von benachbarten Kolumnen auf Grund ihrer Anordnung in einer hexagonalen Stabpackung. Die Unordnung konnte mittels Monte-Carlo Simulationen von zweidimensionalen Ising-Antiferromagnet entsprechenden Modellen erklärt werden. Eine Reduktion der Makrodipolwechselwirkung durch das chemische Design der Moleküle - entweder durch lange, sterisch anspruchsvolle Seitengruppen, die den interkolumnaren Abstand erhöhen, oder durch die Einführung von polaren C-F Bindungen mittels Substitution von Methylgruppen durch Fluoratome, welche die Makrodipolgröße verringern - veränderte Packungseffekte, die ferroelektrische Wechselwirkungen mit den zweitnächsten Nachbarn bewirkten. Hierdurch konnten axial polare Domänen mit spontaner Polarisation in diesen kolumnaren Phasen mittels eines gezielten Design der molekularen Synthese erzeugt werden.

Die Einführung von Fluoratomen ermöglichte nicht nur eine Abstimmung der Makrodipole, sondern resultierte auch in Polymorphismus. Neben der kolumnaren Phase, die mittels Einkristallröntgenbeugung untersucht werden konnte, wurde auch ein zweites Polymorph, das nur mikrokristalline Pulver bildete, gefunden. Realraumstrukturlösung mittels Pulverdaten ergab ein sinnvolles Strukturmodell, erlaubte aber wegen der gleichen Elektronenzahl nicht zwischen Fluoratomen und Methylgruppen zu differenzieren. Deshalb wurden ^{19}F Doppelquantenexperimente, die homonukleare dipolare Wiedereinkopplung in der Gegenwart eines dichten ^1H Spinsystems verwenden, implementiert. Diese erlaubten verschiedene Strukturmodelle, die sich nur in der Fluor-Methyl Anordnung unterschieden, zu differenzieren. Die Strukturlösung zeigte, dass die Fluoratome auf Grund einer schwachen NH-F Wechselwirkung ausgeordnet sind und dass ein zweidimensionales Wasserstoffbrückenmuster zu schichtartigen Aggregaten führt, die nur mittels

Zusammenfassung

van der Waals Wechselwirkungen interagieren und somit eine hochgradig anisotrope Struktur bilden. Der Grund für dieses für BTAs ungewöhnliche Packungsmuster wird in der reduzierten Kooperativität der Selbstassemblierung von kolumnaren Stapeln gesehen, da die polaren C-F Bindungen die Makrodipole reduzieren.

Dieses zweidimensionale Wasserstoffbrückenmuster wurde durch Bisamid-, Bisurea- und Bisacylureaverbindungen nachgeahmt, in denen das molekulare Design ein exaktes Auslösen der Dipole erlaubt. Selbstassemblierung ergab nanoskopische Plättchen mit hohen Aspektverhältnissen; Strukturklärung mittels NMR Kristallgraphie zeigte, dass alle Strukturen ausgedehnte Wasserstoffbrückennetzwerke ausbilden, entweder zweidimensionale Schichten oder eindimensionalen Ketten, welche aber wiederum dicht zu zweidimensionalen Plättchen packen, was die anisotrope Selbstassemblierung erklärt. Die Moleküle nehmen hierbei immer eine Konfiguration ein, die intrinsisch die Dipolmomente im Molekül auslöscht, sodass die Selbstassemblierung nur durch Wasserstoffbrücken getrieben ist.

Abstract

This work aimed to elucidate the structures of disordered or microcrystalline benzene-1,3,5-trisamides (BTAs) using NMR crystallography and total X-ray scattering in order to understand the role of dipole moments in extended supramolecular crystals.

Selected sample BTAs, which assemble into columnar stacks *via* triple helical hydrogen bond formation, resulting in large macrodipole moments along the columnar axis, showed pronounced disorder manifesting in diffuse X-ray scattering from single crystals. The disorder is caused by geometric frustration of the macrodipole interactions of neighbouring columns due to their arrangement in hexagonal rod packings. The disorder could in all cases be explained by Monte-Carlo simulations of two-dimensional Ising antiferromagnet-like models. Reduction of the macrodipole interactions by chemical design of the molecules - namely, the choice of long and bulky side groups enhancing the intercolumnar distance or the introduction of polar C-F bonds *via* substitution of methyl groups by fluorine reducing the macrodipole size - tuned packing effects, which introduced ferroelectric next-nearest neighbour interactions. In this way, the creation of axially polar domains with spontaneous, permanent polarisation was facilitated in these columnar phases solely by targeted design of the molecular synthons.

The introduction of fluorine not only enabled a tuning of the macrodipoles but also resulted in polymorphism. Beside the columnar structure established by single-crystal diffraction, a second polymorph forming only microcrystalline powders was found by solid-state NMR. Real-space structure solution from powder X-ray diffraction data yielded a reasonable model but did not allow for a differentiation of fluorine atoms and methyl groups due to their equal electron number. Therefore, ^{19}F double-quantum experiments using homonuclear dipolar recoupling in the presence of a dense ^1H spin network were implemented. This allowed to distinguish different structure models differing only in the fluorine-methyl ordering and to show that the fluorine atoms are ordered due to a weak NH-F interaction. The structure solution showed that a weak NH-F interaction leads to ordering of the fluorine atoms and that a two-dimensional hydrogen bond pattern results in sheet-like aggregates, which only interact *via* van der Waals forces, leading to a highly anisotropic structure. The reason for this unusual packing pattern of BTAs is assumed to lie in the reduced cooperativity in the

Abstract

self-assembly of columnar stacks because the polar C-F bonds reduce the macrodipole moments.

This two-dimensional hydrogen bond pattern was emulated by bisamides, bisureas and bisacylureas, where the molecular design allows an exact cancellation of dipole moments. Self-assembly yielded nanoscopic sheets with high aspect ratios; structure solution using NMR crystallographic approaches showed that all structures exhibit extended hydrogen bond patterns, forming either two-dimensional layers of molecules or one-dimensional chains, which pack densely to two-dimensional sheets, explaining the anisotropic self-assembly. The molecules always adopt a configuration which intrinsically cancels the dipole moments within the molecule, so that the self-assembly is purely hydrogen-bond driven.

Nomenclature

1D	One-dimensional
2D	Two-dimensional
Benzene-1,3,5-trisamide	BTA
CP	Cross Polarisation
CSA	Chemical Shift Anisotropy
cw	continuous wave
DFT	Density Functional Theory
DQ	Double Quantum
LMO	Low Molecular Mass
MAS	Magic Angle Spinning
ssNMR	solid-state Nuclear Magnetic Resonance

1 Introduction

Modern materials research focuses on solving technological¹, environmental² or human health³ key problems by designing and understanding the performance of evermore advanced materials. The physical properties - optical⁴, electrical⁵, thermal⁶, and mechanical⁷ - depend intimately on the structure of these materials; more precisely, the structure determines the function. This is well-known for the catalytic activities of proteins⁸, non-volatile memory devices¹, and battery materials⁹ or the separation of green house gases such as CO₂ by porous materials².

Particularly supramolecular materials^{10,11} gained considerable interest due to their easy accessibility, versatility and reversible formation¹² since the establishment of supramolecular chemistry¹⁰. The latter is defined as the chemistry of the *intermolecular* bond¹⁰ and aims to create materials by exploiting secondary (i.e. non-covalent) interactions, which direct the molecular building units (referred to as synthons) into ordered assemblies.

An interesting class¹³ of supramolecular synthons is given by benzene-1,3,5-trisamides (BTAs) due to their easily controllable and predictable self-assembly¹³. This render them valuable model systems to study amplification of chirality^{14,15} in and the influence of chirality on self-assembly¹⁶, breaking of symmetry^{15,17}, cooperativity in self-assembly processes^{18,19}, dynamics of supramolecular systems^{20,21} and long-range energy transport²². Their easy and low-cost chemical accessibility enables a wide range of interesting application such as MRI contrast agents²³, organo²⁴- and hydrogelators^{25,26} or for thermoplastic elastomers²⁷.

BTAs also have both academic and commercial use as ultra-efficient nucleation and clarification²⁸⁻³¹, foaming³², and electret³³ additives for isotactic polypropylene in concentrations as low as 50 wt-ppm and as nucleating agents for poly(butylene terephthalate)³⁴, poly(ethylene-*co*-propylene), polyvinylidene fluoride³⁵, and polylactides³⁶.

The chemical design scheme of BTAs (Fig. 1a) aims to guide the molecules into columnar stacks *via* triple helical hydrogen bond networks during self-assembly^{37,38}. As a result of the alignment of the polar N-H and C=O bonds, large dipole moments are formed along the columnar axis³⁹ (Fig. 1b), which have been studied theoretically^{39,40} as well as experimentally⁴¹⁻⁴³. The growth of BTA stacks proved to be particularly efficient due to cooperative effects⁴⁴: on the one hand, the addition of a new molecule to an existing

1 Introduction

stack can be thought as stacking a small dipole moment upon an existing large dipole moment with the same dipole direction. This becomes energetically more attractive the larger the existing dipole is, resulting in a cooperative effect. On the other hand, a redistribution of the NH hydrogen electron density towards the carbonyl oxygen takes place due to polarisation effects, strengthening the hydrogen bonds with increasing stack size and thereby increasing the energy gain through addition of new molecules.

To extract the link between the chemical formula and the resulting supramolecular interactions, the bulk structures of BTAs were often studied and they reveal a general trend for the dependence of the crystal packing from the side groups¹³: short, sterically small side groups form sheet-like hydrogen bond pattern, e.g. for R = methyl²⁴ and R = ethyl⁴⁵, or three-dimensional networks, as e.g. R = propyl⁴⁵. Long, flexible side groups tend to result in liquid crystalline phases, for instance R = n-butyl up to R = n-decyl⁴⁶. Smaller but sterically demanding sidegroups often induce columnar stacks^{47,48}, but heteroatoms may take part in the hydrogen bond network⁴⁹⁻⁵¹. Derivatives with e.g. R = *tert*-butyl^{52,53}, i.e. with bulky, short aliphatic sidegroups, exhibit a triple-helical hydrogen bond packing and a hexagonal or pseudo-hexagonal packing of the resulting columns.

Because exactly those BTAs with short, bulky side groups constitute ideal model systems to study supramolecular interactions - the side groups are big enough to enforce a columnar stacking but not long and flexible enough to induce liquid crystalline behaviour - elucidation of their bulk structures might be particularly insightful. However, past studies revealed either strong correlated disorder and resulting diffuse scattering⁵² or only microcrystallinity⁵³ for exactly those molecules, so that structure elucidation required an analysis of total X-ray scattering and an NMR crystallographical approach, respectively.

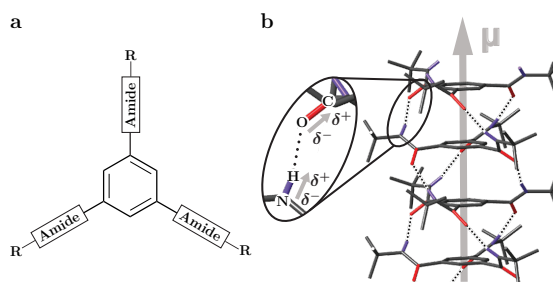


Figure 1: **a**, The molecular structures of BTAs are based on a benzene core, which is linked *via* three amide bonds to easily variable side groups. **b**, This enables triple helical hydrogen bonding so that the molecules self-assemble into columnar stacks, where the alignment of all N-H in one and all C=O bonds in the opposite direction leads to large dipole moments along the stack axis.

1.1 Investigation of correlated disorder by analysis of diffuse scattering

This work is therefore concerned with the structure elucidation in a range of different BTAs and closely related materials to understand the fundamental structure directing interactions in their supramolecular assemblies. In particular the question of interactions between the supramolecular aggregates, as e.g. the interactions between the dipole moments of neighbouring columns, and their implications for the bulk properties - being ignored in many studies due to a focus on the individual columnar supramolecular structures - will be studied. Both analysis of total X-ray scattering and NMR crystallographic approaches are utilised to either understand origin and implications of disorder in the bulk structures or to enhance and support the information content of powder X-ray studies.

1.1 Investigation of correlated disorder by analysis of diffuse scattering

Many materials do not form perfect crystals in the sense of a translational periodic three-dimensional arrangement of atoms or molecules, i.e. they are disordered on the atomic or mesoscale⁵⁴ to a certain extent or completely amorphous⁵⁵. For instance, it can be shown for a simple dense packing of polyhedra that the non-crystalline state is more often encountered than the crystalline one⁵⁶. This disorder is in many cases not just an undesired side-product but is often crucial for targeted functions⁵⁷⁻⁵⁹ so that the synthesis of well-ordered samples might not even be desirable. The disorder violates the fundamental assumption on which classical powder and single-crystal crystallography relies - the existence of perfect translational periodicity - and hence complicates or prevents structural investigations.

In both single-crystalline and powdered samples exhibiting disorder, diffuse scattering may be analysed to deduce information about the structure and about the origin of the disorder^{54,60}. Classic single-crystal and powder crystallography derives an unit cell - i.e. the smallest entity which forms the complete lattice by translations - from Bragg reflections. In disordered materials, Bragg reflections might still be present and encode the average (hence periodic) structure in form of a single unit cell⁶¹. Additionally, diffuse scattering arising from the difference between this average and the real electron density, contains information about local correlations and hence about the origin and form of the disorder⁶¹. Physically spoken, because the

1 Introduction

scattering amplitude is the Fourier transform of the scattering density, the amplitude arising from a periodic crystal is a discrete Fourier series. If, however, the scattering density becomes aperiodic, its Fourier transform is not a discrete Fourier series anymore but a continuous function of the reciprocal space coordinates⁶². Hence, the intensity is distributed over a range of scattering vectors and often several orders of magnitude weaker than Bragg intensities, which are concentrated on isolated directions.

Correlated disorder (Fig. 2) is the intermediate state between random disorder, as encountered in liquids, and periodic crystalline order⁵⁴; although no translational periodicity exists, the arrangement still exhibits local statistical correlations in average over a large region. This may arise from a variety of chemical and physical origins, such as displacive defects⁶³, substitutional

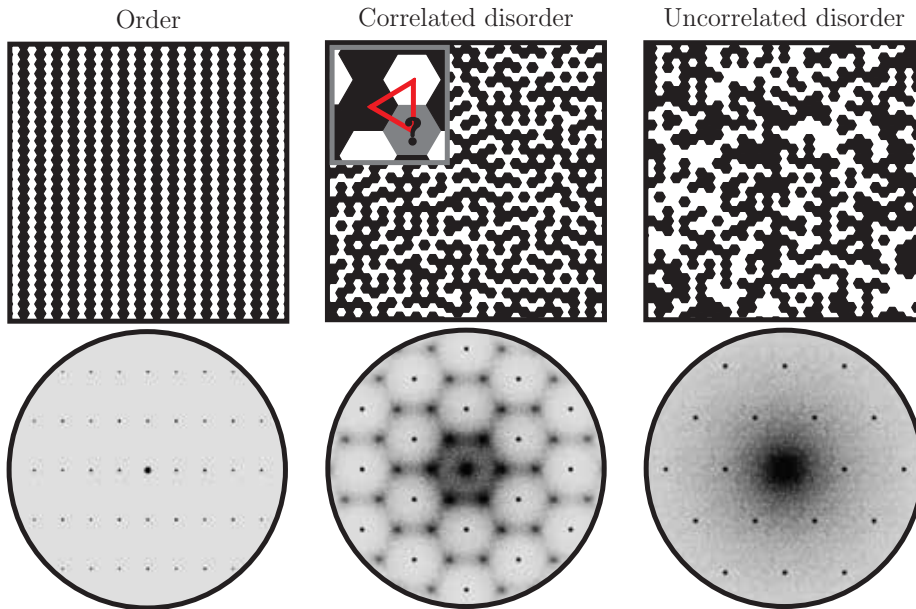


Figure 2: Upper row: tilings of black and white hexagons on a triangular lattice, where each hexagon has always six neighbours, exemplify various degrees of (dis)order. For the ordered system (left), each hexagon is surrounded by four neighbours of different colour in exactly the same arrangement. In the example of the correlated disorder (middle), neighbouring hexagons prefer different colouring, which cannot be fulfilled due to the symmetry of the lattice; this maps directly onto the two-dimensional frustrated Ising antiferromagnet. Here, each hexagon has in average four neighbours of different colour reflecting the interactions between nearest neighbours. For the uncorrelated disorder (right), the distribution of white and black hexagons is random and hence each hexagon has in average three neighbours of different colour. Lower row: all corresponding diffraction patterns exhibit spot-like Bragg reflections, in addition to pronounced diffuse scattering in form of honeycombs in case of correlated (middle) and diffuse Laue background scattering in case of uncorrelated disorder (right).

1.1 Investigation of correlated disorder by analysis of diffuse scattering

disorder⁶⁴ or molecular dynamics⁶⁵, to name only a few. However, many different types of disorder may be mapped onto two simple archetypes⁵⁴: i), overconstrained systems feature geometric frustration⁶⁶ because the system cannot fulfill all constraints at the same time (Fig. 2). A prototype for this is the two-dimensional Ising antiferromagnet⁶⁷, where the antiferromagnetic interaction between neighbouring spins is frustrated due to the triangular symmetry of the underlying lattice. ii), geometric underconstraints may allow several energetically equivalent arrangements and hence induce disorder, as, for instance, in the hydrogen bond pattern in square ice⁶⁸.

In contrast to powder and single-crystal structure solution using Bragg reflections, no general approach exists for analysing diffuse scattering⁶⁰. The origins of diffuse scattering are diverse and so are the different methods employed for extracting the information contained in diffuse intensities.

The most common and powerful approach, however, is the use of Monte-Carlo simulations for creation of atomistic models, for which the X-ray scattering is then simulated. In the big-box approach⁵⁴, a large ensemble of an underlying average unit cell is optimised using Monte-Carlo simulations so that both local statistical correlations as well as the average structure may be captured.

In the direct Monte-Carlo approach, an energy term is defined based on model system parameters and a Monte-Carlo simulation using e.g. the Metropolis algorithm⁶⁹ is performed with respect to that energy term. The parameters are then varied, until a qualitative or quantitative match between experimental and simulated scattering intensities is achieved^{70,71}.

The reverse Monte-Carlo approach uses directly the crystallographic R value, i.e. the deviation between calculated and observed diffuse scattering intensities, as a cost function and minimises that numerically. Instead of refining against diffuse scattering intensities, one could also refine against the Patterson function⁷²⁻⁷⁵, which is the Fourier transform of the intensity. This function is also commonly called pair distribution function, since it describes statistical pairwise correlations of atoms, and has the advantage of being well-defined even for amorphous materials⁵⁵, thus allowing structural investigations independent of translational periodicities.

1.2 Structure solution by NMR crystallography

For many materials, single crystals are unavailable and they form only micro- or nanocrystalline powders⁷⁶. In powder X-ray diffraction, however, the information content is significantly reduced compared to single-crystal X-ray diffraction since the three-dimensional reciprocal space is projected onto a single dimension, where symmetry-equivalent reflections systematically collapse into the same point and accidental signal coincidences occur in addition^{77,78}. Although various approaches utilising direct⁷⁹, real-space⁸⁰ and charge flipping⁸¹ methods were developed, the *ab initio* structure solution from powder data is still challenging⁸².

A powerful method for structural and dynamic investigations of powdered materials is solid-state nuclear magnetic resonance spectroscopy^{83,84} (ss-NMR). It makes use of the interactions of nuclear spins with external magnetic fields to observe internal spin interactions with the chemical environment, which allow to deduce symmetry information^{85,86}, orientations⁸⁷, distances⁸⁸ and connectivities^{89,90}. ssNMR alone and in combination with powder X-ray diffraction - called NMR crystallography⁹¹ - has proven valuable for structure elucidation in diverse materials such as porous materials^{92,93}, polymer systems^{53,94,95}, glasses⁸⁷, molecular solids^{96,97} or proteins⁹⁸.

While a wide variety of experimental ssNMR procedures is reported in the literature⁸⁴, most of them are based on the three strongest spin interactions in solids: the chemical shift, the direct dipole-dipole and the quadrupolar interaction. In comparison to X-ray diffraction - where the X-ray beam averages over a large ensemble of unit cells - these interactions are of local nature and hence independent of translational symmetry.

The chemical shift interaction depends strongly on the symmetry of the chemical spin environment. The number and intensity ratios of signals allow to deduce information about the asymmetric unit⁹⁹ or space groups⁸⁶, whereas the chemical shift values are characteristic for chemical groups and hence may be used to identify structural fragments¹⁰⁰. *Ab initio* calculations of chemical shifts using Density Functional Theory (DFT) methods¹⁰¹ allow to validate structural models¹⁰² or - thanks to the latest increases in computational power - even *ab initio* structure solutions entirely based on chemical shifts¹⁰³. The quadrupolar interaction may similarly be used to deduce symmetry information¹⁰⁴ but it has particular strengths for investi-

gations of dynamics¹⁰⁵.

The most important interaction in ssNMR is the direct dipole-dipole interaction between the magnetic moments of two spins in spatial proximity. Since the interaction strength depends on the distance and orientation of the spins, observation of dipolar couplings between spins allow to measure homo^{88,106–108}- and heteronuclear^{109–111} distances, validate structure models^{53,94}, solve complete structures^{92,98} or localise hydrogen atoms¹¹², which are usually invisible in powder X-ray diffraction.

For investigation of those interactions, recoupling sequences are often employed. The sample is subjected to Magic Angle Spinning¹¹³ (MAS), which averages anisotropic interaction parts and hence greatly enhances the resolution. The dipolar interaction, which has no isotropic component and is averaged to zero, may then be selectively recoupled by interference effects of the MAS and spin manipulations as e.g. radiofrequency pulses^{114,115}.

The recoupled interaction is often used to excite double-quantum (DQ) coherences, which intensities depend on the interaction strength and - since the dipole coupling constant d_{12} between two spins is proportional to r_{12}^{-3} - on the internuclear distance. The latter may then be extracted by measuring a series of DQ filtered spectra (buildup curve), where the signal amplitude encodes the intensities of DQ coherences as a function of the excitation time during the pulse sequence (Fig. 3).

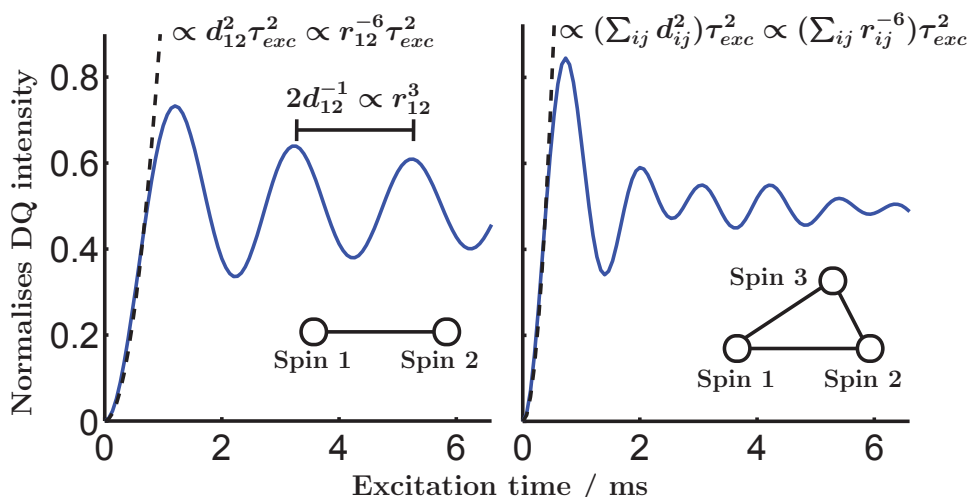


Figure 3: The DQ buildup curve for a spin pair (left, blue curve) allows to directly deduce the dipolar coupling constant and hence the internuclear distance from the oscillations, which is not possible for a three-spin system (right, blue curve) anymore. In both cases, the initial rise of the curves (black dashed line) is governed by the second moments, i.e. the sum of all squared coupling constants.

1 Introduction

For isolated spin pairs (Fig. 3, left), the oscillation frequency of the curve is exactly half the coupling constant⁸⁸ so that the spin-spin distance is directly accessible or by fits using analytical expressions¹¹⁶ for the buildup behaviour. The DQ buildup of an extended spin system (Fig. 3, right), however, is a nonlinear function of all coupling constants. Since the distances are not directly accessible any more, the experiments are usually simulated numerically for model systems, which can be tested in this way. In both cases, the initial rise of the curve is also dependent on the sum of the squared coupling constants¹¹⁷ and hence on $\sum_{ij} r_{ij}^{-6}$, where r_{ij} denotes the internuclear distance of the spins i and j . This may be used for second moment analyses, where the initial rise is fitted for different model systems¹¹⁷.

2 Synopsis

This work consists of three publications and two manuscripts (see chapter 3) dealing with different aspects of the bulk structures of BTAs or closely related materials. Many of them were developed in parallel, so that the timeline of publication does not necessarily reflect the actual connections between the different parts. Therefore, this chapter will focus on highlighting the connection between the different manuscripts and especially on the overall context formed by these results.

The manuscript "Mesoscale Polarisation *via* Geometric Frustration in Columnar Supramolecular Crystals" (no. 5) investigates the role of the dipole moments in solid BTA crystals and the control of dipole ordering by chemical modification of the synthons. As a result of one modification, namely fluorine introduction, polymorphism arises, which requires NMR crystallographic methods for structural investigations.

The publication¹¹⁸ entitled "Influence of proton coupling on symmetry-based homonuclear ^{19}F dipolar recoupling experiments" (no. 4) shows, how homonuclear DQ recoupling experiments developed primarily for distance measurement between dilute spins with weak homonuclear couplings as e.g. ^{13}C may be transferred to sparse but strongly coupled spin systems as e.g. ^{19}F in the simultaneous presence of extended ^1H spin networks.

This approach is then used to elucidate the structure of a fluorinated BTA in the publication⁹⁹ "Influence of fluorine side-group substitution on the crystal structure formation of benzene-1,3,5-trisamides" (no. 2), where the equal electron density of fluorine and methyl groups prevents their differentiation by powder X-ray crystallography. The resulting structure solution exhibits a fundamentally different hydrogen bond pattern and shows that the molecular conformation itself as well as the space group symmetry prevents the formation of large dipole moments in this polymorph.

Finally, the publication¹¹⁹ "NMR-crystallographic study of two-dimensionally (2D) self-assembled cyclohexane based low-molecular-mass organic compounds" (no. 1) uses NMR crystallography to investigate the bulk structures and their consequences on the self-assembly, when the molecular synthons are designed to favour two-dimensional hydrogen bond patterns.

The foundations of ssNMR used in many of the presented works are summarised in the manuscript "Solid-state NMR spectroscopy" (no. 6), which is intended for publication as part of the "Handbook of Solid State Chemistry".

2.1 Investigations of macrodipole ordering in the bulk structures of benzene-1,3,5-trisamides by total X-ray scattering

In the manuscript "Mesoscale Polarisation *via* Geometric Frustration in Supramolecular Crystals" we investigate the structures formed by aggregation of the columnar stacks. Although many experimental and theoretical studies address various aspects of the self-assembly of BTAs *within* a single column, none of them systematically studies the interactions *between* those supramolecular assemblies (Fig. 4).

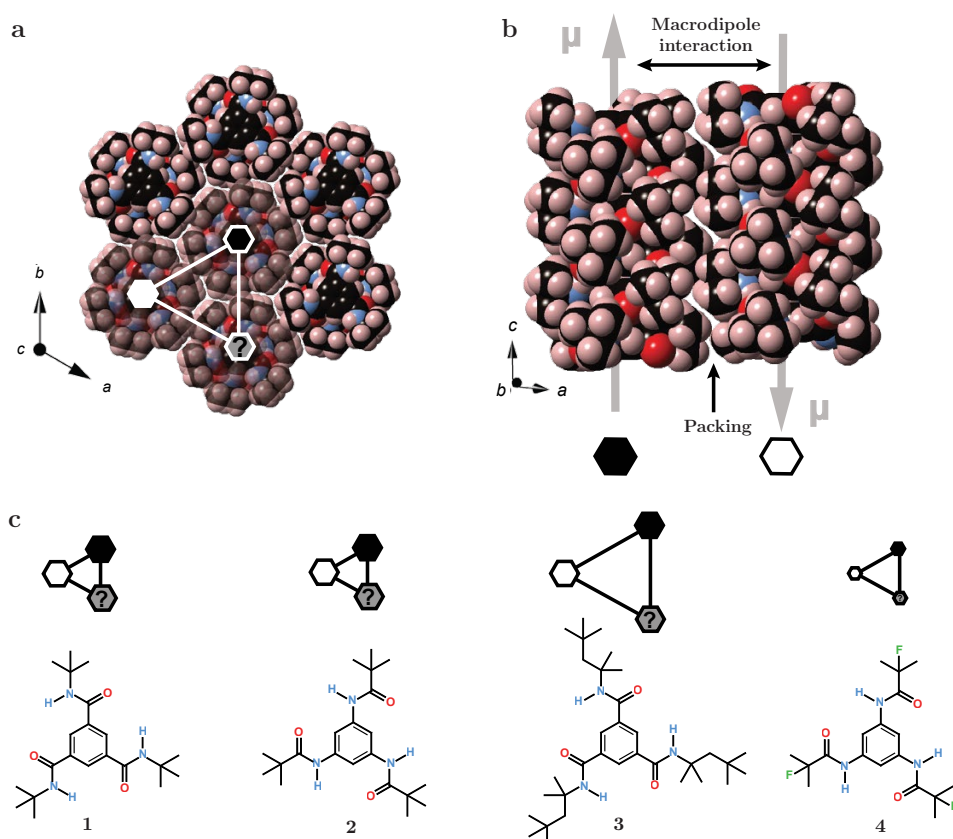


Figure 4: **a**, The columnar stacks of molecules formed by BTAs assemble in hexagonal or pseudo-hexagonal rod packings. The macrodipoles of the columns can only point up (black hexagon) or down (white hexagon) but prefer electrostatically an anti-alignment, so that they frustrate. **b**, In addition, the requirement of a dense packing to maximise van der Waals interactions influences the ordering of the columns. **c**, Four compounds are chosen as model systems to study the dipole ordering in their bulk structures: **1** and **2** are expected to exhibit large macrodipole moments and differ only by the amide connectivity. In **2**, the distance of the macrodipoles is enhanced compared to **1**, while the macrodipoles are expected to be similar. The fluorine atoms in **3** introduce an additional polarity, which is expected to alter the macrodipoles compared to **2**.

2.1 Investigations of macrodipole ordering in BTA bulk structures

Pioneering work showed that the columns formed by BTAs with bulky, aliphatic side groups tend to aggregate in hexagonal⁵² or pseudo-hexagonal⁵³ (i.e. distorted-hexagonal) rod packings (Fig. 4a), which is the natural way of packing columns densely. The large macrodipoles along the columnar axis, however, cannot all arrange antiparallel to each other due to geometric frustration in this triangular lattice (Fig. 4a)⁷⁴.

Beside the electrostatic interactions preferring anti-alignment of neighbouring macrodipoles, the requirement of a dense packing induces additional interactions, which may favour either alignment (Fig. 4b). The latter may be varied by different organic side groups, which determine the texture of the outside of the columns and hence influence the packing. We therefore study the structures of four different model compounds, where we either enhance the distance of the macrodipoles (**1** vs. **3**, Fig. 4c) or alter the size of the macrodipoles (**2** vs. **4**).

The crystal structures derived from single-crystal diffraction data (Fig. 5a) reveal a columnar stacking of the molecules with triple helical hydrogen bond patterns in all cases. However, each stack is disordered across a mirror plane perpendicular to the stacking direction for compounds **1** - **3** with varying occupancies for the up- and down-orientations (Fig. 5b). This type of disorder and diffuse scattering cannot be caused by twinning¹²⁰ because the only possible twinning reverting the dipole orientation results in an inversion twin, where both components lead to the same diffraction pattern. Hence, it must originate from correlated disorder, over which the Bragg reflections contain an average; indeed, the diffraction patterns exhibit intense diffuse scattering for **1** - **3** (Fig. 5c).

Fig. 4a and b suggest to study the disorder by 2D antiferromagnet-type Ising models⁶⁷ (Fig. 6). Hereto, an energy E was calculated for model systems containing 100 x 100 columns ("spins" with spin states σ) which may either point up

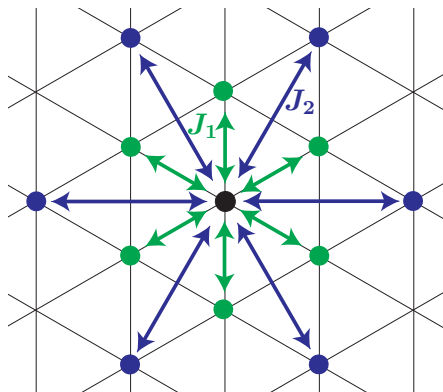


Figure 6: In the 2D antiferromagnetic Ising model, each spin (circles) can either point up or down. The interactions with its nearest-neighbours and with its second-nearest neighbours (green) are given by coupling constants J_1 and J_2 , respectively.

2 Synopsis

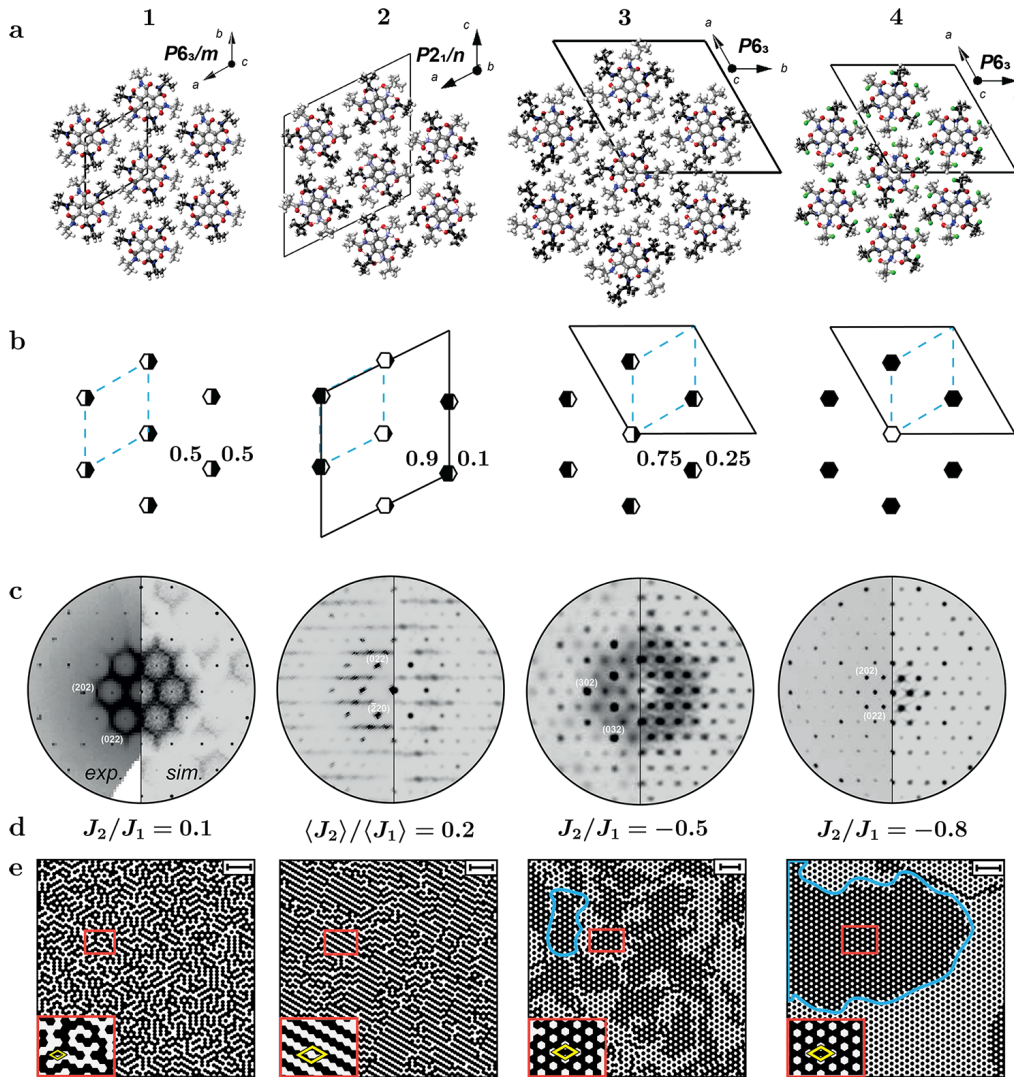


Figure 5: **a**, Single-crystal structure solutions reveal columnar stacks arranged in (pseudo-)hexagonal rod packings for **1** - **4**. **b**, The stacks are disordered across mirror planes perpendicular to the stacking directions and the occupancies for "up" and "down" orientations are given and indicated by the amount of black and white in the hexagons. **c**, The diffraction patterns show intense diffuse scattering, which can be reproduced by simulated diffraction patterns based on 2D Ising models for ensembles of 100×100 columns. **d** These models also result in empirically optimised coupling constants between neighbouring columns, describing effective intercolumnar interactions (positive values indicate antiferroelectric, negative values indicate ferroelectric interactions). **e**, The resulting macrodipole orientations reveal stripe-like macrodipole patterns for **1** and **2** and honeycomb-like patterned domains carrying permanent polarisation for **3** and **4**. The local structure (red-boxed zooms) also explain the results of the structure solutions if one takes into account that the beam averages only within its coherence length.

2.1 Investigations of macrodipole ordering in BTA bulk structures

($\sigma = +1$) or down ($\sigma = -1$):

$$E = J_1 \sum_{\langle i,j \rangle} \sigma_i \sigma_j + J_2 \sum_{\langle\langle i,j \rangle\rangle} \sigma_i \sigma_j, \quad (2.1)$$

where $\langle \rangle$ and $\langle\langle \rangle\rangle$ indicate a summation over the nearest and next-nearest neighbours (Fig. 6), respectively. The model system was then equilibrated using the Metropolis algorithm⁶⁹, the single crystal diffraction pattern calculated and the coupling constants were empirically optimised to achieve the best match between experimental and simulated diffraction intensities (Fig. 5c and d).

It becomes apparent that, while **1** and **2** exhibit positive J_1 and J_2 - indicating effective antiferroelectric interactions between nearest and next-nearest neighbouring columns - **3** and **4** have positive J_1 but negative J_2 and hence a ferroelectric interaction with the next-nearest neighbours. The resulting macrodipole ordering shows stripe-like patterns with local macrodipole cancellation for **1** and **2**, whereas the negative J_2 induce a domain structure with permanent polarisation within each domain for **3** and **4**.

To investigate the relation of the observed coupling constants to the macrodipole interactions, we calculated the latter for stacks of increasing size for **1**, **2** and **4** (Fig. 7a). **2** exhibits slightly smaller macrodipole mo-

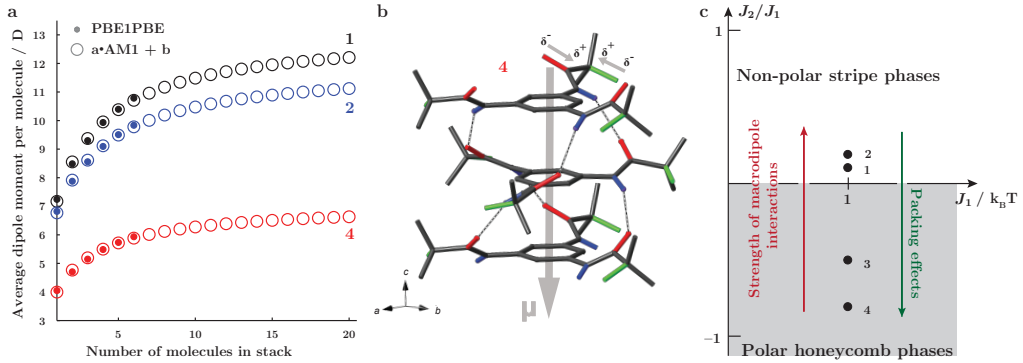


Figure 7: **a**, The average molecular dipole moments for stacks having crystal structure geometry increase due to cooperative effects^{39,44}. The limiting value for an infinite column may be estimated by fitting semiempirical AM1 calculations to PBE1PBE results. **b**, The C-F bonds in **4** are aligned antiparallel to the C=O bonds due to weak NH-F interactions, which reduces the overall macrodipole moment of the stacks drastically. **c**, Summary of the relation between intercolumnar interactions and macrodipole ordering in form of an Ising phase diagram¹²¹.

2 Synopsis

ments than **1** due to the better conjugation of the benzene core with the amide bonds, which restrains the alignment of the latter into stacking direction. The average dipole moment per molecule in **4** has only about half the size of that in **2** because the polar C-F bonds align antiparallel to the C=O bonds (Fig. 7b) and hence their dipoles partially cancel within each stack.

These results imply not only that the dominating interactions in the bulk structures of simple BTAs are intercolumnar dipole-dipole interactions (since all J_1 are positive) but they also show how geometric frustration can be used to purposefully induce interesting phase behaviour: Due to the geometric frustration, minimisation of the intercolumnar dipole-dipole interactions maximises the influence of subtle packing effects, which can induce ferroelectric interactions (negative J_2 values). This allows to move in the Ising ground state phase diagram (Fig. 7c) from local stripe-like macrodipole cancellation schemes to polar honeycomb phases with spontaneous polarisation within each domain by a targeted design of the molecular structures.

This structure-property relationship might be useful for the development of axially polar ferroelectric materials¹²², which are a vibrant research topic¹²³ due to possible applications in ultra-high density memory devices. Moreover, the results imply that the structure solution of BTAs from powder data might be severely hampered because the limited information content is additionally accompanied by structural disorder and diffuse scattering, which is not taken into account by conventional structure solution approaches from powder X-ray data. Interestingly, even for other BTA derivatives with more complicated side groups honeycomb packing pattern was reported, but the origin and implications of this structural feature were not analysed¹²⁴.

2.2 Structure elucidation of microcrystalline BTAs by NMR crystallography: beyond the limits of X-ray diffraction

The easy self-assembly of BTAs into columnar aggregates is largely based on cooperative electronic and dipolar effects⁴⁴. Introduction of additional dipole moments through the C-F bonds in **4** changes these interactions. Additionally, the fluorine atoms in the presented columnar structure might

2.2 Structure elucidation of microcrystalline BTAs by NMR crystallography

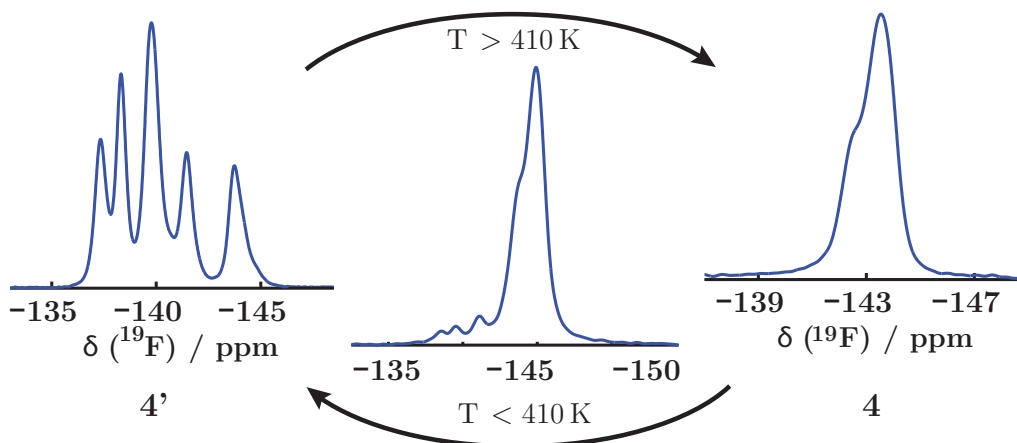


Figure 8: One-dimensional ^{19}F NMR experiments at a MAS rate of 60 kHz show that the BTA **4** exhibits enantiotropic polymorphism, where the structure reported above is stable above 410° K (right spectrum) and converts to a different structure **4'** (left spectrum) below.

reduce the strength of the hydrogen bonds by the NH-F interactions and hence different other packing schemes might have higher stability. Indeed, **4** shows enantiotropic polymorphism with the above investigated structure being stable only above 140° (Fig. 8). The phase being stable below this temperature - denoted as **4'** - does not form suitable single-crystals so that powder methods have to be invoked. Initial structure solution from powder data revealed a layer-like hydrogen bond topology. However, the fluorine and methyl groups could not be differentiated unequivocally since the X-ray diffraction contrast origins in the electron density and methyl groups and fluorine atoms have equal electron density.

We thus attempted to use ^{19}F DQ recoupling experiments to support the powder X-ray structure solution and verify the fluorine positions. Since each molecule contains only three ^{19}F molecules which have strong homonuclear couplings but also many ^1H spins, we have to deal with a sparse but strongly coupled homonuclear ^{19}F network in the presence of a dense and strongly coupled ^1H network. In such cases interference effects occur¹²⁵ which might not admit accurate distance measurements or validation of extended models any more. Hence, we investigated in the publication "Influence of proton coupling on symmetry-based homonuclear ^{19}F dipolar recoupling experiments" the existence of ^1H decoupling regimes during ^{19}F homonuclear recoupling and identified an experimental regime, where distance measurements are possible. The basic theory of ssNMR is hereby contained in the manuscript "Solid state NMR spectroscopy" and will not be discussed here.

2.2.1 Implementation of ^{19}F DQ experiments at high magic angle spinning rates for distance measurements

To systematically investigate the influence of proton coupling and proton decoupling on symmetry-based R sequences for ^{19}F as well as a supercycled version of this sequence, we performed numerical simulations using various model spin systems (Fig. 9). Model a) is a simple ^{19}F spin pair, whereas model b) is derived from the initial structure solution of **4**⁷. In the remaining models, the different couplings were systematically varied but never exceeded the maximum values encountered in the crystal structure.

For model system a) and b), extensive simulations of DQ recoupling with variable continuous wave (cw) ^1H decoupling were performed and compared (Fig. 10). Firstly, simulations for the well-established robust R14₂⁶ sequence⁸⁸ and its supercycled version¹²⁶ at slow MAS show that the protons significantly reduce the maximum DQ efficiency in all regions; even for large decoupling fields, where the strong decoupling limit is approached, no stable decoupling condition can be identified because rotational resonance effects periodically lead to a recoupling of heteronuclear interactions which perturb the homonuclear recoupling periodically.

Since this sequence is not transferable to high spinning rates due to hardware limitations, the R14₄⁵ sequence was identified as suitable alternative for

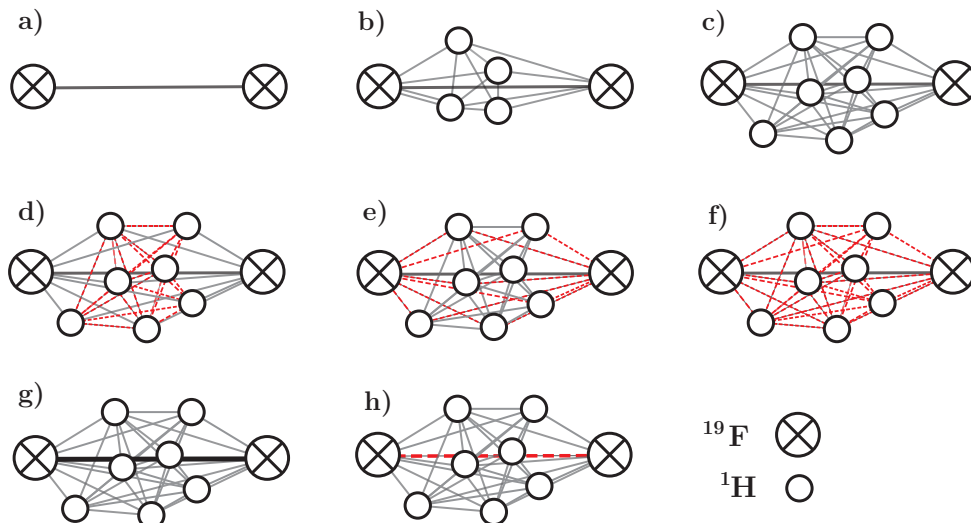


Figure 9: Different model spin systems were used to simulate the influence of proton coupling on symmetry-based ^{19}F DQ recoupling experiments, where the different dipolar interactions were systematically weakened (dashed lines) or strengthened (bold lines).

2.2 Implementation of ^{19}F DQ experiments

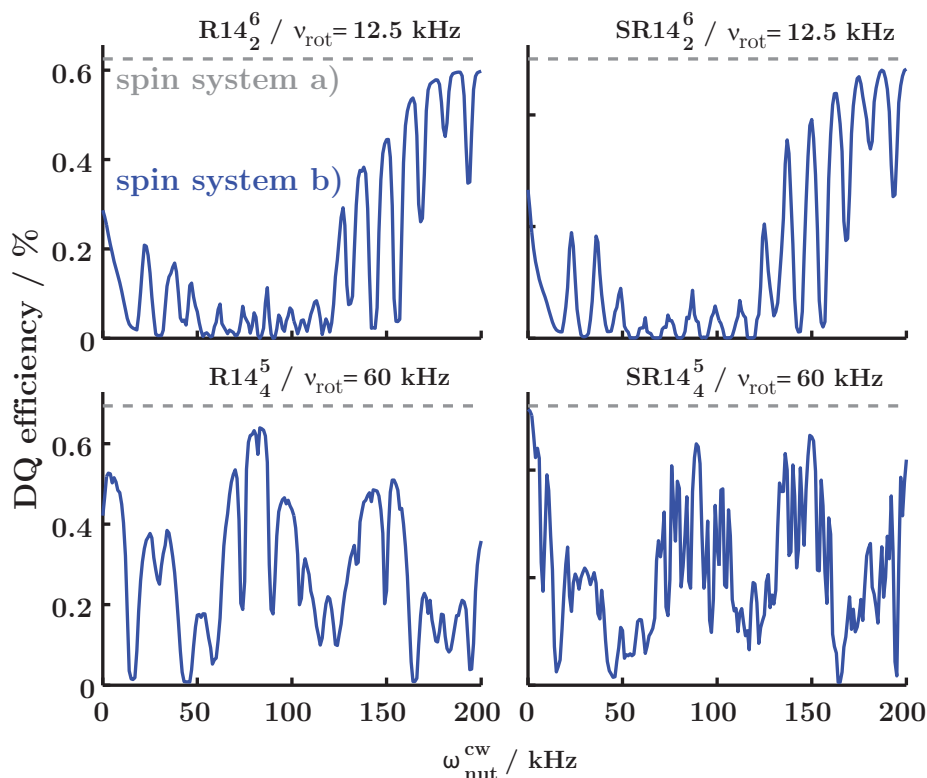


Figure 10: Simulated maximum DQ efficiencies for non-supercycled and supercycled R14_2^6 and R14_4^5 sequences under experimentally realisable spinning speeds (determining the nutation frequencies for R sequences) exhibit no stable strong-decoupling limit. Only for the SR14_4^5 pulse sequences at ultra-fast MAS in the no-decoupling limit are the DQ efficiencies of the model systems b) equivalent to those of the isolated spin pair a) (grey dashed line).

high MAS spinning speeds. The crucial argument beside the applicability at high MAS rates is that the ^1H - ^{19}F heteronuclear dipolar coupling has - in absence of ^1H decoupling fields - the same rotational signature as the Chemical Shift Anisotropy (CSA)¹²⁷. Hence, sequences with intrinsic robustness against CSA - which is indicated by a low number of second-order cross terms between dipolar coupling and CSA in the average Hamiltonian¹²⁸ - are also less prone to heteronuclear perturbations.

Corresponding simulations (Fig. 10) for the R14_4^5 sequence without and with supercycling show that both versions are significantly more robust against the proton couplings in the absence of decoupling fields, but a strong decoupling limit without rotational resonance effects is still not achievable. However, SR14_4^5 recoupling without any cw decoupling - the so-called "no-decoupling limit" - yields almost the same DQ efficiency for the model system b) as for the isolated spin pair a).

The corresponding DQ buildup curves (Fig. 11A, C) show that for the non-

2 Synopsis

supercycled version not only the maximum DQ efficiency decreases but also the course of the curves is heavily distorted by the protons couplings, while supercycling efficiently removes these perturbations; this behaviour is also reproduced by experiments on $4'$ (Fig. 11B, D).

The model system b), however, is a drastic simplification of the real circumstances, where one has often to deal with dense spin systems of strongly coupled protons. Hence, the performance of the no-decoupling regime was probed with model systems c) - f), where the homonuclear ^1H as well as the heteronuclear ^1H - ^{19}F interactions were systematically varied (Fig. 11E). The simulations show that the mainly homonuclear ^1H interactions play a crucial role and quenching them reduces the impact of protons on the ^{19}F DQ buildup curves drastically.

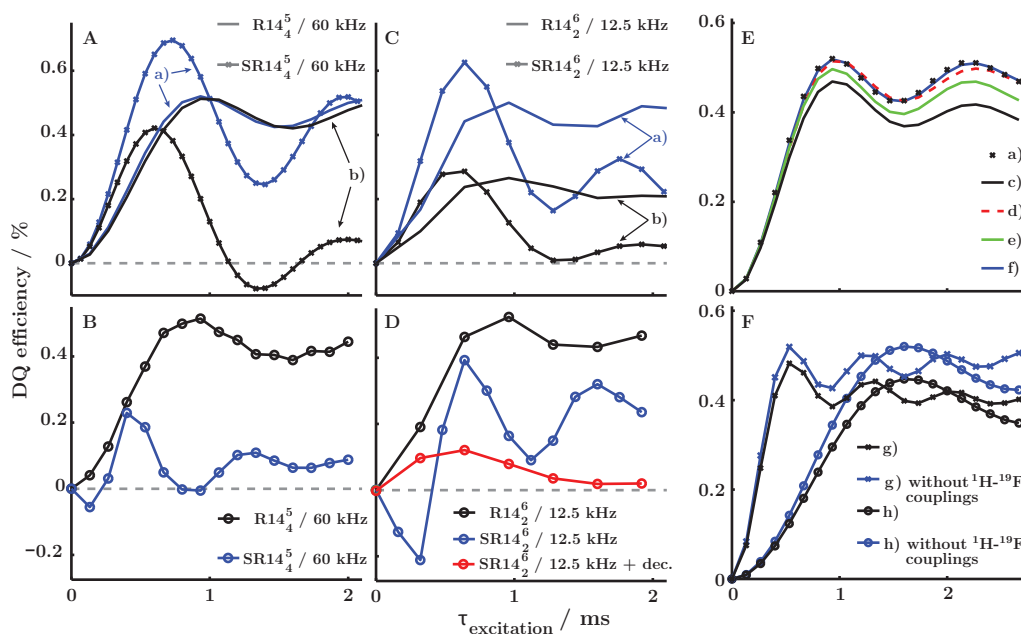


Figure 11: **A**, **C**, The simulation of ^{19}F DQ buildup and **B**, **D**, the experimental DQ buildup curves for $4'$ show that the non-supercycled R sequences are prone to heteronuclear ^1H - ^{19}F couplings contained in the spin systems b), while supercycling removes these perturbations to a great extent. Additional ^1H cw decoupling leads to interference effects which decreases the maximum DQ efficiency. **E**, Simulations for the model system c) show that homonuclear ^1H couplings have strong impact on the ^{19}F DQ buildup and quenching of those (system d)) significantly reduces the heteronuclear interferences, while the simulations for system e) imply that the heteronuclear ^1H - ^{19}F couplings are of minor importance. **F**, Varying the homonuclear ^{19}F coupling strength reveals that the protons scale the buildup curves and the scaling factor increases with decreasing ^{19}F coupling strength.

Hence, the highest possible MAS spinning speeds are favourable because this averages the homonuclear ^1H interactions. Under such conditions, the proton couplings merely scale the DQ curves, where the exact scaling factor depends also on the homonuclear ^{19}F interactions (Fig. 11F) so that experimental DQ buildup curves may be corrected by a constant scaling factor, which, however, has to be optimised empirically as long as the ^{19}F distances are unknown.

2.2.2 Structure elucidation in a fluorinated BTA: the impact of fluorine on the supramolecular interactions

The foregoing results allowed us to investigate the structure of **4'** using NMR crystallography. One-dimensional (1D) spectra of ^{19}F (Fig. 12b) and

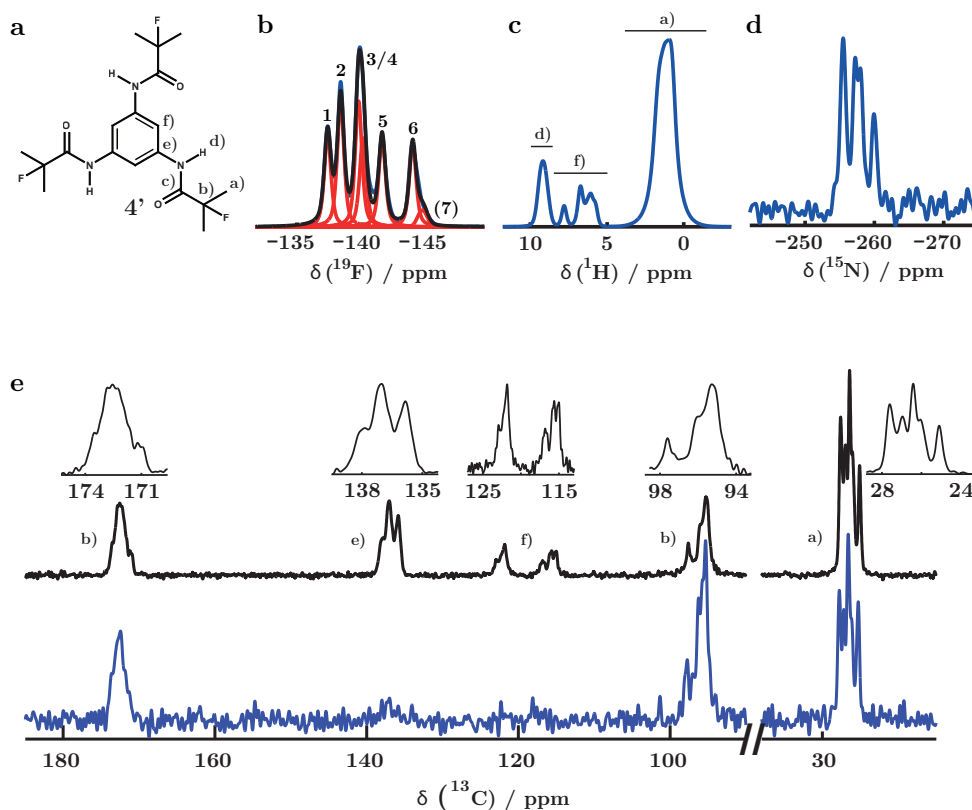


Figure 12: **a**, Molecular structure of **4'**. **b**, The high-resolution 1D ^{19}F MAS spectrum acquired after direct excitation shows six distinct signals with equal intensities (7 demarks an impurity), indicating the presence of two symmetry-independent molecules in the asymmetric unit. **c** - **e**, High-resolution MAS spectra of ^1H (**b**) acquired with direct excitation and CP spectra of ^{15}N (**c**) and ^{13}C (**d**, black curve) support this thesis. The $^{19}\text{F} \rightarrow ^{13}\text{C}$ CP (**d**, blue curve) allows to assign each ^{13}C signal by using sufficiently short $^{19}\text{F} \rightarrow ^{13}\text{C}$ CP contact times, which probe spatial fluorine-carbon proximities; this also shows that the methyl, quaternary carbon and carbonyl groups are close to fluorine atoms.

2 Synopsis

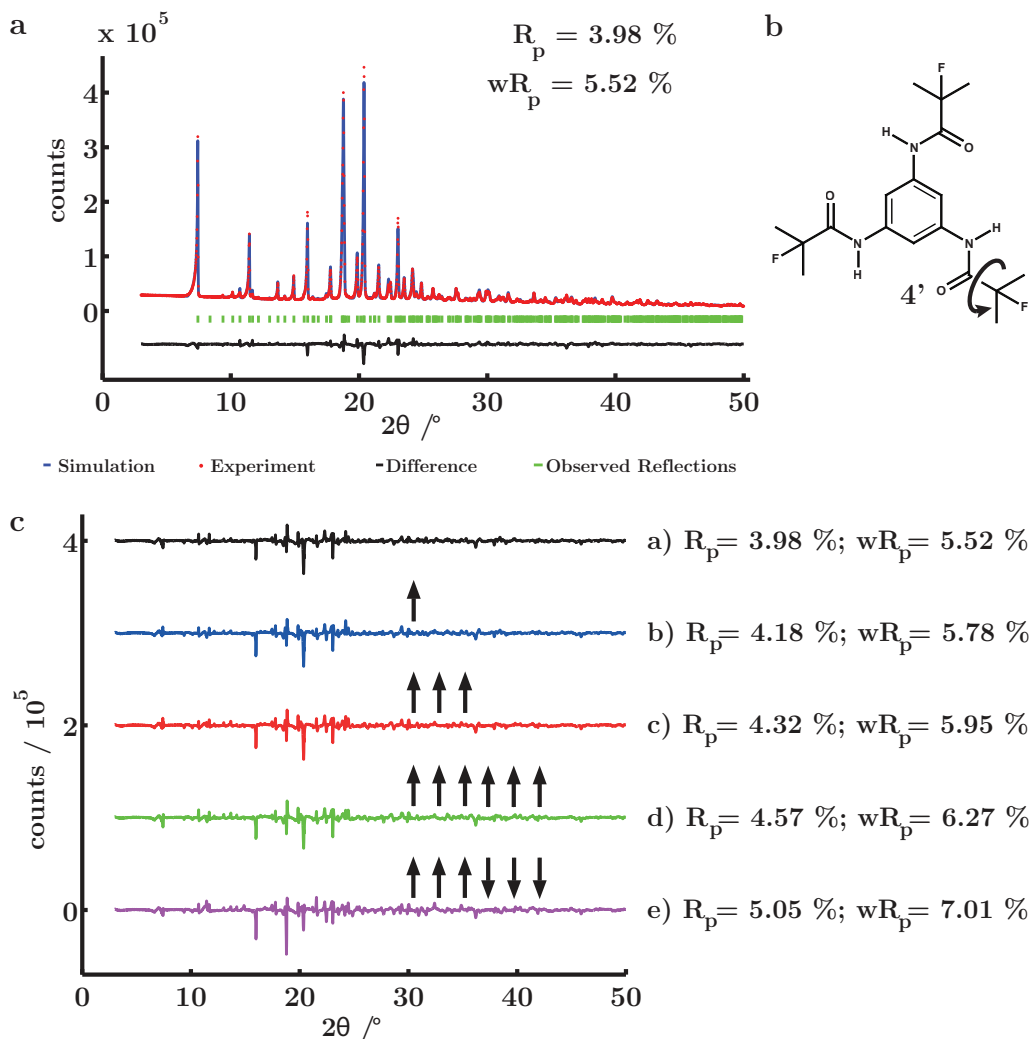


Figure 13: In the structure model for 4' obtained from PXRD structure solution (a), a rotation about the $C(O)-CF(CH_3)_2$ bond by 120° (b) results in new models with equivalent R_p factors and highly similar Rietveld difference curves (c; the arrows demark the number of bonds about which was rotated).

1H (Fig. 12c) with direct excitation as well as ^{15}N (Fig. 12d) and ^{13}C Cross Polarisation (CP) experiments (Fig. 12e) strongly suggest that the structures contains two symmetry-inequivalent molecules.

Indexing of the corresponding powder pattern (Fig. 13a) reveals a monoclinic metric and subsequent Pawley refinement admits a series of different space groups. The combination of PXRD and NMR information was then used to exclude all possibilities except one: Under consideration of the unit cell volume (1924 \AA^3) and of the molecular volume (490 \AA^3 , based on the assumption of 18 \AA^3 for all non-hydrogen atoms) only four molecules can be contained in the unit cell, while NMR predicts two molecules contained

in the asymmetric unit. Since the molecule cannot exhibit a twofold and is unlikely to exhibit a mirror symmetry, it must be located on a general position; this, however, is only possible in the space groups $P2$, $P2_1$, Pm and Pc . Extinction of odd $0k0$ reflections indicates a 2_1 screw axis and hence the space group $P2_1$ is concluded.

Rietveld refinement yields a reasonable structure solution (Fig. 13a), but rotation of the fluoro-dimethyl-propionyl groups about the $C(O)-CF(CH_3)_2$ bonds of 120° (Fig. 13b) results in highly similar Rietveld fits (Fig. 13c). This is due to the equal electron number of fluorine atoms and methyl groups, so that the limited information content of a powder pattern is not sufficient to distinguish them.

Hence, ^{19}F DQ buildup curves were measured and simulations for the various models were fit to the experimental data by applying a scaling factor - numerically optimised for each model - to the simulated curves (Fig. 14). For all models except a), at least one simulation rises faster than any of the experimental curves, which indicates $^{19}F-^{19}F$ distances in the model being shorter than experimentally observed. This behaviour was quantified by

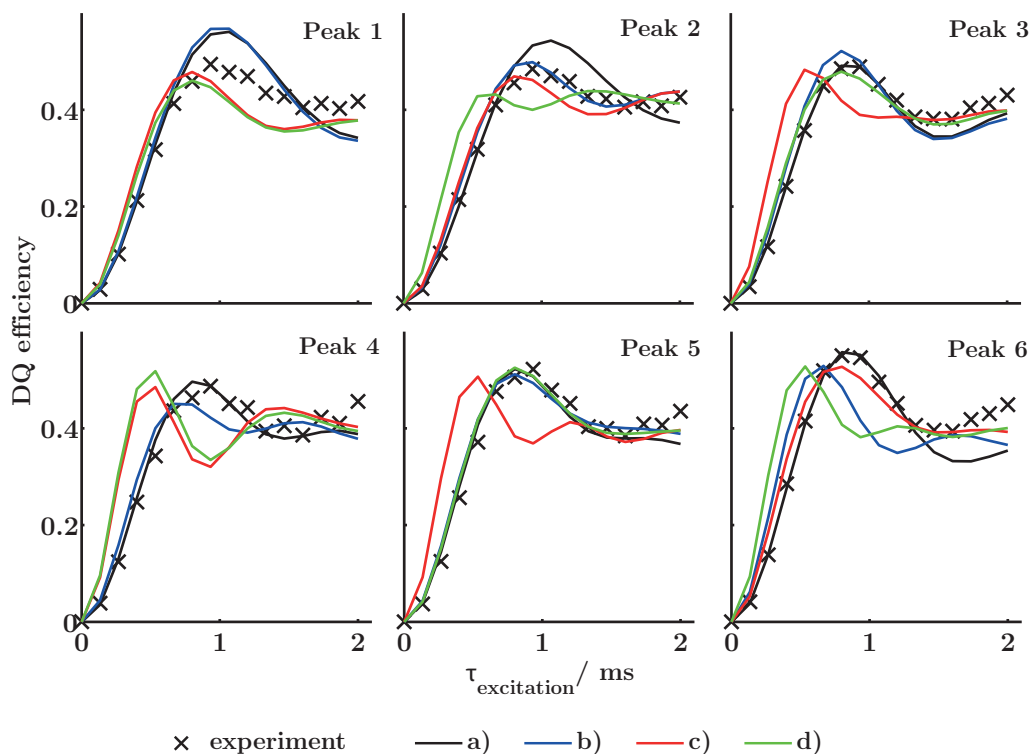


Figure 14: DQ buildup simulations for the different models (cf. Fig. 13) allow to discriminate those and support structure a).

2 Synopsis

calculating the root-mean-square deviations (Fig. 15), where a) is at least 1.5 % better than all others.

Structure a) is the result of initial PXRD structure solution, which uses molecules being geometry optimised by DFT methods as a rigid body during real-space structure solution. Because these molecules are treated as isolated during geometry optimisation, the amide bonds are fully conjugated with the benzene ring and a weak NH-F contact forms. The rotation about the C(O)-CF(CH₃)₂ bonds to form the structure

models b)-e) breaks these contacts and leads to shorter fluorine-fluorine distances, which, however, can be excluded by the DQ buildup curves.

Hence, the structure (Fig. 16) consists of molecules stacked along the *c* axis, but the benzene rings are not coplanar and no columnar packing is formed; hydrogen bonds along the *a* and *b* axes create to a two-dimensional pattern with van der Waals interactions between neighbouring layers.

Interestingly, the carbonyl bonds within a single molecule do not all point into the same direction, as observed for **4**, but two point in one and the remaining bond into the opposite half space of the benzene plane. This intrinsically reduces the dipole moment of a single molecule from **4** to **4'** by a factor of three. A coarse estimation of the dipole moments of the molecules

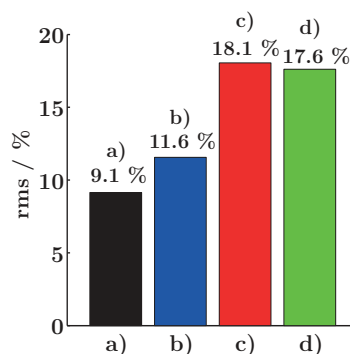


Figure 15: Root-mean-square deviations of experimental and simulated curves favour model a).

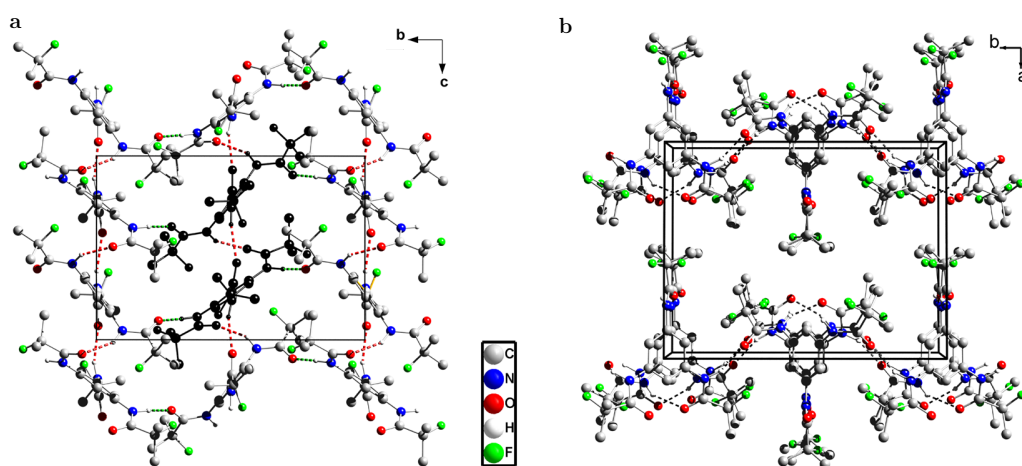


Figure 16: **a**, In the structure of **4'**, a two-dimensional intermolecular hydrogen bond pattern is formed along the *b* and *c* axis. **b**, This leads to a sheet-like structure with van der Waals interactions along the *a* axis between the sheets.

in the asymmetric unit by simple DFT calculations and subsequent addition of all moments in the unit cell show that basically no net dipole moment exists. In contrast to the columnar structure presented above, the growth of supramolecular aggregates supported by cooperative dipole effects does also not take place because the dipole of neighbouring molecules cancel each other. This suggests that, due to the reduction of molecular dipole moments, the cooperativity in the growth of stacks in **4** is reduced so that the columnar structure becomes less stable and polymorphism occurs. This is important for applications such as the nucleation of polymers, where the epitaxial match of the crystal structures of the polymer and additive govern the nucleation efficiency. For instance, polymer processing at temperatures where the undesired modification is formed might then cause unexpected behaviour and even complete failure of the nucleation because this match does not hold any more.

The ^{19}F DQ recoupling method presented here might therefore not only be useful for the particular case of structure solutions in neat materials, but might also aid in structural investigations for complex material systems: for the well-established ^{13}C DQ recoupling, prior work has demonstrated the usefulness not only for NMR crystallographic studies on neat BTAs⁵³, but the method was also successfully transferred to additive-polymer systems to show the structural equivalence of BTA clusters in the polymer matrix and in the bulk phase⁹⁴. Similarly, a transfer of the presented ^{19}F DQ recoupling method could be useful to study the nucleation behaviour of **4/4'**. Since ^{19}F exhibits a higher gyromagnetic ratio than ^{13}C and hence stronger homo- and heteronuclear dipolar couplings, fluorinated BTAs might also be useful model systems to probe the epitaxial match itself, which was not possible before due to the weak homonuclear dipolar ^{13}C interactions between additive and polymer⁹⁴.

2.3 Structure elucidation of 2D self-assembling low-molecular mass organic compounds *via* NMR crystallography

BTAs are designed to favour helical hydrogen bond patterns leading to one-dimensional assemblies, where the cooperative effects allow efficient self-assembly at extremely low concentrations so that even isolated molecular

2 Synopsis

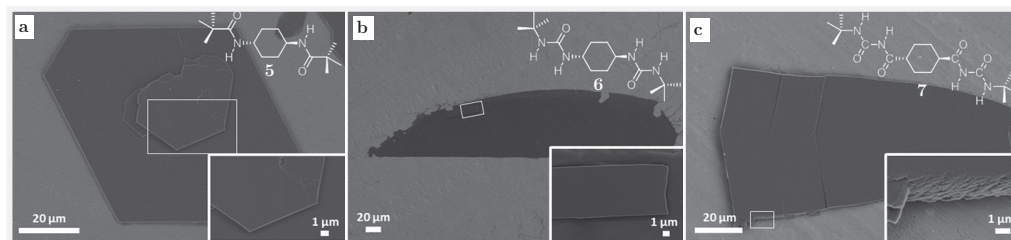


Figure 17: a-c, SEM images show that the compounds **5** - **7** self-assemble into sheet-like supramolecular nanoobjects from organic solvents.

stacks may be formed²². Targeted design of molecular structures forming two-dimensional hydrogen bond patterns resulting in two-dimensional self-assembly, however, proved to be more challenging¹²⁹. One possible explanation might be the lack of or reduced cooperativity, in particular because these systems do often not exhibit macrodipole formation. Here, knowledge of the bulk structures reveals the dominating supramolecular interaction and helps to understand and predict the anisotropic growth of supramolecular nanoobjects.

In the manuscript "NMR-crystallographic study of two-dimensionally self-assembled cyclohexane based low-molecular-mass organic compounds" we studied the crystal structures of three novel low-molecular mass organic (LMO) compounds, which readily assemble into highly anisotropic nanosheets from organic solvents (Fig. 17).

The structure solution for these materials - which form only microcrystalline powders - was achieved using powder X-ray diffraction data and ssNMR in the same combination as for **4'**: first, a complete signal assignment for ^1H , ^{13}C and ^{15}N was carried out using 1D high-resolution (Fig. 18a-d) and 2D heteronuclear correlation (Fig. 18e, f) experiments, which allowed to determine the content of the asymmetric unit to half a molecule for all three compounds. After indexing and Pawley refinement, the space groups could be identified based on the symmetry information from ssNMR and the systematic absences. Subsequent real space structure solution and Rietveld refinement resulted in plausible structure models (Fig. 19).

5 and **6** both form a 2D hydrogen bond network;

between these molecular sheets only van der Waals interactions exist, leading to a highly anisotropic interaction profile and explaining the easy 2D self-assembly (Fig. 17). Surprisingly, **7** forms only 1D molecular chains along the *ab* direction *via* intermolecular hydrogen bonds because the CONH-

2.3 NMR crystallography of 2D self-assembling LMO copounds

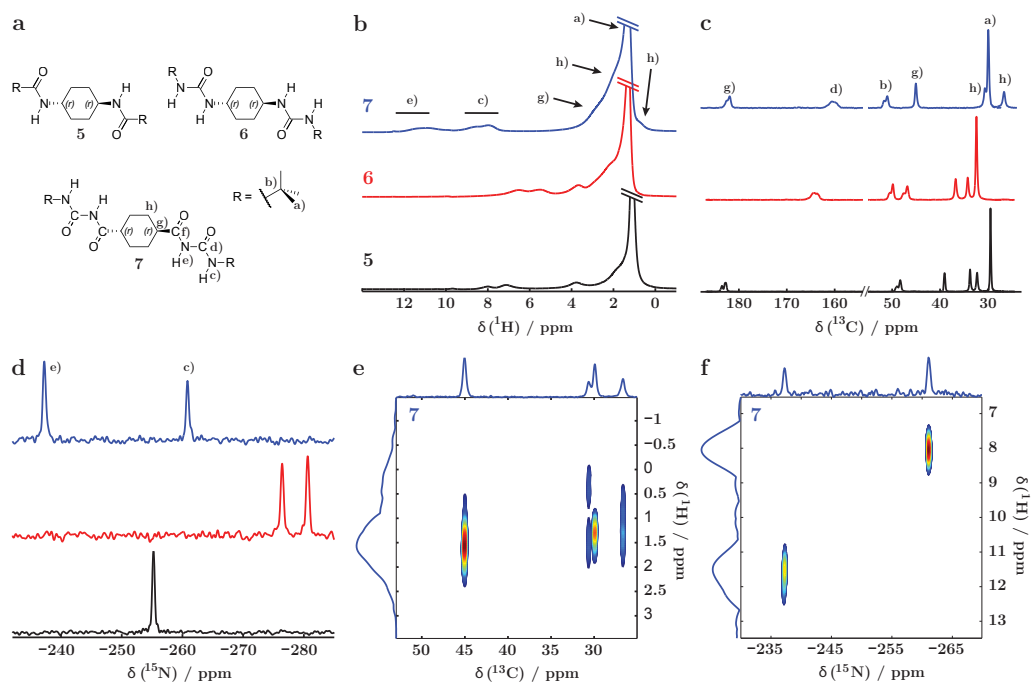


Figure 18: a All chemical units of **5** - **7** can be assigned to the signals in high-resolution ^1H DUMBO (b), $^1\text{H} \rightarrow ^{13}\text{C}$ CP (c), and $^1\text{H} \rightarrow ^{15}\text{N}$ CP spectra by 2D ^1H - ^{13}C (e) and ^1H - ^{15}N (f) correlation experiments which probe spatial proximities; this is exemplarily depicted for **7**.

CONH bond is *cis* configured leading to an intramolecular hydrogen bond, which blocks a CO and NH group; the chains are assembled into sheet-like arrangements, which are stacked along the c^* direction (Fig. 19b). Because the packing is denser within one sheet than between the sheets, the van der

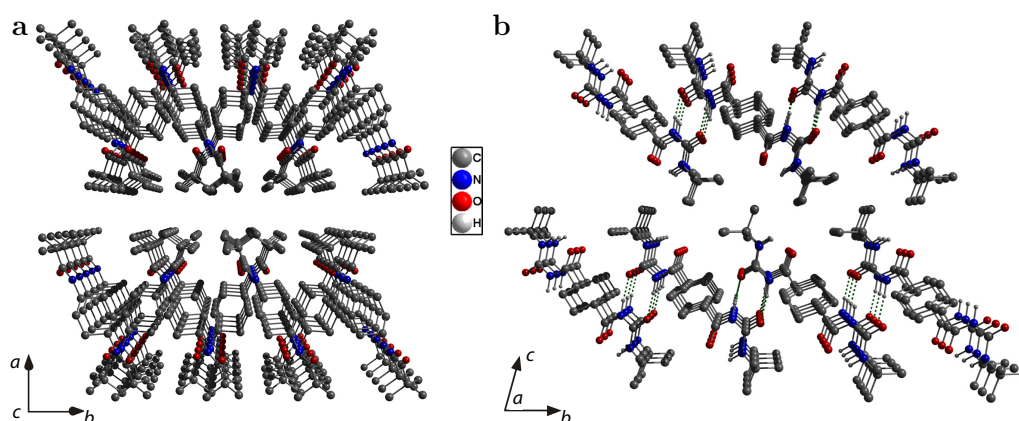


Figure 19: a, In the structure solution of **5**, the molecules are stacked along the c axis and form a 2D hydrogen bond pattern along the b and c direction; between neighbouring layers along the a axis only van der Waals interactions exist. c, In contrast, the molecules of **7** stack along the a axis but form only a 1D hydrogen bond pattern, leading to chain-like building units along the ab direction.

2 Synopsis

Waals interactions are likely to be stronger within it; this might explain the easy self-assembly into 2D nanoobjects despite the 1D hydrogen bond pattern. This implies that - in analogy to chapter 2.1 - packing effects can have significant impact on supramolecular interactions and hence on the resulting self-assembly behaviour.

Moreover, due to the symmetry of the adopted molecular configurations in all three structures, cooperative macrodipole moments cannot play a role in the growth of the hydrogen bond networks and hence these materials are examples of purely hydrogen bond driven supramolecular synthons assembling into highly anisotropic nanoobjects.

Bibliography

- [1] Asadi, K., de Leeuw, D. M., de Boer, B. & Blom, P. W. M. Organic non-volatile memories from ferroelectric phase-separated blends. *Nature Mater.* **7**, 547–550 (2008).
- [2] Li, J.-R. *et al.* Porous materials with pre-designed single-molecule traps for CO₂ selective adsorption. *Nat. Commun.* **4**, 1538 (2013).
- [3] Imani, S. *et al.* A wearable chemical-electrophysiological hybrid biosensing system for real-time health and fitness monitoring. *Nat. Commun.* **7**, 11650 (2016).
- [4] Le-Van, Q., Le Roux, X., Aassime, A. & Degiron, A. Electrically driven optical metamaterials. *Nat. Commun.* **7**, 12017 (2016).
- [5] Schwarze, M. *et al.* Band structure engineering in organic semiconductors. *Science* **352**, 1446–1449 (2016).
- [6] DiSalvo, F. J. Thermoelectric cooling and power generation. *Science* **285**, 703–706 (1999).
- [7] Kaner, R. B., Gilman, J. J. & Tolbert, S. H. Materials science. Designing superhard materials. *Science* **308**, 1268–1269 (2005).
- [8] Lee, D., Redfern, O. & Orengo, C. Predicting protein function from sequence and structure. *Nat. Rev. Mol. Cell Bio.* **8**, 995–1005 (2007).
- [9] Liu, H. *et al.* Capturing metastable structures during high-rate cycling of LiFePO₄ nanoparticle electrodes. *Science* **344**, 1252817 (2014).
- [10] Lehn, J.-M. Perspectives in supramolecular chemistry - from molecular recognition towards molecular information processing and self-organization. *Angew. Chem. Int. Ed.* **29**, 1304–1319 (1990).
- [11] Brunsveld, L., Folmer, B. J. B., Meijer, E. W. & Sijbesma, R. P. Supramolecular Polymers. *Chem. Rev.* **101**, 4071–4098 (2001).
- [12] de Greef, T. F. A. & Meijer, E. W. Materials science: supramolecular polymers. *Nature* **453**, 171–173 (2008).

Bibliography

- [13] Cantekin, S., de Greef, T. F. A. & Palmans, A. R. A. Benzene-1,3,5-tricarboxamide: a versatile ordering moiety for supramolecular chemistry. *Chem. Soc. Rev.* **41**, 6125–6137 (2012).
- [14] Wilson, A. J., van Gestel, J., Sijbesma, R. P. & Meijer, E. W. Amplification of chirality in benzene tricarboxamide helical supramolecular polymers. *Chem. Commun.* **42**, 4404–4406 (2006).
- [15] Smulders, M. M. J. *et al.* Probing the limits of the majority - rules principle in a dynamic supramolecular polymer. *J. Am. Chem. Soc.* **132**, 620–626 (2010).
- [16] Cantekin, S., Balkenende, D. W. R., Smulders, M. M. J., Palmans, A. R. A. & Meijer, E. W. The effect of isotopic substitution on the chirality of a self-assembled helix. *Nat. Chem.* **3**, 42–46 (2011).
- [17] Stals, P. J. M. *et al.* Symmetry breaking in the self-assembly of partially fluorinated benzene-1,3,5-tricarboxamides. *Angew. Chem. Int. Ed.* **51**, 11297–11301 (2012).
- [18] Smulders, M. M. J., Schenning, A. P. H. J. & Meijer, E. W. Insight into the mechanisms of cooperative self-assembly: the "Sergeants-and-Soldiers" principle of chiral and achiral C₃-symmetrical discotic triamides. *J. Am. Chem. Soc.* **130**, 606–611 (2008).
- [19] Markvoort, A. J., ten Eikelder, H. M. M., Hilbers, P. A. J., de Greef, T. F. A. & Meijer, E. W. Theoretical models of nonlinear effects in two-component cooperative supramolecular copolymerizations. *Nat. Commun.* **2**, 509 (2011).
- [20] Albertazzi, L. *et al.* Probing exchange pathways in one-dimensional aggregates with super-resolution microscopy. *Science* **344**, 491–495 (2014).
- [21] Baker, M. B. *et al.* Consequences of chirality on the dynamics of a water-soluble supramolecular polymer. *Nat. Commun.* **6**, 6234 (2015).
- [22] Haedler, A. T. *et al.* Long-range energy transport in single supramolecular nanofibres at room temperature. *Nature* **523**, 196–199 (2015).

- [23] Besenius, P. *et al.* Paramagnetic self-assembled nanoparticles as supramolecular MRI contrast agents. *Contrast Media Mol. I.* **7**, 356–361 (2012).
- [24] Hanabusa, K., Koto, C., Kimura, M., Shirai, H. & Kakehi, A. Remarkable viscoelasticity of organic solvents containing trialkyl-1,3,5-benzenetricarboxamides and their intermolecular hydrogen bonding. *Chem. Lett.* **26**, 429–430 (1997).
- [25] Shi, N., Dong, H., Yin, G., Xu, Z. & Li, S. A smart supramolecular hydrogel exhibiting pH-modulated viscoelastic properties. *Adv. Funct. Mater.* **17**, 1837–1843 (2007).
- [26] Bernet, A., Albuquerque, R. Q., Behr, M., Hoffmann, S. T. & Schmidt, H.-W. Formation of a supramolecular chromophore: a spectroscopic and theoretical study. *Soft Matter* **8**, 66–69 (2012).
- [27] Roosma, J., Mes, T., Leclere, P., Palmans, A. R. A. & Meijer, E. W. Supramolecular materials from benzene-1,3,5-tricarboxamide-based nanorods. *J. Am. Chem. Soc.* **130**, 1120–1121 (2008).
- [28] Abraham, F., Ganzleben, S., Hanft, D., Smith, P. & Schmidt, H.-W. Synthesis and structure-efficiency relations of 1,3,5-benzenetrisamides as nucleating agents and clarifiers for isotactic poly(propylene). *Macromol. Chem. Phys.* **211**, 171–181 (2010).
- [29] Abraham, F., Kress, R., Smith, P. & Schmidt, H.-W. A new class of ultra-efficient supramolecular nucleating agents for isotactic polypropylene. *Macromol. Chem. Phys.* **214**, 17–24 (2012).
- [30] Blomenhofer, M. *et al.* “Designer” nucleating agents for polypropylene. *Macromolecules* **38**, 3688–3695 (2005).
- [31] Kristiansen, P. M., Gress, A., Smith, P., Hanft, D. & Schmidt, H.-W. Phase behavior, nucleation and optical properties of the binary system isotactic polypropylene/*N,N',N''*-tris-isopentyl-1,3,5-benzenetricarboxamide. *Polymer* **47**, 249–253 (2006).
- [32] Stumpf, M., Spörrer, A., Schmidt, H.-W. & Altstädt, V. Influence of supramolecular additives on foam morphology of injection-molded i-PP. *J. Cell. Plast.* **47**, 519–534 (2011).

Bibliography

- [33] Hillenbrand, J. *et al.* The effect of additives on charge decay in electron-beam charged polypropylene films. *J. Phys. D Appl. Phys.* **42**, 65410 (2009).
- [34] Richter, F. & Schmidt, H.-W. Supramolecular nucleating agents for poly(butylene terephthalate) based on 1,3,5-benzenetrisamides. *Macromol. Mater. Eng.* **298**, 190–200 (2013).
- [35] Abraham, F. & Schmidt, H.-W. 1,3,5-benzenetrisamide based nucleating agents for poly(vinylidene fluoride). *Polymer* **51**, 913–921 (2010).
- [36] Nakajima, H., Takahashi, M. & Kimura, Y. Induced crystallization of PLLA in the presence of 1,3,5-benzenetricarboxylamide derivatives as nucleators: preparation of haze-free crystalline PLLA materials. *Macromol. Mater. Eng.* **295**, 460–468 (2010).
- [37] Matsunaga, Y., Miyajima, N., Nakayasu, Y., Sakai, S. & Yonenaga, M. Design of novel mesomorphic compounds - N,N',N''-trialkyl-1,3,5-benzenetricarboxamides. *Bull. Chem. Soc. Jpn.* **61**, 207–210 (1988).
- [38] Bejagam, K. K., Fiorin, G., Klein, M. L. & Balasubramanian, S. Supramolecular polymerization of benzene-1,3,5-tricarboxamide: a molecular dynamics simulation study. *J. Phys. Chem. B* **118**, 5218–5228 (2014).
- [39] Albuquerque, R. Q., Timme, A., Kress, R., Senker, J. & Schmidt, H.-W. Theoretical investigation of macrodipoles in supramolecular columnar stackings. *Chem.-Eur. J.* **19**, 1647–1657 (2013).
- [40] Bejagam, K. K., Kulkarni, C., George, S. J. & Balasubramanian, S. External electric field reverses helical handedness of a supramolecular columnar stack. *Chem. Commun.* **51**, 16049–16052 (2015).
- [41] Sakamoto, A., Ogata, D., Shikata, T. & Hanabusa, K. Controlled large macrodipoles in a supramolecular polymer of tri-3,7-dimethyloctyl-cis-1,3,5-cyclohexanetricarboxamide in n-decane. *Macromolecules* **38**, 8983–8986 (2005).

- [42] Sakamoto, A., Ogata, D., Shikata, T., Urakawa, O. & Hanabusa, K. Large macro-dipoles generated in a supramolecular polymer of N,N',N''-tris(3,7-dimethyloctyl)benzene-1,3,5-tricarboxamide in n-decane. *Polymer* **47**, 956–960 (2006).
- [43] Shikata, T., Kuruma, Y., Sakamoto, A. & Hanabusa, K. Segment sizes of supramolecular polymers of N,N',N''-tris(3,7-dimethyloctyl)benzene-1,3,5-tricarboxamide in n-decane. *J. Phys. Chem. B* **112**, 16393–16402 (2008).
- [44] Filot, I. A. W. *et al.* Understanding cooperativity in hydrogen-bond-induced supramolecular polymerization: a density functional theory study. *J. Phys. Chem. B* **114**, 13667–13674 (2010).
- [45] Jimenez, C. A. *et al.* Influence of the aliphatic wrapping in the crystal structure of benzene tricarboxamide supramolecular polymers. *Cryst. Growth Des.* **9**, 4987–4989 (2009).
- [46] Timme, A., Kress, R., Albuquerque, R. Q. & Schmidt, H.-W. Phase behavior and mesophase structures of 1,3,5-benzene- and 1,3,5-cyclohexanetricarboxamides: towards an understanding of the losing order at the transition into the isotropic phase. *Chem.-Eur. J.* **18**, 8329–8339 (2012).
- [47] Lightfoot, M. P., Mair, F. S., Pritchard, R. G. & Warren, J. E. New supramolecular packing motifs: π -stacked rods encased in triply-helical hydrogen bonded amide strands. *Chem. Commun.* **19**, 1945–1946 (1999).
- [48] Bose, P. P., Drew, M. G. B., Das, A. K. & Banerjee, A. Formation of triple helical nanofibers using self-assembling chiral benzene-1,3,5-tricarboxamides and reversal of the nanostructure's handedness using mirror image building blocks. *Chem. Commun.* **30**, 3196–3198 (2006).
- [49] Rajput, L. & Biradha, K. Three crystalline forms of 1,3,5-benzene-tri(3-pyridinyl)carboxamide from the same solvent system. *J. Mol. Struct.* **876**, 339–343 (2008).

Bibliography

- [50] Rajput, L. & Biradha, K. Crystalline forms of 1,3,5-benzenetri(pyridinyl)carboxamides: isolated site hydrates as polymorphs and solvates. *J. Mol. Struct.* **991**, 97–102 (2011).
- [51] Rajput, L., Mukherjee, G. & Biradha, K. Influence of solvents in assembling tris(4-halophenyl)benzene-1,3,5-tricarboxamides: interplay of N-H···O and halogen···halogen interactions. *Cryst. Growth Des.* **12**, 5773–5782 (2012).
- [52] Kristiansen, M. *et al.* Structural aspects of 1,3,5-benzenetrisamides—a new family of nucleating agents. *Cryst. Growth Des.* **9**, 2556–2558 (2009).
- [53] Schmidt, M. *et al.* Crystal structure of a highly efficient clarifying agent for isotactic polypropylene. *Cryst. Growth Des.* **12**, 2543–2551 (2012).
- [54] Keen, D. A. & Goodwin, A. L. The crystallography of correlated disorder. *Nature* **521**, 303–309 (2015).
- [55] Cheng, Y. T. & Johnson, W. L. Disordered materials: a survey of amorphous solids. *Science* **235**, 997–1002 (1987).
- [56] Damasceno, P. F., Engel, M. & Glotzer, S. C. Predictive self-assembly of polyhedra into complex structures. *Science* **337**, 453–457 (2012).
- [57] Christensen, M. *et al.* Avoided crossing of rattler modes in thermoelectric materials. *Nat. Mater.* **7**, 811–815 (2008).
- [58] Cairns, A. B. & Goodwin, A. L. Structural disorder in molecular framework materials. *Chem. Soc. Rev.* **42**, 4881–4893 (2013).
- [59] Chiritescu, C. *et al.* Ultralow thermal conductivity in disordered, layered WSe₂ crystals. *Science* **315**, 351–353 (2007).
- [60] Welberry, T. R. & Goossens, D. J. Diffuse scattering and partial disorder in complex structures. *IUCrJ* **1**, 550–562 (2014).
- [61] Welberry, T. R. Diffuse x-ray scattering and models of disorder. *Rep. Prog. Phys.* **48**, 1543–1593 (1985).

- [62] Cowley, J. M. *Diffraction physics* (Elsevier Science B.V., Amsterdam and New York, 1995), 3rd rev. ed. edn.
- [63] Hudspeth, J. M., Goossens, D. J. & Welberry, T. R. Approaches to modelling thermal diffuse scattering in triglycine sulfate, $(\text{NH}_2\text{CH}_2\text{COOH})_3 \cdot \text{H}_2\text{SO}_4$. *J. Appl. Crystallogr.* **47**, 544–551 (2014).
- [64] Glas, F., Gors, C. & Hénoc, P. Diffuse scattering, size effect and alloy disorder in ternary and quaternary III–V compounds. *Philos. Mag. B* **62**, 373–394 (1990).
- [65] Pasciak, M., Welberry, T. R., Kulda, J., Kempa, M. & Hlinka, J. Polar nanoregions and diffuse scattering in the relaxor ferroelectric $\text{PbMg}_{1/3}\text{Nb}_{2/3}\text{O}_3$. *Phys. Rev. B* **85**, 224109 (2012).
- [66] Moessner, R. & Ramirez, A. P. Geometrical frustration. *Phys. Today* **59**, 24–29 (2006).
- [67] Wannier, G. H. Antiferromagnetism. The triangular Ising net. *Phys. Rev.* **79**, 357–364 (1950).
- [68] Algara-Siller, G. *et al.* Square ice in graphene nanocapillaries. *Nature* **519**, 443–445 (2015).
- [69] Metropolis, N., Rosenbluth, A. W., Rosenbluth, M. N., Teller, A. H. & Teller, E. Equation of state calculations by fast computing machines. *J. Chem. Phys.* **21**, 1087–1092 (1953).
- [70] Welberry, T. R., Heerdegen, A. P., Goldstone, D. C. & Taylor, I. A. Diffuse scattering resulting from macromolecular frustration. *Acta Crystallogr. B* **67**, 516–524 (2011).
- [71] Cairns, A. B. *et al.* Encoding complexity within supramolecular analogues of frustrated magnets. *Nature Chem.* **8**, 442–447 (2016).
- [72] Schaub, P., Weber, T. & Steurer, W. Exploring local disorder in single crystals by means of the three-dimensional pair distribution function. *Philos. Mag.* **87**, 2781–2787 (2007).
- [73] Weber, T. & Simonov, A. The three-dimensional pair distribution function analysis of disordered single crystals: Basic concepts. *Z. Kristallogr.* **227**, 238–247 (2012).

Bibliography

- [74] Simonov, A., Weber, T. & Steurer, W. Experimental uncertainties of three-dimensional pair distribution function investigations exemplified on the diffuse scattering from a tris-tert-butyl-1,3,5-benzene tricarboxamide single crystal. *J. Appl. Crystallogr.* **47**, 2011–2018 (2014).
- [75] Paddison, J. A. M. *et al.* Hidden order in spin-liquid $\text{Gd}_3\text{Ga}_5\text{O}_{12}$. *Science* **350**, 179–181 (2015).
- [76] Harris, K. D. M., Tremayne, M., Lightfoot, P. & Bruce, P. G. Crystal structure determination from powder diffraction data by Monte Carlo methods. *J. Am. Chem. Soc.* **116**, 3543–3547 (1994).
- [77] Young, R. A., Mackie, P. E. & von Dreele, R. B. Application of the pattern-fitting structure-refinement method of X-ray powder diffractometer patterns. *J. Appl. Crystallogr.* **10**, 262–269 (1977).
- [78] Malmros, G. & Thomas, J. O. Least-squares structure refinement based on profile analysis of powder film intensity data measured on an automatic microdensitometer. *J. Appl. Crystallogr.* **10**, 7–11 (1977).
- [79] Altomare, A. *et al.* EXPO: A program for full powder pattern decomposition and crystal structure solution. *J. Appl. Crystallogr.* **32**, 339–340 (1999).
- [80] Favre-Nicolin, V. & Černý, R. FOX , ‘free objects for crystallography’: A modular approach to ab initio structure determination from powder diffraction. *J. Appl. Crystallogr.* **35**, 734–743 (2002).
- [81] Palatinus, L. & Chapuis, G. SUPERFLIP – a computer program for the solution of crystal structures by charge flipping in arbitrary dimensions. *J. Appl. Crystallogr.* **40**, 786–790 (2007).
- [82] Cheetham, A. K. & Goodwin, A. L. Crystallography with powders. *Nat. Mater.* **13**, 760–762 (2014).
- [83] Waugh, J. S. NMR spectroscopy in solids. A historical perspective. *Anal. Chem.* **65**, 725–729 (1993).

- [84] Laws, D. D., Bitter, H.-M. L. & Jerschow, A. Solid-state NMR spectroscopic methods in chemistry. *Angew. Chem. Int. Ed.* **41**, 3096–3129 (2002).
- [85] Senker, J., Seyfarth, L. & Voll, J. Determination of rotational symmetry elements in NMR crystallography. *Solid State Sci.* **6**, 1039–1052 (2004).
- [86] Taulelle, F. NMR crystallography: crystallochemical formula and space group selection. *Solid State Sci.* **6**, 1053–1057 (2004).
- [87] Senker, J., Sehnert, J. & Correll, S. Microscopic description of the polyamorphic phases of triphenyl phosphite by means of multidimensional solid-state NMR spectroscopy. *J. Am. Chem. Soc.* **127**, 337–349 (2005).
- [88] Carravetta, M. *et al.* Estimation of carbon-carbon bond lengths and medium-range internuclear distances by solid-state nuclear magnetic resonance. *J. Am. Chem. Soc.* **123**, 10628–10638 (2001).
- [89] Jäger, C., Feike, M., Born & Spiess, H.-W. Direct detection of connectivities in glasses by 2D NMR. *J. Non-Cryst. Solids* **180**, 91–95 (1994).
- [90] Martineau, C., Legein, C., Buzaré, J.-Y. & Fayon, F. On the assignment of ^{19}F MAS NMR spectra of fluoroaluminates using through-space spectral edition of ^{19}F - ^{27}Al and ^{19}F - ^{19}F connectivities. *Phys. Chem. Chem. Phys.* **11**, 950–957 (2009).
- [91] Martineau, C., Senker, J. & Taulelle, F. NMR Crystallography. *Annu. Rep. NMR Spectrosc.* **82**, 1–57 (2015).
- [92] Brouwer, D. H., Darton, R. J., Morris, R. E. & Levitt, M. H. A solid-state NMR method for solution of zeolite crystal structures. *J. Am. Chem. Soc.* **127**, 10365–10370 (2005).
- [93] Martineau, C. *et al.* Beyond the limits of X-ray powder diffraction: description of the nonperiodic subnetworks in aluminophosphate-cloverite by NMR Crystallography. *Chem. Mater.* **23**, 4799–4809 (2011).

Bibliography

- [94] Schmidt, M., Wittmann, J., Kress, R., Schmidt, H.-W. & Senker, J. Probing self-assembled 1,3,5-benzenetrisamides in isotactic polypropylene by ^{13}C DQ solid-state NMR spectroscopy. *Chem. Commun.* **49**, 267–269 (2013).
- [95] Seyfarth, L. *et al.* Structure elucidation of cyameluric acid by combining solid-state NMR spectroscopy, molecular modeling and direct-space methods. *J. Mol. Struct.* **889**, 217–228 (2008).
- [96] Brown, S. P., Schnell, I., Brand, J. D., Müllen, K. & Spiess, H. W. An Investigation of $\pi - \pi$ packing in a columnar hexabenzocoronene by fast magic-angle spinning and double-quantum ^1H solid-state NMR spectroscopy. *J. Am. Chem. Soc.* **121**, 6712–6718 (1999).
- [97] Harris, R. K. NMR studies of organic polymorphs & solvates. *Analyst* **131**, 351–373 (2006).
- [98] Castellani, F. *et al.* Structure of a protein determined by solid-state magic-angle-spinning NMR spectroscopy. *Nature* **420**, 98–102 (2002).
- [99] Zehe, C. *et al.* Influence of fluorine side-group substitution on the crystal structure formation of benzene-1,3,5-trisamides. *CrystEngComm* **16**, 9273–9283 (2014).
- [100] Kirkpatrick, R. & Brow, R. K. Nuclear magnetic resonance investigation of the structures of phosphate and phosphate-containing glasses: a review. *Solid State Nucl. Mag.* **5**, 9–21 (1995).
- [101] Casabianca, L. B. & de Dios, A. C. Ab initio calculations of NMR chemical shifts. *J. Chem. Phys.* **128**, 052201 (2008).
- [102] Casabianca, L. B. *et al.* NMR-based structural modeling of graphite oxide using multidimensional ^{13}C solid-state NMR and ab initio chemical shift calculations. *J. Am. Chem. Soc.* **132**, 5672–5676 (2010).
- [103] Pickard, C. J., Salager, E., Pintacuda, G., Elena, B. & Emsley, L. Resolving structures from powders by NMR crystallography using combined proton spin diffusion and plane wave DFT calculations. *J. Am. Chem. Soc.* **129**, 8932–8933 (2007).

- [104] Koller, H., Engelhardt, G., Kentgens, A. P. M. & Sauer, J. ^{23}Na NMR spectroscopy of solids: interpretation of quadrupole interaction parameters and chemical shifts. *J. Phys. Chem.* **98**, 1544–1551 (1994).
- [105] Frydman, L. Multiple-quantum magic-angle spinning experiments on half-integer nuclei: fundamentals. *eMagRes* (2007).
- [106] Tycko, R. & Dabbagh, G. Measurement of nuclear magnetic dipole-dipole couplings in magic angle spinning NMR. *Chem. Phys. Lett.* **173**, 461–465 (1990).
- [107] Sun, B.-Q., Costa, P. R., Kocisko, D., Lansbury, P. T. & Griffin, R. G. Internuclear distance measurements in solid state nuclear magnetic resonance: dipolar recoupling via rotor synchronized spin locking. *J. Chem. Phys.* **102**, 702–707 (1995).
- [108] Schmedt auf der Günne, J. Distance measurements in spin-1/2 systems by ^{13}C and ^{31}P solid-state NMR in dense dipolar networks. *J. Magn. Reson.* **165**, 18–32 (2003).
- [109] Gullion, T. & Schaefer, J. Detection of weak heteronuclear dipolar coupling by rotational-echo double-resonance nuclear magnetic resonance. *Adv. Magn. Reson.* **13**, 57–83 (1989).
- [110] Gullion, T. & Schaefer, J. Rotational-echo double-resonance NMR. *J. Magn. Reson.* **81**, 196–200 (1989).
- [111] Shore, S. E., Ansermet, J.-P., Slichter, C. P. & Sinfelt, J. H. Nuclear magnetic resonance study of the bonding and diffusion of CO chemisorbed on Pd. *Phys. Rev. Lett.* **58**, 953–956 (1987).
- [112] Seyfarth, L. & Senker, J. An NMR crystallographic approach for the determination of the hydrogen substructure of nitrogen bonded protons. *Phys. Chem. Chem. Phys.* **11**, 3522 (2009).
- [113] Andrew, E. R., Bradbury, A. & Eades, R. G. Nuclear Magnetic Resonance spectra from a crystal rotated at high speed. *Nature* **182**, 1659 (1958).
- [114] Jaroniec, C. P. Dipolar recoupling: heteronuclear. *eMagRes* (2009).

Bibliography

- [115] Tycko, R. Dipolar recoupling: homonuclear experiments. *eMagRes* (2009).
- [116] Pileio, G. *et al.* Analytical theory of γ -encoded double-quantum recoupling sequences in solid-state nuclear magnetic resonance. *J. Magn. Reson.* **186**, 65–74 (2007).
- [117] Saalwächter, K., Lange, F., Matyjaszewski, K., Huang, C.-F. & Graf, R. BaBa-xy16: robust and broadband homonuclear DQ recoupling for applications in rigid and soft solids up to the highest MAS frequencies. *J. Magn. Reson.* **212**, 204–215 (2011).
- [118] Zehe, C. S., Siegel, R. & Senker, J. Influence of proton coupling on symmetry-based homonuclear ^{19}F dipolar recoupling experiments. *Solid State Nucl. Mag.* **65**, 122–131 (2015).
- [119] Schmidt, M. *et al.* NMR-crystallographic study of two-dimensionally self-assembled cyclohexane-based low-molecular-mass organic compounds. *CrystEngComm* **15**, 8784–8796 (2013).
- [120] Nespolo, M., Ferraris, G. & Souvignier, B. Effects of merohedric twinning on the diffraction pattern. *Acta Crystallogr. A* **70**, 106–125 (2014).
- [121] Brandt, U. & Stolze, J. Ground states of the Triangular Ising model with two- and three-spin interactions. *Z. Phys. B Con. Mat.* **64**, 481–490 (1986).
- [122] Takezoe, H., Kishikawa, K. & Gorecka, E. Switchable columnar phases. *J. Mater. Chem.* **16**, 2412–2416 (2006).
- [123] Miyajima, D. *et al.* Ferroelectric columnar liquid crystal featuring confined polar groups within core-shell architecture. *Science* **336**, 209–213 (2012).
- [124] Paikar, A., Pramanik, A. & Haldar, D. Influence of side-chain interactions on the self-assembly of discotic tricarboxyamides: a crystallographic insight. *RSC Adv.* **5**, 31845–31851 (2015).

- [125] Marin-Montesinos, I. *et al.* Heteronuclear decoupling interference during symmetry-based homonuclear recoupling in solid-state NMR. *J. Magn. Reson.* **177**, 307–317 (2005).
- [126] Kristiansen, P. E., Carravetta, M., van Beek, J. D., Lai, W. C. & Levitt, M. H. Theory and applications of supercycled symmetry-based recoupling sequences in solid-state nuclear magnetic resonance. *J. Chem. Phys.* **124**, 234510 (2006).
- [127] Levitt, M. H. Symmetry-based pulse sequences in Magic-Angle spinning solid-state NMR. *eMagRes* (2007).
- [128] Kristiansen, P. E., Mitchell, D. J. & Evans, J. N. S. Double-quantum dipolar recoupling at high Magic-Angle spinning rates. *J. Magn. Reson.* **157**, 253–266 (2002).
- [129] Govindaraju, T. & Avinash, M. B. Two-dimensional nanoarchitectonics: organic and hybrid materials. *Nanoscale* **4**, 6102–6117 (2012).

3 Index of Publications

1. Schmidt, M., Zehe, C. S., Siegel, R., Heigl, J. U., Steinlein, C., Schmidt, H.-W., Senker, J. NMR-crystallographic study of two-dimensionally self-assembled cyclohexane based low-molecular-mass organic compounds, *CrystEngComm*, **15**, 8784–8796 (2013).
2. Zehe, C. S., Schmidt, M., Siegel, R., Kreger, K., Daebel, V., Ganzleben, S., Schmidt, H.-W., Senker, J. Influence of fluorine side-group substitution on the crystal structure formation of benzene-1,3,5-trisamides, *CrystEngComm*, **16**, 9273–9283 (2014).
3. Spirkl, S., Grzywa, M., Zehe, C. S., Senker, J., Demeshko, S., Meyer, F., Riegg, S., Volkmer, D. Fe/Ga-CFA-6 – metal organic frameworks featuring trivalent metal centers and the 4,4'-bipyrazolyl ligand, *CrystEngComm*, **17**, 313–322 (2015).
4. Zehe, C. S., Siegel, R., Senker, J. Influence of proton coupling on symmetry-based homonuclear ^{19}F dipolar recoupling experiments, *Solid State Nuclear Magnetic Resonance*, **65**, 122–133 (2015).
5. Zehe, C. S., Hill, J., Funnell, N. P., Kreger, K., van der Zwan, K. P., Goodwin, A. L., Schmidt, H.-W., Senker, J. Mesoscale Polarisation *via* Geometric Frustration in Columnar Supramolecular Crystals, *Angewandte Chemie*, **accepted**.
6. Zehe, C. S., Siegel, R., Senker, J. Solid state NMR spectroscopy, *Handbook of Solid State Chemistry*, **accepted**.

4 Publications

4.1 NMR-crystallographic study of two-dimensionally self-assembled cyclohexane-based low-molecular-mass organic compounds

This work is the result of a cooperation between the Inorganic Chemistry III and the Macromolecular Chemistry I of the University of Bayreuth and will be reproduced from Schmidt, M., Zehe, C. S., Siegel, R., Heigl, J. U., Steinlein, C., Schmidt, H.-W., Senker, J., *CrystEngComm*, **15**, 8784–8796 (2013) in the following with permission from The Royal Society of Chemistry. My contributions are:

- implementation of 2D heteronuclear $^1\text{H} - ^{13}\text{C}$ and $^1\text{H} - ^{15}\text{N}$ correlation pulse sequences and 2D homonuclear $^1\text{H} - ^1\text{H}$ DQ correlation pulse sequences with homonuclear DUMBO decoupling in both dimensions
- measurement of all 1D ^1H DUMBO, $^1\text{H} \rightarrow ^{13}\text{C}$ CP and $^1\text{H} \rightarrow ^{15}\text{N}$ CP spectra
- measurement of all 2D $^1\text{H} - ^{13}\text{C}$, $^1\text{H} - ^{15}\text{N}$, and $^1\text{H} - ^1\text{H}$ correlation spectra
- simulation of ^{14}N influence on ^1H spectra
- evaluation of all NMR data
- co-authorship of the article (authorship of all sections of the publication containing NMR experiments)

The contributions of all other authors are:

- conception and co-/main authorship of the article
- synthesis and characterisation of all chemical compounds
- conduction and evaluation of SEM measurements
- measurement of powder X-ray diffraction patterns
- structure solution from X-ray powder data and evaluation of those
- support of NMR measurements and data evaluation

Cite this: *CrystEngComm*, 2013, 15, 8784

NMR-crystallographic study of two-dimensionally self-assembled cyclohexane-based low-molecular-mass organic compounds†

Marko Schmidt,^a Christoph S. Zehe,^a Renée Siegel,^a Johannes U. Heigl,^b Christoph Steinlein,^b Hans-Werner Schmidt^b and Jürgen Senker^{*a}

Using a combined approach based on scanning electron microscopy, powder X-ray diffraction as well as 1D and 2D multinuclear solid-state NMR spectroscopy, we were able to determine the morphology and the crystal structures for a set of three supramolecular compounds with different hydrogen bonding motifs, namely *N,N'*-(cyclohexane-*trans*-1,4-diyl)bis(2,2-dimethylpropanamide) **1**, 1,1'-(cyclohexane-*trans*-1,4-diyl)bis(3-*tert*-butylurea) **2** and *N,N'*-bis(*tert*-butylcarbamoyl)cyclohexane-*trans*-1,4-dicarboxamide **3**. Based on a complete signal assignment of the 1D solid-state MAS NMR spectra (¹H, ¹³C, ¹⁵N) employing 2D HETCOR experiments and a quantitative evaluation of the corresponding resonances, the content of the asymmetric unit was determined to one half of a molecule. Probing the molecular configuration with ¹H-¹H double-quantum experiments revealed an intramolecular hydrogen bond for compound **3** while **1** and **2** form exclusively intermolecular H-bonds. *Ab initio* structure solutions applying real space methods with an included close-contact penalty were carried out for all compounds. The following Rietveld refinements led to excellent *w*R_p-values between 2.5% and 4.1%. Compounds **1** and **2** crystallise isostructurally in the monoclinic space group *P*2₁/*c* exhibiting a pseudo-biaxial hydrogen bond motif. **3** crystallises in the triclinic space group *P*1̄ with intermolecular head-to-tail hydrogen bonds connecting the molecules to one-dimensional ribbons. Nevertheless, all compounds grow in a sheet-like morphology with lateral dimensions of several hundred micrometres indicating a fast growth in two dimensions along two of the crystal axes. Since all three molecules possess inversion symmetry cancelling the molecular dipole moment the growth mechanism itself has to be dominantly driven by the formation of hydrogen bond networks.

Received 16th June 2013,
Accepted 7th August 2013

DOI: 10.1039/c3ce41158c

www.rsc.org/crystengcomm

Introduction

Within the last decades the field of supramolecular chemistry has attracted significant attention resulting in the synthesis and design of functional molecules evolving into ordered superstructures *via* self-assembly mechanisms. Driven by non-covalent interactions between the constituent parts,¹ like hydrogen bonding, aromatic π - π stacking, CH- π interactions, electrostatic or hydrophobic interactions, these complex structures offer a wide diversity of functions highlighting the versatility and flexibility within this field of research. The dimensionality of the resulting nanostructures (from one- to

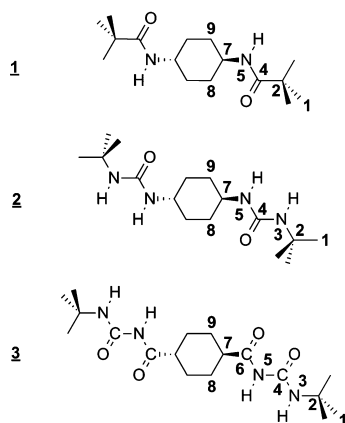
three-dimensional), however, plays a fundamental role in order to vary macroscopic properties.

Certain types of supramolecular building blocks form predominantly one-dimensional nanostructures. Here, benzene-1,3,5-tricarboxamides (BTAs) represent an important class and are described in detail by Cantekin *et al.*² The choice of appropriate substituents results in a broad range of materials. For example organogels,³⁻⁵ hydrogels,^{6,7} discotic liquid crystals,⁸ metal complexation⁹ and MRI-contrast agents,¹⁰ as well as nucleating agents and clarifiers for semi-crystalline polymers¹¹⁻¹⁸ have been reported. The hydrogen bond mediated cooperative effect results in the formation of one-dimensional rod-like nanoobjects. The topological arrangement of these columnar nanostructures is dominated by a (pseudo)hexagonal rod packing.^{19,20} Since each BTA possesses an intrinsic dipole moment, the build-up of these rods is strongly connected to the formation of a macrodipole with a high intrinsic potential energy.²¹ Only the macroscopic compensation of these macrodipoles by neighbouring rods being directed antiparallel and leading to

^a Inorganic Chemistry III and Bayreuth Center for Colloids and Interfaces, University of Bayreuth, 95440, Bayreuth, Germany. E-mail: juergen.senker@uni-bayreuth.de; Fax: +49 921-55-2788; Tel: +49 921-55-2532

^b Macromolecular Chemistry I, Bayreuth Institute of Macromolecular Research and Bayreuth Center for Colloids and Interfaces, University of Bayreuth, 95440, Bayreuth, Germany. E-mail: hans-werner.schmidt@uni-bayreuth.de; Fax: +49 921-55-3206

† Electronic supplementary information (ESI) available. See DOI: 10.1039/c3ce41158c



Scheme 1 Chemical structures of *N,N'*-(cyclohexane-*trans*-1,4-diyl)bis(2,2-dimethylpropanamide) **1**, 1,1'-(cyclohexane-*trans*-1,4-diyl)bis(3-*tert*-butylurea) **2** and *N*¹,*N*¹-bis(*tert*-butylcarbamoyl)cyclohexane-*trans*-1,4-dicarboxamide **3** with labelling of the atoms for the NMR signal assignment.

an antiferroelectric arrangement allows for a fast one-dimensional growth.

Recently, two-dimensional nanostructures with a high aspect ratio have gained increasing interest²² with lateral dimensions ranging from a few hundred nanometres up to the micron scale. Well known inorganic examples are layered silicates²³ and graphene with exceptional properties.^{24–29} Lately, a new pathway to two-dimensional nanoobjects has emerged based on supramolecular self-assembly of low-molecular-mass organic molecules (LMOs).²² Among others, Zentel and co-workers reported a couple of bis-acylurea compounds possessing a C₅ or C₆ alkyl spacer with different functional end groups.^{30,31} An in-depth understanding of the formation of these nanosheets is still challenging. It is quite evident that hydrogen bonding is important. However, the role of dipole moments or even macrodipoles as a driving force for the two-dimensional growth is still an open question.

In order to derive a deeper understanding of the structure–property relations of two-dimensional nanosheets, we selected three materials with different hydrogen bond motifs. The materials (Scheme 1) are based on symmetric substituted *trans*-(1,4)-cyclohexane derivatives with increasing number of donor (NH) and acceptor groups (CO), namely amide **1**, urea **2** and acylurea **3** moieties. We focus on the *ab initio* structure solutions as well as the hydrogen bond networks of these three LMOs. Since the lack of suitable single crystals prevents using single crystal X-ray diffraction experiments, we employ NMR-crystallographic strategies to derive both detailed local and topological features of these compounds. To complement powder diffraction data with solid-state NMR experiments and computational modeling at various steps of the structure

elucidation^{32–35} has proven to be an efficient way to validate or disprove structure models.

Experimental section

Materials and instruments

All solvents were purified and dried prior to use according to standard procedures. The starting materials were purchased from ABCR, Acros, Aldrich, and TCI Europe and used as received. Elementary analysis (C, H, N) were carried out using a Vario elemental EL III instrument. Mass spectra were recorded at RT on a FINNIGAN MAT 112S instrument (70 eV) with electronic impact ionisation and direct probe inlet. SEM was performed on a Zeiss 1530 FESEM (3 kV) with a preceding platinum sputtering using a Cressington Sputter Coater 208HR.

Syntheses of 1–3

The general reaction schemes are depicted in Scheme S1 within the ESI†

N,N'-(Cyclohexane-*trans*-1,4-diyl)bis(2,2-dimethylpropanamide) **1**

Compound **1** was synthesised by dropping pivalic acid chloride (7.3 g, 61 mmol) to a mixture of *trans*-1,4-diaminocyclohexane (3 g, 26 mmol), pyridine (10 mL), LiCl (0.05 g) and *N*-methyl-2-pyrrolidone (NMP, 180 mL) at 0 °C under nitrogen atmosphere. The reaction mixture was heated to 80 °C and stirred overnight. The mixture was precipitated in cold water and the white solid was filtered off, dried under vacuum for 2 h (70 °C, 100 mbar) and re-crystallised from methanol. Yield: 4.5 g (16 mmol, 61.5%, based on *trans*-1,4-diaminocyclohexane). Anal. calculated for **1**: C, 68.04; H, 10.71; N, 9.92. Found: C, 67.34; H, 12.23; N, 9.80%. MS (70 eV), *m/z* (%): 282 (M⁺, 3.3); 197 (10.4); 181 (74.5); 127 (5.7); 102 (100); 85 (9.4); 80 (6.6); 57 (3.8).

1,1'-(Cyclohexane-*trans*-1,4-diyl)bis(3-*tert*-butylurea) **2**

Compound **2** was synthesised by dropping *tert*-butyl isocyanate (dissolved in 400 mL THF at room temperature, 5 g, 101 mmol) to a solution of *trans*-1,4-diaminocyclohexane in THF (10 g, 44 mmol) at 0 °C under argon atmosphere. The mixture was stirred overnight at 80 °C, filtered off, dried under vacuum and re-crystallised from methanol. Yield: 12 g (38 mmol, 87.3%, based on *trans*-1,4-diaminocyclohexane). Anal. calculated for **2**: C, 61.5; H, 10.32; N, 17.93. Found: C, 61.17; H, 11.10; N, 17.78%. MS (70 eV), *m/z* (%): 312 (M⁺, 9.4); 212 (29.2); 197 (18.8); 139 (7.5); 113 (13.2); 96 (18.8); 68 (9.4); 58 (100); 41 (11.3).

*N*¹,*N*¹-Bis(*tert*-butylcarbamoyl)cyclohexane-*trans*-1,4-dicarboxamide **3**

Compound **3** was synthesised by dropping a mixture of cyclohexane-*trans*-1,4-dicarbonyl dichloride (3.14 g, 15 mmol) and 3.65 mL pyridine to a solution of 1-*tert*-butyl urea (3.49 g, 30 mmol) in THF at 0 °C under argon atmosphere. The reaction mixture was stirred overnight at 70 °C, filtered off, dried

under vacuum for 2 h at 70 °C and re-crystallised from DMF. Yield: 2.2 g (6 mmol, 40%, based on cyclohexane-*trans*-1,4-dicarbonyl dichloride). Anal. calculated for 3: C, 58.64; H, 8.75; N, 15.21. Found: C, 58.42; H, 8.81; N, 15.16%. MS (70 eV), m/z (%): 353 (M^+ , 91.5); 313 (4.7); 280 (33.9); 254 (15.1); 240 (7.5); 197 (6.6); 169 (14.1); 126 (29.2); 109 (3.7); 81 (17.9); 59 (100).

Ab initio structure determination with powder X-ray diffraction

PXRD measurements for compounds 1–3 were carried out in Debye–Scherrer geometry on a STOE StadiP diffractometer, which was equipped with Cu $K\alpha_1$ radiation ($\lambda = 1.5406 \text{ \AA}$) and a curved germanium monochromator (oriented according to the 111 plane). The samples were filled in capillary tubes with a diameter of 0.5 mm and measured in the 2θ range of 3–50° with a step size of 0.015°. The powder diffractograms were fully handled using the module REFLEX PLUS from the commercial program package Accelrys MS Modeling (version 5.0).³⁶ After indexing, Pawley refinement and space group assignment, the structure solution step was performed by means of real-space methods using the parallel tempering algorithm. For every structure solution, the molecule was first geometry optimised using DFT methods (see section Computational methods). As starting models for compounds 1–3 only half a molecule was set into the asymmetric unit as one motion group. Besides the possible rotational and translational degrees of freedom, all sustainable torsion angles in each molecule fragment were set free during the structure solution. Additionally, a preferred orientation model (March–Dollase) was applied during the solution with focus on the shape of the crystallites (R_0) as well as the orientation of the normal of the crystal faces (a^* , b^* , c^*).³⁷

For the Rietveld refinement, at first four cycles including a relaxation of atomic parameters, a global isotropic temperature factor and a preferred orientation correction according to the Rietveld–Toraya equation^{38,39} were carried out. By taking into account energy considerations using the COMPASS force field,⁴⁰ the molecular structure was maintained without limiting rotational and translational degrees of freedom. The resulting number of refined structural parameters (see Table 1) is hence not strictly representative due to the application of the energy constraint during the refinement. This force field assisted refinement is based on a combined figure of merit (R_{comb}) with

$$R_{\text{comb}} = (1 - w_{\text{comb}})wR_p + w_{\text{comb}}R_{\text{Energy}} \quad (1)$$

where w_{comb} represents the energy weighting factor that was set to 0.5. The energetic contribution, R_{Energy} , to the combined figure of merit is defined as follows:

$$R_{\text{Energy}} = \tanh\left(0.1 \frac{E - E_{\text{min}}}{E_{\text{tol}}}\right) \quad (2)$$

where E represents the total energy, E_{min} the energy in the global minimum and E_{tol} the energy window above E_{min} in which possible structure solutions are tolerated. Here, the

Table 1 Relevant crystallographic data for 1–3 from PRXD

	1	2	3
Formula	C ₁₆ H ₃₀ N ₂ O ₂	C ₁₆ H ₃₂ N ₄ O ₂	C ₁₈ H ₃₂ N ₄ O ₄
$M/g \text{ mol}^{-1}$	282.42	312.45	368.47
Crystal system	Monoclinic	Monoclinic	Triclinic
Space group	$P2_1/c$	$P2_1/c$	$P1$
$a/\text{\AA}$	14.183(3)	15.435(7)	6.092(3)
$b/\text{\AA}$	6.159(1)	6.762(3)	7.325(4)
$c/\text{\AA}$	9.889(2)	8.883(4)	12.473(6)
$\alpha/^\circ$	90	90	73.828(3)
$\beta/^\circ$	98.383(1)	96.343(2)	83.507(3)
$\gamma/^\circ$	90	90	87.597(2)
$V/\text{\AA}^3$	854.6(8)	921.4(12)	531.1(8)
Z/Z	0.5/2	0.5/2	0.5/1
$\rho/g \text{ cm}^{-3}$	1.097(1)	1.125(2)	1.151(2)
T/K	293	293	293
U	0.20(1)	0.14(1)	0.23(1)
V	-0.021(3)	0.005(3)	-0.012(4)
W	0.0029(2)	0.0013(2)	0.0025(2)
NA	0.42(2)	0.79(4)	0.76(3)
NB	0.001(1)	0.002(2)	0.00(2)
Zero-point shift	-0.031(1)	0.009(1)	-0.021(1)
R_0^a	0.223	0.654	0.868
a^*	0.9877(2)	-0.9885(3)	-0.109(5)
b^*	0.137(1)	0.147(2)	-0.087(9)
c^*	0.074(1)	0.030(2)	-0.990(1)
No. ref. struct. par. ^b	81	87	93
R_p	0.0272	0.0217	0.0157
wR_p	0.0411	0.0301	0.0254

^a Preferred orientation coefficient of the sample according to the March–Dollase function representing a dimensionless value reflecting the shape of the crystallites; $R_0 < 1$ for platelets, $R_0 > 1$ for needles.³⁷ The number of refined structural parameters includes one isotropic temperature factor and three translational elements of each atom within the asymmetric unit. Since a COMPASS force field with an energy constraint was applied, the refinement of the atomic positions is not handled independently.

default value of 40 kcal mol⁻¹ was used prohibiting the breaking of covalent bonds during the refinement and thus reducing the independent number of refined structural parameters markedly.

Afterwards, besides the adjustment of the lattice parameters, the pseudo-Voigt peak profile including FWHM with its profile parameters NA and NB were optimized. The pseudo-Voigt peak shape function as a linear combination of a Gaussian (G) and a Lorentzian (L) includes a θ -dependent mixing parameter η whose θ -dependence is thus given by

$$\eta(\theta) = (NA + NB)2\theta \quad (3)$$

where NA and NB are adjustable parameters. Besides, the zero-point shift, sample off-centering, asymmetry correction (Finger–Cox–Jephcoat)⁴¹ and the experimental background using 20 orthogonal polynomials were refined. For both refinement steps, 15 evaluations per cycle per degree of freedom were performed. Relevant crystallographic data are summarized in Table 1. Atomic parameters, the temperature factor and the occupancy of 1–3 are included in the CIF files which are provided in the ESI.†

Solid-state NMR spectroscopy

¹H and ¹³C chemical shifts are referenced to TMS ($\delta_{\text{ref}}(^1\text{H}_3\text{C})_4\text{Si}$) = 0 ppm, $\delta_{\text{ref}}(\text{H}_3^{13}\text{C})_4\text{Si}$) = 0 ppm), ¹⁵N

chemical shifts are reported with respect to nitromethane ($\delta_{\text{ref}}(\text{H}_3\text{C}-^{15}\text{NO}_2) = 0$ ppm). The spin rate for all MAS experiments was set to $10\,000 \pm 1$ Hz. The 1D ^1H -DUMBO and 2D ^1H - ^1H double-quantum-single-quantum (DQ-SQ) correlation experiments were performed on a Bruker Avance III spectrometer at a proton resonance frequency of 400 MHz with a 3.2 mm triple resonance probe. The CP and the HETCOR experiments on ^{13}C and ^{15}N were performed on a Bruker Avance II spectrometer with a proton frequency of 300 MHz using a 4 mm triple resonance probe. For the latter experiments proton broadband decoupling was realised with a SPINAL64 sequence during acquisition. The nutation frequency and pulse length were set to 72 kHz and 5.6 μs (^{15}N)/6.8 μs (^{13}C), respectively.

For the ^1H -DUMBO experiments the DUMBO pulse length and the nutation frequency were adjusted to 30.50 μs and 89.3 kHz, respectively. The total window length between the DUMBO pulses during acquisition was set to 5.6 μs with a dead time delay of 1.2 μs before acquiring a point. A CRAMPS scaling factor of $\lambda_{\text{scaling}} = 0.5$ was determined on glycine, where all isotropic chemical shifts are well known.⁴² Subsequently, the shifts of all ^1H DUMBO spectra were corrected accordingly.

In the case of the ^1H - ^1H DQ-SQ correlation experiments, double quantum excitation and reconversion was achieved through the R20₂ sequence⁴³ and high resolution in both dimensions through a DUMBO sequence.⁴⁴ For the R-elements, 90–270° composite pulses were used with 80 μs excitation/reconversion time (corresponding to 8 R-elements each) and 100 kHz of nutation frequency. The desired coherences were selected through an eight-fold phase cycling. For DUMBO in the indirect dimension the window length was set to 4.6 μs with an increment of three DUMBO cycles, whereas all remaining parameters for DUMBO in both dimensions were the same as in the one-dimensional DUMBO experiments. For both the indirect and direct dimension a scaling factor of $\lambda_{\text{scaling}} = 0.5$ was determined as described above.

The 1D CP spectra of ^{13}C and ^{15}N were recorded using a ramp on the proton channel and a contact time of 5 ms with nutation frequencies of 35/45 kHz for $^{15}\text{N}/^{13}\text{C}$. For the ^1H - $^{15}\text{N}/^{13}\text{C}$ HETCOR experiments a DUMBO sequence was applied in the indirect dimension with a pulse length of 28.8 μs , a nutation frequency of 91 kHz, a delay of 2 μs and four/three DUMBO cycles as increment. Magnetization transfer was achieved using the PRESTO-II sequence.⁴⁵ It ensures that spin diffusion between the protons during the contact time is suppressed in contrast to conventional magnetisation transfer by CP. For all compounds, the transfer time for PRESTO was set to 178 μs according to 16 R-elements before and after the 90° pulse probing only the closest ^1H - ^{13}C and ^1H - ^{15}N distances. Thus, correlation signals only correspond to covalently bonded nuclei. The nutation frequency for ^1H and $^{15}\text{N}/^{13}\text{C}$ during PRESTO was set to 90 kHz and 39/70 kHz, while the FID was recorded after a spin echo for refocusing the chemical shift interaction. The refocusing period was chosen to one/two rotor periods for $^{15}\text{N}/^{13}\text{C}$, respectively. An eight-fold phase cycling allowed the selection of the desired coherences.

Computational methods

Before the *ab initio* structure solutions of compounds 1–3, all molecules were geometry optimised by DFT methods using the module DMol3 from the program package Accelrys MS Modeling (version 5.0).³⁶ Here, the double zeta plus polarisation basis set with the GGA functional PW91 was applied.⁴⁶ The self-consistent field (SCF) energy convergence was set to 1.0–6 eV per atom.

Results and discussion

Morphology

Morphological analyses using scanning electron microscopy (SEM) reveal a two-dimensional growth of compounds 1, 2 and 3. Large platelets possessing a high aspect ratio were obtained from hot isotropic solutions of butan-2-one with concentrations between 50 and 500 ppm depending on their solubility. Bisamide 1 shows platelets with well-defined edges and a widely homogenous surface (Fig. 1a) whereas bisurea 2 exhibits partly fringed edges but also a homogenous surface (Fig. 1b). At a first glance the bisacylurea 3 shows sharp edges and a homogenous surface as well. However, when magnifying the edge of the platelet, it becomes clear that one platelet consists of several thin sheets (Fig. 1c). In contrast, no fine structure can be determined by using SEM in case of 1 and 2.

Structural information obtained from solid-state NMR spectroscopy

Compounds 1–3 form only microcrystalline powders preventing structure analysis by single crystal X-ray diffraction. Since this circumstance is not specific for our samples but a common case for organic substances, the development of alternative structure elucidation methods for powder samples is necessary. *Ab initio* structure solutions employing solely PXRD data are often hampered by a severe loss of information. Symmetry equivalent reflexes always coincide and higher order reflexes overlap heavily, reducing the number of independent intensity information.⁴⁷ While topological information might still be obtained with reasonable accuracy, local structural details are strongly affected.^{34,47} In this context, solid-state NMR spectroscopy provides complementary data and thus evolved into an important element of NMR crystallographic strategies. Meanwhile, solid-state NMR is able to participate in nearly all steps of the structure solution process starting from space group selection, over model building up to the final Rietveld refinement.^{19,47–50} Symmetry information including the content of the asymmetric unit might be obtained by deriving Wyckoff spectra^{48,51} from high-resolution experiments and by determining rotational symmetry elements^{47,52,53} based on orientation correlations of CSA tensors of neighbouring nuclei. Analysing hetero- and homonuclear connectivities, distances, distance sums and even torsion angles measured by 1D and 2D dipolar recoupling experiments support the construction of structure models.^{19,20,32–34,49,50} The expressiveness of such measurements is significantly increased by

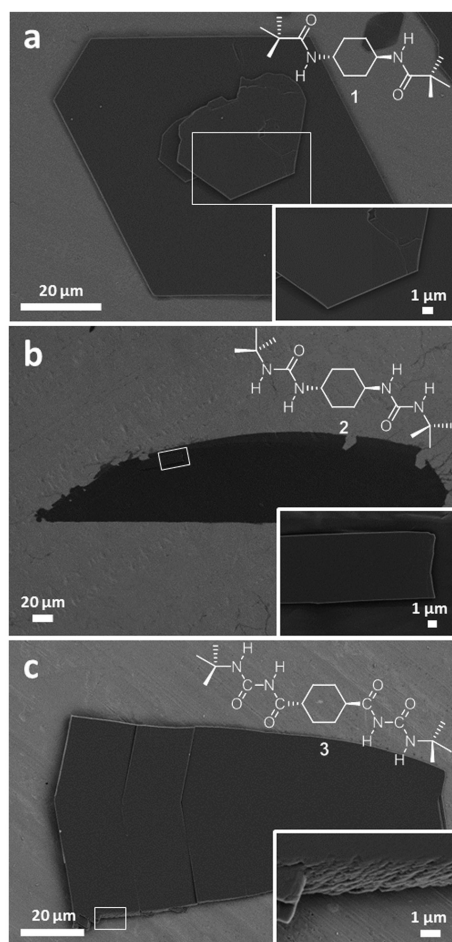


Fig. 1 SEM images of two-dimensional structures of (a) bisamide **1** (500 ppm), (b) bisurea **2** (200 ppm) and (c) bisacylurea **3** (50 ppm) formed in butan-2-one. The regions where the magnified images (insets) have been collected are marked using white boxes.

combination with quantum chemical calculations.^{54,55} For instance, hydrogen bond scenarios can be probed by combining *ab initio* chemical shift calculations and high-resolution NMR measurements.^{34,54,56} Even the substructure of light atoms like hydrogen has successfully been determined.^{32,50} Since most of these methods require high resolution spectra, hetero- and homonuclear decoupling of strongly coupled spin systems like protons is necessary. Moreover, for a correct interpretation of these spectra, a complete assignment of all signals is essential, which can be obtained through 2D heteronuclear correlation experiments.

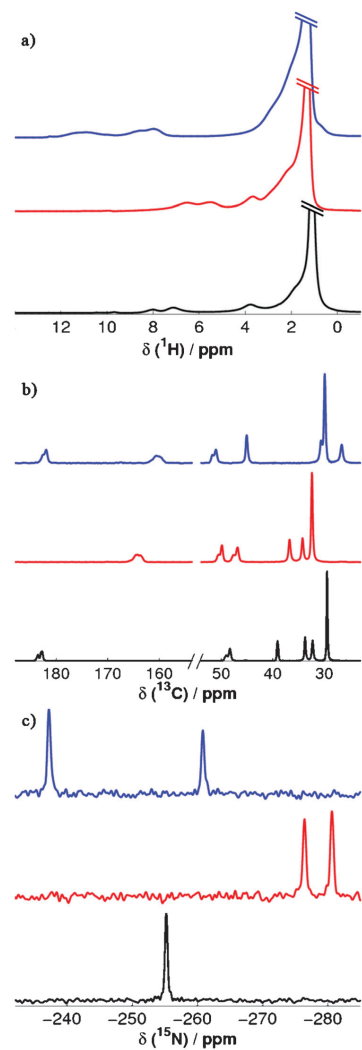


Fig. 2 1D MAS spectra at $\nu_{\text{MAS}} = 10$ kHz for compounds **1** (black), **2** (red) and **3** (blue): (a) ^1H -DUMBO ($B_0 = 9.4$ T); the strong signal of the methyl groups is truncated to highlight the weaker resonances, in particular the NH signals; (b) ^{13}C CP-MAS ($B_0 = 7.04$ T); (c) ^{15}N CP-MAS ($B_0 = 7.04$ T). For the CRAMPS experiments the chemical shifts are corrected according to glycine ($\lambda_{\text{scaling}} = 0.5$).

Following this strategy, information about hydrogen bond patterns, configurations and symmetries of the crystal structures of compounds **1–3** are deduced. In particular, we support the *ab initio* structure solutions by PXRD through solid-state NMR experiments on the three NMR-active nuclei

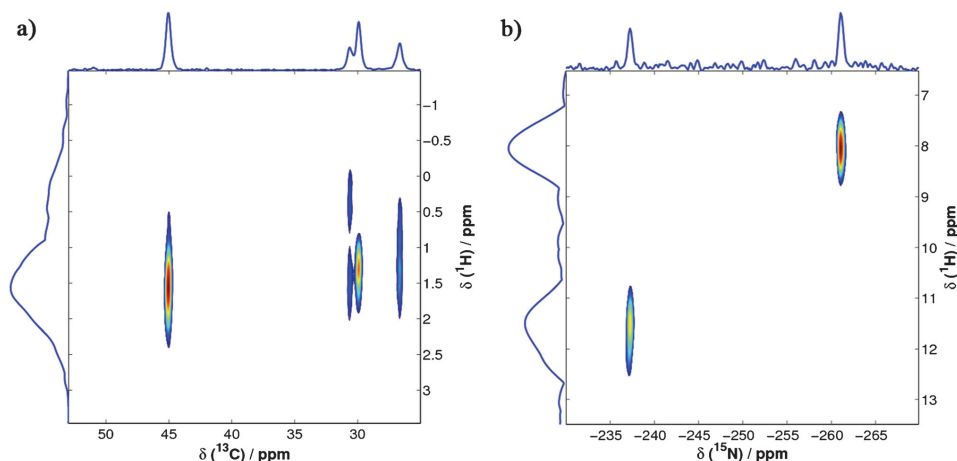


Fig. 3 (a) ^1H - ^{13}C -HETCOR and (b) ^1H - ^{15}N -HETCOR spectrum of compound **3**, at $B_0 = 7.04$ T and $\nu_{\text{MAS}} = 10$ kHz. The ^1H chemical shifts in the f1 domains are corrected according to glycine ($\nu_{\text{scaling}} = 0.5$). The transfer time was set to 178 μs visualising only directly bonded protons.

^1H , ^{13}C and ^{15}N . First, a complete assignment of 1D high-resolution spectra of ^1H , ^{13}C , ^{15}N experiments through 2D ^1H - ^{13}C and ^1H - ^{15}N HETCOR spectra is conducted. Fig. 2 depicts high-resolution 1D spectra of ^1H , ^{13}C and ^{15}N for all three compounds. The assignment will be done exemplarily for compound **3**, since the procedure for the remaining samples is almost identical. The 2D ^1H - ^{13}C -HETCOR and ^1H - ^{15}N -HETCOR experiments for that purpose are pictured in Fig. 3a and 3b.

The ^1H -DUMBO spectrum of **3** shows a sharp, intense peak at $\delta = 1.3$ ppm (Fig. 2a). This signal couples in the ^1H - ^{13}C -HETCOR to a carbon signal at $\delta = 29.9$ ppm (Fig. 3a). Both the ^{13}C and ^1H shifts are indicative for CH_3 groups. Moreover, the sharpness and high intensity of both peaks are characteristic for CH_3 for the following reasons: first, the well-known rotation of the groups around the $\text{C}-\text{CH}_3$ bond truncates dipolar coupling to other spins, which raises the transversal relaxation time and thus reduces the width of the peaks for both spins. Second, the high abundance of CH_3 protons increases their signals in DUMBO as well as in ^{13}C CP. The carbon signals at $\delta = 30.6$ ppm and – remarkably shielded – at $\delta = 26.6$ ppm correspond to the two different sets of CH_2 groups within the cyclohexane ring, one carbon signal with couplings to the resolved proton shifts at $\delta = 0.4$ and 1.6 ppm, the other one with two overlapping proton signals at *ca.* $\delta = 0.8$ and 1.3 ppm. The CH unit of the ring is assigned to the more deshielded peak at $\delta = 1.6$ ppm for ^1H , coupling to the carbon signal at $\delta = 45.0$ ppm, since both carbon and proton shifts are typical for CH groups. The remaining signals in the ^{13}C CP (Fig. 2b, $\delta = 51.2$ ppm, 155.3 ppm and 177.2 ppm) do not give rise to cross correlation peaks in the ^1H - ^{13}C -HETCOR and are thus not covalently bonded to protons. The peak at $\delta = 51.2$ ppm in the ^{13}C CP spectrum is unequivocally

assigned to the quaternary carbon atom of the *tert*-butyl group while the two remaining signals at $\delta = 155.3$ ppm and 177.2 ppm belong to the $\text{C}=\text{O}$ groups. A comparison of their line shapes observed at different magnetic fields of 7.1 T and 9.4 T, respectively, reveals an inverse dependence of the splitting on the field strength. This line shape is, therefore, caused by second order quadrupolar interaction between the neighbouring ^{14}N nucleus and the ^{13}C spins.⁵⁷ This was also reproduced by simulations of 1D spectra for a ^{13}C - ^{14}N spin pair with the program WSOLIDS1 (see Fig. S2b in the ESI†).^{20,58}

To assign the remaining peaks in the ^1H -DUMBO at $\delta = 8.0$ ppm, 8.6 ppm and 11.2 ppm, ^1H - ^{15}N HETCOR experiments were performed (Fig. 3b). The ^{15}N CP spectrum of **3** (Fig. 2c) reveals two different peaks at $\delta = -237.2$ ppm and -261.0 ppm. Here, the ^{15}N site at $\delta = -261.0$ ppm shows correlations with a single proton signal at $\delta = 8.4$ ppm. Since already the carbon atoms directly bound to a nitrogen atom were influenced through second order quadrupolar interaction, a single-pulse experiment under MAS at a higher magnetic field strength and a line shape simulation using WSOLIDS1 were conducted (Fig. S1 and Table S1 in the ESI†).⁵⁸ It becomes clear that the two peaks at $\delta = 8.0$ and 8.6 ppm correspond to a single proton with an isotropic shift of $\delta = 8.4$ ppm. This effect is well-known for NH groups.⁵⁷ The remaining ^{15}N signal at $\delta = -237.2$ ppm shows only one correlation in the ^1H - ^{15}N HETCOR to the proton signal at $\delta = 11.2$ ppm and thus corresponds to the second NH group.

In order to assign the two carbonyl and the two NH signals to the corresponding chemical units, the experimental resonances were compared to chemical shifts in solution-state NMR, being calculated based on an increment system according to ref. 58 (see Table S2 in the ESI†).⁵⁹ Here, the carbon groups C_4 and C_6 of the acylurea group which are

Table 2 Chemical shifts in ppm for all ^1H , ^{13}C and ^{15}N of compounds 1–3 (for labelling see Scheme 1). The asterisks indicate average shifts for cases where the corresponding signals show a splitting due to second order quadrupolar interaction with ^{15}N . All spectra used for assignment of 1 and 2 are contained in the ESI† (Fig. S3 and S4)

Atom	1	2	3	Unit
C ₁	29.5	32.4	29.9	CH ₃
C ₂	39.0	50.0*	51.2*	C _q
C ₄	178.2*	159.2*	155.3*	C=O
C ₆	—	—	177.2*	C=O
C ₇	48.7*	47.2*	45.0	CH
C ₈	32.3	34.2	26.6	CH ₂
C ₉	33.7	36.7	30.6	CH ₂
N ₃	—	-280.6	-261.0	NH
N ₅	-255.2	-276.4	-237.2	NH
H ₁	1.1	1.3	1.3	CH ₃
H ₃	—	6.0*	8.4*	NH
H ₅	7.4*	6.1*	11.2	NH
H ₇	3.5	3.3	1.6	CH
H ₈	1.4	0.5/1.0	0.8/1.3	CH ₂
H ₉	1.0	1.0/1.5	0.4/1.6	CH ₂

connected to the *tert*-butyl unit and the cyclohexane ring, respectively, show a shift of $\delta = 155.7$ ppm and $\delta = 179.4$ ppm, which is close to the observed shifts of $\delta = 155.3$ ppm and 177.2 ppm in the solids. In the case of ^{15}N , for the two nitrogen atoms N₃ and N₅ shifts of $\delta = -277.2$ ppm and -246.0 ppm are predicted, whereas the observed shifts are $\delta = -261.0$ ppm and -237.2 ppm. Considering that the solid-state shifts of ^{15}N in NH groups are usually influenced more strongly by *e.g.* hydrogen bonds than in the case of ^{13}C , the predicted values show a sufficient agreement with the observed ones.

Thus, all signals in the 1D ^1H , ^{13}C and ^{15}N spectra have unequivocally been assigned to the molecular units of compound 3. This procedure was also applied to compounds 1

and 2. The corresponding values for the chemical shifts are summarized in Table 2.

The 1D CP spectra of ^{15}N show only one NH peak for compound 1 and two peaks for 2 and 3. The molecular structures, however, exhibit two nitrogen atoms in the case of 1 and four in the case of 2 and 3. The same comparison applies for the 1D CP spectra of ^{13}C and the ^1H -DUMBO, where the structures always show twice the number of groups than the number of observed resonances. Thus, the asymmetric unit contains just half a molecule and, therefore, both molecular and space group symmetry include a two-fold axis or an inversion centre. The number of possible space groups for structure solutions is thus reduced which will be discussed at a later point.

In order to gain information about spatial proximities of NH protons and thus also possible hydrogen bond patterns of the molecules, we used ^1H - ^1H DQ-SQ correlation experiments. The NH regions of these spectra are exemplarily depicted in Fig. 4 for compound 2 and 3 (for compound 1 see Fig. S5 in the ESI†).

For compound 2, both peaks around $\delta = 5.4$ ppm and 6.4 ppm correspond to two overlapping NH signals of the urea unit with isotropic shifts of $\delta = 6.0$ ppm and 6.1 ppm (extracted from ^1H - ^{15}N HETCOR, see Fig. S4 in the ESI†), both split by the neighbouring ^{14}N (see Table 2). Besides correlations of the NH protons to the aliphatic region (see Fig. S6 in the ESI†), correlations of the NH signals among themselves between $\delta = 10.8$ ppm and 12.8 ppm in the double-quantum dimension are observed. Since the line shapes are affected by the ^{14}N nuclei, we cannot distinguish between cross correlations and autocorrelations. However, both cases indicate spatial proximity of NH protons to other

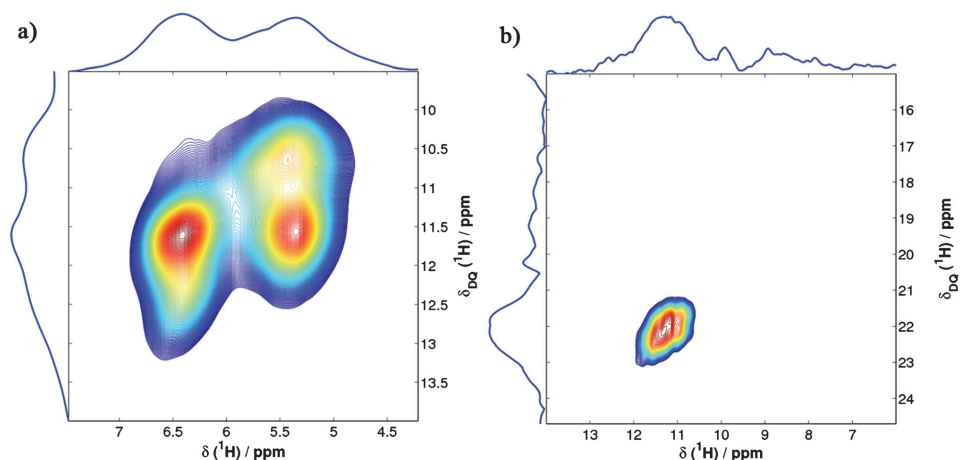


Fig. 4 ^1H - ^1H DQ-SQ correlation spectra of (a) compound 2 and (b) compound 3 at $B_0 = 9.4$ T and $\nu_{\text{MAS}} = 10$ kHz. The excitation and reconversion time was set to 80 μs in both cases for which only the shortest distance correlations are observed. Both chemical shifts of f1 and f2 are corrected according to glycine ($\nu_{\text{scaling}} = 0.5$). Here, the region around the NH protons is shown (the whole spectra are depicted in Fig. S6 and S7 in the ESI†).

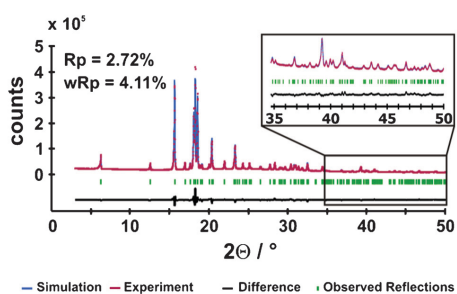


Fig. 5 Rietveld profile plot of the powder X-ray diffraction pattern of **1** for the solution in space group $P2_1/c$ collected at room temperature in the 2θ range 3–50°. The section of the 2θ range of 35–50° shows that even at high 2θ values the simulation fits excellently to the experimental powder pattern.

NH protons. Since the NH units in urea groups usually favour a *trans-trans* configuration each with the connected carbonyl group (e.g. as depicted in Scheme 1 for compound **2**) due to energetic reasons, typical H–H distances for this configuration score around 2 Å.⁶⁰ Strong DQ coherences as detected in Fig. 4a for **2** are thus characteristic for such short distance.

In contrast, for compound **3** only one weak autocorrelation signal is observed for the NH proton H_5 ($\delta(\text{SQ/DQ}) = 11.4 \text{ ppm}/22.8 \text{ ppm}$). First, this clearly indicates a spatial proximity between H_5 protons of the inner NH groups. This is only possible when neighbouring molecules are arranged in a hydrogen bond pattern. Second, for the NH signal of proton H_3 at $\delta = 8.4 \text{ ppm}$ no self-correlation signal is observed ($\delta(\text{DQ, theo}) = 16.8 \text{ ppm}$) and thus the intermolecular distances of H_3 protons have to be much longer compared to the ones of H_5 . Additionally, no correlation between H_3 and H_5 was detected either ($\delta(\text{DQ, theo}) = 19.9 \text{ ppm}$). This implies a long intermolecular distance between those NH protons of the same acylurea unit ($d > 2 \text{ \AA}$) and thus allows determining the molecular configuration. In compound **3** just an additional C=O group is inserted compared to **2** (acylurea compared to urea unit). For an all-*trans* configuration of the acylurea group again a distance around 2 Å between H_3 and H_5 and, therefore, an intense DQ correlation signal similar to Fig. 4a is expected. However, a *trans-cis-trans* configuration leads to a distance of more than 3.5 Å rendering the H_3 – H_5 DQ correlation unobservable under the chosen experimental conditions. The resulting spatial proximity between the oxygen atom of the inner C=O group and the NH proton H_3 favours the formation of an intramolecular hydrogen bond which might stabilise this configuration. The encapsulation of H_3 in this intramolecular hydrogen bond might also explain the absence of any autocorrelation signal. These results indicate a pair-like arrangement of the molecules within the crystal structure.

Structural information obtained by powder X-ray diffraction

The crystal structures for **1–3** were all obtained by *ab initio* structure solutions based on powder X-ray diffraction applying

real-space methods using the combination of a close-contact penalty and wR_p , respectively, as cost functions. All molecules were DFT geometry optimised before performing the structure solutions revealing in all cases a chair conformation of the cyclohexane ring as well as C_1 symmetry which is energetically favoured over the also previously discussed C_2 symmetry. The inversion centre is thereby positioned in the centre of gravity of the cyclohexane ring. In accordance to the ^1H – ^1H DQ-SQ experiments the *trans-cis-trans* configuration of the acylurea unit in compound **3** revealed the lowest energy during DFT optimisation.

$\text{C}_{16}\text{H}_{30}\text{N}_2\text{O}_2$ **1** and $\text{C}_{16}\text{H}_{32}\text{N}_4\text{O}_2$ **2**. The indexing of the powder patterns lead unequivocally to a monoclinic metric in both cases and could subsequently be refined in $P2$ using the Pawley algorithm. Assuming that all non-hydrogen atoms within these compounds possess a volume of roughly 18 \AA^3 , the molecular volumes can be estimated to 360 \AA^3 and 396 \AA^3 , respectively. This size restriction just allows for two molecules within the unit cell at maximum. The reflection conditions do not provide reasonable results for any of the five C -centred space groups but, nevertheless, all remaining 8 primitive ones might be possible. However, based on the symmetry considerations obtained by 1D ^{15}N and ^{13}C solid-state NMR (compare Fig. 3b and 3c) whereupon only half a molecule is located in the asymmetric unit, all possible space groups with the multiplicity of 2 on general positions ($P2$, $P2_1$, Pm and Pc) – then leading to only one molecule in the unit cell – could be excluded. Therefore, only four space groups ($P2/m$, $P2_1/m$, $P2/c$ and $P2_1/c$) remained and, taking into account the reflection conditions, $P2_1/c$ fitted the experimental powder pattern best.

The structure solutions with subsequent Rietveld refinement reveal that **1** and **2** are isostructural and crystallise in the monoclinic space group $P2_1/c$ (for crystallographic information: see Table 1 in the experimental details section). Representative for both compounds, the Rietveld profile plot for **1** is depicted in Fig. 5 (the Rietveld profile plot for **2** is visualised in Fig. S8 in the ESI†). The a -axis of **2** is roughly 1.2 Å longer than for **1** while the c -axis is shortened by ca. 1 Å. The monoclinic angle is slightly reduced by 2° resulting in an increased cell volume of about 65 \AA^3 which perfectly agrees with the volume requirement of two additional NH groups.

Fig. 6 shows the molecular crystal structure as well as extended packing plots of N,N' -(cyclohexane-*trans*-1,4-diyl)bis(2,2-dimethylpropanamide) **1**. Here, the cyclohexane ring exists in the low-energy chair conformation while the (1,4)-amide linkage exhibits *trans*-configuration on the tertiary carbon atom in the ring as synthesised. The internal $\text{H}_4\text{N}_4\text{C}_4\text{O}_4$ torsion angle within the molecule picturing the amide bond is 179.5° which is close to 180° as expected for an amide function (see Fig. 6a) leading to almost coplanarity caused by the inversion symmetry of the molecule itself.

The bisamide compound is characterised by an extended 2D hydrogen bond network. Due to the internal C_1 symmetry, only one $\text{NH}\cdots\text{O}$ length of 2.11 Å is observed. The corresponding $\text{N}\cdots\text{O}$ distance amounts to 3.1 Å while the $\text{NH}\cdots\text{O}$ angle of almost 167° is only slightly below the ideal value of 180° demonstrating medium-strong hydrogen bonds. The *trans*-configuration

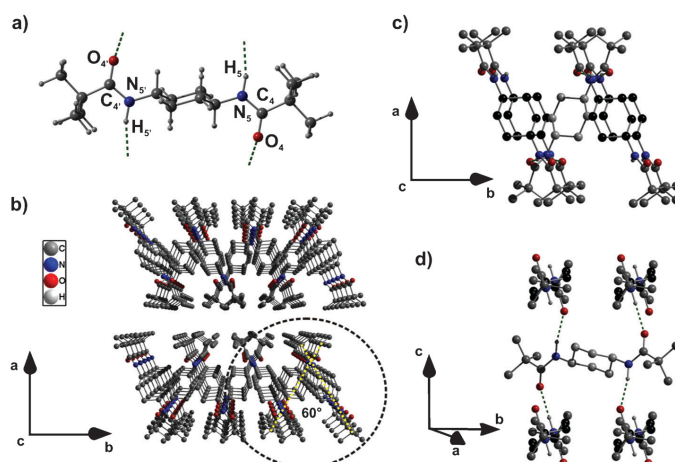


Fig. 6 Molecular structure and extended crystal packing plots of compound **1** with hydrogen bonds highlighted in green dashed lines. (a) Molecular structure of **1** represented with all four hydrogen bond interactions with labelling of the amide function as performed in Scheme 1. (b) Section of the crystal structure viewing along the *c*-axis. The dashed yellow lines represent the opening angle of the molecules main axes projected into the *ab*-plane of the crystal. (c) Cutout of the structure presented in panel b (black dashed circle) showing that one molecule (grey cyclohexane carbon atoms) is enclosed by four molecules (black cyclohexane carbon atoms), two below and two above. This cutout is rotated by 5° along the *b*-axis. (d) Packing plot showing that every molecule builds hydrogen bonds to four neighbouring molecules in one direction. This packing plot is obtained by -90° rotation along the *a*-axis followed by a -35° rotation along the *b*-axis as presented in panel c. All hydrogen atoms except the nitrogen-bonded ones have been omitted in (b)–(d) for clarity.

of the amide functions hence guarantees the formation of two H-bond strands in one direction which is schematically depicted in Fig. 6a.

The propagating direction of the H-bond strands is thereby aligned parallel to the *c*-axis of the crystal leading to a fast growth along this crystal axis. A closer look on the packing motif reveals two additional important features. First, both molecules within the unit cell are twisted towards each other. When assuming a straight line along the main axis of each molecule propagating through the quaternary carbon atoms of the *t*-butyl group followed by a projection into the *ab*-plane of the crystal, an opening angle of 60° is obtained (see Fig. 6b, yellow dashed lines). Second, each amide function within one molecule (NH/CO as donor/acceptor) is connected to one independent counterpart within another molecule. So, every molecule is attached to four neighbouring molecules (see Fig. 6c and 6d) where one donor group interacts with one acceptor group (and *vice versa*). Due to the twist of the molecules, however, a second 'indirect' propagation direction along the *b*-axis that also possesses the tendency of growing fast is observed. Since along the crystals' *a*-axis only van der Waals interactions seem to play the major role – the shortest proton–proton distance being obtained along this crystal axis amounts to 2.44 Å – the corresponding rate of growth is much smaller compared to the growth along the *b*- and *c*-axis, respectively.

Analogous results are obtained for the bisurea compound **2** with an identical molecular geometry as observed for **1** (see Fig. 7a). Nevertheless, the urea group is not perfectly planar with corresponding torsion angles ($H_3N_3C_4O_4$ and $H_3N_5C_4O_4$)

of almost 167°. So, the oxygen atom of the carbonyl group is shifted slightly out of the planar $H_3N_3C_4N_5H_5$ -plane in order to form a hydrogen bond network properly. Since one urea group possesses two NH-donor groups, two different H-bond lengths might be observed. Nevertheless, the two bonds are almost equal with bond lengths of 2.19 Å and 2.23 Å, which is consistent with the results extracted from the 1H and ^{15}N chemical shifts (compare Fig. 2a and 2b), while the corresponding $N\cdots O$ distances result in 3.13 Å and 3.17 Å. All these distances are slightly longer than found for the bisamide **1**. This tendency is also true for the related $NH\cdots O$ angles which are 154.2° and 153.5°. Therefore, the hydrogen bonds for the bisurea are supposed to be weaker than the ones obtained for the bisamide. However, the H-bond pattern obtained for **2** is more complex than for **1** due to the additional NH group. Compared to **1**, the urea group undertakes the same role as the amide function. Therefore, one acceptor carbonyl group is connected to two NH-donor groups and *vice versa* so that one molecule is H-bond connected to four neighbouring molecules, too (see Fig. 7c and 7d).

This is, for example, in contrast to other bisurea compounds where each molecule is hydrogen-bonded to only two other molecules placed below and above it to self-assemble into 1D fibrillar aggregates.^{60,61} Nevertheless, the nature of the urea group itself enables the molecules to form again two H-bond strands as already observed for compound **1**. The propagation direction can also be described as parallel to the *c*-axis of the crystal, so a comparable fast growth in this direction is obtained. Moreover, since also an opening angle

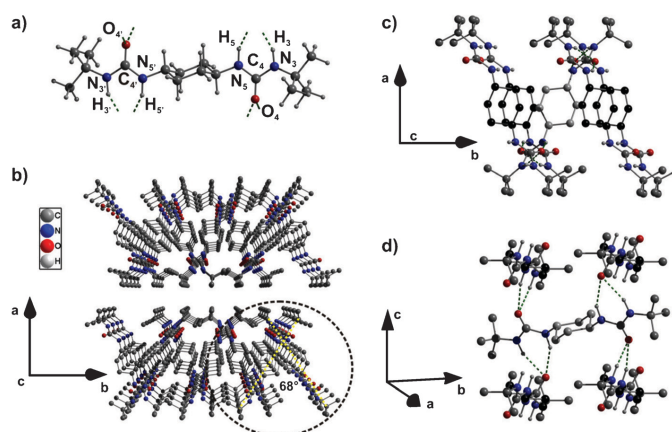


Fig. 7 Molecular structure and extended crystal packing plots of compound **2** with hydrogen bonds highlighted in green dashed lines. (a) Molecular structure of **2** represented with all eight hydrogen bond interactions with labelling of the amide function as performed in Scheme 1. (b) Section of the crystal structure viewing along the *c*-axis. The dashed yellow lines represent the opening angle of the molecules' main axes projected into the *ab*-plane of the crystal. (c) Cutout of the structure presented in panel (b) (black dashed circle) showing that one molecule (grey cyclohexane carbon atoms) is enclosed by four molecules (black cyclohexane carbon atoms), two below and two above. This cutout is rotated by 5° along the *b*-axis. (d) Packing plot showing that every molecule builds hydrogen bonds to four neighbouring molecules in one direction. This packing plot is obtained by -90° rotation along the *a*-axis followed by a -25° rotation along the *b*-axis as presented in panel (c). All hydrogen atoms except the nitrogen-bonded ones have been omitted in (b)–(d) for clarity.

between the two twisted molecules within the unit cell of 68° is observed (see Fig. 7b, yellow dashed lines), a second fast growth direction along the *b*-axis is ensured. The discrepancy of 8° is based on the increased length of the bisurea molecule with its accompanying H-bond capabilities that need a broadening of this angle to achieve a sufficient donor–acceptor interaction. Due to the van der Waals forces as the dominating interaction along the crystals' *a*-axis – as already observed for **1** – a fast growth in this direction is inhibited. Here, the shortest intermolecular proton–proton distance with 2.46 \AA is thereby identical as obtained for the bisamide.

$\text{C}_{18}\text{H}_{32}\text{N}_4\text{O}_4$ **3**. The indexing of the powder pattern of compound **3** revealed a triclinic metric that was successfully refined in *P1* using the Pawley algorithm. Based on the symmetry information obtained by the 1D ^{15}N and ^{13}C spectra (Fig. 2b and 2c), respectively, where the content of the asymmetric unit was limited to half a molecule, *P1* was considered to be the correct space group. Therefore, **3** crystallises in *P1* with crystallographic data summarised in Table 1. The Rietveld profile plot is depicted in Fig. S9 in the ESI.†

The unit cell consists of one C_1 -symmetric molecule based on only half a crystallographic independent molecule in the asymmetric unit. The molecule itself possesses similar structural behaviour as already obtained for compounds **1** and **2** (chair conformation of the cyclohexane ring, see Fig. 8a). The acylurea unit itself is perfectly planar with amide torsion angles of 178.8° ($\text{H}_3\text{N}_3\text{C}_4\text{O}_4$ and $\text{H}_5\text{N}_5\text{C}_6\text{O}_6$, both *trans*-configured) and 0.8° ($\text{H}_5\text{N}_5\text{C}_4\text{O}_4$, *cis*-configured) respectively, leading to a perfect coplanarity (see Fig. 8a). Furthermore, the directly bonded non-urea carboxylic group is

twisted towards the cyclohexane ring with a torsion angle ($\text{H}_7\text{C}_7\text{C}_6\text{O}_6$) of almost 133° . This alignment far beyond the ideal 180° might explain the significant shielding of the CH_2 group with a chemical shift of $\delta = 26.6 \text{ ppm}$ obtained in the ^{13}C CP spectrum (see Fig. 2b) and, moreover, can guarantee the formation of an H-bond network which will be discussed later. As already confirmed by ^1H – ^1H DQ–SQ solid-state NMR (see Fig. 4, right side) and strongly supported by the DFT geometry optimisation, the acylurea unit possesses a *trans-cis-trans* configuration (Fig. 8a). Here, an intrinsic (1,6)-hydrogen bond with a length of 1.96 \AA forming a stable six-membered ring is built. The corresponding $\text{N}\cdots\text{O}$ distance as well as the $\text{NH}\cdots\text{O}$ angle are 2.69 \AA and 126° .

In 2007, Davis *et al.* reported the structure of a similar bisacylurea compound obtained by single crystal X-ray diffraction where an aliphatic pentyl group was chosen as a linker between the acylurea groups (BUC5BU).³¹ Here, the molecule possesses an intrinsic C_2 symmetry with the same configuration of the acylurea group as observed for our molecule. The two-fold axis thereby propagates directly through the middle carbon atom of the C_5 linking unit.

Beyond that, the *cis* HNCO units forming the intramolecular hydrogen bond point in the same direction as in contrast to the C_1 symmetric compound **3** (see Fig. 8b). However, the intramolecular H-bond distance of 2.09 \AA and the corresponding $\text{N}\cdots\text{O}$ distance of 2.74 \AA is longer than observed for the cyclohexane derivative while, surprisingly, the $\text{NH}\cdots\text{O}$ angle (128.6°) is larger. When comparing the planarity, it becomes obvious that the acylurea group of the BUC5BU compound is slightly out of plane with torsion angles of 169.9° ($\text{H}_5\text{N}_5\text{C}_6\text{O}_6$, *trans*),

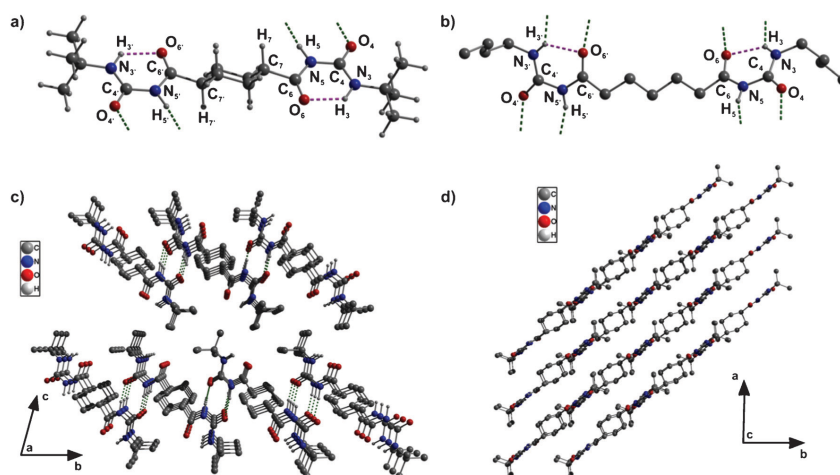


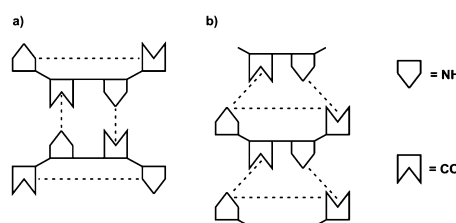
Fig. 8 Molecular structures of compound **3** (a) and BUC5BU³¹ (b) represented with intra- and intermolecular hydrogen bonds (dashed pink and green lines, respectively) with labeling of the acylurea units as performed in Scheme 1. (c) Section of the crystal structure of **3** viewed along the *a*-axis. The dashed green lines represent the intermolecular hydrogen bonds to two neighbouring molecules parallel to the crystals' *c*-axis. (d) Section of the crystal structure of **3** viewed along the *c*-axis. This packing plot is obtained by 100° rotation along the *a*-axis, followed by a small rotation (−10°) along the *b*-axis. All hydrogen atoms except the nitrogen-bonded ones have been omitted in (c) and (d) for clarity.

3.9° ($\text{H}_3\text{N}_5\text{C}_4\text{O}_4$, *cis*) and 180° ($\text{H}_3\text{N}_3\text{C}_4\text{O}_4$, *trans*), respectively, analogous to the angles obtained for **3**. But, moreover, the acylurea moieties of the molecule do show a non-coplanarity with a mutual interplanar angle of 43.3°.

The crystal structure of **3** is schematically pictured in Fig. 8c and 8d. According to the H-bond pattern, it is worth mentioning that only the *cis*-configured amide functions participate in two intermolecular hydrogen bonds each forming in principle one intermolecular six-membered ring (similar to the one already observed in case of the intramolecular H-bond). Interestingly, the corresponding counterpart within a neighbouring molecule also belongs to the *cis*-configured amide function (see Scheme 2a). The number of neighbouring molecules for each molecule therefore is two, which is in contrast to the ones obtained for the compounds **1** and **2**. This alignment in pairs could already be validated by ^1H - ^1H DQ-SQ solid-state NMR experiments (see Fig. 4). While no cross correlation signal between the two different NH-protons (H_3 and H_5) was observed since the proton-proton distance of ~3.6 Å is too long, an auto correlation signal for the NH-protons H_5 was found ($d(\text{H}_5-\text{H}_5) = 2.5$ Å). In case of the BUC5BU compound from ref. 31, however, a similar ^1H - ^1H DQ-SQ spectrum as obtained for compound **2** could be expected (compare Fig. 4a), since an intermolecular H_3 - H_5 distance of ~3 Å might still be detectable within the applied excitation time.

However, an extensive 2D hydrogen bond pattern – as observed for **1** and **2** – is impossible to realise due to this intermolecular *cis*-arrangement of the amide functions (compare Scheme 2a). Nevertheless, the obtained H-bond of 1.75 Å is very short with an $\text{N}\cdots\text{O}$ distance of 2.75 Å and, therefore, has to be categorised as strong which is in very good

agreement with the chemical shift of roughly $\delta = 11.4$ ppm for this NH-proton obtained in the 1D ^1H solid-state NMR spectrum (see Table 2). This fact is, furthermore, corroborated by the $\text{NH}\cdots\text{O}$ angle of 174° which is very close to the ideal 180°. The direction of the intermolecular hydrogen bonds is therefore parallel to the *c*-axis of the crystal. Since only three molecules are involved in this pattern, the self-assembly can – per definition – only be described as classical monoaxial. Though, the self-assembly direction is established by stepwise adding of new molecules along the crystals' *b*-axis *via* hydrogen bonds and, therefore, the fast growth is also observed along this axis. Nevertheless, since the molecules themselves are twisted by almost 45° compared to both the H-bond direction (*c*-axis) as well as the growth direction (*b*-axis), a two-dimensional morphology as observed in SEM can still be obtained (see Fig. 8d).



Scheme 2 Donor-acceptor interactions observed for (a) compound **3** forming one intra- and two intermolecular hydrogen bonds per half molecule and (b) BUC5BU forming one intra- and four intermolecular hydrogen bonds per half molecule. The black dashed lines represent the hydrogen bonds between the NH- and CO-groups.

In comparison, the BUC5BU structure presented in ref. 31 shows a different hydrogen bond pattern. It is evident that the *cis*-configured amide function ($\text{O}_4\text{C}_4\text{N}_2\text{H}_5$) builds intermolecular hydrogen bonds, but they are not connected to other *cis*-configured amide functions but rather with the appropriate donor/acceptor counterpart that also forms the intramolecular H-bond (see Scheme 2b). So, in principle every molecule is involved in four six-membered rings, two intramolecular and four intermolecular ones. Here, the correspondent hydrogen bond lengths result in 2.11 Å and 2.16 Å, respectively, while the $\text{N}\cdots\text{O}$ distances of 2.88 Å and 2.99 Å are much longer than observed for the cyclohexane derivative 3. Interestingly, the particular $\text{NH}\cdots\text{O}$ angles are 135° and 159° , respectively, suggesting that the intermolecular H-bonds for our bisacylurea compound are much stronger than observed for BUC5BU. Nevertheless, the compound investigated by Davis *et al.* possesses a classic biaxial hydrogen bond system where each BUC5BU molecule is hydrogen-bonded to four adjacent molecules as already described for 1 and 2. This, however, might be caused due to the intrinsic molecular C_2 symmetry while a centrosymmetric molecular symmetry (compound 3) leads only to a classical monoaxial hydrogen bond system.

Conclusion

In summary, three cyclohexane-based compounds with different hydrogen bond motifs were characterised by scanning electron microscopy, solid-state NMR, PXRD and computational methods based on DFT. SEM measurements revealed sheet-like morphologies for all three compounds with lateral dimensions of several hundred micrometres with substantial aspect ratios. The crystal structures of those compounds were elucidated by means of NMR-crystallographic strategies. Based on an unequivocal signal assignment of the 1D spectra by performing ^1H - ^{13}C - and ^1H - ^{15}N HETCOR experiments also considering the $^1\text{H}/^{14}\text{N}$ - and $^{13}\text{C}/^{14}\text{N}$ second-order quadrupolar interaction we were able to restrict the space group symmetry and to determine the content of the asymmetric unit. The evaluation of ^1H - ^1H DQ-SQ spectra revealed spatial proton-proton connectivities of the NH groups for all compounds. Additionally for compound 3, they allowed probing both the molecular configuration such as the existence of the intramolecular hydrogen bond and the local environment like the H-bond pattern leading to a pair-like molecular arrangement. This information was crucial to make the *ab initio* structure solutions by real-space methods more efficient and remove ambiguities.

Compounds 1 and 2 crystallise in $P2_1/c$ and their crystal structures exhibit an interesting "pseudo-biaxial" hydrogen bond system where each molecule is directly connected to four neighbouring molecules *via* moderate H-bonds. Caused by the crossed alignment of the molecules within the unit cell (see Fig. 6d and 7d), the H-bond mediated strands are growing fast in two directions even though both H-bond strands are parallel, while the growth in the third dimension is retarded resulting in two-dimensional nanosheets. Although such a structural motif was also observed for one

similar benzene-based compound⁶² no connection to a fast two-dimensional growth was made. This arrangement is an alternative to the classical variant where the hydrogen bond strands are crossed instead of the molecules. In compound 3 (crystallising in $P\bar{1}$), on the other hand, each molecule forms H-bonds to two adjacent molecules, leading to a one-dimensional ribbon-like structure per definition. It is remarkable that this compound still shows a sheet-like morphology. This might be caused by the special arrangement of the molecules in the packing with respect to the crystal axes.

An important aspect with respect to the growth process of the sheets deals with the role of dipole moments for the growth mechanism. For the growth of one-dimensional rod like nanostructures – e.g. cyclohexane- or benzenetrissamides – it is known that dipole forces play an important role.²¹ Here, every molecule possesses an intrinsic dipole moment. Within one rod, this dipole moment strongly increases and so-called macrodipoles are generated. In order to obtain an anti-ferroelectric crystal being energetically favoured, all macrodipoles must be compensated by an antiparallel arrangement of themselves.⁶³ The net dipole moment of zero is thereby achieved during the crystallisation process. This argument is also valid for the BUC5BU compound investigated in ref. 31. Even if a two-dimensional self-assembly is achieved, the intrinsic C_2 symmetry of the molecules implies an intrinsic dipole moment, too, which is only compensated due to the space group symmetry during crystallisation as well. In contrast, for the two-dimensional sheet like nanostructures presented here, dipole forces or even macrodipoles do not play a major role. The dipole moment is already cancelled in each molecule due to the inversion symmetry of the molecules themselves. So, the fast growth of the nanostructures in two directions (1 and 2) (or one direction for compound 3, respectively) giving two-dimensional nanosheets is, therefore, mainly induced by the hydrogen bond mediated donor-acceptor interactions between the appropriate molecular counterparts.

Acknowledgements

The authors want to thank the DFG (SFB 840, Project B4) for funding this work, Anna-Maria Dietel for performing the elementary analysis and Dr. Wolfgang Milius for the adjuvant discussions with respect to crystallographic issues.

References

- 1 J.-M. Lehn, *Angew. Chem., Int. Ed. Engl.*, 1990, 29, 1304.
- 2 S. Cantekin, T. F. A. de Greef and A. R. A. Palmans, *Chem. Soc. Rev.*, 2012, 41, 6125.
- 3 Y. Yasuda, E. Iishi, H. Inada and Y. Shirota, *Chem. Lett.*, 1996, 575.
- 4 K. Hanabusa, C. Koto, M. Kimura, H. Shirai and A. Kakehi, *Chem. Lett.*, 1997, 429.
- 5 J. J. van Gorp, J. A. J. M. Vekemans and E. W. Meijer, *J. Am. Chem. Soc.*, 2002, 124, 14759.

- 6 N. Shi, H. Dong, G. Yin, Z. Xu and S. Li, *Adv. Funct. Mater.*, 2007, 17, 1837.
- 7 A. Bernet, R. Q. Albuquerque, M. Behr, S. T. Hoffmann and H.-W. Schmidt, *Soft Matter*, 2012, 8, 66.
- 8 Y. Matsunaga, N. Miyajima, Y. Nakayasu, S. Sakai and M. Yonemaga, *Bull. Chem. Soc. Jpn.*, 1988, 61, 207.
- 9 M. Gelinsky, R. Vogler and H. Vahrenkamp, *Inorg. Chem.*, 2002, 41, 2560.
- 10 P. Besenius, J. L. M. Heynens, R. Straathof, M. M. L. Nieuwenhuizen, P. H. H. Bomans, E. Terreno, S. Aime, G. J. Strijkers, K. Nicolay and E. W. Meijer, *Contrast Media Mol. Imaging*, 2012, 7, 356.
- 11 M. Blomenhofer, S. Ganzleben, D. Hanft, H.-W. Schmidt, M. Kristiansen, P. Smith, K. Stoll, D. Maeder and K. Hoffmann, *Macromolecules*, 2005, 38, 3688.
- 12 P. M. Kristiansen, A. Gress, P. Smith, D. Hanft and H.-W. Schmidt, *Polymer*, 2006, 47, 249.
- 13 F. Abraham, S. Ganzleben, D. Hanft, P. Smith and H.-W. Schmidt, *Macromol. Chem. Phys.*, 2010, 211, 171.
- 14 J. Wang, Q. Dou, X. Chen and D. Li, *J. Polym. Sci., Part B: Polym. Phys.*, 2008, 46, 1067.
- 15 F. Richter and H.-W. Schmidt, *Macromol. Mater. Eng.*, 2013, 298, 190.
- 16 H. Nakajima, M. Takahashi and Y. Kimura, *Macromol. Mater. Eng.*, 2010, 295, 460.
- 17 H. Bai, W. Zhang, H. Deng, Q. Zhang and Q. Fu, *Macromolecules*, 2011, 44, 1233.
- 18 P. Song, Z. Wei, J. Liang, G. Chen and W. Zhang, *Polym. Eng. Sci.*, 2012, 52, 1058.
- 19 M. Schmidt, J. J. Wittmann, R. Kress, D. Schneider, S. Steuernagel, H.-W. Schmidt and J. Senker, *Cryst. Growth Des.*, 2012, 12, 2543.
- 20 M. Schmidt, J. J. Wittmann, R. Kress, H. W. Schmidt and J. Senker, *Chem. Commun.*, 2013, 49, 267.
- 21 R. Q. Albuquerque, A. Timme, R. Kress, J. Senker and H.-W. Schmidt, *Chem.-Eur. J.*, 2013, 19, 1647.
- 22 T. Govindaraju and M. B. Avinash, *Nanoscale*, 2012, 4, 6102.
- 23 M. Stöter, D. A. Kunz, M. Schmidt, D. Hirsemann, H. Kalo, B. Putz, J. Senker and J. Breu, *Langmuir*, 2013, 29, 1280.
- 24 M. B. Avinash, K. S. Subrahmanyam, Y. Sundarayya and T. Govindaraju, *Nanoscale*, 2010, 2, 1762.
- 25 K. S. Novoselov, D. Jiang, F. Schedin, T. J. Booth, V. V. Khotkevich, S. V. Morozov and A. K. Geim, *Proc. Natl. Acad. Sci. U. S. A.*, 2005, 102, 10451.
- 26 J. C. Meyer, A. K. Geim, M. I. Katsnelson, K. S. Novoselov, T. J. Booth and S. Roth, *Nature*, 2007, 446, 60.
- 27 A. K. Geim and K. S. Novoselov, *Nat. Mater.*, 2007, 6, 183.
- 28 C. N. R. Rao, A. K. Sood, K. S. Subrahmanyam and A. Govindaraj, *Angew. Chem., Int. Ed.*, 2009, 48, 7752.
- 29 K. S. Subrahmanyam, P. Kumar, U. Maitra, A. Govindaraj, K. P. S. Hembram, U. V. Waghmare and C. N. R. Rao, *Proc. Natl. Acad. Sci. U. S. A.*, 2011, 108, 2674.
- 30 J.-U. Kim, R. Davis and R. Zentel, *J. Colloid Interface Sci.*, 2011, 359, 428.
- 31 R. Davis, R. Berger and R. Zentel, *Adv. Mater.*, 2007, 19, 3878.
- 32 L. Seyfarth, J. Seyfarth, B. V. Lotsch, W. Schnick and J. Senker, *Phys. Chem. Chem. Phys.*, 2010, 12, 2227.
- 33 E. Wirmhier, M. Döblinger, D. Gunzelmann, J. Senker, B. V. Lotsch and W. Schnick, *Chem.-Eur. J.*, 2011, 17, 3213.
- 34 L. Seyfarth, J. Schnert, N. El-Gamel, W. Milius, E. Kroke, J. Breu and J. Senker, *J. Mol. Struct.*, 2008, 889, 217.
- 35 R. K. Harris, *Analyst*, 2006, 131, 351.
- 36 Accelrys software inc. *MS Modeling v5.0.0.0* Copyright 2009.
- 37 W. A. Dollase, *J. Appl. Crystallogr.*, 1986, 19, 267.
- 38 H. M. Rietveld, *J. Appl. Crystallogr.*, 1969, 2, 65.
- 39 H. Toraya and F. Marumo, *Mineral. J.*, 1981, 10, 211.
- 40 H. Sun, *J. Phys. Chem. B*, 1998, 102, 7338.
- 41 L. W. Finger, D. E. Cox and A. P. Jephcoat, *J. Appl. Crystallogr.*, 1994, 27, 892.
- 42 E. Salager, R. S. Stein, S. Steuernagel, A. Lesage, B. Elena and L. Emsley, *Chem. Phys. Lett.*, 2009, 469, 336.
- 43 M. H. Levitt, *Encycl. Nucl. Magn. Reson.*, 2002, 9, 165.
- 44 D. Sakellariou, A. Lesage, P. Hodgkinson and L. Emsley, *Chem. Phys. Lett.*, 2000, 319, 253.
- 45 X. Zhao, W. Hoffbauer, J. S. auf der Günne and M. H. Levitt, *Solid State Nucl. Magn. Reson.*, 2004, 26, 57.
- 46 J. P. Perdew and Y. Wang, *Phys. Rev. B: Condens. Matter Mater. Phys.*, 1992, 45, 13244.
- 47 J. Senker, L. Seyfarth and J. Voll, *Solid State Sci.*, 2004, 6, 1039.
- 48 F. W. Karau, L. Seyfarth, O. Oeckler, J. Senker, K. Landskron and W. Schnick, *Chem.-Eur. J.*, 2007, 13, 6841.
- 49 D. Hirsemann, T. K.-J. Köster, J. Wack, L. van Wüllen, J. Breu and J. Senker, *Chem. Mater.*, 2011, 23, 3152.
- 50 L. Seyfarth and J. Senker, *Phys. Chem. Chem. Phys.*, 2009, 11, 3522.
- 51 F. Taulelle, *Solid State Sci.*, 2004, 6, 1053.
- 52 J. Senker, J. Sehnert and S. Correll, *J. Am. Chem. Soc.*, 2005, 127, 337.
- 53 J. Sehnert and J. Senker, *Chem.-Eur. J.*, 2007, 13, 6339.
- 54 J. Sehnert, K. Bärwinkel and J. Senker, *J. Mol. Struct. (THEOCHEM)*, 2007, 824, 58.
- 55 J. Sehnert, K. Baerwinkel and J. Senker, *J. Phys. Chem. B*, 2007, 111, 10671.
- 56 J. Schmidt, A. Hoffmann, H. W. Spiess and D. Sebastiani, *J. Phys. Chem. B*, 2006, 110, 23204.
- 57 R. Harris and A. Olivieri, *Prog. Nucl. Magn. Reson. Spectrosc.*, 1992, 24, 435.
- 58 K. Eichele, *WSolids1, version 1.20.17*, Universität Tübingen, 2012.
- 59 Predicted NMR data calculated using Advanced Chemistry Development, Inc. (ACD/Labs) *Software V12.5* (© 1994–2013 ACD/Labs).
- 60 J. H. van Esch, F. Schoonbeek, M. de Loos, H. Kooijman, A. L. Spek, R. M. Kellogg and B. L. Feringa, *Chem.-Eur. J.*, 1999, 5, 937.
- 61 M. de Loos, J. van Esch, R. M. Kellogg and B. L. Feringa, *Angew. Chem., Int. Ed.*, 2001, 40, 613.
- 62 H.-Z. Guo, G.-D. Yin, N.-F. She and A.-X. Wu, *Acta Cryst.*, 2005, E61, 04062.
- 63 J. Senker and J. Lüdecke, *Z. Naturforsch., B: J. Chem. Sci.*, 2001, 56b, 1089.

Electronic Supplementary Information

to

NMR-Crystallographic Study of Two-Dimensionally Self-Assembled Cyclohexane Based Low-Molecular-Mass Organic Compounds†

Marko Schmidt,^a Christoph S. Zehe,^a Renée Siegel,^a Johannes U. Heigl,^b
Christoph Steinlein,^b Hans-Werner Schmidt^b and Jürgen Senker*^a

^a Inorganic Chemistry III and Bayreuth Center for Colloids and Interfaces, University of Bayreuth, Universitätsstr. 30, 95447 Bayreuth, Germany.

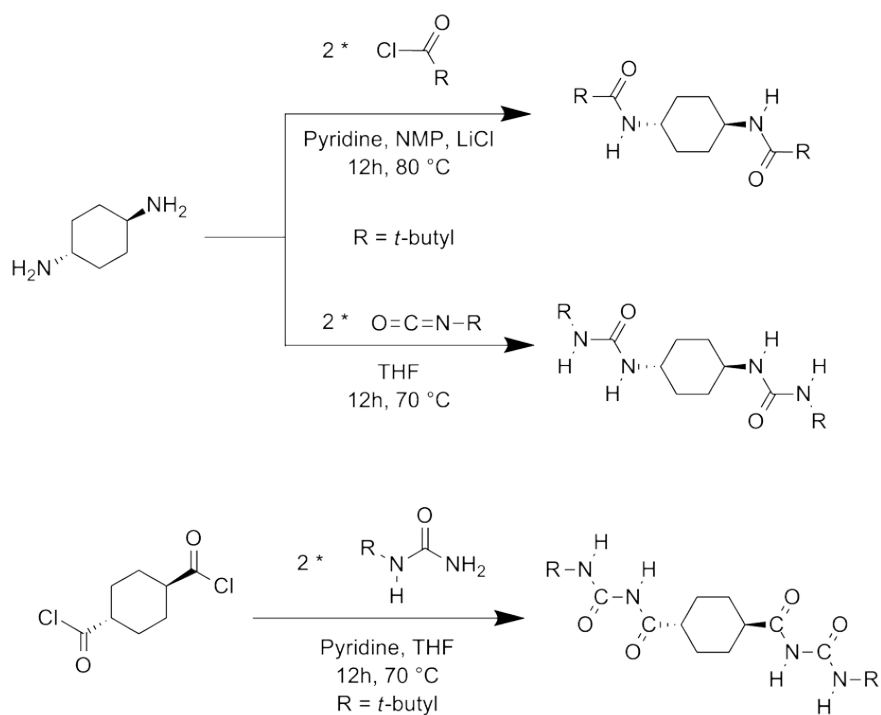
Tel: +49(0)921552532; E-mail: juergen.senker@uni-bayreuth.de

^b Macromolecular Chemistry I, Bayreuth Institute of Macromolecular Research and Bayreuth Center for Colloids and Interfaces, University of Bayreuth, Universitätsstr. 30, 95447 Bayreuth, Germany.

Tel: +49(0)921553200; E-mail: hans-werner.schmidt@uni-bayreuth.de

Synthesis of compounds 1 - 3

The principal reaction schemes of the classical addition and elimination reactions is visualised in Scheme S1. The full conversion of the educts as well as the purity of the products was confirmed by means of elementary analysis (CHN), mass spectrometry and powder X-ray diffraction. The CHN analysis revealed a good agreement between calculated and experimental values (compare experimental section in the main article).



Scheme S1 Schematic representation of the synthetic routes to obtain **1** and **2** (based on *trans*-1,4-diaminocyclohexane) and **3** (based on cyclohexane-*trans*-1,4-dicarbonyl dichloride).

Explanation of the ^{14}N - effect

A comparison of ^{13}C CP measurements on 300 MHz and 400 MHz spectrometers is depicted in Figure S1a. Here, for each compound the spectrum measured at higher field shows a decrease of the splitting. This is in accordance with the trend of the second-order quadrupolar interaction which depends inversely on the field strength. For ^1H , the influence of ^{14}N can be visualised in the same way by comparing one-pulse proton spectra measured at different magnetic fields. Exemplarily, this is pointed out for compound **1** in Figure S1b. Here, the blue line represents a ^1H one-pulse experiment at a proton frequency of 400 MHz with $\nu_{\text{rot}} = 22.5$ kHz (bottom), while the black line corresponds to a measurement at a 300 MHz device with $\nu_{\text{rot}} = 32.5$ kHz (top). The former shows only one signal without additional splitting perfectly matching with the molecular structure obtained for **1**. The latter one, on the other hand, possesses a shoulder which can easily be misinterpreted as a second signal but is based on the ^{14}N interaction. Complementary results are obtained for **2** and **3** (not shown here).

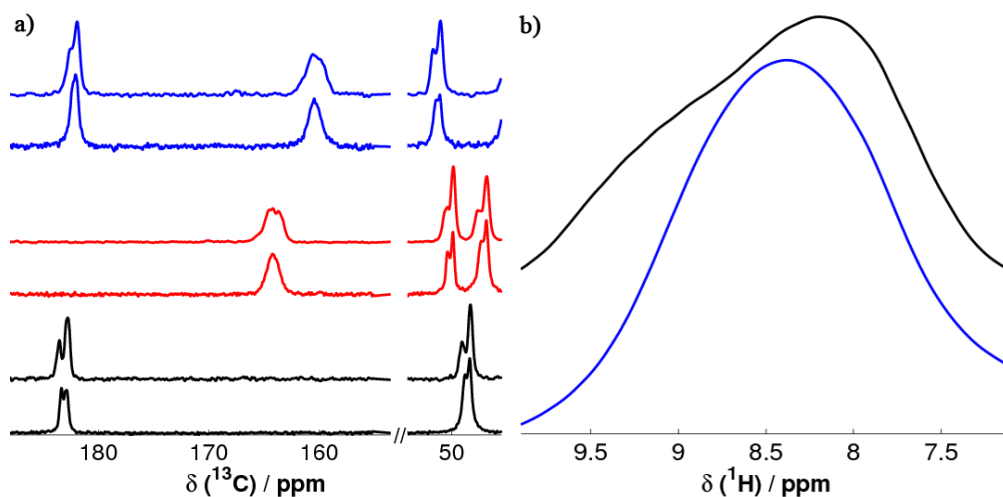


Fig. S1 (a) ^{13}C CP spectra of the three compounds (black = **1**, red = **2**, blue = **3**), where for each compound the lower spectrum corresponds to proton frequency of 400 MHz and the upper spectrum to 300 MHz; all spectra are recorded at a spinning rate of 10 kHz; (b) ^1H one-pulse spectra of compound **3** measured at a proton frequency of 400 MHz and a rotation frequency of 22.5 kHz (blue line, bottom) and 300 MHz at a rotation frequency of 32.5 kHz (black line, top).

4 Publications

To strengthen this argument, simulations of both ^{13}C CP and ^1H DUMBO spectra (both measured at $B_0 = 7.04$ T) including a ^{14}N effect were performed using the freeware program WSOLIDS1.¹ The simulations were done exemplarily for C_6 and H_3 (compare Table 2 in the main article) within the acylurea unit of compound **3** since the resonances of these nuclei are sustainably influenced by the neighboured ^{14}N nucleus. For getting reasonable starting values for ^{13}C , a comparable OC-NH system was taken from literature.² Here the quadrupolar coupling constant ($C_Q = -3.2$ MHz), the asymmetry parameter ($\eta = 0.22$), the azimuth angle of the internuclear ^{13}C - ^{14}N vector in the principal axis system of the electric field gradient (EFG) tensor ($\alpha = 43^\circ$) as well as the polar angle of the internuclear ^{13}C - ^{14}N vector in the principal axis system of the EFG tensor ($\beta = 90^\circ$) were extracted. The isotropic chemical shift was set to $\delta = 177.15$ ppm while the direct dipolar coupling constant ($d_{\text{C}-\text{N}}^{13,14} = 840$ Hz) was calculated according to the crystal structure obtained by PXRD. For the indirect scalar dipolar coupling between ^{13}C and ^{14}N (“ J -coupling”) 7 Hz was adjusted. A similar procedure was performed for the ^1H spectrum. Due to the same orientations of the EFG tensors of both ^{14}N nuclei the values for C_Q and η are equal. The isotropic chemical shift was set to $\delta = 8.29$ ppm while the direct dipolar coupling constant ($d_{\text{H}-\text{N}}^{1,14} = 8250$ Hz) was calculated according to the crystal structure. For the indirect scalar dipolar coupling between ^1H and ^{14}N 65 Hz was chosen which was recalculated from $^1J(^1\text{H},^{15}\text{N})$ -couplings of comparable compounds from literature.³ For both simulations, the values of the direct as well as scalar dipolar coupling constant were not varied while all other values were refined during the simulation. Both the simulated and experimental spectra are depicted in Figure S2. For a more detailed description of the theoretical background the reader is referred to ref. 2.

Table S1 Summary of the parameters used for the simulations of the ^1H and ^{13}C spectrum, respectively.

	^1H (H_3)	^{13}C (C_6)
$\delta_{\text{CS}} / \text{ppm}$	8.29	177.15
$d_{\text{X}-\text{N}}^{14} / \text{Hz}$	8250	840
$J_{\text{X}-\text{N}}^{14} / \text{Hz}$	65	7
C_Q / MHz	-3.1	-3.1
η	0.42	0.4
$\alpha / ^\circ$	5	44
$\beta / ^\circ$	85	85

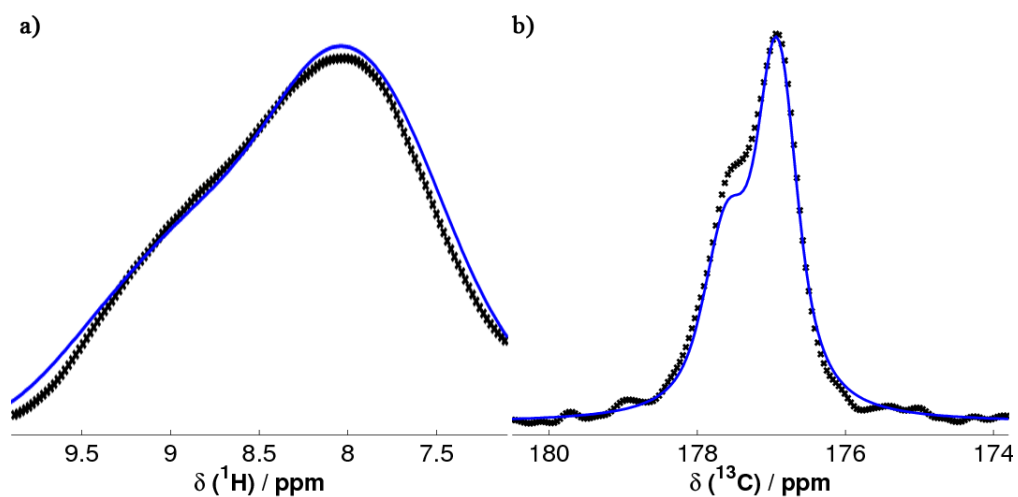


Fig S2 Experimental spectra from Figure S1 (black crosses) and simulated spectra of H₃ (a) and C₆ (b) (blue lines, compare Table S1) of the acylurea unit of compound **3**.

Prediction of ¹³C and ¹⁵N chemical shifts

Table S2 Predicted solution-state NMR chemical shifts⁴ for the carbon atoms of the carbonyl groups as well as the nitrogen atoms of compounds **1** - **3**. Since the ¹⁵N calculations are performed without proton decoupling only a mean value is shown, without taking into account any ¹J(¹H, ¹⁵N)-couplings. All values are based on single molecule calculations without considering any inter- or intramolecular interaction, e.g. hydrogen bonding.

	1	2	3	Unit
C ₄	178.5	158.1	155.7	C=O
C ₆	-	-	179.4	C=O
N ₃	-	-278.2	-277.2	NH
N ₅	-250.9	-274.8	-246.0	NH

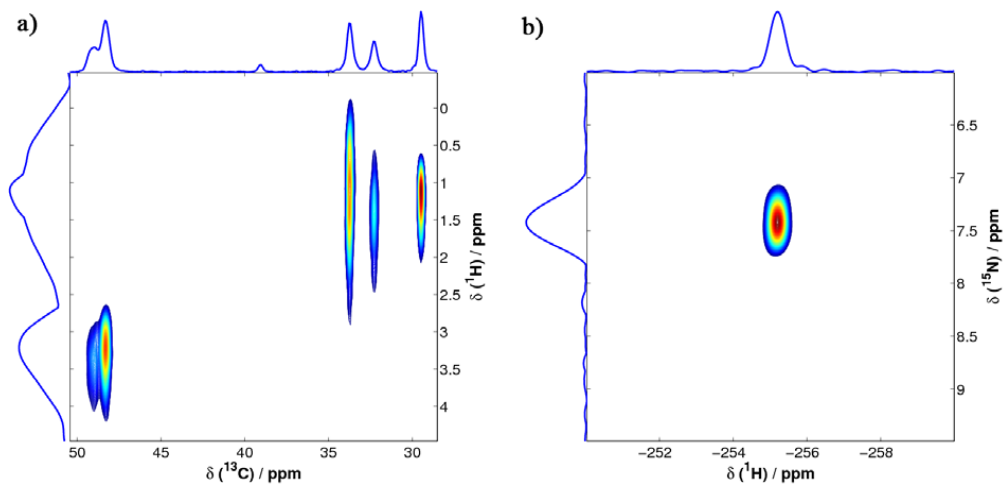
HETCOR spectra of compound 1 and 2

Fig S3 ^1H - ^{13}C -HETCOR on a 300 MHz spectrometer (left) and ^1H - ^{15}N -HETCOR on a 400 MHz spectrometer (right) of compound **1** at a spinning speed of 10 kHz each. The contact time was set to 178 μs .

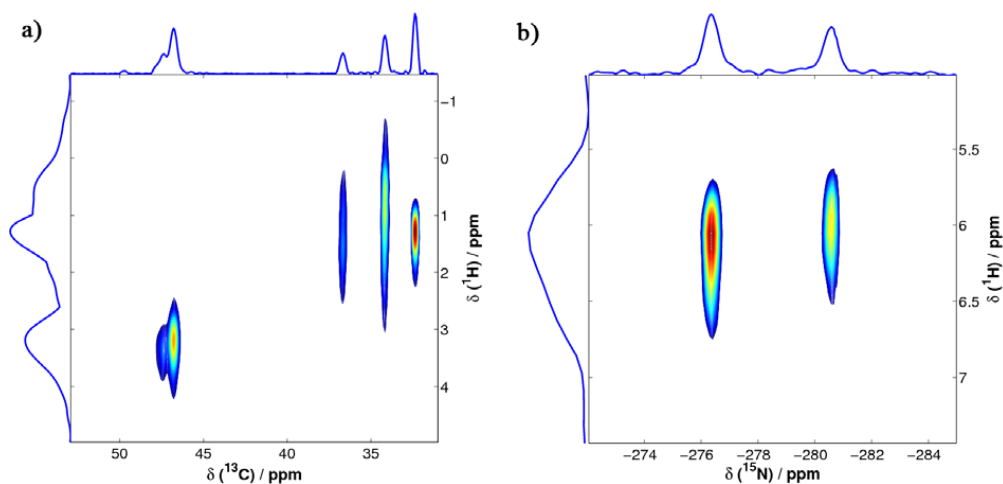


Fig S4 ^1H - ^{13}C -HETCOR (left) and ^1H - ^{15}N -HETCOR (right) spectrum of compound **2** at a spinning speed of 10 kHz on a 300 MHz spectrometer. The contact time was set to 178 μs .

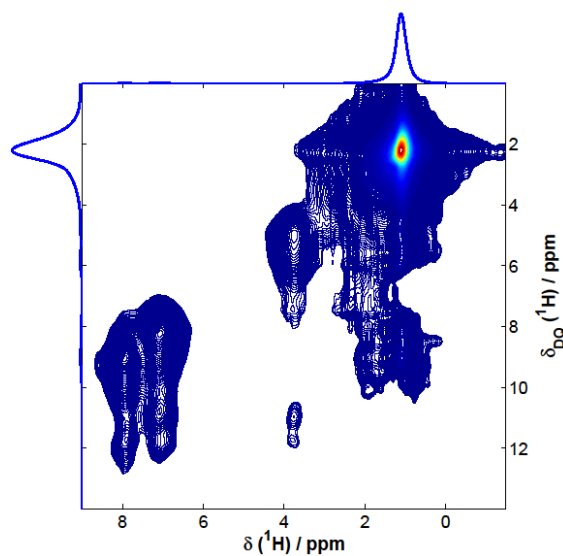
^1H - ^1H double-quantum-single-quantum spectra of 1 – 3

Fig. S5 ^1H - ^1H DQ-SQ correlation spectra of compound **1**. The excitation and reconversion time was set to $80\ \mu\text{s}$ so that only shortest distance correlations are visible. The protons of the CH_3 -groups are truncated due to the long relaxation times leading to a streak along both the SQ- as well as the DQ-axis in the spectrum.

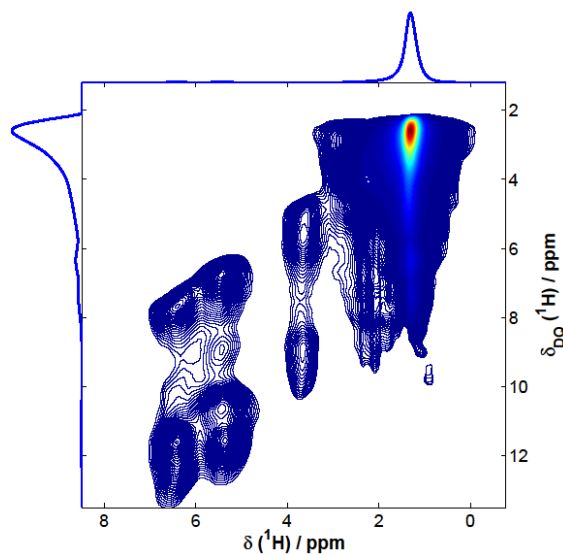


Fig. S6 ^1H - ^1H DQ-SQ correlation spectrum of compound **2**. The excitation and reconversion time was set to $80\ \mu\text{s}$ so that only shortest distance correlations are visible. The protons of the CH_3 -groups are truncated due to the long relaxation times leading to a streak along both the SQ- as well as the DQ-axis in the spectrum.

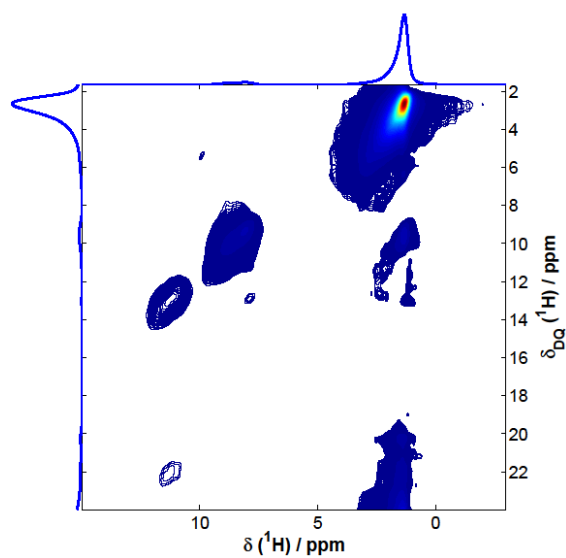


Fig. S7 ^1H - ^1H DQ-SQ correlation spectrum of compound **3**. The excitation and reconversion time was set to $80\ \mu\text{s}$ so that only shortest distance correlations are visible. The protons of the CH_3 -groups are truncated due to the long relaxation times leading to a streak along both the SQ- as well as the DQ-axis in the spectrum.

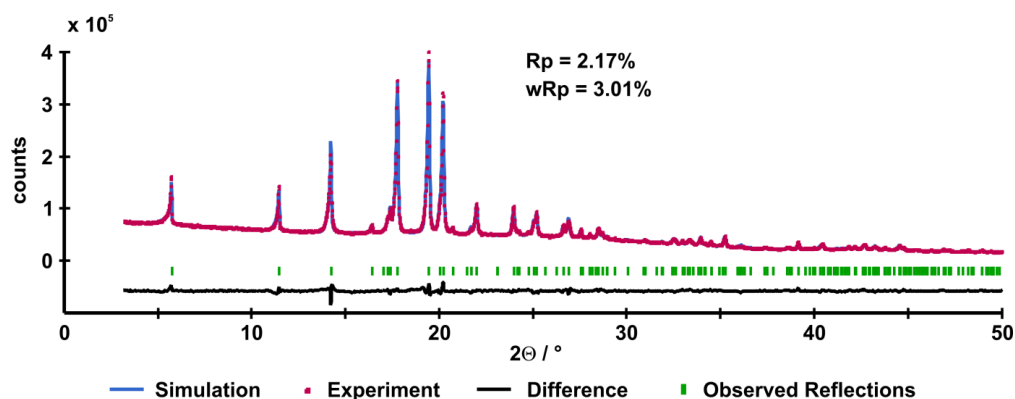
Rietveld profile plots of 2 and 3

Fig. S8 Rietveld profile plot of compound **2** measured at room temperature in the 2Θ range of 3° - 50° using $\text{CuK}\alpha_1$ radiation ($\lambda = 1.5406 \text{ \AA}$).

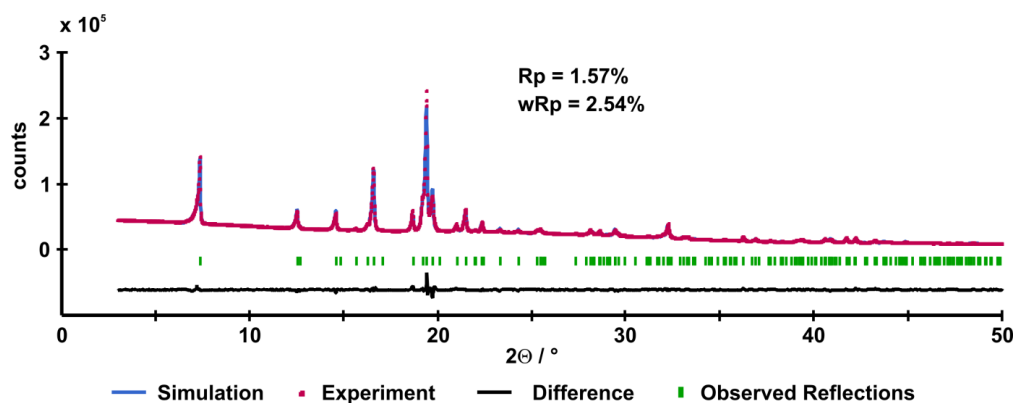


Fig. S9 Rietveld profile plot of compound **3** measured at room temperature in the 2Θ range of 3° - 50° using $\text{CuK}\alpha_1$ radiation ($\lambda = 1.5406 \text{ \AA}$).

References

- 1 K. Eichele, *WSolids1 version 1.20.17*, Universität Tübingen, 2012.
- 2 K. Eichele, M. D. Lumsden and R. E. Wasylshen, *J. Phys. Chem.*, 1993, **97**, 8909.
- 3 M. Hesse, H. Meier and B. Zeeh, *Spektroskopische Methoden in der organischen Chemie*, 5th edn., 1995.
- 4 *Predicted NMR data calculated using Advanced Chemistry Development, Inc. (ACD/Labs) Software V12.5* (© 1994-2013 ACD/Labs).

4.2 Influence of Fluorine Side-Group Substitution on the Crystal Structure Formation of Benzene-1,3,5-trisamides

This work is the result of a cooperation between the Inorganic Chemistry III and Macromolecular Chemistry I of the University of Bayreuth and Bruker Biospin GmbH and will be reproduced from Zehe, C. S., Schmidt, M., Siegel, R., Kreger, K., Daebel, V., Ganzleben, S., Schmidt, H.-W., Senker, J., *CrystEngComm*, **16**, 9273–9283 (2014) in the following with permission from The Royal Society of Chemistry. My contributions are:

- conception and main authorship of the article
- measurement of all 1D ^1H , ^{19}F , $^1\text{H}\rightarrow^{13}\text{C}$ CP, $^{19}\text{F}\rightarrow^{13}\text{C}$ CP, and $^1\text{H}\rightarrow^{15}\text{N}$ CP spectra
- implementation of homonuclear DQ recoupling pulse sequences
- measurement of 2D ^{19}F - ^{19}F DQ correlation spectra and ^{19}F DQ buildup curves
- simulation of all ^{19}F DQ buildup curves including creation of spin systems from structure models
- evaluation of all NMR data and simulations

The contributions of all other authors are:

- conception and co-authorship of the article
- synthesis and characterisation of the chemical compound
- measurement of powder X-ray diffraction patterns
- structure solution from X-ray powder data and evaluation of those
- support of NMR experiments and data evaluations
- co-authorship of the article



Cite this: *CrystEngComm*, 2014, 16, 9273

Influence of fluorine side-group substitution on the crystal structure formation of benzene-1,3,5-trisamides†

Christoph Zehe,^a Marko Schmidt,^a Renée Siegel,^a Klaus Kreger,^b Venita Daebel,^c Sandra Ganzleben,^b Hans-Werner Schmidt^b and Jürgen Senker^{*a}

By a combination of powder X-ray diffraction, multidimensional and multinuclear solid-state NMR spectroscopy and quantum chemical calculations, we were able to determine the crystal structure of 1,3,5-tris(2-fluoro-2-methylpropionylamino)benzene. Solid-state NMR experiments guided the structure solution by predicting the content of the asymmetric unit and the presence of a NH...OC hydrogen bond network. In addition to real-space structure solution and Rietveld refinement, quantitative symmetry-based ¹⁹F double-quantum recoupling experiments provided a cost function to determine the positions of the methyl groups and fluorine atoms. The structure solution of this particular fluorine-substituted trisamide illustrates the impact of fluorine side-group substitution on the common columnar packing motif of benzene-1,3,5-tricarboxamides. As also in the case 1,3,5-tris(2,2-dimethylpropionylamino)benzene, the supramolecular aggregation is then guided by the formation of triple helical NH...OC hydrogen bond networks within the individual columns. In contrast, the substitution of one methyl group by a fluorine atom in each side chain results in a two-dimensional NH...OC hydrogen bond pattern, leading to a lamellar crystal structure with only van der Waals interactions between the layers. Since fluorine is not involved in the hydrogen bond network and both chemical units exhibit a similar steric demand, the fundamental differences of the packing are most probably caused by changes in the molecular polarity.

Received 25th May 2014,
Accepted 11th August 2014

DOI: 10.1039/c4ce01077a

www.rsc.org/crystengcomm

Introduction

The ability of reversibly forming complex supramolecular structures and polymers by secondary intermolecular interactions like hydrogen bonding, aromatic π - π stacking or electrostatic and dispersion interactions between the constituting parts leads to the field of supramolecular chemistry.^{1,2} Via the concept of molecular recognition, the targeted synthesis and design of molecules allow for tuning strength and direction of the secondary intermolecular interactions.² For instance, adjusting the number and direction of intermolecular interactions leads to columnar,³⁻⁵ layer-like⁶ or three-dimensionally propagating hydrogen bond networks.⁷

In particular, the class of benzene-1,3,5-tricarboxamides (BTAs) has evolved into an attractive supramolecular motif in

recent years.⁸ Through cooperative hydrogen bonding in a helical pattern, one-dimensional columnar aggregates which exhibit large dipole moments are formed.^{4,5,9-11} The anti-parallel arrangement of such macrodipoles leads to fast one-dimensional growth resulting in columnar supramolecular structures.^{12,13} The easy chemical accessibility and tunability render BTAs into a versatile class of advanced materials with increasing importance in many fields of research.⁸ For instance, they show potential as organogelators,^{7,14} hydrogelators,¹⁵ liquid crystals,¹⁶ MRI contrast reagents,¹⁷ and metal complexation reagents.¹⁸ In addition, some derivatives are known to be highly efficient electrets clarifying and nucleating agents for semicrystalline polymers, e.g., isotactic polypropylene,¹⁹ polybutylene terephthalate,²⁰ poly(ethylene-co-propylene),²¹ polyvinylidene fluoride²² or polylactides.²³

The structure solution of BTA compounds, however, is often difficult since only microcrystalline powders are available, rendering single-crystal X-ray diffraction experiments impossible. Due to the coincidence of symmetry-equivalent reflexes and the heavy overlap of higher-order reflexes,²⁴ structure solutions based on *ab initio* powder X-ray diffraction (PXRD) are often hampered. Topological information such as unit cell constants and global arrangements of molecules might still be obtained with reasonable accuracy,

^a Inorganic Chemistry III and Bayreuth Center for Colloids and Interfaces, University of Bayreuth, 95447, Bayreuth, Germany.

E-mail: juergen.senker@uni-bayreuth.de; Tel: (+49) 921 55 2788

^b Macromolecular Chemistry I, Bayreuth Institute of Macromolecular Research and Bayreuth Center for Colloids and Interfaces, University of Bayreuth, 95447, Bayreuth, Germany

^c Bruker Biospin GmbH, Silberstreifen 4, 76287 Rheinstetten, Germany

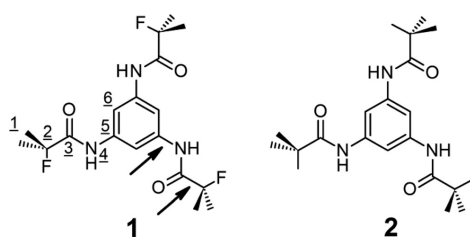
† Electronic supplementary information (ESI) available. See DOI: 10.1039/c4ce01077a

but local structural details are usually strongly affected.^{24,25} Here, solid-state nuclear magnetic resonance (NMR) spectroscopy offers complementary information based on the three basic interactions – chemical shift,²⁶ dipolar interaction²⁷ and quadrupolar splitting²⁸ – the local structural properties may be extracted and combined with PXRD data at different steps of the structure solution.²⁹

Symmetry information such as the content of the asymmetric unit can be obtained through Wyckoff spectra,³⁰ high-resolution experiments or direct determination of symmetry elements by exploiting orientational correlations of chemical shift tensors.^{24,31} Hetero- and homonuclear dipole interactions may be used to extract distances and torsion angles as well as to select correct space groups and to verify structure models, respectively.^{13,25,32–34} This combination of X-ray diffraction experiments and solid-state NMR spectroscopy, often called NMR crystallography, has proven to be a powerful tool for structure elucidation, which is capable of tackling problems that are unsolvable by any of these methods alone.^{6,13,25,33–35} A more thorough discussion of the topic NMR crystallography including an overview of the recent literature can be found in ref. 36.

For a better understanding of the structure-directing interactions, the bulk structures of several BTA derivatives were examined in the past by PXRD.^{3,9,13,37,38} Here, sterically less demanding side groups, *e.g.*, methyl groups, prefer two- or three-dimensional hydrogen bond networks.^{7,37} In contrast, bulky moieties such as *t*-butyl were found to predominantly lead to columnar packing motifs with triple helical hydrogen bonds.^{3,9,11,13} Similarly, long linear or only short-branched aliphatic side groups often induce columnar mesophases with an analogous supramolecular organisation pattern at low transition temperatures.^{16,39} For such large aliphatic residues, hydrogen bond networks with a two-dimensional topology are rarely observed.³⁸

In order to investigate the effect of a side-chain substitution with an equal steric demand but different polarity, we synthesized and 1,3,5-tris(2-fluoro-2-methylpropionylamino)benzene and solved its structure (1) (Scheme 1). In comparison with the structurally similar 1,3,5-tris(2,2-dimethylpropionylamino)benzene (2),



Scheme 1 Left: molecular structure of 1,3,5-tris(2-fluoro-2-methylpropionylamino)benzene (1) including a labeling scheme for different chemical groups. The black arrows assign the structure-directing torsion angles $C_{Ar}C_{Ar}NH$ and $NC_{O}C_{O}F$ of the side groups. Right: molecular structure of 1,3,5-tris(2,2-dimethylpropionylamino)benzene (2).

one methyl group in each side chain is replaced by a fluorine atom. The structure solution was performed using a combined approach of PXRD, *ab initio* quantum chemical calculations and solid-state NMR experiments.

Experimental

Molecular characterisation

¹H NMR and ¹³C NMR solution-state spectra were recorded with a Bruker AC-300 spectrometer (300 and 75 MHz, respectively) at room temperature and referenced to TMS. Mass spectra were recorded with a Varian MAT 8500 instrument using a direct probe inlet and electron impact ionization. Matrix-assisted laser desorption ionization spectrometry with time-of-flight mass spectrometry (MALDI-TOFMS) measurements was performed with a Bruker Reflex III in reflection mode using *trans*-2-(3-(4-*tert*-butylphenyl)-2-methyl-2-propenylidene)malononitrile (DCTB) as the matrix. Solutions of the analyte (1 mg per 100 μ L) and the matrix (1 mg per 100 μ L) in tetrahydrofuran were mixed in a ratio of 5:20(v:v) and spotted onto the MALDI target plate prior to the measurement. The laser intensity was set to around 20%. Elemental analysis (EA) was performed with a HEKAtech EA 3000 elemental analyzer (EuroVector CHNS) charged with tungsten oxide and copper. Detection was performed utilizing a GC setup equipped with a thermal conductivity detector.

Synthesis

All solvents were purified and dried using standard procedures. 2-Fluoroisobutyric acid (97%) was purchased from ABCR and used without further purification. 1,3,5-Triaminobenzene was freshly synthesized from 3,5-dinitroaniline (obtained from Aldrich and used as received) as described in the literature.¹³ 2-Fluoroisobutyric acid chloride was synthesized from 2-fluoroisobutyric acid and oxalyl chloride. 2 g (18.8 mmol) of 2-fluoroisobutyric acid was dissolved in 30 mL of CH_2Cl_2 (DCM). The mixture was cooled down to 0 $^{\circ}C$, and after addition of 4.78 g (37.7 mmol) of oxalyl chloride and three drops of DMF it was refluxed overnight. After cooling to room temperature, an excess of potassium stearate was added dropwise (to react the excess oxalyl chloride) until no further gas evolution was observed. The 2-fluoroisobutyric acid chloride was then distilled under normal pressure. All resonances in the ¹H liquid NMR spectra could be unequivocally assigned to solvents and products. Yield: 1.9 g (15.3 mmol, 81.4%); ¹H-NMR (300 MHz, $CDCl_3$): δ = 1.65 ppm (d, ³ $J(^1H, ^{19}F)$ = 20.7 Hz, 6H, $-CH_3$).

Compound 1 was synthesized by dropping 1.9 g (15.3 mmol) of 2-fluoroisobutyric acid chloride to a mixture of 0.56 g (2.6 mmol) of 1,3,5-triaminobenzene, 15 ml of pyridine and 0.08 of LiCl in 80 mL of THF at 0 $^{\circ}C$ under an argon atmosphere. The reaction was stirred over 2 days at 70 $^{\circ}C$ and cooled down to RT, and the solvents were evaporated under vacuum. The residual reaction mixture was poured into an excess of water. The precipitate was filtered off, dried

under reduced pressure and recrystallised from methanol. To remove further impurities, the solid was refluxed in 50 mL of *n*-hexane for 3 hours, filtered off hot and dried again. Yield: 0.44 g (3.53 mmol, 23%). ¹H-NMR (300 MHz, DMSO-*d*₆): δ = 1.56 ppm (d, ³J(¹H, ¹⁹F) = 21.7 Hz, 6H, -CH₃); 7.75 ppm (s, 3H, Ar-H); 9.94 ppm (d, ⁴J(¹H, ¹⁹F) = 3.2 Hz, 3H, -NH). ¹³C-NMR (75 MHz, DMSO-*d*₆): δ = 25.3 ppm (d, ²J(¹³C, ¹⁹F) = 24 Hz, -CH₃); 95.6 ppm (d, ¹J(¹³C, ¹⁹F) = 182 Hz, -CF); 110.7 ppm (s, -ArH); 138.4 ppm (s, -Ar); 171.3 ppm (d, ²J(¹³C, ¹⁹F) = 22 Hz, -C=O). MS (70 eV), *m/z* (%): 387 (M⁺, 100); 344 (22); 326 (47); 299 (17); 69 (8); 61 (31). MALDI-TOFMS: *m/z* calcd: 387.18 ([M]⁺), 410.17 ([M+Na]⁺), 426.14 ([M+K]⁺) g mol⁻¹, found: 387.05 ([M]⁺), 410.05 ([M+Na]⁺), 426.01 ([M+K]⁺) g mol⁻¹. Elemental analysis (N, C, H): calcd 10.8%, 55.8%, 6.2%; found 11.1%, 57.6%, 6.3%.

Solid-state NMR experiments

¹H, ¹³C and ¹⁹F chemical shifts are referenced to TMS and CFCl₃. The ¹⁵N chemical shifts are reported relative to nitromethane, where all values are shifted by -380.5 ppm compared to those for liquid NH₃. All ¹H and ¹⁹F experiments were performed using a 1.3 mm double-resonance probe in a Bruker Avance III HD spectrometer at a field strength of *B*₀ = 14.1 T. The spin rate for magic angle spinning (MAS) was set to *v*_{rot} = 60 000 ± 3 Hz for ¹⁹F and *v*_{rot} = 65 000 ± 3 Hz for ¹H. All ¹³C and ¹⁵N experiments were collected with a 4 mm triple-resonance probe in a Bruker Avance II spectrometer at a field strength of *B*₀ = 7.1 T and at a MAS spin rate of *v*_{rot} = 12 500 ± 1 Hz.

The ¹H/¹⁹F direct excitation experiments were performed using a nutation frequency of *v*_{nut} = 179/150 kHz for the 90° pulse without decoupling of ¹⁹F/¹H. For the ¹⁹F/¹⁹F double-quantum experiments, a symmetric R14₄⁵ double-quantum recoupling protocol with the S₀S₀S_zS_z supercycle was used.⁴⁰ Excitation and reconversion were realised through 90°-270° composite pulses as *R*-elements with a nutation frequency of *v*_{nut} = 210 kHz and a maximum excitation time of 2 ms.

The ¹³C and ¹⁵N cross polarisation (CP) spectra were recorded using a ramped lock pulse consisting of 100 intervals with a linear decrease from 50/93 kHz to 25/46.5 kHz on the ¹H/¹⁹F channel, and the power for ¹³C/¹⁵N was experimentally adjusted to the Hartmann-Hahn conditions. The contact time was set to 3 ms for both ¹H/¹³C and ¹⁹F/¹³C experiments. Due to the high spin density and the large gyromagnetic ratio of protons, this time is sufficiently long to allow magnetization transfer from protons to all carbon atoms and hence all carbon atoms will give rise to signals in the ¹H/¹³C CP. In contrast, only carbon atoms in spatial proximity to the ¹⁹F labels appear in the ¹⁹F/¹³C CP since the used contact time of 3 ms is sufficiently short due to the low spin density of ¹⁹F compared to that of ¹H.

Proton broadband decoupling was realised using a SPINAL-64 sequence during acquisition where the nutation frequency and pulse length were set to 65 kHz and 7 μs, respectively. For ¹⁹F decoupling a XiX sequence⁴¹ with a pulse length of 7 μs and a nutation frequency of 70 kHz was used.

Solid-state NMR simulations

Simulations of the ¹⁹F/¹⁹F DQ build-up curves were performed with the simulation software package SIMPSON.⁴² Relative orientations and principal values of the ¹⁹F/¹⁹F dipole tensors were calculated based on the possible structure models obtained from PXRD. The asymmetry and anisotropy parameters for the chemical shift anisotropy were estimated from a MAS 1D experiment at *v*_{rot} = 3000 ± 2 Hz. The corresponding Euler angles were set to zero for all spins since they seem to show only negligible influence on the supercycled build-up curves,⁴³ which was tested with different arbitrary angles. For powder averaging, 232 (α,β) orientations in combination with 40 γ angles were used.

In all cases, the experimental curves exhibited lower double-quantum efficiencies than the simulations (see the ESI† Fig. S1), which might be caused by residual proton coupling.⁴⁴ For this reason, all simulated curves were fitted to the experimental ones by applying a constant scaling factor, which was determined as follows: for each structure model, every possible assignment of simulated to experimental curves was taken into account with one individual scaling factor for every set of simulated curves. Each scaling factor was optimised with the software package MATLAB in a least-square sense.⁴⁵ Subsequently, for every assignment, a rms value was calculated in percent according to

$$\text{rms} = 100 \times \sqrt{\frac{\sum_i (\text{exp}_i - \text{sim}_i)^2}{\sum_i (\text{exp}_i)^2}}$$

where exp_{*i*} is the experimental data point and sim_{*i*} the simulated data point corresponding to the *i*th abscissa value. Finally, for each structure model, only the assignment with the lowest rms value was considered for the subsequent analysis.

Ab initio structure determination using PXRD

PXRD measurements on compound 1 were carried out using a STOE STADI P diffractometer equipped with a curved germanium monochromator (oriented according to the (111) plane) creating CuKα₁ radiation (λ = 1.5406 Å). The samples were filled in a 0.7 mm capillary tube and measured in Debye-Scherrer geometry in a 2θ range of 2°-50°. Above 50°, reflections were hardly observed. The powder patterns were fully handled using REFLEX PLUS from the commercial program package Accelrys MS Modeling (version 5.0).⁴⁶ After indexing, Pawley refinement and assignment of the correct space group, the structure solution step was performed by means of real-space methods with the simulated annealing algorithm.⁴⁷ For the structure solution, the molecule was first geometry optimised with DFT methods (see the section Computational methods). As a starting model, two molecules were set into the asymmetric unit as one motion group each. Besides the possible translational and rotational degrees of freedom, the structure-directing torsion angles in each molecule were set free during the structure solution

(see Scheme 1, right). Additionally, a preferred orientation correction following the model of March–Dollase was applied during the solution step.⁴⁸

Concerning the Rietveld refinement, at first, four cycles, where the atomic parameters were allowed to relax, were carried out using a global isotropic temperature factor for all atoms and a preferred orientation adjustment according to Rietveld–Toraya.⁴⁹ The molecular structure was retained without any limitations for the rotational and translational degrees of freedom by taking into account the energy considerations by applying the COMPASS force field.⁵⁰ Nevertheless, the final number of refined structural parameters (see Table 1) is not strictly representative due to the adopted energy constraint. This force field-assisted refinement is based on a *combined figure of merit* (R_{comb}) with

$$R_{\text{comb}} = (1 - w_{\text{comb}})wR_p + w_{\text{comb}}R_{\text{Energy}} \quad (1)$$

where w_{comb} represents the energy weighting factor that was set to 0.5. The energetic contribution, R_{Energy} , is defined as follows:

$$R_{\text{Energy}} = \tan h \left(0.1 \frac{E - E_{\text{min}}}{E_{\text{tol}}} \right) \quad (2)$$

Table 1 Relevant crystallographic data for **1** from PRXD

1	
Formula	C ₁₈ H ₂₄ F ₃ N ₃ O ₃
M/g mol ⁻¹	387.38
Crystal system	Monoclinic
Space group	<i>P</i> 2 ₁
<i>a</i> /Å	11.886(4)
<i>b</i> /Å	15.395(5)
<i>c</i> /Å	10.554(4)
<i>a</i> /°	90
<i>β</i> /°	95.012(2)
<i>γ</i> /°	90
<i>V</i> /Å ³	1924(2)
<i>Z</i> / <i>Z</i>	2/4
<i>ρ</i> /g cm ⁻³	1.337
<i>T</i> /K	293
<i>U</i>	0.24(1)
<i>V</i>	-0.033(3)
<i>W</i>	0.0024(2)
NA	0.22(3)
NB	0.005(1)
Zero-point shift	0.0061(9)
<i>R</i> ₀ ^a	0.8413
<i>a</i> *	0.142(14)
<i>b</i> *	0.984(2)
<i>c</i> *	0.098(20)
No. of refined structural parameters ^b	307
<i>R</i> _p	0.0398
<i>wR</i> _p	0.0552

^a Preferred orientation coefficient of the sample according to the March–Dollase function representing a dimensionless value reflecting the shape of the crystallites; $R_0 < 1$ for platelets, $R_0 > 1$ for needles.

^b The number of refined structural parameters include one isotropic temperature factor and three translational elements of each atom within the asymmetric unit. Since a COMPASS force field with an energy constraint was applied, the refinement of the atomic positions is not handled independently.

where E represents the total energy, E_{min} the energy in the global minimum and E_{tol} the energy window above E_{min} in which possible structure solutions are tolerated. Here, a default value of 40 kcal mol⁻¹ was used, preventing the break of covalent bonds as well as an overlap of atoms or atom groups during the refinement step, which reduced the absolute number of refined structural parameters noticeably.

Afterwards, the peak profile including FWHM (pseudo-Voigt) with its profile parameters NA and NB was refined. The pseudo-Voigt peak shape function as a linear combination of Lorentzian (L) and Gaussian (G) includes the θ -dependent mixing parameter η given by

$$\eta(\theta) = (NA + NB) \times 20 \quad (3)$$

where NA and NB are adjustable parameters. Besides, the lattice parameters, the zero-point shift, the sample off-centering, the asymmetry correction (Finger–Cox–Jephcoat)⁵¹ and the experimental background using 20 orthogonal polynomials were refined. Relevant crystallographic data are summarized in Table 1. Atomic parameters, the temperature factor and the occupancy of compound **1** are included in the crystallographic information file which is available in the ESL†

Creation of additional structure models

In the structure model obtained from the PXRD structure solution, the N_HC_OC_QF torsions (see Scheme 1) of the two molecules of the asymmetric unit were altered by 60° and 120° in different combinations in order to test the influence on PXRD patterns and ¹⁹F/¹⁹F double-quantum build-up curves. During the subsequent Rietveld refinement described above, the structures were allowed to relax. In all cases, N_HC_OC_QF torsion angles of 0° or 120° compared to those of the original model a) were observed afterwards. Four models were selected for the double-quantum simulations: in model b), one torsion of molecule **1** changed by 120° (symbolic representation: †); in model c), all three torsions of molecule **1** changed by 120° (†††); in model d), all torsions of both molecules changed by 120° (†††††); and in model e), all torsions of molecule **1** changed by 120° and all torsions of molecule **2** by -120° (††††††). For these models, the Rietveld profiles were calculated and the double-quantum build-up curves were simulated.

Computational methods

Before the *ab initio* structure solution of compound **1**, the molecule was geometry optimised by DFT methods using the module DMol3 of the program package Accelrys MS Modeling (version 5.0).⁴⁶ A double-zeta plus polarisation basis set with the GGA functional PW91 was applied.⁵² The self-consistent field (SCF) energy convergence was set to 10⁻⁶ eV per atom.

Results and discussion

To gain insight into the structure-directing effect of fluorine substitution in the side groups of **2**, the crystal structure of **1**

was solved by a combination of PXRD and solid-state NMR experiments. First, we deduce the content of the asymmetric unit from multinuclear 1D solid-state NMR experiments. With this information, a structure model is obtained from PXRD data based on real-space methods and quantum chemical calculations. Finally, the structural disorder of the side groups is probed by double-quantum dipolar recoupling experiments.

Symmetry considerations using solid-state NMR

Fig. 1 and 2 depict the high-resolution 1D spectra of ^1H , ^{19}F , ^{13}C and ^{15}N . The ^1H spectrum (Fig. 1a) exhibits three signal groups. Group 1 is located between $\delta = 9$ ppm and 8.5 ppm, group 2 between $\delta = 8.5$ ppm and 5 ppm and group 3 below $\delta = 4$ ppm. The intensity ratio of groups 1, 2 and 3 is 1.0:1.0:6.1. The shift of group 1 is characteristic of the NH protons (4) (compare Scheme 1 for labeling) participating in weak hydrogen bonds,⁵³ the shift of group 2 is characteristic of the aromatic CH groups (6), and group 3 exhibits a typical shift region for the methyl groups (1). Furthermore, the intensity ratio fits the ratio expected from the molecular

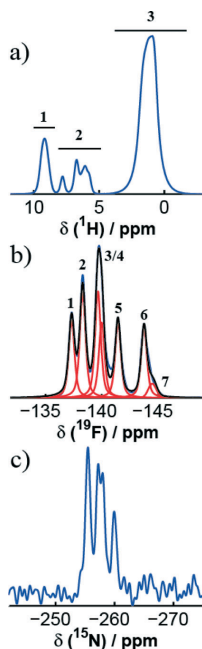


Fig. 1 Solid-state NMR spectra of 1. a) ^1H MAS spectrum obtained with single-pulse excitation. The intensity ratio of spectral regions 1–3 is 1:1.0:6.1. b) ^{19}F spectrum obtained with single-pulse excitation and deconvolution into peaks 1–7. The intensity ratio of peaks 1–6 is 1.4:1.4:1.1:0.9. Peak 7 is assigned to an impurity (see text and Fig. 3). c) ^{15}N spectrum obtained by $^1\text{H}^{15}\text{N}$ cross polarization.

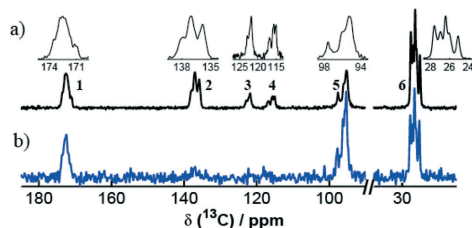


Fig. 2 ^{13}C solid-state NMR spectra of compound 1. a) $^1\text{H}^{13}\text{C}$ CP experiments with close-ups of the six groups. b) $^{19}\text{F}^{13}\text{C}$ CP experiment with the same shift region. The groups are labelled 1–6 as depicted.

structure (compare Scheme 1, $3\text{NH}:3\text{CH}:18\text{CH}_3$ protons). Since the aromatic CH signals split into at least four different resonances, more than one molecule must be contained in the asymmetric unit.

The ^{19}F spectrum (Fig. 1b) shows five well-separated signal groups. High-resolution 2D double-quantum single-quantum (DQSQ) correlation experiments (see Fig. 3a and b) reveal that the most intense signal in the middle corresponds to two coinciding peaks (peaks 3 and 4 of Fig. 1b). The deconvolution of the spectrum reveals an additional signal on the right side of the signal group (peak 7 of Fig. 1b). Since it does not show any DQ coherences with one of the remaining peaks in the 2D DQSQ correlation experiment (Fig. 3a), it is identified as an impurity and can be neglected for the following discussion. The remaining peaks 1–6 exhibit an intensity ratio of 1.0:1.4:1.4:1.0:1.0:0.9, which implies that the asymmetric unit must contain at least two molecules. The relatively high intensities of peaks 2 and 3 are probably due to uncertainties in background correction.

In the $^1\text{H}^{15}\text{N}$ CP spectrum (Fig. 1c), a signal group around $\delta = -258$ ppm is observed, which is typical for the amide units (4). It exhibits at least four distinct resonances, which support the assumption of two or more independent molecules contained in the asymmetric unit.

In order to assign the ^{13}C resonances, $^1\text{H}^{13}\text{C}$ and $^{19}\text{F}^{13}\text{C}$ CP experiments are analysed (Fig. 2). Herein, the contact time was chosen in order to highlight the strongest $^1\text{H}^{13}\text{C}$ and $^{19}\text{F}^{13}\text{C}$ connectivities (for details, see the Experimental section). First, in the $^1\text{H}^{13}\text{C}$ CP, six signal groups appear (Fig. 2a). Group 1 at $\delta = 172$ ppm is characteristic of the carbonyl groups (3), and group 6 around $\delta = 25$ ppm is typical for the methyl groups (1). Due to their spatial proximity to fluorine atoms, they are also observed in the $^{19}\text{F}^{13}\text{C}$ CP (see Fig. 2b). Group 2 of the $^1\text{H}^{13}\text{C}$ CP is characteristic of the quaternary aromatic carbon atoms (2) and groups 3 and 4 of the aromatic CH units (6). Since their distance to the fluorine atoms in the molecular structure is long, they do not appear in the $^{19}\text{F}^{13}\text{C}$ CP. The remaining group 5 must, therefore, belong to the quaternary carbons (2) which are directly attached to the ^{19}F spins. This is supported by the $^{19}\text{F}^{13}\text{C}$ CP, in which group 5 exhibits quite intense signals. Since groups 3 and 4 together show at least 5 distinct

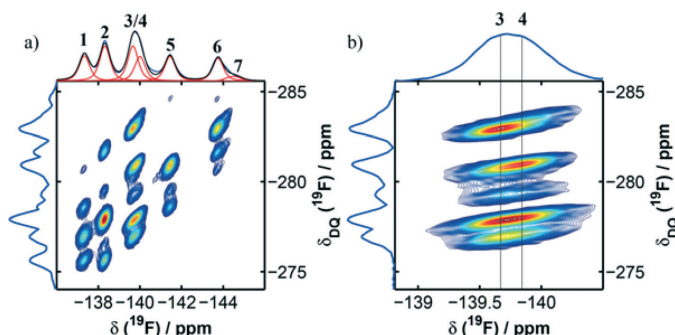


Fig. 3 a) ^{19}F - ^{19}F double-quantum single-quantum correlation spectrum of 1. At the top, the deconvolution of the one-pulse experiment (compare Fig. 1b) is depicted. Only the area containing signals is depicted. b) Close-up of the area around peaks 3 and 4 of a), where the lines mark the shifts of the two distinct signals. Signal 7 exhibits no correlations.

resonances for the aromatic CH groups, the ^{13}C signals also indicate that two molecules are contained in the asymmetric unit.

In conclusion, most resonances for the individual chemical building units are split into several signals. For the aromatic CH groups, at least four resonances are visible in the ^1H spectrum and five resonances in the ^{13}C spectrum, six signals with roughly equal intensities appear in the ^{19}F direct excitation experiment, and the ^{15}N spectrum exhibits at least four resonances for the NH groups. Therefore, the asymmetric unit has to contain at least two molecules. Moreover, the ^1H chemical shift of the NH group is indicative of moderate hydrogen bonds and only one peak is present for the NH protons. Thus, all of them are expected to participate in a homogeneous hydrogen bond network without significant differences in the strength of the hydrogen bonds.^{5,13}

Crystal structure solution of 1,3,5-tris(2-fluoro-2-methylpropionylamino)benzene from PXRD and solid-state NMR spectroscopy

Indexing of the powder pattern leads to a monoclinic metric. The subsequent refinement in $P2$ using the Pawley algorithm⁵⁴ results in lattice constants of $a = 11.916 \text{ \AA}$, $b = 15.433 \text{ \AA}$, $c = 10.580 \text{ \AA}$ and $\beta = 95.011^\circ$ and a unit cell volume of 1924 \AA^3 . Analysing the integral extinction conditions leads to 8 possible space groups ($P2$, $P2_1$, Pc , Pm , $P2/m$, $P2_1/m$, $P2/c$, and $P2_1/c$). Assuming that all non-hydrogen atoms within this compound (C, F, N, and O) possess a volume of approximately 18 \AA^3 , the molecular volume can be estimated to be roughly 490 \AA^3 . Compared to a unit cell volume of 1924 \AA^3 , this size restriction allows a maximum of four molecules within the unit cell. Additionally, the ^1H , ^{13}C , ^{15}N and ^{19}F solid-state NMR spectra indicate that the asymmetric unit consists of at least two BTA molecules. Since the molecule itself does not possess a mirror plane or an intrinsic C_2 symmetry, a location of all atoms on special positions

within the unit cell is very unlikely. Therefore, the multiplicity of the general position must be 2 and only $P2$, $P2_1$, Pm and Pc remain as the possible space groups. A more detailed analysis of the experimental powder pattern reveals that odd reflections of the $0k0$ series are systematically absent, which strongly favours the space group $P2_1$.

Within the space group $P2_1$, *ab initio* structure solution with real-space methods was performed based on a combination of a close-contact penalty and wR_p as a cost function. The DFT geometry-optimized molecule was set twice in the unit cell and treated independently as rigid bodies with three rotational and three translational degrees of freedom for each molecule during the solution step. Additionally, the two most important structure-directing torsion angles (see Scheme 1, left) were varied during the solution step. The wR_p value after the solution accounted for 14.66%; full Rietveld refinement finally led to a wR_p value of 5.5%. The resulting metric has unit cell constants of $a = 11.886(4) \text{ \AA}$, $b = 15.394(5) \text{ \AA}$, $c = 10.553(4) \text{ \AA}$ and $\beta = 95.011(2)^\circ$ and contains four molecules in the unit cell. The experimental powder data and the Rietveld profile are depicted in Fig. 4. Relevant refinement parameters are given in Table 1.

Since the electron density gives rise to the scattering in X-ray diffraction, the difference between atoms or groups with similar or equal electron densities is blurred. The methyl groups and fluorine atoms both possess 9 electrons which make them hard to distinguish by PXRD experiments. This indicates that their positions could be exchanged and even a random distribution might be possible.

To probe this hypothesis, the methyl groups and fluorine atoms of one or both molecules in the asymmetric unit were rotated in different ways by changing the $\text{N}_\text{H}\text{C}_\text{O}\text{C}_\text{Q}\text{F}$ torsion angles (see Scheme 1, left) and the subsequent Rietveld refinement described in the Experimental section. From the resulting structure models, three were selected in addition to the original structure solution a) in order to probe the effect of methyl-fluorine exchange on the calculated Rietveld patterns. In model b), one $\text{N}_\text{H}\text{C}_\text{O}\text{C}_\text{Q}\text{F}$ torsion of the

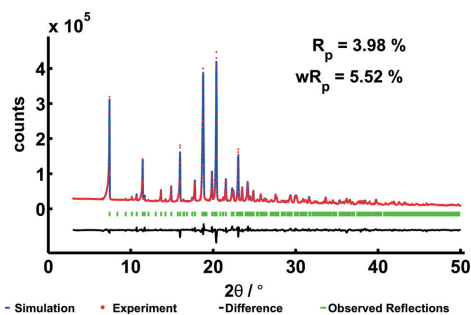


Fig. 4 Rietveld profile plot of the PXRD pattern in the space group $P2_1$ collected at room temperature in a 2θ range of 2° – 50° using $\text{CuK}\alpha_1$ radiation. The difference plot is shifted by -0.6×10^{-5} counts.

first molecule of the asymmetric unit was changed by approximately 120° , which will be symbolically depicted by 1. In model c), all $\text{N}_\text{H}\text{C}_\text{O}\text{C}_\text{Q}\text{F}$ torsions of the first molecule changed by approximately 120° (111) and in model d) all $\text{N}_\text{H}\text{C}_\text{O}\text{C}_\text{Q}\text{F}$ torsions of both molecules changed by approximately 120° (11111). Finally, in model e), all $\text{N}_\text{H}\text{C}_\text{O}\text{C}_\text{Q}\text{F}$ torsions of the first molecule changed by approximately 120° and all $\text{N}_\text{H}\text{C}_\text{O}\text{C}_\text{Q}\text{F}$ torsions of the second molecule by -120° (111111). The Rietveld profiles calculated from these models are contained in Fig. S2 and S3 in the ESI.† Fig. 5 (left) depicts the difference plots between the observed powder diffractogram and calculated Rietveld profiles.

The significantly higher R_p and wR_p values of model e) imply that the resulting structure is unlikely to have larger deviations in the packing compared to the other models. For b)–d), however, the difference plots are quite similar and the wR_p values differ by 0.75% at most, which imply similar electron density distributions. In conclusion, the $\text{N}_\text{H}\text{C}_\text{O}\text{C}_\text{Q}\text{F}$

torsions cannot be determined with reasonable accuracy by PXRD.

Here, solid-state NMR can assist by probing distance relations through quantitative symmetry-based DQ dipolar recoupling experiments. The ^{19}F – ^{19}F homonuclear dipolar interaction was selectively recoupled by applying a SR14_4^5 sequence which leads to the excitation of ^{19}F – ^{19}F double-quantum coherences. Since the dipolar interaction constant depends inversely on the third power of the internuclear distance, the recoupling efficiency encodes the structural environment of each spin. Moreover, the inverse cubic relation implies that already small structural changes may lead to high deviations in dipolar coupling. Here, we used symmetric build-up curves which were simulated for structure models a)–d). For every model, a 9-spin system was created for each ^{19}F of the asymmetric unit by taking all spins into account within a sphere with a diameter of 13.4 Å at least (see the ESI† Fig. S4). The relevant rms values are depicted in Fig. 5 (right).

The original structure solution a) shows the best rms value of 9.1%, whereas for the remaining models, the rms values are at 11.6% or higher. Fig. 6 depicts the experimental build-up curves for the six ^{19}F resonances with the simulated curves for the four structure models a)–d).

The simulations are scaled by a unique constant factor for each model in order to compensate for residual dipolar proton coupling. This leaves the position of the first maximum and minimum, and therefore, the structural information is unaffected. In all cases, the experimental curves show a fast build-up with maxima around an excitation time of $\tau_{\text{excitation}} = 1$ ms. For the original structure model a), the curves fit very well for peaks 3–6. For peaks 1 and 2, the scaled simulations reach higher double-quantum efficiencies as the experimental curves. These two peaks reach their maximum at slightly longer excitation times compared to signals 3–6, which imply weaker homonuclear ^{19}F – ^{19}F

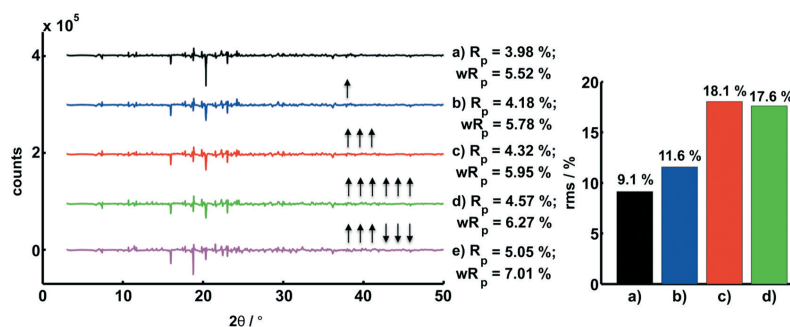


Fig. 5 Left: difference plots between the experimental PXRD data and the calculated Rietveld profiles for the different structure models (a–e) after refinement. The difference plots are shifted by 4×10^{-5} counts in model a), 3×10^{-5} counts in model b), 2×10^{-5} counts in model c) and 10^{-5} counts in model d). Right: rms values of the deviations between the ^{19}F – ^{19}F DQ build-up simulations for the different structure models (a–e) and the experimental data. For a detailed explanation of the models, see text and the Experimental section.

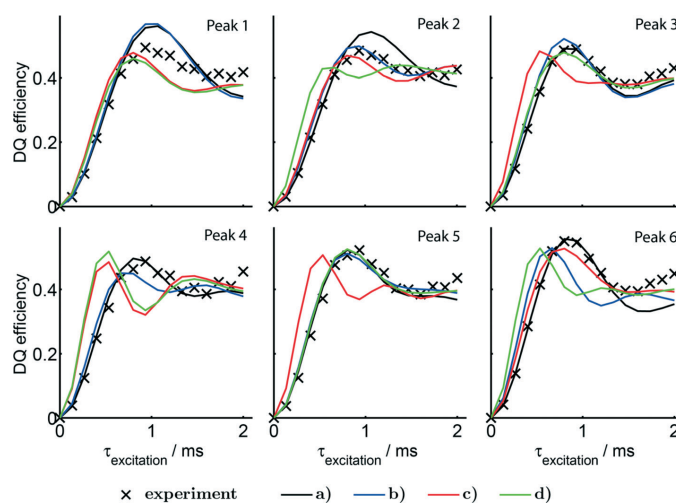


Fig. 6 Experimental and simulated $^{19}\text{F}^{19}\text{F}$ build-up curves. The assignment of simulated to experimental curves was chosen according to the smallest rms values. The experimental curves are labeled with respect to the corresponding peaks in the ^{19}F spectrum (see Fig. 1b) and simulations a)–d) according to the structure models (see Fig. 5 and text). Each set of simulations was scaled by a constant factor of 0.75 in the case of a) and c) and 0.79 in the case of b) and d).

interactions with the consequence of a stronger influence of residual dipolar proton coupling.

In contrast to model a), the remaining structure models b)–d) show more pronounced deviations compared to the experiment. In all cases, at least two build-up curves exist which exhibit a faster rise, *e.g.*, as in the case of models c) and d) for peak 4. This implies shorter $^{19}\text{F}^{19}\text{F}$ distances since the total number of ^{19}F is the same for all simulations. In fact, the shortest $^{19}\text{F}^{19}\text{F}$ distances in models a)–d) are 3.9 Å, 3.8 Å, 3.4 Å and 3.4 Å, respectively, and hence the corresponding coupling constants are -1794 Hz, -1940 Hz, and -2708 Hz. Thus, the sensitivity of this experiment towards structural details is high, complementing the information obtained from the PXRD experiment. The lowest wR_p value of 5.52% together with the superior rms value of 9.1% strongly favours structure model a).

Crystal structure of 1,3,5-tris(2-fluoro-2-methylpropionylamino)benzene

The molecular structures of the two independent molecules (1a and 1b) after the Rietveld refinement are depicted in Fig. 7 and the most important intramolecular distances and angles are listed in Table 2.

Interestingly, both molecules exhibit weak intramolecular $\text{NH}\cdots\text{F}$ contacts with proton–fluorine distances between 2.1 Å and 2.3 Å. Herein, the proton positions were determined through DFT geometry optimisation of a single molecule and retained during Rietveld refinement due to the energy constraint by the applied force field. Moreover, both molecules exhibit a

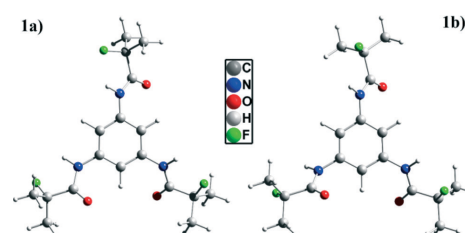


Fig. 7 Molecular structures of the two independent molecules of the asymmetric unit of 1,3,5-tris(2-fluoro-2-methylpropionylamino)benzene (1) as derived from the PXRD experiment.

high topological similarity although they are not related through symmetry operations. For both molecules, two of the three carbonyl groups point up and one points downwards with respect to the benzene plane leading to an intrinsically frustrated molecular system. The corresponding $\text{C}_{\text{Ar}}\text{C}_{\text{Ar}}\text{NH}$ torsion angles are 40.65° , 40.82° and -152.85° for molecule 1 and 36.49° , 57.0° and -124.53° for molecule 2. The NHCO torsion angles representing the amide groups show values between 173° and 177° which are typical values for partial double bonds. Besides, the torsions including the fluorine atoms within the side groups ($\text{N}_\text{H}\text{C}_\text{O}\text{C}_\text{F}$) are also distinguishable with values between roughly 7° and 32° . These locally different fluorine environments are in agreement with the six distinct resonances observed in the 1D ^{19}F solid-state NMR (see Fig. 1b).

Table 2 Intramolecular distances in angstrom and angles in degree derived from PXRD with restrictions based on the COMPASS force field used for the first Rietveld refinement step. The distances marked by * use the positions of the protons determined through DFT geometry optimisation of a single molecule

	Molecule 1	Molecule 2
$d(\text{C}=\text{O})$	1.214	1.211–1.213
$d(\text{C}_{\text{Ar}}-\text{N})$	1.390–1.396	1.397–1.398
$d(\text{C}_{\text{O}}-\text{N})$	1.368–1.369	1.368–1.373
$d(\text{C}_{\text{Ar}}-\text{C}_{\text{Ar}})$	1.381–1.387	1.382–1.386
$d(\text{C}_{\text{q}}-\text{C}_{\text{Me}})$	1.525–1.529	1.526–1.533
$d(\text{C}-\text{F})$	1.390	1.388–1.391
$d(\text{NH}\cdots\text{F})$	2.121–2.171*	2.239–2.268*
$\angle(\text{NH}\cdots\text{F})$	107.0–109.2	103.9–105.9
$\angle(\text{HNCO})$	173.2–177.1	176.5–177.0
$\angle(\text{C}_{\text{Ar}}\text{C}_{\text{Ar}}\text{NH})$	–152.9, 40.7, 40.8	–124.5, 36.5, 57.0
$\angle(\text{N}_{\text{H}}\text{C}_{\text{O}}\text{C}_{\text{q}}\text{F})$	6.86–25.04	26.15–31.81
$\angle(\text{OC}_{\text{O}}\text{C}_{\text{q}}\text{F})$	156.0–175.1	150.7–158.4

The crystal structure of **1** can be described as a hydrogen bond-mediated layer-like structure including a molecular zigzag motif due to the 2_1 screw axis along the b axis of the unit cell. The two independent molecules of the asymmetric unit (see Fig. 8, black) are incorporated into one strand along the crystal's c axis *via* four moderate $\text{NH}\cdots\text{OC}$ H bonds with lengths of 2.03 Å and 2.22 Å (corresponding to $\text{NH}\cdots\text{OC}$ lengths of 2.93 Å and 3.20 Å, see Fig. 8, dashed pink lines) and $\text{NH}\cdots\text{O}$ angles located in the range of 146.9° and 162.1°.

The distances between the aromatic cores of the molecules within one strand accounts for 5.15 Å up to 5.64 Å,

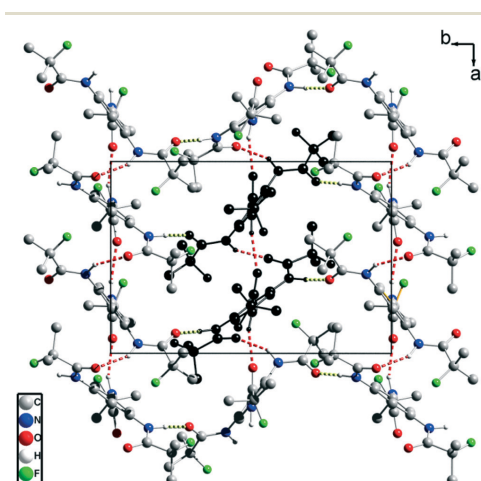


Fig. 8 Hydrogen bond pattern of compound **1**. The two independent molecules of the asymmetric unit (black) are connected to strands through four H bonds (dashed red lines). The strands are further connected by two lateral hydrogen bonds along the b axis of the crystal (dashed green lines), leading to a two-dimensional layer-like hydrogen bond pattern. All protons except the amide ones as well as the $\text{C}_{\text{q}}(\text{CH}_3)_2\text{F}$ groups are omitted for clarity.

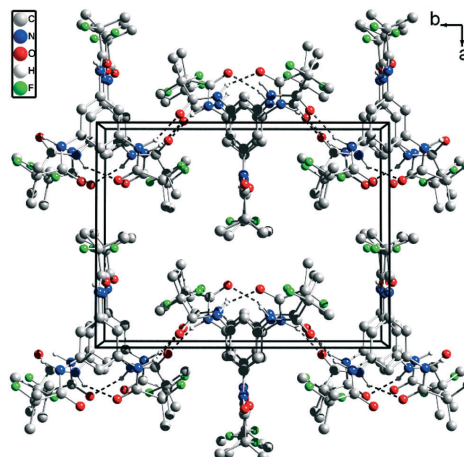


Fig. 9 Perspective view of the two unit cells along the c axis demonstrating the layer-like character of the structure. All protons except those of the amide group are removed to retain clarity. Between neighbouring layers, only van der Waals interactions are possible.

ruling out the existence of π - π interactions as observed in other BTA-related systems.^{9,11,13} The aromatic benzene rings thereby show a tilt angle of roughly 16° towards each other. These one-dimensional strands are connected with a neighbouring strand which arises from the translation through the 2_1 screw axis along the monoclinic axis. Here, two lateral medium strong $\text{NH}\cdots\text{OC}$ hydrogen bonds with $\text{N}\cdots\text{O}$ lengths of 2.89 Å and 2.94 Å are observed (see Fig. 8, dashed green lines), and the related $\text{NH}\cdots\text{O}$ angles account for 157.9° and 160.7°. Interestingly, none of the six independent fluorine atoms participate in intermolecular hydrogen bonds.

Thus, a two-dimensional layer-like structure within the b - c plane of the crystal is observed and due to the translational symmetry, a second layer arises along the crystalline a axis (see Fig. 9). Since between neighbouring layers only van der Waals interactions are relevant, the interaction pattern in the structure is highly anisotropic.

Conclusion

We used a concerted approach of multidimensional and multinuclear solid-state NMR spectroscopy, *ab initio* real-space PXRD methods and computer simulations to solve the structure of 1,3,5-tris(2-fluoro-2-methylpropionylamino)benzene. It can be described by a lamellar arrangement of molecules. Within each layer, strong to moderate two-dimensional hydrogen bond patterns along the b and c axes with $\text{N}\cdots\text{O}$ distances ranging from 2.9 Å up to 3.2 Å are formed. The molecules are stacked along the c axis, where neighbouring

benzene rings exhibit a non-coplanar arrangement and distances ranging from 5.15 Å up to 5.64 Å, which prevent π - π interactions. In each molecule the amide bonds are tilted with respect to the benzene rings in a way that only two out of three carbonyl groups point into the same direction. Surprisingly, the fluorine atoms contribute only to weak intramolecular NH...F contacts but not to the intermolecular hydrogen bond network. Since between neighbouring layers only van der Waals interactions are possible, the interaction pattern is highly anisotropic and one might expect fast two-dimensional crystal growth along the crystal's *b* and *c* axes, rendering this BTA an interesting candidate for formation of two-dimensional structures *via* self-assembly.

In the analogous BTA 1,3,5-tris(2,2-dimethylpropionylamino)benzene (**2**), where just the fluorine atoms of **1** are replaced by methyl groups, the molecules are arranged in columnar stacks. The latter are stabilized by moderate helical hydrogen bonds in combination with π - π interactions.¹³ All amide bonds of the molecules within one column are also tilted with respect to the benzene core and point into the same direction so that a macrodipole is formed. Due to an antiparallel arrangement of these macrodipoles in neighbouring columns of the pseudo-hexagonal rod packing, the net dipole moment is cancelled. This allows for fast one-dimensional growth through cooperative effects in the hydrogen bond network.^{12,13,55}

In spite of the similarities in the molecular structures of **1** and **2**, in particular with respect to the steric demand of the side groups, completely different crystal structures are formed. Since fluorine does not participate in the hydrogen bond network, we assume that the different molecular polarity is responsible for this effect. This illustrates the versatility of BTAs and the easy accessibility of new packing motifs by small chemical modifications.

Acknowledgements

The authors want to thank the DFG (SFB 840, Project B4) for funding this work and Dr. Wolfgang Milius for the fruitful discussions with respect to crystallographic issues. C.Z. thanks the Elitenetzwerk Bayern (ENB) for additional support. Martin Hufnagel is gratefully acknowledged for performing MALDI-TOFMS measurements.

References

- (a) J.-M. Lehn, *Angew. Chem.*, 1988, **100**, 91; (b) L. Brunsveld, B. J. B. Folmer, E. W. Meijer and R. P. Sijbesma, *Chem. Rev.*, 2001, **101**, 4071.
- J.-M. Lehn, *Angew. Chem., Int. Ed. Engl.*, 1990, **29**, 1304.
- P. J. M. Stals, M. M. J. Smulders, R. Martin-Rapun, A. R. A. Palmans and E. W. Meijer, *Chem. – Eur. J.*, 2009, **15**, 2071.
- P. J. M. Stals, J. C. Everts, R. de Bruijn, I. A. W. Filot, M. M. J. Smulders, R. Martin-Rapun, E. A. Pidko, T. F. A. de Greef, A. R. A. Palmans and E. W. Meijer, *Chem. – Eur. J.*, 2010, **16**, 810.
- M. Wegner, D. Dudenko, D. Sebastiani, A. R. A. Palmans, T. F. A. de Greef, R. Graf and H. W. Spiess, *Chem. Sci.*, 2011, **2**, 2040.
- M. Schmidt, C. S. Zehe, R. Siegel, J. U. Heigl, C. Steinlein, H.-W. Schmidt and J. Senker, *CrystEngComm*, 2013, **15**, 8784.
- K. Hanabusa, C. Koto, M. Kimura, H. Shirai and A. Kakehi, *Chem. Lett.*, 1997, **26**, 429.
- S. Cantekin, T. F. A. de Greef and A. R. A. Palmans, *Chem. Soc. Rev.*, 2012, **41**, 6125.
- M. P. Lightfoot, F. S. Mair, R. G. Pritchard and J. E. Warren, *Chem. Commun.*, 1999, 1945.
- (a) L. Brunsveld, A. P. H. J. Schenning, M. A. C. Broersen, H. M. Janssen, J. A. J. M. Vekemans and E. W. Meijer, *Chem. Lett.*, 2000, **99**, 292; (b) D. Kluge, F. Abraham, S. Schmidt, H.-W. Schmidt and A. Fery, *Langmuir*, 2010, **26**, 3020; (c) D. Kluge, J. C. Singer, J. W. Neubauer, F. Abraham, H.-W. Schmidt and A. Fery, *Small*, 2012, **8**, 2563.
- M. Kristiansen, P. Smith, H. Chanzy, C. Baerlocher, V. Gramlich, L. McCusk, T. Weber, P. Pattison, M. Blomenhofer and H.-W. Schmidt, *Cryst. Growth Des.*, 2009, **9**, 2556.
- R. Q. Albuquerque, A. Timme, R. Kress, J. Senker and H.-W. Schmidt, *Chem. – Eur. J.*, 2013, **19**, 1647.
- M. Schmidt, J. Wittmann, R. Kress, D. Schneider, S. Steuernagel, H.-W. Schmidt and J. Senker, *Cryst. Growth Des.*, 2012, **12**, 2543.
- (a) Y. Yasuda, E. Iishi, H. Inada and Y. Shirota, *Chem. Lett.*, 1996, **25**, 575; (b) J. J. van Gorp, J. A. J. M. Vekemans and E. W. Meijer, *J. Am. Chem. Soc.*, 2002, **124**, 14759.
- (a) N. Shi, H. Dong, G. Yin, Z. Xu and S. Li, *Adv. Funct. Mater.*, 2007, **17**, 1837; (b) A. Bernet, R. Q. Albuquerque, M. Behr, S. T. Hoffmann and H.-W. Schmidt, *Soft Matter*, 2012, **8**, 66.
- Y. Matsunaga, N. Miyajima, Y. Nakayasu, S. Sakai and M. Yonenaga, *Bull. Chem. Soc. Jpn.*, 1988, **61**, 207.
- P. Besenius, J. L. M. Heynens, R. Straathof, M. M. L. Nieuwenhuizen, P. H. H. Bomans, E. Terreno, S. Aime, G. J. Strijkers, K. Nicolay and E. W. Meijer, *Contrast Media Mol. Imaging*, 2012, **7**, 356.
- M. Gelinsky, R. Vogler and H. Vahrenkamp, *Inorg. Chem.*, 2002, **41**, 2560.
- (a) M. Blomenhofer, S. Ganzleben, D. Hanft, H.-W. Schmidt, M. Kristiansen, P. Smith, K. Stoll, D. Mäder and K. Hoffmann, *Macromolecules*, 2005, **38**, 3688; (b) P. M. Kristiansen, A. Gress, P. Smith, D. Hanft and H.-W. Schmidt, *Polymer*, 2006, **47**, 249; (c) F. Abraham, S. Ganzleben, D. Hanft, P. Smith and H.-W. Schmidt, *Macromol. Chem. Phys.*, 2010, **211**, 171.
- F. Richter and H.-W. Schmidt, *Macromol. Mater. Eng.*, 2013, **298**, 190.
- J. Wang, Q. Dou, X. Chen and L. Di, *J. Polym. Sci., Part B: Polym. Phys.*, 2008, **46**, 1067.
- F. Abraham and H.-W. Schmidt, *Polymer*, 2010, **51**, 913.
- (a) H. Nakajima, M. Takahashi and Y. Kimura, *Macromol. Mater. Eng.*, 2010, **295**, 460; (b) H. Bai, W. Zhang, H. Deng,

- Q. Zhang and Q. Fu, *Macromolecules*, 2011, **44**, 1233; (c) P. Song, Z. Wei, J. Liang, G. Chen and W. Zhang, *Polym. Eng. Sci.*, 2012, **52**, 1058.
- 24 J. Senker, L. Seyfarth and J. Voll, *Solid State Sci.*, 2004, **6**, 1039.
- 25 L. Seyfarth, J. Sehnert, N. El-Gamel, W. Milius, E. Kroke, J. Breu and J. Senker, *J. Mol. Struct.*, 2008, **889**, 217.
- 26 J. C. Facelli and A. M. Orendt, Magnetic Shielding and Chemical Shifts: Basics, in *eMagRes*, 2007.
- 27 R. E. Wasylshen, Dipolar and Indirect Coupling: Basics, in *eMagRes*, 2007.
- 28 P. P. Man, *Quadrupolar Interactions*, in *eMagRes*, 2007.
- 29 (a) M. Duer, *Introduction to solid-state NMR spectroscopy*, Blackwell, Oxford, U.K., 2004; (b) R. K. Harris, R. E. Wasylshen and M. J. Duer, *NMR Crystallography*, Wiley, Chichester, U.K., 2nd edn, 2009.
- 30 (a) F. Taulelle, *Solid State Sci.*, 2004, **6**, 1053; (b) F. W. Karau, L. Seyfarth, O. Oeckler, J. Senker, K. Landskron and W. Schnick, *Chem. - Eur. J.*, 2007, **13**, 6841.
- 31 (a) J. Senker, J. Sehnert and S. Correll, *J. Am. Chem. Soc.*, 2005, **127**, 337; (b) J. Sehnert and J. Senker, *Chem. - Eur. J.*, 2007, **13**, 6339-6350.
- 32 (a) M. Schmidt, J. Wittmann, R. Kress, H.-W. Schmidt and J. Senker, *Chem. Commun.*, 2013, **49**, 267; (b) E. Wirnhier, M. Döblinger, D. Gunzelmann, J. Senker, B. V. Lotsch and W. Schnick, *Chem. - Eur. J.*, 2011, **17**, 3213; (c) D. Hirsemann, T. K.-J. Köster, J. Wack, L. van Wüllen, J. Breu and J. Senker, *Chem. Mater.*, 2011, **23**, 3152.
- 33 L. Seyfarth, J. Seyfarth, B. Lotsch, W. Schnick and J. Senker, *Phys. Chem. Chem. Phys.*, 2010, **12**, 2227.
- 34 L. Seyfarth and J. Senker, *Phys. Chem. Chem. Phys.*, 2009, **11**, 3522.
- 35 (a) J. Senker and J. Lüdecke, *Z. Naturforsch., B: J. Chem. Sci.*, 2001, **56**, 1089; (b) E. Salager, R. S. Stein, C. J. Pickard, B. Elena and L. Emsley, *Phys. Chem. Chem. Phys.*, 2009, **11**, 2610; (c) D. V. Dudenko, P. A. Williams, C. E. Hughes, O. N. Antzutkin, S. P. Velaga, S. P. Brown and K. D. M. Harris, *J. Phys. Chem. C*, 2013, **117**, 12258; (d) M. R. Chierotti, R. Gobetto, C. Nervi, A. Bacchi, P. Pelagatti, V. Colombo and A. Sironi, *Inorg. Chem.*, 2014, **53**, 139.
- 36 C. Martineau, J. Senker and F. Taulelle, NMR Crystallography, in *Annu. Rep. NMR Spectros.*, vol. 82, p. 1.
- 37 C. A. Jimenez, J. B. Belmar, L. Ortiz, P. Hidalgo, O. Fabelo, J. Pasan and C. Ruiz-Perez, *Cryst. Growth Des.*, 2009, **9**, 4987.
- 38 X. Hou, M. Schober and Q. Chu, *Cryst. Growth Des.*, 2012, **12**, 5159.
- 39 (a) Y. Matsunaga, Y. Nakayasu, S. Sakai and M. Yonenaga, *Mol. Cryst. Liq. Cryst.*, 1986, **141**, 327; (b) A. Timme, R. Kress, R. Q. Albuquerque and H.-W. Schmidt, *Chem. - Eur. J.*, 2012, **18**, 8329.
- 40 M. H. Levitt, Symmetry-Based Pulse Sequences in Magic-Angle Spinning Solid-State NMR, in *eMagRes*, 2007.
- 41 A. Detken, E. H. Hardy, M. Ernst and B. H. Meier, *Chem. Phys. Lett.*, 2002, **356**, 298.
- 42 M. Bak, J. T. Rasmussen and N. C. Nielsen, *J. Magn. Reson.*, 2000, **147**, 296.
- 43 P. E. Kristiansen, M. Carravetta, J. D. van Beek, W. C. Lai and M. H. Levitt, *J. Chem. Phys.*, 2006, **124**, 234510.
- 44 Y. K. Lee, N. D. Kurur, M. Helmle, O. G. Johannessen, N. C. Nielsen and M. H. Levitt, *Chem. Phys. Lett.*, 1995, **242**, 304.
- 45 The MathWorks Inc., *MATLAB 2014a*, Natick, Massachusetts, United States, 2014.
- 46 Accelrys Inc., *MS Modeling v5.0.0.0*, San Diego, California, United States, 2009.
- 47 M. W. Deem and J. M. Newsam, *Nature*, 1989, **342**, 260.
- 48 W. A. Dollase, *J. Appl. Crystallogr.*, 1986, **19**, 267.
- 49 (a) H. M. Rietveld, *J. Appl. Crystallogr.*, 1969, **2**, 65; (b) H. Toraya and F. Marumo, *Mineral. J.*, 1981, **10**, 211.
- 50 H. Sun, *J. Phys. Chem. B*, 1998, **102**, 7338.
- 51 L. W. Finger, D. E. Cox and A. P. Jephcoat, *J. Appl. Crystallogr.*, 1994, **27**, 892.
- 52 J. P. Perdew and Y. Wang, *Phys. Rev. B: Condens. Matter Mater. Phys.*, 1992, **45**, 13244.
- 53 M. R. Chierotti and R. Gobetto, *Chem. Commun.*, 2008, 1621.
- 54 G. S. Pawley, *J. Appl. Crystallogr.*, 1981, **14**, 357.
- 55 I. A. W. Filot, A. R. A. Palmans, P. A. J. Hilbers, R. A. van Santen, E. A. Pidko and T. F. A. de Greef, *J. Phys. Chem. B*, 2010, **114**, 13667.

Electronic Supplementary Information

to

**Influence of Fluorine Side-Group Substitution on the Crystal Structure Formation of
Benzene-1,3,5-trisamides**

Christoph Zehe,^[a] Marko Schmidt,^[a] Renée Siegel,^[a] Klaus Kreger,^[b] Venita Daebel,^[c] Sandra Ganzleben,^[b] Hans-Werner Schmidt,^[b] and Jürgen Senker*^[a]

[a] Inorganic Chemistry III and Bayreuth Center for Colloids and Interfaces, University of Bayreuth, 95447, Bayreuth, Germany; E-mail: juergen.senker@uni-bayreuth.de; Tel: (+49) 921-55-2788;

[b] Macromolecular Chemistry I, Bayreuth Institute of Macromolecular Research and Bayreuth Center for Colloids and Interfaces, University of Bayreuth, 95447, Bayreuth, Germany

[c] Bruker Biospin GmbH, Silberstreifen 4, 76287 Rheinstetten, Germany

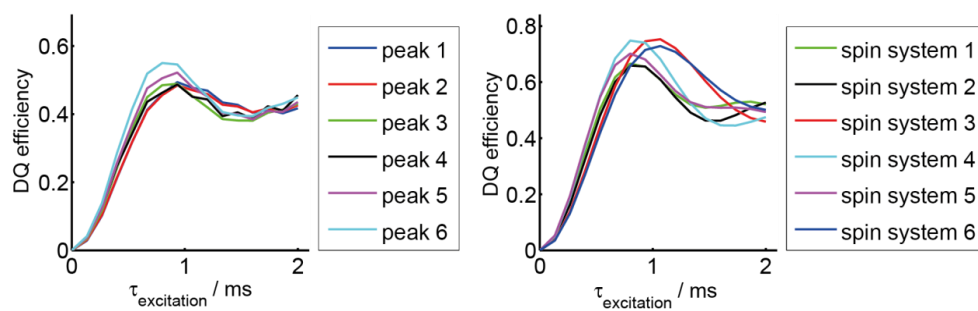
Scaling of the ^{19}F ^{19}F DQ curves

Figure S1. Left: Experimental ^{19}F ^{19}F double-quantum buildup curves of **1**. The peaks are labeled according to Figure 1. Right: Simulations of the buildup experiments for the structure model a) (see section Results and Discussion) using 9 spins systems. The numbering of the spin systems accounts for the number of the observed spin in the crystallographic information file (see below).

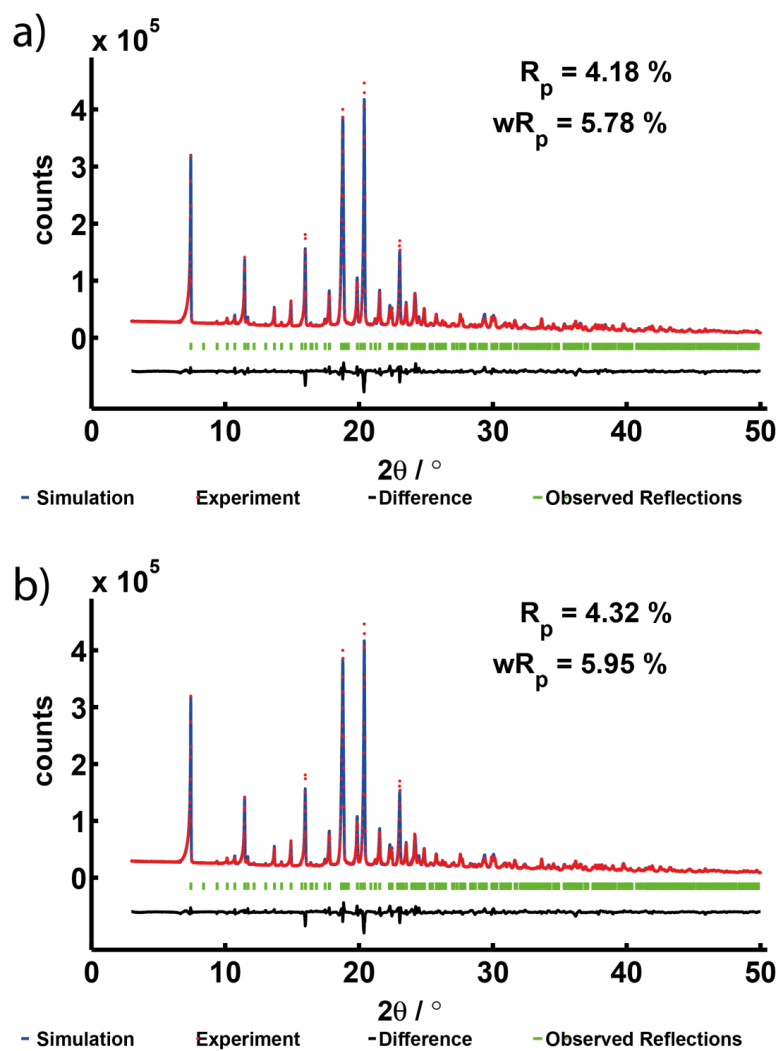
Rietveld Profile Plots for modified structures

Figure S2. Calculated Rietveld profiles of after refinement where a) one $N_H C_O C_Q F$ torsion (see scheme 1) of the first molecule of the asymmetric unit changed by approximately 120° (symbolic representation: \uparrow); b) all $N_H C_O C_Q F$ torsions of the first molecule (see Figure 4) changed by approximately 120° ($\uparrow\uparrow$).

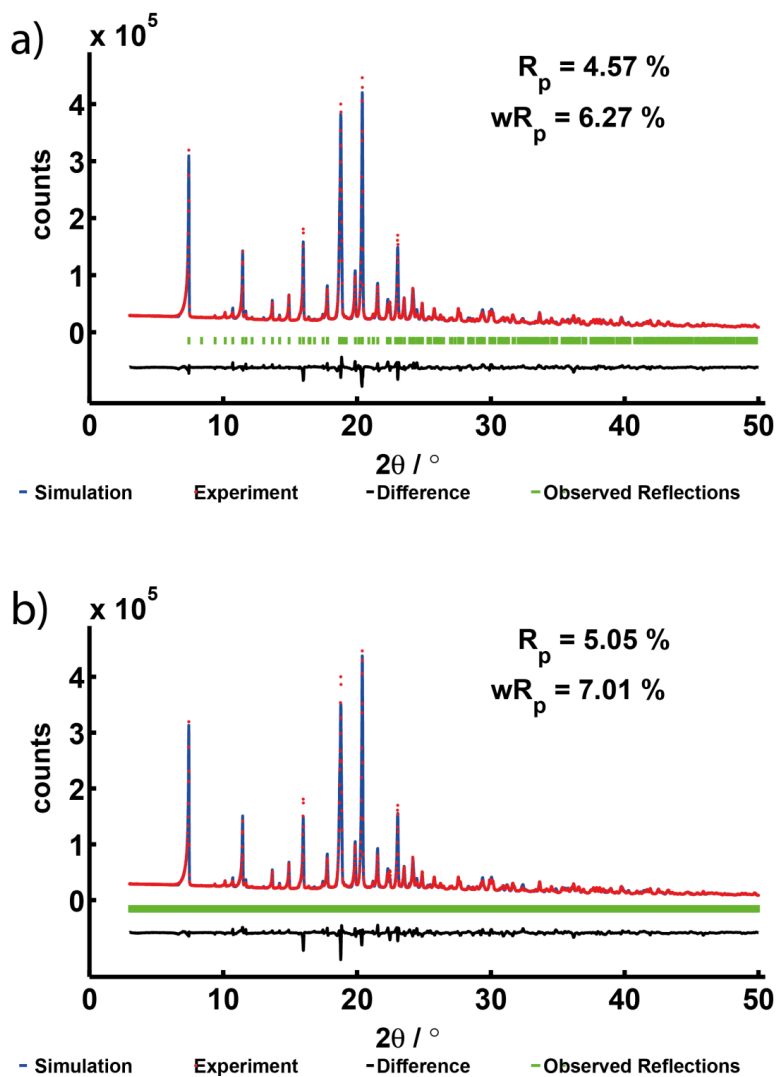


Figure S3. Calculated Rietveld profiles of after refinement where a) all $N_H C_O C_Q F$ torsions of both molecules changed by approximately 120° ($\uparrow\uparrow\uparrow\uparrow$); b) all $N_H C_O C_Q F$ torsions of the first molecule changed by approximately 120° and all $N_H C_O C_Q F$ torsions of the second molecule by -120° ($\uparrow\uparrow\downarrow\downarrow$).

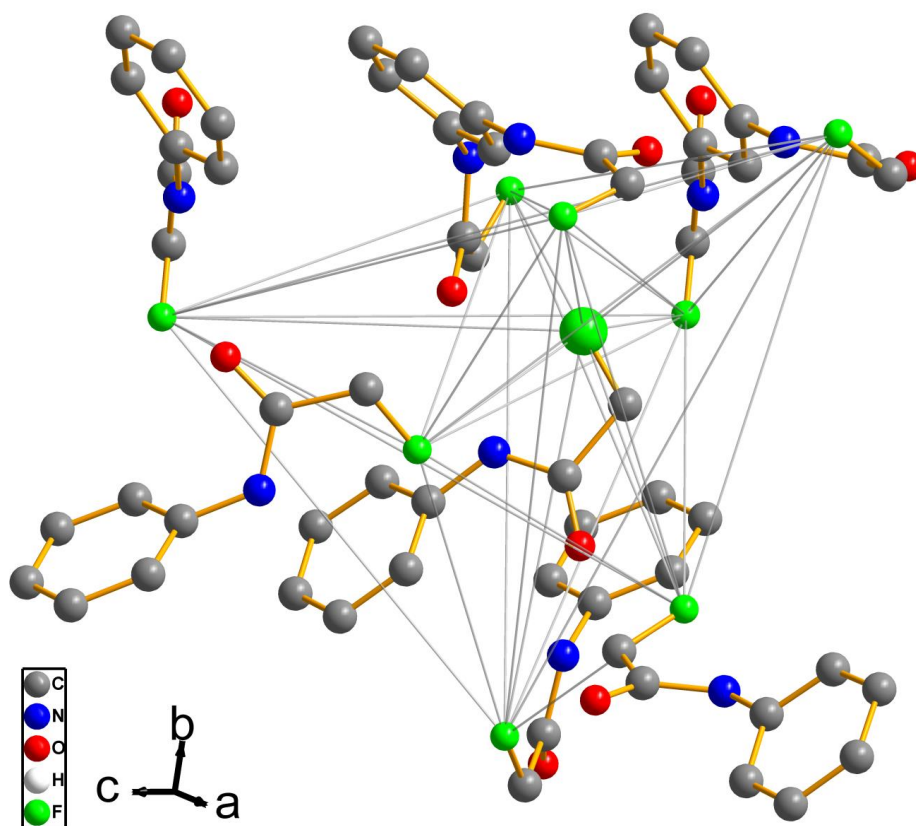
Selection of spin systems

Figure S4. Spin system No. 2 with grey lines indicating the $^{19}\text{F}^{19}\text{F}$ couplings. The observed ^{19}F atom is emphasized through a big symbol and nine ^{19}F were taken into account located within a sphere with a radius of 6.7 Å around the central atom. All hydrogen atoms, CH_3 groups and side chains without participating ^{19}F atoms are omitted for clarity.

Input files for simulations of final structure solution with SIMPSON

Par, pulseq and main section

```

par {
variable      N 14.
variable      n 4.
variable      nu 5.
start_operator Inz
detect_operator 11p
spin_rate     60000
gamma_angles  40
crystal_file  zcw232
np            90
proton_frequency 600e6
verbose       11110
}

proc pulseq {} {
  global par
  maxdt 1.0

  set rf [expr $par(spin_rate)*$par(N)/$par(n)]
  set p90 [expr 0.25e6/$rf]
  set p270 [expr 0.75e6/$rf]
  set ph10 [expr 180.00*$par(nu)/$par(N)]
  set ph11 [expr 180.00*$par(nu)/$par(N)+180.00]
  set ph12 [expr (-1)*180.00/$par(N)*$par(nu)+360]
  set ph13 [expr (-1)*180.00/$par(N)*$par(nu)+180.00]

  reset
  for {set i 0} {$i < [expr $par(N)/2]} {incr i} {
    pulse $p90 $rf $ph10
    pulse $p270 $rf $ph11
    pulse $p90 $rf $ph12
    pulse $p270 $rf $ph13
  }
  for {set i 0} {$i < [expr $par(N)/2]} {incr i} {
    pulse $p90 $rf $ph12
    pulse $p270 $rf $ph13
    pulse $p90 $rf $ph10
    pulse $p270 $rf $ph11
  }
  store 1

  reset

```

```

for {set i 0} {$i < [expr $par(N)/2]} {incr i} {
  pulse $p90 $rf $ph13
  pulse $p270 $rf $ph12
  pulse $p90 $rf $ph11
  pulse $p270 $rf $ph10
}
for {set i 0} {$i < [expr $par(N)/2]} {incr i} {
pulse $p90 $rf $ph11
  pulse $p270 $rf $ph10
  pulse $p90 $rf $ph13
  pulse $p270 $rf $ph12
}
store 2

```

```

reset
for {set n 0} {$n < $par(np)} {incr n} {
prop [expr $n % 2 + 1]
store 9
matrix set 1 totalcoherence {-2 2}
filter 1
prop 9
matrix set 2 totalcoherence {0}
filter 2
pulseid 1 250000 -y
acq
reset
prop 9
}
}

```

```

proc main {} {
global par
set f [fsimpson]
fexpr $f {$re} {$sim}
fsave $f $par(name).dat -xreim
}

```

4 Publications

Spinsystems for structure model a)

Spinsystem 1

```
spinsys {
channels 19F
nuclei 19F 19F 19F 19F 19F 19F 19F 19F 19F
shift 1 0.0p -25.0p 0.45 0.0 0.0 0
shift 2 0.0p -25.0p 0.45 0.0 0.0 0
shift 3 0.0p -25.0p 0.45 0.0 0.0 0
shift 4 0.0p -25.0p 0.45 0.0 0.0 0
shift 5 0.0p -25.0p 0.45 0.0 0.0 0
shift 6 0.0p -25.0p 0.45 0.0 0.0 0
shift 7 0.0p -25.0p 0.45 0.0 0.0 0
shift 8 0.0p -25.0p 0.45 0.0 0.0 0
shift 9 0.0p -25.0p 0.45 0.0 0.0 0
dipole 1 2 -1750.14958968 180.0 34.4066476848 -60.9200471646
dipole 1 3 -715.105921667 180.0 78.5327174345 53.0044794181
dipole 1 4 -316.567489629 180.0 102.998076974 7.57944255997
dipole 1 5 -646.460659107 180.0 106.57999128 9.79527094101
dipole 1 6 -573.20595359 180.0 137.698605112 42.1263749075
dipole 1 7 -509.725830077 180.0 108.693316564 -39.2195461318
dipole 1 8 -362.481690333 180.0 36.8802309453 -14.0932963035
dipole 1 9 -325.729456589 180.0 84.0319818435 -83.6058171485
dipole 2 3 -340.335206426 180.0 108.830830522 71.4357131042
dipole 2 4 -213.210459891 180.0 127.311951564 26.7079614726
dipole 2 5 -180.552630075 180.0 124.99295002 24.3821383787
dipole 2 6 -150.879202231 180.0 146.979105514 68.6292668668
dipole 2 7 -423.988060148 180.0 144.661100591 -26.2059834011
dipole 2 8 -656.6885888 180.0 67.6640497975 11.0973585709
dipole 2 9 -642.30720942 180.0 117.407763801 -86.2713577838
dipole 3 4 -636.968424125 180.0 118.374743082 -42.1870358491
dipole 3 5 -132.616945593 180.0 106.359751429 -21.4063752612
dipole 3 6 -636.381370147 180.0 163.15118707 -79.9892043967
dipole 3 7 -183.487166913 180.0 110.752061711 -80.9376205172
dipole 3 8 -118.101864874 180.0 63.8108405985 -36.2025625946
dipole 3 9 -75.4985693663 180.0 91.7245903613 -77.8315768369
dipole 4 5 -63.278770806 180.0 90.0 0.0
dipole 4 6 -859.446988066 180.0 122.19214842 23.4975470839
dipole 4 7 -827.99249173 180.0 93.8338931321 -62.020703376
dipole 4 8 -51.2095877063 180.0 57.3740555549 -9.99242948655
dipole 4 9 -106.510530869 180.0 76.8167763071 -52.2958028527
dipole 5 6 -166.29854803 180.0 107.94746913 11.8377271408
dipole 5 7 -91.3667069035 180.0 91.8378533948 -25.0148346963
dipole 5 8 -279.561956338 180.0 18.3161742922 -54.9658952496
dipole 5 9 -106.776511618 180.0 76.8056136655 -52.3608851345
dipole 6 7 -350.202623065 180.0 69.8316169166 -76.1946301762
```

```

dipole 6 8 -58.7389695405 180.0 38.5376287477 -27.837137763
dipole 6 9 -84.3682097513 180.0 62.8202575695 -77.4731925068
dipole 7 8 -74.917235466 180.0 50.0536816673 17.4328955428
dipole 7 9 -636.968339336 180.0 61.6252619972 -42.1870361883
dipole 8 9 -158.506886221 180.0 121.692077717 -51.5648175347
}

```

Spinsystem 2

```

spinsys {
channels 19F
nuclei 19F 19F 19F 19F 19F 19F 19F 19F
shift 1 0.0p -25.0p 0.45 0.0 0.0 0.0
shift 2 0.0p -25.0p 0.45 0.0 0.0 0.0
shift 3 0.0p -25.0p 0.45 0.0 0.0 0.0
shift 4 0.0p -25.0p 0.45 0.0 0.0 0.0
shift 5 0.0p -25.0p 0.45 0.0 0.0 0.0
shift 6 0.0p -25.0p 0.45 0.0 0.0 0.0
shift 7 0.0p -25.0p 0.45 0.0 0.0 0.0
shift 8 0.0p -25.0p 0.45 0.0 0.0 0.0
shift 9 0.0p -25.0p 0.45 0.0 0.0 0.0
dipole 1 2 -598.076996747 180.0 100.064843505 39.8233331211
dipole 1 3 -1536.68283483 180.0 152.37359285 78.3334599328
dipole 1 4 -330.019158238 180.0 99.3164786433 84.0441997188
dipole 1 5 -292.522328546 180.0 136.780928824 11.4598823524
dipole 1 6 -362.481624939 180.0 36.8802327232 14.0932941284
dipole 1 7 -573.093870717 180.0 70.0693138243 -50.7674406653
dipole 1 8 -656.688527918 180.0 67.664048299 -11.0973500044
dipole 1 9 -845.74860721 180.0 131.203517965 -43.2209972565
dipole 2 3 -859.447149033 180.0 122.192152801 -23.4975511841
dipole 2 4 -979.866274127 180.0 91.5273546702 41.877731173
dipole 2 5 -97.1881741627 180.0 114.164698329 -15.8943606074
dipole 2 6 -89.4475880719 180.0 53.5242667001 -17.5932996336
dipole 2 7 -187.217548364 180.0 69.3025205802 -83.6199038356
dipole 2 8 -86.9564959269 180.0 73.4052519415 -26.1467820748
dipole 2 9 -350.202675687 180.0 110.168382714 -76.1946312506
dipole 3 4 -642.30720942 180.0 62.5922361994 86.2713577838
dipole 3 5 -646.460577246 180.0 106.57998714 -9.79526611829
dipole 3 6 -107.906628535 180.0 25.8918594074 -11.8642949723
dipole 3 7 -159.214573131 180.0 50.3156085076 -63.4541821812
dipole 3 8 -185.284046395 180.0 46.609817268 -27.9963478663
dipole 3 9 -827.992718657 180.0 86.1661029501 -62.0207051105
dipole 4 5 -148.477265928 180.0 117.210520364 -46.3539790511
dipole 4 6 -114.281299079 180.0 48.845322258 -51.562458272
dipole 4 7 -67.8084102933 180.0 74.7591498584 -76.1182531642
dipole 4 8 -104.279351581 180.0 71.5751453442 -53.7301243251
dipole 4 9 -113.669053036 180.0 102.940959928 -77.61292903

```

4 Publications

dipole 5 6 -90.3980670427 180.0 5.01159945732 -3.11737997644e-05
dipole 5 7 -61.3812524539 180.0 53.4923763398 -32.0614562125
dipole 5 8 -249.188933756 180.0 14.9938439327 -85.3614135892
dipole 5 9 -170.384176552 180.0 77.1481330849 -25.2360610388
dipole 6 7 -123.895883155 180.0 110.773887759 -35.2195359513
dipole 6 8 -1750.15016418 180.0 145.593361469 -60.9200416929
dipole 6 9 -71.2587781613 180.0 138.928386879 -28.2378401203
dipole 7 8 -149.504274533 180.0 89.1839202286 20.8923819282
dipole 7 9 -634.7097557 180.0 162.047545517 67.7044412758
dipole 8 9 -123.214855491 180.0 124.345762624 -11.8245283095
}

Spinsystem 3

spinsys {
channels 19F
nuclei 19F 19F 19F 19F 19F 19F 19F 19F 19F
shift 1 0.0p -25.0p 0.45 0.0 0.0 0.0
shift 2 0.0p -25.0p 0.45 0.0 0.0 0.0
shift 3 0.0p -25.0p 0.45 0.0 0.0 0.0
shift 4 0.0p -25.0p 0.45 0.0 0.0 0.0
shift 5 0.0p -25.0p 0.45 0.0 0.0 0.0
shift 6 0.0p -25.0p 0.45 0.0 0.0 0.0
shift 7 0.0p -25.0p 0.45 0.0 0.0 0.0
shift 8 0.0p -25.0p 0.45 0.0 0.0 0.0
shift 9 0.0p -25.0p 0.45 0.0 0.0 0.0
dipole 1 2 -979.866274127 180.0 91.5273546702 41.877731173
dipole 1 3 -859.447149033 180.0 122.192152801 -23.4975511841
dipole 1 4 -636.381414336 180.0 163.151185826 79.9892362235
dipole 1 5 -634.709745618 180.0 17.9524501356 67.704404563
dipole 1 6 -598.076996747 180.0 79.9351564947 -39.8233331211
dipole 1 7 -573.206006191 180.0 137.698604699 -42.12637029
dipole 1 8 -573.093616697 180.0 70.0693173124 50.7674314291
dipole 1 9 -473.326758651 180.0 59.8414187352 -59.2262021471
dipole 2 3 -642.30720942 180.0 117.407763801 -86.2713577838
dipole 2 4 -423.988060148 180.0 144.661100591 -26.2059834011
dipole 2 5 -309.595680705 180.0 39.9141235216 -21.0064042388
dipole 2 6 -330.019158238 180.0 80.6835213567 -84.0441997188
dipole 2 7 -122.878571399 180.0 115.42370199 -41.9886217493
dipole 2 8 -272.368032177 180.0 73.5358132024 7.95807577733
dipole 2 9 -94.3120835352 180.0 72.2026274172 -50.9775532828
dipole 3 4 -636.968339336 180.0 118.374738003 42.1870361883
dipole 3 5 -117.922517018 180.0 35.1533727912 35.7950397604
dipole 3 6 -1536.68283483 180.0 27.6264071505 -78.3334599328
dipole 3 7 -316.567559342 180.0 102.998075294 -7.57943983677
dipole 3 8 -94.8999825128 180.0 63.7183884997 38.7934958965
dipole 3 9 -139.075153252 180.0 51.3680627989 -23.3816866811

```

dipole 4 5 -90.3980670427 180.0 5.01159945732 -3.11737997644e-05
dipole 4 6 -145.580871808 180.0 46.0160309851 -52.1661649236
dipole 4 7 -715.106110998 180.0 78.5327164088 -53.004485356
dipole 4 8 -173.366525827 180.0 31.8681724543 35.1281301489
dipole 4 9 -86.017619635 180.0 39.1276014595 -64.0196274311
dipole 5 6 -188.248518194 180.0 121.033452152 -46.2644017513
dipole 5 7 -90.2117443042 180.0 153.609264938 -62.0291847251
dipole 5 8 -845.74819169 180.0 131.203512727 43.2210035612
dipole 5 9 -340.335342023 180.0 108.830833117 -71.4357152604
dipole 6 7 -153.213519955 180.0 125.974488154 7.78856561245
dipole 6 8 -82.3046549821 180.0 84.9349604508 45.2074863942
dipole 6 9 -272.368062655 180.0 73.5358109696 -7.95807022429
dipole 7 8 -139.26522743 180.0 47.6053671468 85.3735936561
dipole 7 9 -249.188933756 180.0 14.9938439327 -85.3614135892
dipole 8 9 -157.734338895 180.0 82.7283672666 -85.3708660734
}

```

Spinsystem 4

```

spinsys {
channels 19F
nuclei 19F 19F 19F 19F 19F 19F 19F 19F
shift 1 0.0p -25.0p 0.45 0.0 0.0 0.0
shift 2 0.0p -25.0p 0.45 0.0 0.0 0.0
shift 3 0.0p -25.0p 0.45 0.0 0.0 0.0
shift 4 0.0p -25.0p 0.45 0.0 0.0 0.0
shift 5 0.0p -25.0p 0.45 0.0 0.0 0.0
shift 6 0.0p -25.0p 0.45 0.0 0.0 0.0
shift 7 0.0p -25.0p 0.45 0.0 0.0 0.0
shift 8 0.0p -25.0p 0.45 0.0 0.0 0.0
shift 9 0.0p -25.0p 0.45 0.0 0.0 0.0
dipole 1 2 -325.729456589 180.0 95.9680181565 83.6058171485
dipole 1 3 -1536.68283483 180.0 27.6264071505 -78.3334599328
dipole 1 4 -859.447149033 180.0 57.8078471991 23.4975511841
dipole 1 5 -642.30720942 180.0 62.5922361994 86.2713577838
dipole 1 6 -636.968339336 180.0 118.374738003 42.1870361883
dipole 1 7 -316.567559342 180.0 102.998075294 -7.57943983677
dipole 1 8 -646.460577246 180.0 106.57998714 -9.79526611829
dipole 1 9 -827.992718657 180.0 86.1661029501 -62.0207051105
dipole 2 3 -116.187217045 180.0 63.3600268844 -87.5054741556
dipole 2 4 -234.305472778 180.0 63.984702877 -47.9018131252
dipole 2 5 -1750.14958968 180.0 34.4066476848 -60.9200471646
dipole 2 6 -509.725830077 180.0 108.693316564 -39.2195461318
dipole 2 7 -85.2269056022 180.0 94.5156111566 -45.8392037085
dipole 2 8 -150.12464154 180.0 95.4560939951 -60.1842879338
dipole 2 9 -65.9790409074 180.0 84.8458744739 -74.4804651882
dipole 3 4 -598.076996747 180.0 100.064843505 39.8233331211

```

4 Publications

dipole 3 5 -330.019158238 180.0 99.3164786433 84.0441997188
dipole 3 6 -145.580871808 180.0 133.983969015 52.1661649236
dipole 3 7 -153.213519955 180.0 125.974488154 7.78856561245
dipole 3 8 -292.522328546 180.0 136.780928824 11.4598823524
dipole 3 9 -845.74860721 180.0 131.203517965 -43.2209972565
dipole 4 5 -979.866274127 180.0 91.5273546702 41.877731173
dipole 4 6 -636.381414336 180.0 163.151185826 79.9892362235
dipole 4 7 -573.206006191 180.0 137.698604699 -42.12637029
dipole 4 8 -97.1881741627 180.0 114.164698329 -15.8943606074
dipole 4 9 -350.202675687 180.0 110.168382714 -76.1946312506
dipole 5 6 -423.988060148 180.0 144.661100591 -26.2059834011
dipole 5 7 -122.878571399 180.0 115.42370199 -41.9886217493
dipole 5 8 -148.477265928 180.0 117.210520364 -46.3539790511
dipole 5 9 -113.669053036 180.0 102.940959928 -77.61292903
dipole 6 7 -715.106110998 180.0 78.5327164088 -53.004485356
dipole 6 8 -114.619170332 180.0 83.8003478766 -25.3209170535
dipole 6 9 -183.487162416 180.0 69.2479384661 -80.9376155936
dipole 7 8 -63.278770806 180.0 90.0 0.0
dipole 7 9 -509.725834709 180.0 71.306683377 -39.2195466008
dipole 8 9 -170.384176552 180.0 77.1481330849 -25.2360610388
}

Spinsystem 5

spinsys {
channels 19F
nuclei 19F 19F 19F 19F 19F 19F 19F 19F 19F
shift 1 0.0p -25.0p 0.45 0.0 0.0 0.0
shift 2 0.0p -25.0p 0.45 0.0 0.0 0.0
shift 3 0.0p -25.0p 0.45 0.0 0.0 0.0
shift 4 0.0p -25.0p 0.45 0.0 0.0 0.0
shift 5 0.0p -25.0p 0.45 0.0 0.0 0.0
shift 6 0.0p -25.0p 0.45 0.0 0.0 0.0
shift 7 0.0p -25.0p 0.45 0.0 0.0 0.0
shift 8 0.0p -25.0p 0.45 0.0 0.0 0.0
shift 9 0.0p -25.0p 0.45 0.0 0.0 0.0
dipole 1 2 -1750.14958968 180.0 145.593352315 60.9200471646
dipole 1 3 -330.019158238 180.0 80.6835213567 -84.0441997188
dipole 1 4 -979.866274127 180.0 88.4726453298 -41.877731173
dipole 1 5 -642.30720942 180.0 117.407763801 -86.2713577838
dipole 1 6 -423.988060148 180.0 144.661100591 -26.2059834011
dipole 1 7 -656.6885888 180.0 67.6640497975 11.0973585709
dipole 1 8 -473.326801737 180.0 59.8414194332 59.2262055091
dipole 1 9 -340.335206426 180.0 108.830830522 71.4357131042
dipole 2 3 -116.187217045 180.0 63.3600268844 -87.5054741556
dipole 2 4 -234.305472778 180.0 63.984702877 -47.9018131252

```

dipole 2 5 -325.729456589 180.0 84.0319818435 -83.6058171485
dipole 2 6 -509.725830077 180.0 108.693316564 -39.2195461318
dipole 2 7 -362.481690333 180.0 36.8802309453 -14.0932963035
dipole 2 8 -225.997776157 180.0 35.9345942453 34.3380113988
dipole 2 9 -715.105921667 180.0 78.5327174345 53.0044794181
dipole 3 4 -598.076996747 180.0 100.064843505 39.8233331211
dipole 3 5 -1536.68283483 180.0 152.37359285 78.3334599328
dipole 3 6 -145.580871808 180.0 133.983969015 52.1661649236
dipole 3 7 -153.700481804 180.0 83.7584380962 61.1270791037
dipole 3 8 -63.023581582 180.0 80.6005238926 73.2172359361
dipole 3 9 -43.056730138 180.0 104.131198235 77.904467016
dipole 4 5 -859.447149033 180.0 122.192152801 -23.4975511841
dipole 4 6 -636.381414336 180.0 163.151185826 79.9892362235
dipole 4 7 -118.109317764 180.0 78.3839059522 26.0479233094
dipole 4 8 -187.217585187 180.0 69.3025191609 83.6199083646
dipole 4 9 -117.441118552 180.0 103.859324783 80.7764322871
dipole 5 6 -636.968339336 180.0 118.374738003 42.1870361883
dipole 5 7 -158.506886221 180.0 58.3079222827 51.5648175347
dipole 5 8 -73.2695477859 180.0 60.4620112049 72.2297118782
dipole 5 9 -75.4985693663 180.0 88.2754096387 77.8315768369
dipole 6 7 -74.917235466 180.0 50.0536816673 17.4328955428
dipole 6 8 -98.6989715689 180.0 36.8957591242 84.561084746
dipole 6 9 -183.487166913 180.0 69.2479382888 80.9376205172
dipole 7 8 -174.573605218 180.0 83.3428360045 24.9055477833
dipole 7 9 -118.101864874 180.0 116.189159401 36.2025625946
dipole 8 9 -634.7097557 180.0 162.047545517 67.7044412758
}

```

Spinsystem 6

```

spinsys {
channels 19F
nuclei 19F 19F 19F 19F 19F 19F 19F 19F 19F
shift 1 0.0p -25.0p 0.45 0.0 0.0 0.0
shift 2 0.0p -25.0p 0.45 0.0 0.0 0.0
shift 3 0.0p -25.0p 0.45 0.0 0.0 0.0
shift 4 0.0p -25.0p 0.45 0.0 0.0 0.0
shift 5 0.0p -25.0p 0.45 0.0 0.0 0.0
shift 6 0.0p -25.0p 0.45 0.0 0.0 0.0
shift 7 0.0p -25.0p 0.45 0.0 0.0 0.0
shift 8 0.0p -25.0p 0.45 0.0 0.0 0.0
shift 9 0.0p -25.0p 0.45 0.0 0.0 0.0
dipole 1 2 -509.725830077 180.0 71.3066834357 39.2195461318
dipole 1 3 -636.381414336 180.0 16.8488141745 -79.9892362235
dipole 1 4 -634.709745618 180.0 162.047549864 -67.704404563
dipole 1 5 -636.968339336 180.0 61.6252619972 -42.1870361883
dipole 1 6 -423.988060148 180.0 35.3388994086 26.2059834011

```

4 Publications

dipole 1 7 -715.106110998 180.0 78.5327164088 -53.004485356
dipole 1 8 -845.74819169 180.0 131.203512727 43.2210035612
dipole 1 9 -827.99249173 180.0 86.1661068679 62.020703376
dipole 2 3 -234.305472778 180.0 63.984702877 -47.9018131252
dipole 2 4 -122.373797273 180.0 138.484164739 -54.112191008
dipole 2 5 -325.729456589 180.0 84.0319818435 -83.6058171485
dipole 2 6 -1750.14958968 180.0 34.4066476848 -60.9200471646
dipole 2 7 -85.2269056022 180.0 94.5156111566 -45.8392037085
dipole 2 8 -153.213501546 180.0 125.974488055 -7.7885575794
dipole 2 9 -316.567489629 180.0 102.998076974 7.57944255997
dipole 3 4 -90.3980670427 180.0 174.988400543 3.11737997644e-05
dipole 3 5 -859.447149033 180.0 122.192152801 -23.4975511841
dipole 3 6 -979.866274127 180.0 91.5273546702 41.877731173
dipole 3 7 -573.206006191 180.0 137.698604699 -42.12637029
dipole 3 8 -111.620081597 180.0 150.589637462 59.2685957809
dipole 3 9 -203.369332065 180.0 127.767744288 70.8969662572
dipole 4 5 -169.452621112 180.0 23.3348898818 -29.7218086117
dipole 4 6 -76.1217714774 180.0 21.6692118013 50.4545020435
dipole 4 7 -225.997738406 180.0 35.9345966798 -34.3380178043
dipole 4 8 -573.093616697 180.0 70.0693173124 50.7674314291
dipole 4 9 -159.214571373 180.0 50.3156100172 63.4541712872
dipole 5 6 -642.30720942 180.0 62.5922361994 86.2713577838
dipole 5 7 -316.567559342 180.0 102.998075294 -7.57943983677
dipole 5 8 -93.1825420002 180.0 124.486071865 42.6394683061
dipole 5 9 -106.510530869 180.0 103.183223693 52.2958028527
dipole 6 7 -122.878571399 180.0 115.42370199 -41.9886217493
dipole 6 8 -94.110591597 180.0 144.169708673 9.157928253
dipole 6 9 -213.210459891 180.0 127.311951564 26.7079614726
dipole 7 8 -205.942183236 180.0 122.863492068 86.7867887795
dipole 7 9 -163.961804352 180.0 94.7442729196 84.9276494592
dipole 8 9 -1536.68324318 180.0 27.6264009906 78.3334557026
}

Crystallographic information file

```

data_1.3.5-tris(2-fluoro-2-methylpropionylamino)benzene
_audit_creation_date      2014-05-06
_audit_creation_method    'Materials Studio'
_symmetry_space_group_name_H-M  'P21'
_symmetry_Int_Tables_number 4
_symmetry_cell_setting    monoclinic
_chemical_formula_sum     'C18 H24 F3 N3 O3'
_chemical_formula_weight   387.403

loop_
_symmetry_equiv_pos_as_xyz
  x,y,z
  -x,y+1/2,-z
_cell_length_a            11.8863(44)
_cell_length_b            15.3948(59)
_cell_length_c            10.5539(40)
_cell_angle_alpha        90.0000
_cell_angle_beta         95.0116(23)
_cell_angle_gamma        90.0000
_cell_volume              1923.84
_cell_formula_units_Z     4
_cell_measurement_temperature 293(2)
_diffraction_ambient_temperature 293(2)
_diffraction_radiation_wavelength 1.54056
_diffraction_radiation_type CuK\alpha
_diffraction_measurement_device_type 'STOE StadiP'

loop_
_atom_site_label
_atom_site_type_symbol
_atom_site_fract_x
_atom_site_fract_y
_atom_site_fract_z
_atom_site_U_iso_or_equiv
_atom_site_adp_type
_atom_site_occupancy

F1      F      0.1824(9)      -0.2217(5)      1.4597(12)
        0.08432      Uiso          1
F2      F      0.1821(12)     0.3414(6)      1.0457(18)
        0.08432      Uiso          1
F3      F      -0.4530(5)     0.1111(13)     1.1392(12)
        0.08432      Uiso          1
F4      F      0.2413(12)     0.2203(3)      0.3916(13)
        0.08432      Uiso          1
F5      F      0.2493(10)     -0.0956(6)     1.1513(10)
        0.08432      Uiso          1
F6      F      -0.4375(5)     0.0090(17)     0.6405(14)
        0.08432      Uiso          1

```

4 Publications

C7	C	-0.1301 (5)	0.0621 (5)	1.2285 (7)
	0.08432	Uiso	1	
C8	C	-0.0708 (5)	-0.0004 (5)	1.3009 (7)
	0.08432	Uiso	1	
C9	C	-0.0690 (5)	0.1231 (5)	1.1674 (7)
	0.08432	Uiso	1	
H10	H	-0.1149 (5)	0.1729 (5)	1.1100 (7)
	0.08432	Uiso	1	
H11	H	-0.1179 (5)	-0.0496 (5)	1.3493 (8)
	0.08432	Uiso	1	
C12	C	0.0477 (5)	0.1232 (5)	1.1758 (8)
	0.08432	Uiso	1	
C13	C	0.1035 (5)	0.0593 (5)	1.2494 (8)
	0.08432	Uiso	1	
N14	N	0.1041 (5)	0.1876 (5)	1.1131 (8)
	0.08432	Uiso	1	
H15	H	0.1959 (5)	0.0580 (5)	1.2572 (9)
	0.08432	Uiso	1	
C16	C	0.2099 (6)	0.1837 (5)	1.0717 (7)
	0.08432	Uiso	1	
O17	O	0.2668 (10)	0.1182 (6)	1.0759 (16)
	0.08432	Uiso	1	
C18	C	0.2476 (5)	0.2718 (5)	1.0117 (6)
	0.08432	Uiso	1	
C19	C	0.2342 (19)	0.2631 (9)	0.8670 (6)
	0.08432	Uiso	1	
H20	H	0.2582 (19)	0.3248 (10)	0.8242 (7)
	0.08432	Uiso	1	
H21	H	0.2883 (28)	0.2116 (8)	0.8338 (14)
	0.08432	Uiso	1	
C22	C	0.3707 (7)	0.2887 (10)	1.0595 (18)
	0.08432	Uiso	1	
H23	H	0.3807 (19)	0.2947 (14)	1.1637 (17)
	0.08432	Uiso	1	
H24	H	0.3989 (7)	0.3495 (10)	1.0182 (18)
	0.08432	Uiso	1	
H25	H	0.0619 (6)	0.2442 (6)	1.0974 (16)
	0.08432	Uiso	1	
N26	N	-0.2474 (5)	0.0640 (5)	1.2135 (8)
	0.08432	Uiso	1	
H27	H	-0.2817 (5)	0.0768 (10)	1.1245 (9)
	0.08432	Uiso	1	
C28	C	-0.3192 (5)	0.0568 (7)	1.3075 (8)
	0.08432	Uiso	1	
C29	C	-0.4461 (5)	0.0643 (6)	1.2522 (10)
	0.08432	Uiso	1	
C30	C	-0.5131 (8)	0.1121 (16)	1.3474 (12)
	0.08432	Uiso	1	
H31	H	-0.4807 (13)	0.1779 (16)	1.3666 (25)
	0.08432	Uiso	1	
O32	O	-0.2883 (5)	0.0448 (13)	1.4189 (8)
	0.08432	Uiso	1	

4.2 Publication II

H33	H	-0.5123(8)	0.0769(26)	1.4381(10)
	0.08432	Uiso	1	
H34	H	0.4266(6)	0.2365(12)	1.0315(30)
	0.08432	Uiso	1	
C35	C	-0.4943(8)	-0.0266(6)	1.2262(27)
	0.08432	Uiso	1	
H36	H	-0.4466(12)	-0.0621(12)	
	1.1581(34)	0.08432	Uiso	1
H37	H	-0.5824(9)	-0.0207(7)	1.1858(28)
	0.08432	Uiso	1	
H38	H	-0.4936(10)	-0.0651(12)	
	1.3139(36)	0.08432	Uiso	1
H39	H	0.1461(23)	0.2487(14)	0.8330(13)
	0.08432	Uiso	1	
C40	C	0.0460(5)	-0.0031(5)	1.3132(8)
	0.08432	Uiso	1	
N41	N	0.1014(5)	-0.0688(5)	1.3854(8)
	0.08432	Uiso	1	
C42	C	0.1986(6)	-0.0625(5)	1.4646(7)
	0.08432	Uiso	1	
O43	O	0.2439(12)	0.0060(5)	1.4945(13)
	0.08432	Uiso	1	
H44	H	0.0668(7)	-0.1287(5)	1.3755(14)
	0.08432	Uiso	1	
C45	C	0.2438(4)	-0.1531(5)	1.5166(6)
	0.08432	Uiso	1	
C46	C	0.3666(5)	-0.1620(8)	1.4861(16)
	0.08432	Uiso	1	
H47	H	0.3734(14)	-0.1594(11)	1.3830(18)
	0.08432	Uiso	1	
H48	H	0.4202(6)	-0.1107(9)	1.5316(25)
	0.08432	Uiso	1	
C49	C	0.2334(15)	-0.1560(8)	1.6600(6)
	0.08432	Uiso	1	
H50	H	0.1449(18)	-0.1488(11)	1.6810(14)
	0.08432	Uiso	1	
H51	H	0.2834(22)	-0.1046(7)	1.7102(9)
	0.08432	Uiso	1	
H52	H	0.3999(6)	-0.2247(8)	1.5218(16)
	0.08432	Uiso	1	
H53	H	0.2646(15)	-0.2190(8)	1.6976(7)
	0.08432	Uiso	1	
H54	H	-0.6016(8)	0.1173(17)	1.3081(13)
	0.08432	Uiso	1	
C55	C	-0.1110(4)	0.0627(1)	0.7397(7)
	0.08432	Uiso	1	
C56	C	-0.0498(4)	0.1095(1)	0.6569(7)
	0.08432	Uiso	1	
H57	H	-0.0953(4)	0.1466(2)	0.5798(7)
	0.08432	Uiso	1	
N58	N	-0.2289(4)	0.0621(3)	0.7227(8)
	0.08432	Uiso	1	

4 Publications

H59	H	-0.2617 (4)	0.0619 (8)	0.6310 (8)
	0.08432	Uiso	1	
C60	C	0.0670 (4)	0.1108 (0)	0.6678 (7)
	0.08432	Uiso	1	
C61	C	-0.3040 (5)	0.0589 (7)	0.8144 (9)
	0.08432	Uiso	1	
O62	O	-0.2770 (5)	0.0627 (14)	0.9279 (9)
	0.08432	Uiso	1	
C63	C	-0.4305 (4)	0.0537 (5)	0.7552 (10)
	0.08432	Uiso	1	
C64	C	-0.4998 (7)	0.0044 (19)	0.8469 (15)
	0.08432	Uiso	1	
H65	H	-0.4667 (12)	-0.0614 (20)	
	0.8649 (33)	0.08432	Uiso	1
H66	H	-0.5874 (7)	-0.0010 (18)	0.8047 (16)
	0.08432	Uiso	1	
C67	C	-0.4779 (10)	0.1453 (5)	0.7320 (34)
	0.08432	Uiso	1	
H68	H	-0.4778 (12)	0.1823 (14)	0.8211 (45)
	0.08432	Uiso	1	
H69	H	-0.4295 (13)	0.1820 (14)	0.6659 (44)
	0.08432	Uiso	1	
H70	H	-0.5658 (9)	0.1401 (6)	0.6905 (34)
	0.08432	Uiso	1	
H71	H	-0.5013 (6)	0.0382 (33)	0.9385 (10)
	0.08432	Uiso	1	
C72	C	-0.0510 (4)	0.0155 (0)	0.8349 (7)
	0.08432	Uiso	1	
H73	H	-0.0970 (4)	-0.0228 (0)	0.9011 (7)
	0.08432	Uiso	1	
C74	C	0.0659 (4)	0.0140 (1)	0.8482 (7)
	0.08432	Uiso	1	
N75	N	0.1268 (4)	-0.0340 (2)	0.9435 (7)
	0.08432	Uiso	1	
H76	H	0.1839 (8)	-0.0009 (4)	1.0015 (11)
	0.08432	Uiso	1	
C77	C	0.1167 (7)	-0.1214 (2)	0.9632 (7)
	0.08432	Uiso	1	
O78	O	0.0479 (12)	-0.1666 (2)	0.9025 (11)
	0.08432	Uiso	1	
C79	C	0.2092 (6)	-0.1590 (4)	1.0647 (8)
	0.08432	Uiso	1	
C80	C	0.1542 (7)	-0.2313 (8)	1.1369 (13)
	0.08432	Uiso	1	
H81	H	0.2163 (6)	-0.2577 (9)	1.2102 (14)
	0.08432	Uiso	1	
C82	C	0.3083 (9)	-0.1928 (10)	0.9951 (10)
	0.08432	Uiso	1	
H83	H	0.3726 (9)	-0.2204 (11)	1.0649 (12)
	0.08432	Uiso	1	
H84	H	0.3475 (8)	-0.1404 (15)	0.9438 (12)
	0.08432	Uiso	1	

4.2 Publication II

H85	H	0.0819 (5)	-0.2066 (14)	1.1842 (14)
	0.08432	Uiso	1	
H86	H	0.2819 (16)	-0.2443 (12)	0.9269 (12)
	0.08432	Uiso	1	
H87	H	0.1245 (13)	-0.2853 (6)	1.0747 (19)
	0.08432	Uiso	1	
N88	N	0.1283 (4)	0.1581 (0)	0.5842 (7)
	0.08432	Uiso	1	
H89	H	0.1835 (8)	0.1244 (1)	0.5356 (11)
	0.08432	Uiso	1	
C90	C	0.1185 (6)	0.2455 (1)	0.5625 (6)
	0.08432	Uiso	1	
O91	O	0.0513 (11)	0.2911 (3)	0.6118 (11)
	0.08432	Uiso	1	
C92	C	0.2081 (5)	0.2828 (1)	0.4755 (6)
	0.08432	Uiso	1	
C93	C	0.3121 (9)	0.3130 (12)	0.5595 (6)
	0.08432	Uiso	1	
H94	H	0.3528 (7)	0.2590 (18)	0.6137 (12)
	0.08432	Uiso	1	
H95	H	0.2906 (16)	0.3635 (15)	0.6268 (10)
	0.08432	Uiso	1	
H96	H	0.3735 (8)	0.3411 (12)	0.4988 (7)
	0.08432	Uiso	1	
C97	C	0.1529 (7)	0.3586 (8)	0.4004 (15)
	0.08432	Uiso	1	
H98	H	0.2124 (7)	0.3846 (9)	0.3359 (15)
	0.08432	Uiso	1	
H99	H	0.0760 (5)	0.3378 (16)	0.3429 (16)
	0.08432	Uiso	1	
H100	H	0.1302 (15)	0.4117 (5)	0.4628 (24)
	0.08432	Uiso	1	
C101	C	0.1231 (4)	0.0624 (1)	0.7639 (7)
	0.08432	Uiso	1	
H102	H	0.2156 (4)	0.0622 (2)	0.7734 (8)
	0.08432	Uiso	1	

loop_		
_geom_bond_atom_site_label_1	_geom_bond_atom_site_label_2	_geom_bond_distance
C22	H24	1.0978 (219)
C22	H34	1.0994 (221)
C22	H23	1.0993 (259)
C18	C22	1.5277 (113)
F2	C18	1.3898 (142)
C18	C19	1.5269 (88)
C19	H20	1.0996 (203)
C19	H39	1.0992 (338)
C19	H21	1.0984 (291)

4 Publications

C16	C18	1.5783 (110)
C16	O17	1.2139 (130)
N14	C16	1.3680 (97)
N14	H25	1.0114 (120)
C12	N14	1.3958 (109)
C12	C13	1.3860 (105)
C13	H15	1.0954 (77)
C13	C40	1.3867 (106)
C8	C40	1.3845 (77)
C8	H11	1.0939 (104)
C7	C8	1.3822 (101)
C7	C9	1.3813 (103)
C9	H10	1.0938 (101)
C9	C12	1.3820 (77)
C40	N41	1.3953 (103)
N41	H44	1.0116 (114)
N41	C42	1.3694 (92)
C42	O43	1.2140 (123)
C42	C45	1.5767 (107)
C45	C46	1.5277 (99)
C46	H47	1.0987 (253)
C46	H48	1.0984 (184)
C46	H52	1.0982 (175)
C45	C49	1.5293 (97)
C49	H50	1.0992 (280)
C49	H51	1.0986 (204)
C49	H53	1.0999 (168)
F1	C45	1.3896 (116)
C7	N26	1.3903 (77)
N26	H27	1.0107 (122)
N26	C28	1.3682 (109)
C28	O32	1.2143 (117)
C28	C29	1.5733 (84)
F3	C29	1.3895 (180)
C29	C30	1.5246 (184)
C30	H31	1.0971 (335)
C30	H54	1.1005 (141)
C30	H33	1.0991 (274)
C29	C35	1.5288 (132)
C35	H38	1.0989 (413)
C35	H36	1.0976 (350)
C35	H37	1.0998 (181)
C93	H96	1.1002 (156)
C93	H95	1.0978 (231)
C93	H94	1.0976 (263)
C92	C93	1.5298 (116)
C92	C97	1.5261 (130)
C97	H100	1.0986 (221)
C97	H98	1.0997 (183)
C97	H99	1.0987 (157)
F4	C92	1.3883 (117)
C90	C92	1.5740 (91)

4.2 Publication II

C90	O91	1.2134 (127)
N88	C90	1.3678 (26)
N88	H89	1.0109 (107)
C60	N88	1.3971 (82)
C60	C101	1.3820 (79)
C101	H102	1.0955 (74)
C74	C101	1.3833 (84)
C72	C74	1.3851 (74)
C72	H73	1.0961 (81)
C55	C72	1.3863 (80)
C55	C56	1.3859 (85)
C56	H57	1.0967 (84)
C56	C60	1.3840 (74)
C74	N75	1.3975 (83)
N75	H76	1.0112 (107)
N75	C77	1.3682 (51)
C77	O78	1.2132 (124)
C77	C79	1.5773 (98)
F5	C79	1.3913 (120)
C79	C80	1.5279 (142)
C80	H87	1.0979 (191)
C80	H81	1.0996 (164)
C80	H85	1.0986 (158)
C79	C82	1.5327 (140)
C82	H84	1.0988 (230)
C82	H83	1.0995 (164)
N58	H59	1.0109 (114)
C61	O62	1.2147 (125)
N58	C61	1.3731 (109)
C61	C63	1.5793 (82)
F6	C63	1.3890 (206)
C63	C67	1.5296 (120)
C67	H68	1.0990 (525)
C67	H69	1.0987 (432)
C67	H70	1.1004 (217)
C63	C64	1.5263 (205)
C64	H71	1.0989 (322)
C64	H66	1.1000 (132)
C64	H65	1.0979 (399)
C82	H86	1.0985 (205)
C55	N58	1.3977 (74)

loop_			
_geom_angle_atom_site_label_1			
_geom_angle_atom_site_label_2			
_geom_angle_atom_site_label_3			
_geom_angle			
H94	C93	H96	108.456 (1106)
H95	C93	H96	107.66 (104)
C92	C93	H96	109.027 (958)
H94	C93	H95	108.416 (1839)

4 Publications

F4	C92	C93	108.659(502)
C93	C92	C97	110.969(542)
C92	C93	H95	111.591(926)
C92	C93	H94	111.567(774)
C90	C92	C93	109.106(430)
H98	C97	H100	107.762(1528)
H98	C97	H99	108.237(945)
H99	C97	H100	108.188(1663)
C92	C97	H100	111.982(966)
C92	C97	H98	109.214(1216)
C92	C97	H99	111.325(949)
F4	C92	C97	109.374(500)
C90	C92	C97	107.421(444)
F4	C92	C90	111.321(642)
O91	C90	C92	122.882(782)
N88	C90	C92	113.826(166)
H89	N88	C90	118.074(163)
C60	N88	H89	116.695(595)
N88	C60	C101	120.004(154)
C56	C60	N88	122.054(223)
C60	C101	H102	118.952(457)
C55	C56	C60	122.256(340)
H57	C56	C60	118.630(429)
C60	C101	C74	122.045(257)
C56	C55	C72	117.656(232)
C56	C55	N58	119.877(410)
C72	C74	C101	118.060(359)
C74	C101	H102	119.002(477)
C55	C56	H57	119.114(328)
H73	C72	C74	118.621(203)
C55	C72	H73	119.336(132)
N75	C74	C101	119.712(316)
C74	N75	H76	116.597(809)
H76	N75	C77	117.799(496)
N75	C77	O78	123.283(375)
N75	C77	C79	113.477(392)
O78	C77	C79	123.072(845)
F5	C79	C77	111.570(691)
C77	C79	C80	107.618(614)
C79	C82	H84	111.298(1017)
C79	C82	H86	111.906(1218)
C79	C82	H83	109.215(1079)
C79	C80	H81	109.258(1233)
C79	C80	H85	111.101(857)
C79	C80	H87	112.524(1028)
F5	C79	C82	108.632(765)
F5	C79	C80	108.714(706)
H83	C82	H84	108.210(1434)
H84	C82	H86	108.447(1739)
H83	C82	H86	107.630(1342)
H81	C80	H87	107.533(1441)
H81	C80	H85	108.184(914)

4.2 Publication II

H85	C80	H87	108.088 (1547)
N58	C55	C72	122.431 (390)
C72	C74	N75	122.227 (377)
C55	N58	H59	114.889 (648)
C55	N58	C61	127.997 (521)
H59	N58	C61	117.077 (879)
N58	C61	O62	124.139 (840)
N58	C61	C63	112.211 (474)
O62	C61	C63	123.600 (682)
C61	C63	C67	109.975 (647)
C61	C63	C64	108.773 (517)
F6	C63	C61	110.575 (651)
C63	C67	H69	111.675 (1351)
H68	C67	H69	108.373 (2988)
H69	C67	H70	108.378 (1407)
H68	C67	H70	107.981 (1791)
F6	C63	C67	108.939 (932)
C64	C63	C67	110.361 (1106)
C63	C64	H65	111.323 (2024)
C63	C64	H71	111.957 (1131)
C63	C64	H66	108.974 (874)
H66	C64	H71	107.694 (1437)
H65	C64	H71	108.557 (2529)
N88	C90	H66	108.201 (1389)
C56	C60	O91	123.152 (255)
C55	C72	C101	117.937 (272)
C18	C19	C74	122.035 (259)
H21	C19	H39	110.978 (939)
H20	C19	H39	108.526 (2722)
H20	C19	H39	108.306 (2067)
C18	C19	H21	108.154 (1565)
C18	C19	H20	109.122 (687)
F2	C18	H21	111.656 (982)
C19	C18	C19	108.289 (882)
C16	C18	C22	111.057 (803)
O17	C16	C19	108.536 (569)
N14	C16	C18	123.505 (799)
C18	C22	C18	113.049 (607)
C18	C22	H24	109.338 (934)
C18	C22	H34	111.720 (842)
F2	C18	H23	111.241 (1430)
C16	C18	C22	108.975 (806)
H24	C22	C22	108.108 (664)
H23	C22	H34	107.657 (1690)
H23	C22	H24	108.440 (2003)
C12	N14	H34	108.324 (2127)
C16	N14	C16	127.824 (603)
N14	C16	H25	116.282 (724)
C9	C12	O17	123.373 (850)
C13	C12	N14	119.444 (543)
C12	N14	N14	122.978 (742)
		H25	115.889 (949)

4 Publications

H10	C9	C12	118.965 (624)
C12	C13	H15	118.831 (648)
C12	C13	C40	122.203 (740)
C7	C9	C12	122.462 (545)
C8	C7	C9	117.907 (709)
C9	C12	C13	117.565 (555)
C9	C7	N26	119.705 (539)
C7	C8	C40	122.108 (560)
C7	N26	H27	115.425 (673)
C7	N26	C28	126.767 (546)
C8	C40	C13	117.753 (537)
C8	C40	N41	119.626 (557)
C7	C8	H11	118.836 (808)
H11	C8	C40	119.055 (607)
C8	C7	N26	122.372 (563)
H15	C13	C40	118.966 (624)
C40	N41	H44	115.907 (885)
C40	N41	C42	127.899 (631)
C13	C40	N41	122.598 (725)
N26	C28	C29	111.282 (497)
N26	C28	O32	123.979 (816)
F3	C29	C28	109.875 (655)
C28	C29	C30	109.258 (577)
C28	C29	C35	109.348 (634)
C29	C28	O32	124.731 (676)
C29	C30	H54	108.936 (1006)
C29	C30	H31	111.813 (1823)
C29	C30	H33	111.819 (1125)
C29	C35	H36	111.504 (1265)
C30	C29	C35	110.539 (1052)
C29	C35	H37	108.820 (958)
C29	C35	H38	111.554 (1192)
F3	C29	C35	109.082 (936)
H36	C35	H37	108.434 (1316)
H37	C35	H38	107.924 (1642)
H36	C35	H38	108.493 (2474)
F3	C29	C30	108.726 (851)
H31	C30	H54	108.087 (1539)
H33	C30	H54	107.424 (1381)
H31	C30	H33	108.600 (2377)
N41	C42	O43	123.484 (861)
N41	C42	C45	113.202 (597)
O43	C42	C45	123.284 (751)
F1	C45	C42	111.798 (662)
C42	C45	C49	108.424 (582)
C42	C45	C46	107.959 (571)
F1	C45	C49	108.706 (732)
F1	C45	C46	108.438 (643)
C45	C46	H47	111.071 (1112)
C45	C46	H52	109.207 (725)
C45	C46	H48	111.839 (689)
H47	C46	H52	108.446 (1756)

4.2 Publication II

H47	C46	H48	108.449 (1982)
C45	C49	H50	111.018 (1048)
C45	C49	H51	111.649 (760)
C45	C49	H53	109.243 (714)
H50	C49	H53	108.286 (1750)
H50	C49	H51	108.458 (2094)
H51	C49	H53	108.084 (1275)

4.3 Influence of proton coupling on symmetry-based homonuclear ^{19}F dipolar recoupling experiments

This work has entirely originated from the Inorganic Chemistry III of the University of Bayreuth and will be reproduced from Zehe, C. S., Siegel, R., Senker, J., *Solid State Nuclear Magnetic Resonance*, **65**, 122–133 (2015) in the following with permission from Elsevier. My contributions are:

- conception and main authorship of the article
- implementation, conduction and evaluation of homonuclear DQ recoupling pulse experiments
- conduction and evaluation of all simulations, including creation of model spin systems

The contributions of all other authors are:

- conception and main authorship of the study
- support of NMR experiments and data evaluation



Contents lists available at ScienceDirect

Solid State Nuclear Magnetic Resonance

journal homepage: www.elsevier.com/locate/ssnmr

Influence of proton coupling on symmetry-based homonuclear ^{19}F dipolar recoupling experiments



Christoph S. Zehe, Renée Siegel, Jürgen Senker*

Inorganic Chemistry III, University of Bayreuth, 95447 Bayreuth, Germany

ARTICLE INFO

Article history:

Received 3 September 2014

Received in revised form

3 December 2014

Accepted 5 December 2014

Available online 16 December 2014

Keywords:

Solid-state NMR spectroscopy

 ^{19}F homonuclear DQ recoupling

Symmetry based dipolar recoupling

 ^1H decoupling

ABSTRACT

We study the efficiency of two symmetry based homonuclear ^{19}F double-quantum recoupling sequences for moderate ($R14_2^2$) and ultra-fast ($R14_3^2$) MAS under the influence of strong ^1H - ^{19}F and ^{19}F - ^{19}F dipolar interactions and ^1H continuous wave decoupling. Simulations based on various spin systems derived from the organic solid 1,3,5-tris(2-fluoro-2-methylpropionylamino)benzene (F-BTA), used as a model system, reveal that the strong-decoupling limit is not accessible even for moderate spinning speeds. Additionally, for the no-decoupling limit improved DQ efficiencies are predicted for both moderate and ultra-fast MAS. Strong perturbations of build-up curves can be avoided by additional stabilisation through supercycling. Additional ^1H cw decoupling during ^{19}F recoupling rapidly reduces the maximum DQ efficiency when deviating from the no-decoupling limit. These effects were confirmed by experimental data on F-BTA. For moderate spinning the influence of ^1H - ^{19}F and ^{19}F - ^{19}F couplings is markedly stronger compared to ultra-fast MAS. For the latter case those influences reduce to a constant scaling if only short excitation times up to the first minimum are taken into account. Based on this analysis the experimental build-up curves of 1,3,5-tris(2-fluoro-2-methylpropionylamino)benzene can be refined with homonuclear ^{19}F spin systems which allow to probe even subtle structural differences for the fluorine atoms of F-BTA.

© 2014 Elsevier Inc. All rights reserved.

1. Introduction

Magic Angle Spinning (MAS) [1,2] has become one of the greatest advances in modern solid-state NMR spectroscopy. By averaging anisotropic interactions, high-resolution NMR spectra can be obtained for solid samples [3]. Thus, by enhancing the feasibility of identifying chemical building units based on the isotropic chemical shift, a wide field of applications in chemistry and material science was opened up [3–7]. For structure determination, however, MAS averages the direct homo- and heteronuclear interactions as well as quadrupolar couplings and thus prevents access to interatomic distances and electron density distributions [3]. To overcome this major drawback, recoupling experiments have been developed allowing to reintroduce specific nuclear interactions during MAS, while retaining high-resolution [8,9]. By a clever combination of radio-frequency pulses and MAS, additional time dependence is introduced into the interaction Hamiltonian, which interferes with averaging through physical rotation of the sample [8–10]. This concept has proven to be groundbreaking for determining homo- and heteronuclear

distances based on dephasing [11], zero quantum [12] and double quantum (DQ) [13,14] experiments. In particular, symmetry based recoupling experiments [10,15–17], such as the class of RN_n^m sequences, have been applied most frequently for efficient dipolar recoupling [18–20] due to their rational design. Meanwhile, such sequences proved to be an indispensable tool for structural investigations in a wide range of materials and are often used in NMR crystallography [5,18,21–23].

Dipolar recoupling experiments were employed extensively for materials with mainly one type of NMR active nuclei. Well-known examples are homonuclear ^1H DQ experiments in organic [24], supramolecular, polymer [22,25–27] and biopolymer materials [28,29] as well as ^{19}F and ^{31}P measurements on inorganic fluorides [30–32] and phosphates [33,34]. Due to the high natural abundance in such cases isotope enrichment is unnecessary. In particular, for ^1H and ^{19}F , the two NMR-active nuclei with the highest gyromagnetic ratios, the resulting strong homonuclear dipolar interactions broaden the individual resonances significantly, even for fast spinning [35]. In such cases, structure determination has benefited greatly by developing and commercialising MAS probes allowing for ultra-fast MAS with spinning speeds up to 110 kHz [36,37]. Even strong dipolar couplings are averaged efficiently enough to result in high-resolution spectra [36]. By using appropriate symmetry based R sequences adapted to ultra-fast MAS,

* Corresponding author.

E-mail address: juergen.senker@uni-bayreuth.de (J. Senker).<http://dx.doi.org/10.1016/j.ssnmr.2014.12.002>

0926-2040/© 2014 Elsevier Inc. All rights reserved.

homonuclear DQ dipolar recoupling was achieved for ^1H and ^{19}F and applied to structural investigations of inorganic fluorides [30,31] and peptides [29].

Dipolar recoupling on heteronuclei (X) like ^{13}C , ^{15}N , and ^{29}Si is usually more demanding. First the low natural abundance of such nuclei requires extensive isotope labelling which is expensive and time consuming. More important, however, is the presence of dense proton spin baths leading to a severe reduction of the X DQ efficiencies by interferences [28] and faster spin–spin relaxation [38]. Heteronuclear decoupling in rotating solids requires a reduction of the effective heteronuclear spin–spin interactions by at least three orders of magnitude [39] which is not an easy task to accomplish. For the most common nuclei in molecular solids, polymers or biopolymers – ^{13}C and ^{15}N – essentially two working limits have been established in the past [12,39–41].

At low spinning speeds, both high-resolution spectra and high recoupling efficiencies can be obtained, when strong resonant radiofrequency (RF) pulses – usually continuous wave (cw) decoupling – are applied on the proton channel to suppress heteronuclear interactions [40]. Although, several broadband decoupling sequences such as PISSARO [42], XIX [43], TPPM [44] or SPINAL-64 [45] provide a better decoupling performance as cw, they introduce additional time dependencies. This requires a careful theoretical analysis using e.g. Floquet theory [46] and makes the system less predictable and less robust against imperfections and mismatches. Thus up to date most studies exploiting dipolar recoupling for distance measurements rely on the cw decoupling scheme to remove the influence of heteronuclear interactions. The scenario of strong cw irradiation is called the strong decoupling limit, since the proton nutation frequencies must be at least 2.5–3 times stronger compared to the ones applied on the X channel, in order to avoid destructive interferences between the recoupling and decoupling fields [47,48]. Missing this requirement unavoidably leads to weak DQ efficiencies [40]. Commercially available probes allow for maximum nutation frequencies between 100 and 200 kHz, in particular, for the proton channel. This leads to constraints on the recoupling strength and via symmetry restrictions of the R sequences also limits the maximal possible spinning speed [49].

At faster spinning, the heteronuclear dipolar couplings are reduced efficiently enough through MAS and the R sequences alone, leading to a no-decoupling regime [12,40]. Here, high DQ efficiencies are already reached without the need for additional heteronuclear proton decoupling schemes. R sequences with a high stability against chemical shift anisotropy (CSA) should provide favourable performances in this regime, since CSA and heteronuclear dipolar coupling exhibit the same rotational symmetry in the absence of irradiation on the ^1H channel [16].

In this work, we focus on materials possessing both dense spin systems for protons and fluorine like many molecular solids do [23]. Such systems pose a fabulous challenge since the dipolar couplings between all nuclear combinations – ^1H – ^1H , ^1H – ^{19}F and ^{19}F – ^{19}F – are quite strong (in the order of several kHz). For instance, with the same interatomic distances heteronuclear ^1H – ^{19}F couplings are 3.7 times stronger as ^1H – ^{13}C interactions due to the high gyromagnetic ratios of both ^1H and ^{19}F . This requires significantly higher decoupling powers and spinning speeds, respectively. At the same time, the small difference in resonance frequencies (35 MHz for a field of 14.1 T, according to a proton resonance frequency of 600 MHz) makes the design of probes more difficult. Early works from Harris [50–52], Scheler [51,52] and Hagaman [53] showed the feasibility using doubly tuned probes. These are commercialised nowadays by e.g. Bruker, but the design limits the maximum applicable power for both channels markedly.

In this stress field we strive at developing a systematic picture

of strong ^1H – ^{19}F and ^1H – ^1H dipole interactions as function of the recoupling sequence, spinning speed and decoupling power.

We have chosen the fluorine containing molecular solid 1,3,5-tris(2-fluoro-2-methylpropionylamino)benzene (F-BTA) [23] as a model system. Typical ^1H – ^1H , ^1H – ^{19}F and ^{19}F – ^{19}F couplings strengths are in the region of 20, 10–15, and 1–2 kHz, respectively. Based on spin systems derived from the crystal structure [23], numerical simulations of DQ recoupling efficiencies have been carried out for moderate (12.5 kHz) and ultrafast (60 kHz) spinning frequencies as a function of the field strength of ^1H cw decoupling. Both the $R14_2^6$ and the $R14_4^5$ sequence have been chosen due to their superior performance at moderate and ultrafast spinning [17,29,31]. Hereby, we restrict to ^1H cw decoupling in order to minimise possible interferences as mentioned above [40]. We investigate the existence of the no- and strong-decoupling limit and probe the effect of the $S_0S_xS_xS_x$ supercycling scheme during recoupling. Supercycling imposes additional selection rules on excitation and reconversion of DQ coherences. The resulting enhanced suppression of undesirable higher-order terms arising from CSA and heteronuclear dipole interactions, might improve the stability of the recoupling sequences further [17]. The results of the simulations are accompanied by ^{19}F – ^{19}F DQ experiments on F-BTA for the no-decoupling limit of both moderate and ultra-fast MAS.

2. Pulse sequences

The following essential requirements for ^{19}F dipolar recoupling sequences should be obeyed for efficient recoupling. (i) Due to the large homonuclear dipolar ^{19}F couplings, they should be suitable for spinning speeds larger than 10 kHz to achieve high-resolution. (ii) The CSA and large isotropic shift range of ^{19}F require sequences with a high stability against these interactions. Since CSA and heteronuclear dipolar couplings exhibit the same rotational symmetry in the absence of ^1H irradiation, this would also lead to a better intrinsic stability against ^1H – ^{19}F interactions. A qualitative indicator of the robustness of a sequence against CSA is hereby provided by the number of second-order cross terms between the dipolar interaction and CSA [19,39]. (iii) A fast DQ build-up reduces the impact of relaxation, experimental errors and other perturbations. This can be estimated by the scaling factors for the recoupled dipolar terms according to first-order average Hamiltonian theory [54]. Higher scaling factors lead to a more efficient recoupling and hence to a faster build-up.

Based on these considerations, the $R14_2^6$ sequence was chosen [19] for moderate spinning speeds. The number of 16 second-order cross terms between dipolar coupling and CSA is the smallest one observed for a variety of recoupling symmetries [54], leading to a good CSA compensation [19,54]. Moreover, the scaling factor of 0.172 for $(90^\circ)_x(270^\circ)_x$ composite pulses is close to the maximum observed values of 0.174 [54]. Since the ^{19}F nutation frequency is proportional to the MAS frequency by a factor of 7, only moderate spinning speeds are possible. We fix the MAS rate to 12.5 kHz, resulting in a ^{19}F nutation frequency of 87.5 kHz. This value is close to the probe limit for commercially available 3.2 mm HFX quadruple resonance MAS probe designs.

We also select the $R14_4^5$ sequence at ultra-fast MAS of 60 kHz. This sequence exhibits 34 cross terms with the CSA, which is the maximum observed [54]. However, due to a multiplier of 3.5 between nutation and rotation frequency, dipolar recoupling is possible with this sequence at ultra-fast MAS of 60 kHz [29,31]. Commercially available probes can achieve the resulting nutation frequency of 210 kHz with rotor diameters of 1.3 mm or below. At this spinning speed, even large CSA and other interactions are

is about 9% smaller than the one for the $R14_2^5$ sequence [54], ensuring a good DQ recoupling [29,31].

3. Experimental

3.1. Solid-state NMR simulations

All data were handled with the software package MATLAB [55]. Simulations were performed with the simulation software package SIMPSON [56,57].

The crystal structure of F-BTA is presented in reference [23], where all relevant NMR parameters are included. For creating model systems, relative orientations and principal values of the ^{19}F - ^{19}F and ^1H - ^{19}F dipole tensors were calculated from this structure solution. Afterwards, the coupling strengths were adjusted for each model system in the way described below. In all cases the CSA parameter of $\delta_{\text{aniso}} = -25$ ppm and $\eta = 0.45$ [23] were used. Since the Euler angles for the CSA tensors show only negligible influence on the build-up curves [17], which was also tested with different arbitrary angles, they were set to zero. For powder averaging, 40 γ angles were used in combination with 232 (α, β) pairs, which were calculated according to the Zaremba-Conroy-Wolfsberg scheme [58–60]. The input files for all model systems may be found in the ESI†.

3.2. Solid-state NMR experiments

All experiments were conducted on a Bruker Avance III HD spectrometer at a field of $B_0 = 14.1$ T. The measurements at a MAS spinning speed of 60 kHz were performed in a Bruker 1.3 mm double resonance probe. For the ^{19}F double-quantum recoupling experiments a symmetric $R14_4^5$ double-quantum recoupling protocol was used with 90° - 270° composite pulses as R -elements [49,10]. For both one-dimensional direct excitation experiments and double-quantum excitation and reconversion, a nutation frequency of 210 kHz was adjusted. The measurements at a MAS spinning speed of 12.5 kHz were conducted in a Bruker 3.2 mm HFXQ quadrupole resonance probe. Hereby, a symmetric $R14_2^5$ double quantum recoupling protocol was used with 90° - 270°

composite pulses as R -elements [49,10], leading to a nutation frequency of 87.5 kHz. In an analogous experiment, cw decoupling was irradiated on the ^1H channel with a nutation frequency of 20 kHz and 100 kHz during the R sequence, respectively. SPINAL-64 [45] decoupling with a pulse length and nutation frequency of 5.8 μs and 83 kHz, respectively, was applied during acquisition. For both MAS frequencies, the double-quantum intensities were normalised through repeating the experiment with a phase cycle adjusted to select only coherence order 0 during the recoupling sequence [61].

4. Results and discussion

4.1. Influence of ^1H decoupling during ^{19}F dipolar recoupling

As a model compound, we use 1,3,5-tris(2-fluoro-2-methylpropionylamino)benzene **1**, whose molecular formula is depicted in Fig. 1 (right, top). In the crystal structure, the molecules are stacked along the c axis and connected along the b and c axes via intermolecular hydrogen bonds, resulting in a layered build-up with only van der Waals forces acting between neighbouring layers [23]. The ^{19}F spectrum exhibits six different signals, since two molecules are contained in the asymmetric unit (Fig. 1, top of right side).

In this structure, fluorine forms a spin system of medium density, since a sphere with a radius of 6.5 Å around each fluorine atom of the asymmetric unit contains at most 8 other fluorine neighbours. Hereby, the minimum F-F distance is 3.9 Å, corresponding to a coupling constant of -1750 Hz. In contrast, as in many organic materials, the high natural and structural abundance of ^1H leads to a dense proton spin system. Fig. 1 (right, bottom) depicts a close-up containing two fluorine atoms with a distance of 3.9 Å. In the two spheres around each fluorine atom with a radius of 4 Å, 22 protons are located. The closest proton-fluorine distance is hereby 2 Å with a resulting coupling constant of $-14,134$ Hz, whereas the closest proton-proton contact is 1.7 Å corresponding to $-24,450$ Hz.

Since the size of density matrix within the simulations grows with 2^N , where N is the number of spins, a realistic simulation

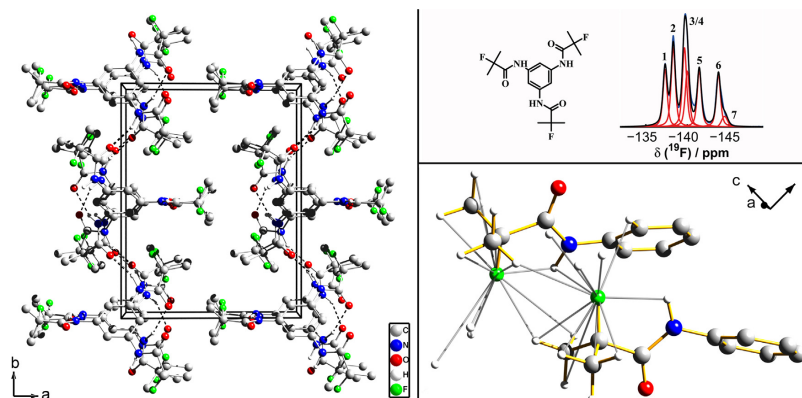


Fig. 1. Left side: perspective view along the c -axis of the crystal structure of F-BTA [23]. For clarity, all protons except those of the amide groups are removed. Right side, top: Molecular structure of compound F-BTA and ^{19}F direct excitation experiment with deconvolution using 7 signals. Signal 7 arises from an impurity and will, therefore, be neglected [23]. Right side, bottom: Close-up of two molecules of one layer. For clarity, only the benzene cores and two side-groups including two fluorine atoms of interest are shown. All protons (22 in total) located in a sphere with a radius of 4.0 Å around one of the two fluorine atoms are added and connected to the respective fluorine by a

including several fluorine atoms and all protons surrounding each of those is impossible. Therefore, model systems, which mirror the coupling strengths and contain at maximum 6–9 spins at the same time, were created (Fig. 2). For model system (a), two fluorine atoms with a distance of 3.9 Å and the four closest protons of one of the two fluorine atoms were selected, leading to a spin system with 6 spins in total. Furthermore, the ^1H – ^{19}F couplings constants to the second ^{19}F were increased, emulating the case where the protons are all located in the middle of the two fluorine atoms. Hereby, the influence of the Euler angles of the ^1H – ^{19}F dipolar coupling tensors was negligible. The size of this spin system allows extensive simulations but may underestimate the impact of the proton spin system on the ^{19}F – ^{19}F DQ recoupling.

Therefore, three additional protons were added to model (a) in the same manner, resulting in model system (b) with 9 spins and an extended proton spin system (Fig. 1b). Table 1 lists the average ^1H – ^1H , ^1H – ^{19}F and the ^{19}F – ^{19}F coupling constants to provide a qualitative indicator for the strength of the interactions. For model system (a) and (b) they are all similar, demonstrating that both spin systems differ merely in the size of the proton spin network. Moreover, the strongest couplings never exceed the maximum values of the experimental structure as discussed above.

For model system (a) simulations of ^{19}F DQ build-up curves with a systematic variation of cw nutation frequency $\omega_{\text{nutation}}^{\text{cw}}$ were performed (Fig. 3). The depicted area of $\omega_{\text{nutation}}^{\text{cw}} = 0$ –200 kHz contains the experimentally accessible region. In the case of the $R14_2^{\text{DQ}}$ sequence with and without supercycling at a spinning frequency of 12.5 kHz, the maximum DQ efficiencies are reached for a cw decoupling strength of $\omega_{\text{nutation}}^{\text{cw}} = 200$ kHz. Hereby, the highest DQ efficiency reached without supercycling is approximately 60%.

Table 1
Average dipolar coupling constants $(1/N)\sum_{i,j}(1/d_{ij})$ for all N ^1H – ^{19}F or N ^1H – ^1H dipolar couplings, respectively, for the different model systems (compare Fig. 2). All values are given in Hz.

Model	H-H	F-H	F-F
(a)	–15,566	–9217	–1750
(b)	–14,187	–8480	–1750
(c)	–634	–8480	–1750
(d)	–14,187	–5054	–1750
(e)	–3,519	–5054	–1750
(f)	–14,187	–8480	–3000
(g)	–14,187	–8480	–1000

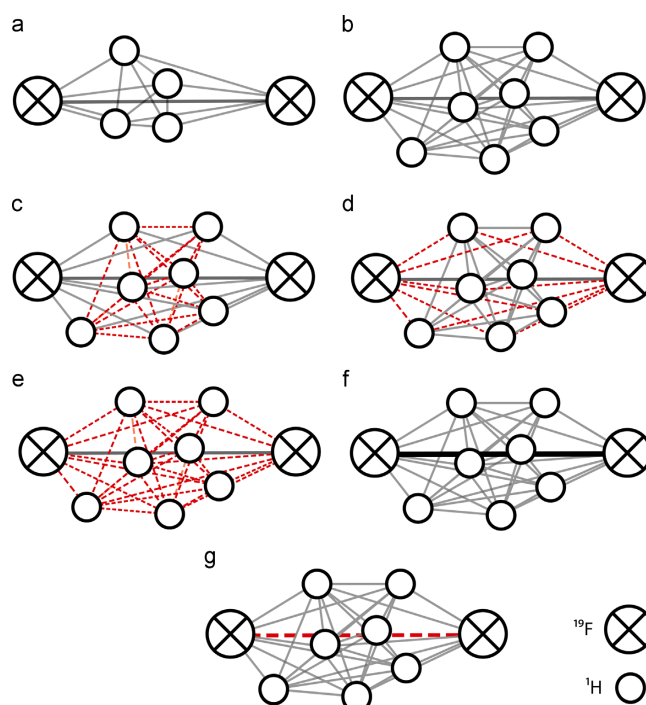


Fig. 2. Model systems for numerical simulations. For (a), the two fluorine atoms with the shortest possible distance in the structure of F-BTA and the four closest protons surrounding one of the two fluorine atoms were selected. The couplings to the second ^{19}F were adapted as if the ^1H were located in between the two fluorine atoms. As an extension of (a), for creation of model (b) two protons were added and all ^1H – ^1H and ^1H – ^{19}F coupling constants were adapted. For model (c), the ^1H – ^1H , for model (d) the ^1H – ^{19}F and for model (e) both of these interactions were weakened compared to (b), which is indicated by red dashed lines. In model (f), the ^{19}F – ^{19}F coupling constant was increased (black thickened line) and in (g) this constant was weakened (red dashed line) compared to (b). In all cases, none of the coupling constants exceeded the maximum possible value based on the distances of the structure. Table 1 summarises the average coupling constants. (For interpretation of the references to color in this figure legend, the reader is referred to the web version of this article.)

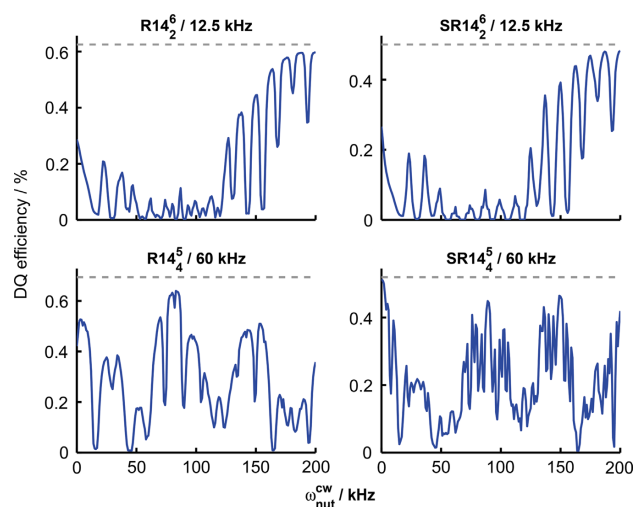


Fig. 3. Maximum ^{19}F DQ efficiencies reached for model systems (a) with the indicated R sequences and MAS frequencies as a function of the nutation frequency for ^1H cw decoupling. The dashed grey line indicates maximum DQ efficiency for an isolated ^{19}F spin pair without heteronuclear couplings and without cw decoupling. The smallest increment for the ^1H nutation frequency is 1 kHz. The nutation frequency on the ^{19}F channel is hereby fixed to 210 kHz and 87.5 kHz for the $R14_4^5$ and $R14_2^6$ sequence, respectively.

which is 96% of the value of 62.5% for an isolated ^{19}F spin pair. Since supercycling removes the γ -encoding, the maximum efficiency of a spin pair is 51% and the maximum reached for model system (a) is 48%, which is 94% of the spin pair value.

In the region around $\omega_{\text{nut}}^{\text{cw}} = 200$ kHz, several local minima in DQ efficiency are present. The ^{19}F nutation frequency is fixed to 87.5 kHz and, therefore, the resulting factor between ^1H and ^{19}F nutation frequencies is 2.3. Usually, a factor of 2.5–3 is necessary to avoid interferences [40] and hence polarisation transfer to ^1H can explain these minima. This may be avoided by higher decoupling power, which, however, is outside of current probe specifications.

In the area of $\omega_{\text{nut}}^{\text{cw}} = 50$ –100 kHz, where the cw nutation frequencies are close to the ^{19}F nutation rate of $\omega_{\text{nut}}^{\text{RN}} = 87.5$ kHz, a region with low efficiencies is observed. This is caused by recoupling of heteronuclear terms in the first-order Hamiltonian at $\omega_{\text{nut}}^{\text{cw}} = (15/2)\omega_{\text{rot}}$, amounting to $\omega_{\text{nut}}^{\text{cw}} = 94$ kHz for a rotation frequency of $\omega_{\text{rot}} = 12.5$ kHz [40].

For $\omega_{\text{nut}}^{\text{cw}} \rightarrow 0$, an increase of the DQ efficiencies up to 27% and 29% are observed with and without supercycling, according to 53% and 46% of the respective spin pair value. These low values indicate remaining heteronuclear interferences. For ^{13}C without supercycling, significantly higher DQ efficiencies up to 60% were reported for this regime, when the homonuclear ^1H interactions are weak, as e.g. for $^{13}\text{C}_2$ labelled alanine. In contrast, for systems with both strong heteronuclear and ^1H homonuclear interactions as e.g. $^{13}\text{C}_2$ glycine, the latter significantly reduce the maximum reachable efficiencies [40]. This suggests, that in particular strong dipolar ^1H – ^{19}F interactions as in e.g. model system (a) are responsible for heteronuclear interferences for the no-decoupling limit for both ^{13}C and, in our case, ^{19}F .

Therefore, at high MAS frequencies, where both the ^1H – ^{19}F couplings and the homonuclear ^1H interaction are averaged more efficiently, the no-decoupling limit might improve. Hence, the $R14_4^5$ was examined at ultra-fast MAS of 60 kHz (Fig. 3) with and

between the recoupling and decoupling nutation frequencies to avoid interferences imposes the requirement of at least $\omega_{\text{nut}}^{\text{cw}} = 525$ kHz. This, however, is experimentally out of the power range of conventional probe designs. Fig. 3 (bottom) shows frequent alternations between low and high recoupling efficiencies over the complete range of ^1H nutation frequencies. Around $\omega_{\text{nut}}^{\text{cw}} = 50$ kHz, 120 kHz and 160 kHz, broader regions with very low DQ recoupling efficiencies are present. Between those, higher efficiencies up to 64% at $\omega_{\text{nut}}^{\text{cw}} = 83$ kHz for the R sequence, corresponding to 93% of a spin pair and with supercycling 46% at $\omega_{\text{nut}}^{\text{cw}} = 150$ kHz, corresponding to 88% of a spin pair, are reached. However, the frequent alternations of good and poor recoupling conditions are not experimentally favourable.

In the case of $\omega_{\text{nut}}^{\text{cw}} \rightarrow 0$, that is, in the no-decoupling limit, both the R and supercycled R sequences show an increase of DQ efficiencies. Whereas the R sequence exhibits a DQ efficiency of 42%, which is 61% of the spin pair value, the same efficiency as a spin pair, 52%, is reached with supercycling. Thus, the no-decoupling limit could be reached at ultra-fast MAS using supercycled sequences.

In conclusion, the strong-decoupling limit is inaccessible for both moderate and ultrafast spinning. The no-decoupling limit is usable in both cases, but provides recoupling efficiencies higher by a factor of 2 for ultra-fast MAS with and without supercycling. However, for structural investigations the quantitative development of the DQ efficiencies with respect to the excitation and the reconversion time is important. Therefore, we investigate the influence of heteronuclear interactions on DQ build-up curves in the no-decoupling limit in more detail in the following.

Fig. 4A depicts the simulated build-up curves using the $R14_4^5$ sequence for model (a) (black curves) corresponding to the limit $\omega_{\text{nut}}^{\text{cw}} = 0$ and for the corresponding isolated spin pairs (blue curves). In the case of the R sequence a curve shape with negative efficiencies and huge deviations compared to the corresponding spin pair is observed for model system (a). This means that the

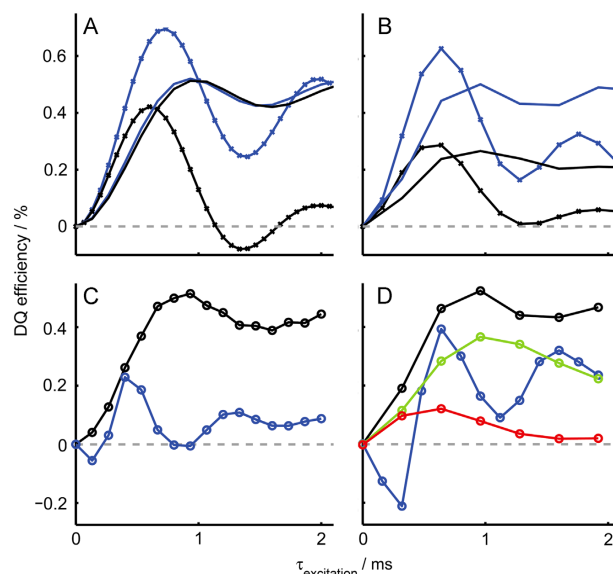


Fig. 4. ^{19}F DQ build-up curves. (A) Simulations for an isolated ^{19}F spin pair without supercycling (-x, blue), with supercycling (-, blue) and for model system (a) without supercycling (-x, black) and with supercycling (-, black) using the $R14_4^2$ sequence at a MAS frequency of 60 kHz. (B) $R14_4^2$ Simulations for an isolated ^{19}F spin pair without supercycling (-x, blue), with supercycling (-, blue) and for model system (a) without supercycling (-x, black) and with supercycling (-, black) using the $R14_4^2$ sequence at a MAS frequency of 12.5 kHz. (C) Experimental DQ build-up curves (integrated over peak 1–6, compare Fig. 1) for F-BTA without (-o, blue) and with (-o, black) supercycling using the $R14_4^2$ sequence at a MAS frequency of 60 kHz. (D) Experimental DQ build-up curves (integrated over peak 1–6, compare Fig. 1) for F-BTA without (-o, blue) and with (-o, black) supercycling using the $R14_4^2$ sequence at a MAS frequency of 12.5 kHz. Moreover, a measurement with an additional cw decoupling of a strength of 20 kHz (-o, green) and 100 kHz (-o, red) during the recoupling is depicted. (For interpretation of the references to color in this figure legend, the reader is referred to the web version of this article.)

using a homonuclear ^{19}F spin pair model any more. Hence, although high DQ efficiencies around 42% are reached, corresponding to 61% of the DQ efficiency of a spin pair, structural information are remarkably affected due to perturbations of the curve.

Application of a supercycle leads to lower maximum DQ efficiencies of 52% for the spin pair model and smaller oscillations of the curve, since it removes the γ -encoding. However, model system (a) exhibits only small deviations from the spin pair model with equal maximum DQ efficiency and hence the structural information may still be deduced with high accuracy.

Fig. 4B shows simulations for the $R14_4^2$ and the $SR14_4^2$ sequence under moderate spinning for model (a) (black curves) and for the corresponding isolated spin pairs (blue curves) for the limit $\omega_{nut}^{cw} = 0$. As in the case of the $R14_4^2$ scheme, the R sequence without supercycling exhibits for model system (a) a curve shape with severely reduced efficiencies and huge deviations compared to the corresponding spin pair. Supercycling reduces the proton influence, but the curves still show a reduction of the maximum DQ efficiency from 50% for the isolated ^{19}F spin pair to 27% for model system (a). This is in contrast to the behaviour of the simulations for the $SR14_4^2$ sequence (Fig. 4A, black and blue curves) where both the spin pair and model (a) lead to similar build-up curves with maximum DQ efficiencies of 50%. Therefore, for moderate spinning and under the influence of protons, only half of the efficiency reached for ultra-fast MAS is observed.

Fig. 4C depicts experimental build-up curves for the $R14_4^2$ and $SR14_4^2$ sequence at a MAS frequency of 60 kHz, integrated over the

exhibits a maximum DQ efficiency of 23%, but the curve shows an alternation of negative and positive intensities for excitation times up to 1 ms. The shape of the curve is very similar to the one of the simulated build-up curve of model system (a) (Fig. 4A). Application of a supercycle leads to a maximum DQ efficiency of 51%, without negative values in analogy to the simulations. Here, it is important to keep in mind that this experiment does not correspond to an isolated ^{19}F spin pair, but to an extended ^{19}F spin system.

Fig. 4D depicts measurements without and with supercycling for the $R14_4^2$ sequence at a MAS frequency of 12.5 kHz (black and blue curves). The R sequence exhibits a maximum DQ efficiency of 39%, but the curve shows an alternation of negative and positive intensities for excitation times up to 1 ms as for the $R14_4^2$ scheme at 60 kHz (Fig. 4B). Again, supercycling removes these distortions and leads to similar maximum DQ efficiencies of about 50% as observed for ultra-fast spinning. This is higher than expected from the according simulations (see above). The better performance might be explained by the interplay of the dense proton and dense fluorine spin system in F-BTA for which model system (a) might not fully account for. Additional ^1H cw irradiation during the recoupling with a nutation frequency of 20 kHz and 100 kHz (Fig. 4D, green and red curves) clearly reduces the maximum DQ efficiency as expected from the simulations (Fig. 3).

For probing structural features in organic solids by ^{19}F DQ NMR spectroscopy usually the ^{19}F spin systems have to be sufficiently large to avoid finite size effects caused by the strong homonuclear ^{19}F couplings. This, however, limits the number of protons

the spin density matrix with increasing number of spins. Thus only recoupling schemes are feasible which minimise the influences of ^1H – ^1H and ^1H – ^{19}F interactions. The simulations and experimental data presented above show that these conditions are not fulfilled for the SR14₅ sequence at moderate MAS frequencies. In contrast, the simulations for the SR14₄ sequence at ultra-fast MAS show only a negligible influence of ^1H , and hence we will focus on the no-decoupling limit for these conditions in the following. An additional advantage for this scenario is the short increment for excitation and reconversion time, which allows probing even stronger couplings and hence shorter distances. Moreover, the longer relaxation time of the DQ coherences reduces the flattening of oscillations.

The simulations for model system (a) for the SR14₄ sequence at 60 kHz showed the same DQ efficiencies and a behaviour almost identical to the one of a spin pair. However, in this model system only four protons are contained and hence it may underestimate the influence of ^1H . In order to probe the impact of an extended proton spin system, simulations for model system (b) were carried out. As discussed above, this system exhibits similar dipolar couplings as (a), but contains a higher number of ^1H .

The corresponding simulations are depicted in Fig. 5. For model system (b), the curve shows a dampening of DQ efficiencies compared to the simulation of a ^{19}F spin pair with an identical ^{19}F coupling constant and compared to model system (a). Since the average ^1H – ^1H and ^{19}F – ^1H dipolar interactions for the systems (a) and (b) are similar (compare Table 1), this effect can be correlated to the ^1H spin system size. This implies for the experimental build-up curves of F-BTA an even more pronounced dampening due to the larger number of protons in the structure.

In order to investigate the origin of the dampening, additional model systems were created (Fig. 2c–e). As discussed before, the strong homonuclear ^1H interactions are supposed to significantly contribute to heteronuclear interferences. Therefore, at first the ^1H – ^1H dipolar coupling constants have been reduced in model system (b), leading to system (c). According to Table 1, the average ^1H – ^1H coupling constant is scaled down by a factor of 22. The corresponding simulation does not exhibit a dampening and only small deviations from the curve of the corresponding spin pair are visible. Next, the ^1H – ^{19}F coupling constants in (b) were partially decreased, modelling the case of a 40% weaker average ^1H – ^{19}F coupling (see Table 1). The simulation for the resulting model (d) shows less dampening. In model system (e), both ^1H – ^{19}F and ^1H – ^1H coupling constants have been reduced compared to (b). The resulting average ^1H – ^1H and ^1H – ^{19}F coupling constant is 4 and

1.5 times smaller compared to (b), respectively. Fig. 5 shows that the corresponding curve exhibits a behaviour almost identical to the one of a ^{19}F spin pair. Therefore, for heteronuclear interferences in the no-decoupling limit, not only the strength of heteronuclear ^1H – ^{19}F interactions, but also the homonuclear ^1H dipolar couplings play a crucial role.

In order to estimate the impact of the ^{19}F – ^{19}F coupling strength, the ^{19}F – ^{19}F dipole constant of -1750 Hz in model (b) was altered to -3000 Hz in model system (f) and to -1000 Hz in model system (g). The simulations including the curves for corresponding isolated ^{19}F spin pairs are depicted in Fig. 5B. The curve corresponding to (f) shows increasing deviations to the spin pair simulation for longer excitation times, suggesting a constant intensity scaling in combination with an exponential decay. However, model (g) illustrates that for maximum excitation times chosen not to exceed the first intensity minimum, this can be reduced to a constant scaling factor, minimising the degrees of freedom and hence improving the unambiguity between experiment and simulation.

In order to develop a more quantitative picture of the impact of both homonuclear ^1H and heteronuclear couplings on the scaling factor, average root-sum-square (rss) dipolar coupling constants [62] have been calculated according to

$$\langle d_{ij}^{\text{rss}} \rangle = \left\langle \sqrt{\sum_{k \neq j} d_{jk}^2} \right\rangle \quad (1)$$

where $\langle \cdot \rangle$ indicates the average over all spins of the same isotope for which the constant is defined. Hence, we obtained an average rss ^1H – ^1H coupling constant $\langle d_{HH}^{\text{rss}} \rangle$ and an average ^{19}F – ^1H rss coupling constant $\langle d_{FH}^{\text{rss}} \rangle$. Fig. 6 depicts the scaling factors of the build-up curves for model systems (a)–(e) as a function of these two coupling constants.

Model (b) and (d) with strong proton–proton couplings but strong or weak proton–fluorine interactions exhibit intensity scaling factors of 0.9 and 0.95, respectively. The increase of the factor with decreasing ^1H – ^{19}F couplings strengths is obvious since the limit of $\langle d_{FH}^{\text{rss}} \rangle = 0$ corresponds to an isolated ^{19}F spin pair. Although model system (c) exhibits a significantly higher average ^1H – ^{19}F rss coupling constant as model (e), both lead to a scaling factor of essentially 1. This reflects the observation that strong homonuclear ^1H interactions contribute significantly to the heteronuclear interferences. For model system (a), the average heteronuclear and homonuclear ^1H interactions are slightly higher than the respective values for model system (b) (Table 1). Due to

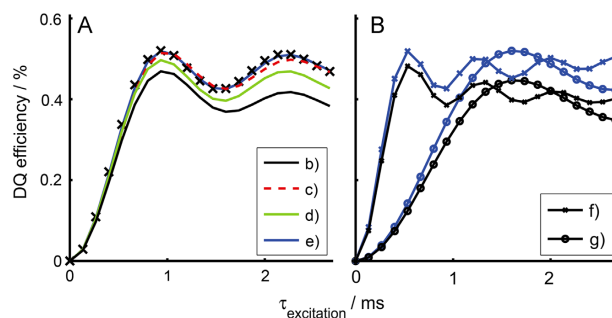


Fig. 5. Simulated ^{19}F DQ build-up curves using the R14₄ sequence and a MAS frequency of 60 kHz for the indicated model systems. The simulation for an isolated ^{19}F spin pair (\times , black) with the same ^{19}F – ^{19}F coupling constant as in the model system (b)–(e) is depicted additionally in (A). Moreover, simulations for isolated ^{19}F spin pairs corresponding to the model system (f) (\times , blue) and (g) (\circ , blue), are contained in (B). For the systems (b)–(e), the ^{19}F – ^{19}F coupling constant is -1750 Hz, for (f) -3000 Hz

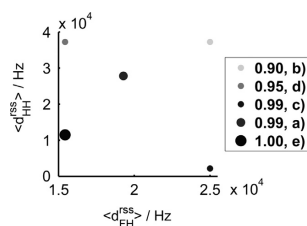


Fig. 6. Scaling factors of the first maxima of simulated ^{19}F build-up curves for the model systems indicated as a function of the average rss coupling constants (compare Eq. (1) and text). The ^{19}F - ^{19}F dipolar coupling constant was -1750 Hz in all cases.

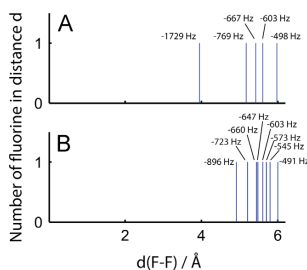


Fig. 7. Number of fluorine atoms in distance $d(\text{F}-\text{F})$ from a selected fluorine atom in the crystal structure of F-BTA. The dipolar coupling constants according to these distances are also contained. In A an exemplary distance distribution of the first type of fluorine atoms, in B an exemplary distance distribution for the second type is depicted.

the small number of protons, it nevertheless exhibits only intermediate homonuclear ^1H and ^1H - ^{19}F rss coupling constants. Therefore, the scaling factor close to 1 may indicate that the size of the proton spin system plays an important role for the interferences. Experimental intensity scaling factors of F-BTA, which will be analysed in the following, should, therefore, be smaller than the ones observed for all model systems.

4.2. Analysis of experimental build-up curves of 1

Fig. 7 depicts exemplary internuclear ^{19}F - ^{19}F distances for two fluorine atoms of the crystal structure of F-BTA including the corresponding dipolar coupling constants. The six fluorine atoms of the asymmetric unit can be split into two groups according to their local structural environment.

For the first group, the distance distribution is exemplarily depicted in Fig. 7A. Here, the closest fluorine is located in a distance of around 4 Å, corresponding to a coupling constant of -1729 Hz. The second closest fluorine atom, however, has a distance of around 5.2 Å and hence the coupling constant of -769 Hz is much smaller. Four of the six fluorine atoms of the asymmetric unit exhibit a distance distribution of this kind, with a short fluorine-fluorine distance of around 4 Å (compare Table 2) and a gap of around 1 Å between this and the next neighbour.

For the fluorine atoms of the second group, as depicted exemplarily in Fig. 7B, the closest fluorine atom exhibits a distance of around 5 Å, corresponding to -896 Hz. This is followed by a larger number of atoms with similar distances and coupling constants around -723 to -491 Hz. A similar distance distribution applies for the last remaining fluorine atom of the asymmetric

Table 2

^{19}F - ^{19}F coupling constants d_{sp} used for the fit of the experimental build-up curves of F-BTA in the spin pair approximation and coupling constants d_{sh} , corresponding to the shortest fluorine-fluorine distance of the spin system assigned to the signals according to the fit presented in Fig. 8. Moreover, the root-sum-square dipole coupling constant d_{rss} (compare Eq. (1)) for the observed ^{19}F in the 9-spin system used for the simulations in Fig. 8 is given. All values are stated in Hz.

Peak	d_{sp}	d_{sh}	d_{rss}
1	-1650	-979	-2028
2	-1650	-845	-1979
3	-1780	-1536	-2211
4	-1750	-1750	-2294
5	-1860	-1750	-2424
6	-2050	-1536	-2361

Since the fluorine atoms within one of these two groups exhibit very similar distance distributions, they show a highly similar DQ build-up curve [23]. This is quantified in Table 2 by the rss ^{19}F - ^{19}F coupling constant for the observed fluorine, which is a measure of the coupling strengths to the next eight closest ^{19}F neighbours. The first two rss constants, corresponding to the two fluorine atoms with smallest dipole constants of -979 Hz and -845 Hz, are around -2000 Hz and thus about 200 Hz larger than the remaining four neighbours. Although a differentiation between the two groups should, therefore, be possible, an unambiguous assignment of all ^{19}F signals to the content of the asymmetric unit can probably not be achieved. In the following, we analyse to which extend the subtle structural differences between the two groups may be probed by DQ build-up curves in the presence of a dense ^1H spin network in the no-decoupling limit.

Fig. 8 depicts experimental DQ build-up curves. Whereas the signals 1 and 2 exhibit a maximum of DQ efficiency at an excitation time of around 1 ms, it is located for the remaining peaks 3–6 around 0.8 ms. Hence, a discrimination of the two groups discussed above is possible with an assignment of the peaks 1 and 2 to the second group and the signals 3–6 to the first group.

The first rise of the experimental curves was fitted with a ^{19}F spin pair approximation (Fig. 8), Table 2 summarises the resulting ^{19}F - ^{19}F coupling constants. In this approximation, the coupling will be stronger for each spin as for the smallest possible coupling constant, since it takes also the contribution of all other couplings into account. Hence, it provides a lower boundary for the coupling constants. For signal 1 and 2, the coupling constant of -1650 Hz achieved the best fit, for the remaining signals constants of -1750 Hz down to -2050 Hz resulted. This reflects the distance distribution discussed above, where for the first group corresponding to signals 3–6 (with a closest ^{19}F - ^{19}F distance of around 4 Å) the build-up is faster compared to the second group corresponding to the peaks 1 and 2.

In Fig. 8, simulations extracted from the crystal structure [23] using spin systems with nine ^{19}F are also depicted. They exhibit significantly higher DQ efficiencies up to 74% compared to the experiments, where a maximum of 56% is reached. Scaling of the simulated curves by a constant factor of 0.75 achieves a good coincidence. Table 2 contains the strongest coupling constants of the spin systems according to the shortest ^{19}F - ^{19}F distances. As discussed above, the assignment according to the least square deviations is not unambiguous due to the similarity of the local fluorine environments. However, the positions of the maxima around 1 ms for signal 1 and 2 and around 0.8 ms for the remaining peaks are reproduced and hence these two groups can be distinguished.

Table 2 also states the coupling constants corresponding to the shortest fluorine-fluorine distances of the spin systems assigned to each signal. The simulations for the peaks 1 and 2 exhibit the

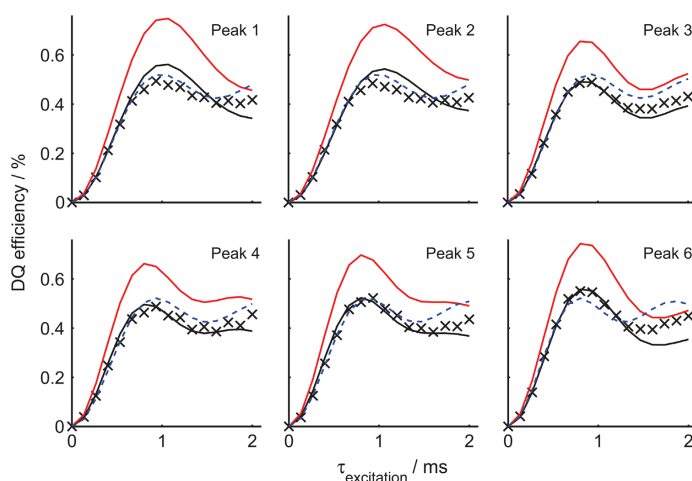


Fig. 8. Experimental ^{19}F DQ build-up curves of F-BTA (\times), simulations based on 9-spin systems extracted from the crystal structure of F-BTA (—, red) and the same simulations scaled by a factor of 0.75 (—, black). The experimental curves are labelled with respect to the corresponding peaks in the ^{19}F spectrum (see Fig. 1). Moreover, simulations for ^{19}F spin pairs fitting the first rise of the build-up are depicted (---, blue, compare also Table 2). The SR14_2^5 sequence was applied at a MAS frequency of 60 kHz. (For interpretation of the references to color in this figure legend, the reader is referred to the web version of this article.)

according to the shortest distances in the spin systems. This is in accordance to the fact of the smallest coupling constants in the spin pair approximation, but since the latter contain contributions of all remaining couplings, they are by a factor of approximately 2 smaller. For the remaining peaks 3–6, both constants exhibit a better accordance, in particular for peaks 3 and 4 they are practically identical. This might be explained by the fact that the strong coupling to the closest ^{19}F dominates the build-up for those.

In contrast to signals 3–6, for peaks 1 and 2, the scaled simulations and the experiments deviate already around the maxima of the curves. Since signals 1 and 2 exhibit only comparatively weak ^{19}F – ^{19}F interactions, the influence of heteronuclear ^1H interactions and relaxation is higher, stronger attenuating the curves.

In comparison to the previous section, the scaling factor of 0.75 is significantly smaller than the factor of 0.9 for model system (b). As discussed above, the size of the proton spin system is crucial for the heteronuclear interferences and hence the experimental factor must be smaller due to the extended proton network.

5. Conclusion

Simulations with fluorine spin pairs with and without four additional protons to model the ^1H – ^1H and ^1H – ^{19}F interactions indicate that the strong decoupling limit for heteronuclear proton decoupling during symmetry based ^{19}F dipolar recoupling in organic solids might be reached only for very high cw nutation frequencies. However, for both the R14_2^5 recoupling sequence at ultra-fast MAS of 60 kHz and the R14_2^5 sequence at moderate MAS of 12.5 kHz, the no-decoupling limit reaches reasonable DQ efficiencies. An additional $\text{S}_0\text{S}'_0\text{S}'_\pi\text{S}_\pi$ supercycle considerably reduces heteronuclear interferences. Hereby, the SR14_2^5 scheme at ultra-fast MAS of 60 kHz shows to be unaffected by heteronuclear interferences in the simulations. The SR14_2^5 sequence at moderate MAS of 12.5 kHz is more sensitive to the latter and exhibits a reduction of DQ amplitudes by a factor of approximately

Experiments with the model compound 1,3,5-tris(2-fluoro-2-methylpropionylamino)benzene confirm the heteronuclear interferences without supercycling and the reduction of the influence of those through supercycling for both sequences. Surprisingly, the no-decoupling limit exhibits DQ efficiencies for the SR14_2^5 scheme at moderate MAS being comparable to those of the SR14_2^5 sequence at 60 kHz. This is probably due to the dense homonuclear ^{19}F and ^1H spin systems in the sample, leading to complex interplay of both at moderate MAS. Experiments carried out with simultaneous ^1H cw decoupling and ^{19}F recoupling using a HFX quadruple resonance probe exhibit a strong influence on the ^{19}F maximum DQ efficiencies. With increasing ^1H nutation frequencies up to 100 kHz corresponding to the power limit of the probe, a severe reduction of maximum DQ efficiencies were observed. This behaviour confirms the trend of the simulations.

Simulations with several extended model systems reveal that for the SR14_2^5 scheme at a MAS rate of 60 kHz even the strong ^1H – ^1H and ^1H – ^{19}F interactions are diminished sufficiently to be taken into account by a constant reduction factor only. Hereby, the suppression of strong ^1H – ^1H dipolar interactions plays a crucial role already reducing the interferences significantly. As a consequence, the analysis of experimental ^{19}F DQ build-up curves can be achieved with simulations based on homonuclear ^{19}F spin systems only.

This trend was corroborated using the SR14_2^5 scheme at a MAS rate of 60 kHz experimentally for the model compound 1,3,5-tris(2-fluoro-2-methylpropionylamino)benzene. The experimental DQ build-up curves reveal efficiencies scaled by a factor of roughly 0.75. Using this as a correction for simulations, subtle structural details may be probed. Two types of fluorine atoms, differing in their coupling strengths to the next ^{19}F spins can be discriminated.

Acknowledgments

The authors thank the DFG (SFB 840, Project B4) for funding

Appendix A. Supporting information

Supplementary data associated with this article can be found in the online version at <http://dx.doi.org/10.1016/j.ssnmr.2014.12.002>.

References

- [1] E.R. Andrew, A. Bradbury, R.G. Eades, *Nature* 183 (1959) 1802.
- [2] E.R. Andrew, A. Bradbury, R.G. Eades, *Nature* 182 (1958) 1659.
- [3] E.R. Andrew, Magic Angle Spinning, in: *eMagRes*, John Wiley & Sons, Ltd, 2007, <http://dx.doi.org/10.1002/9780470034590.emrstm0283>.
- [4] J.C. Facelli, A.M. Orendt, Magnetic Shielding and Chemical Shifts: Basics, in: *eMagRes*, John Wiley & Sons, Ltd, 2007, <http://dx.doi.org/10.1002/9780470034590.emrstm1056>.
- [5] C. Martineau, J. Senker, F. Taulelle, NMR Crystallography, in: *Annu. Rep. NMR Spectrosc.*, pp. 1–57, <http://dx.doi.org/10.1016/B978-0-12-800184-4.00001-1>.
- [6] B. Lotsch, M. Döblinger, J. Sehnert, L. Seyfarth, J. Senker, O. Oeckler, W. Schnick, *Chem. Eur. J.* 13 (2007) 4969–4980.
- [7] M. Schmidt, C.S. Zehe, R. Siegel, J.U. Heigl, C. Steinlein, H.-W. Schmidt, J. Senker, *CrystEngComm* 15 (2013) 8784.
- [8] J.M. Griffiths, A.E. Bennett, R.G. Griffin, Homonuclear Recoupling Schemes in MAS NMR, in: *eMagRes*, John Wiley & Sons, Ltd, 2007, <http://dx.doi.org/10.1002/9780470034590.emrstm0214>.
- [9] R. Tycko, Dipolar Recoupling: Homonuclear Experiments, in: *eMagRes*, John Wiley & Sons, Ltd, 2007, <http://dx.doi.org/10.1002/9780470034590.emrstm1070>.
- [10] M.H. Levitt, Symmetry-Based Pulse Sequences in Magic-Angle Spinning Solid-State NMR, in: *eMagRes*, John Wiley & Sons, Ltd, 2007, <http://dx.doi.org/10.1002/9780470034590.emrstm0551>.
- [11] T. Gullion, J. Schaefer, *J. Magn. Reson.* 213 (2011) 421.
- [12] Y. Ishii, *J. Chem. Phys.* 114 (2001) 8473.
- [13] M. Feike, D.E. Demco, R. Graf, J. Gottwald, S. Hafner, H.W. Spiess, *J. Magn. Reson., Ser. A* 122 (1996) 214.
- [14] M. Hohwy, H.J. Jakobsen, M. Edén, M.H. Levitt, N.C. Nielsen, *J. Chem. Phys.* 108 (1998) 2686.
- [15] M. Carravetta, M. Edén, X. Zhao, A. Brinkmann, M.H. Levitt, *Chem. Phys. Lett.* 321 (2000) 205.
- [16] M.H. Levitt, *J. Chem. Phys.* 128 (2008) 52205.
- [17] P.E. Kristiansen, M. Carravetta, J.D. van Beek, W.C. Lai, M.H. Levitt, *J. Chem. Phys.* 124 (2006) 234510.
- [18] D.H. Brouwer, P.E. Kristiansen, C.A. Fyfe, M.H. Levitt, *J. Am. Chem. Soc.* 127 (2005) 542.
- [19] M. Carravetta, M. Edén, O.G. Johannessen, H. Luthman, P.J.E. Verdegem, J. Lugtenburg, A. Sebald, M.H. Levitt, *J. Am. Chem. Soc.* 123 (2001) 10628.
- [20] Y.K. Lee, N.D. Kurur, M. Helmle, O.G. Johannessen, N.C. Nielsen, M.H. Levitt, *Chem. Phys. Lett.* 242 (1995) 304.
- [21] D.H. Brouwer, R.J. Dorton, R.E. Morris, M.H. Levitt, *J. Am. Chem. Soc.* 127 (2005) 10365.
- [22] L. Seyfarth, J. Senker, *Phys. Chem. Chem. Phys.* 11 (2009) 3522.
- [23] C. Zehe, M. Schmidt, R. Siegel, K. Kreger, V. Daebel, S. Ganzleben, H.-W. Schmidt, J. Senker, *CrystEngComm* (2014).
- [24] S.P. Brown, I. Schnell, J.D. Brand, K. Müllen, H.W. Spiess, *J. Am. Chem. Soc.* 121 (1999) 6712.
- [25] L. Seyfarth, J. Seyfarth, B. Lotsch, W. Schnick, J. Senker, *Phys. Chem. Chem. Phys.* 12 (2010) 2227.
- [26] R. Graf, D.E. Demco, S. Hafner, H.W. Spiess, *Solid State Nucl. Magn. Reson.* 12 (1998) 139.
- [27] N.J.L. Rodriguez, S.M. De Paul, C.J. Barrett, L. Reven, H.W. Spiess, *Adv. Mater.* 2 (2000) 1934.
- [28] J.P. Bradley, C. Tripon, C. Filip, S.P. Brown, *Phys. Chem. Chem. Phys.* 11 (2009) 6941.
- [29] L. Mafra, R. Siegel, C. Fernandez, D. Schneider, F. Aussenac, J. Rocha, *J. Magn. Reson.* 199 (2009) 111.
- [30] Q. Wang, B. Hu, F. Fayon, J. Trebosc, C. Legein, O. Lafon, F. Deng, J.-P. Amoureux, *Phys. Chem. Chem. Phys.* 11 (2009) 10391.
- [31] Q. Wang, B. Hu, O. Lafon, J. Trébosc, F. Deng, J.-P. Amoureux, *J. Magn. Reson.* 203 (2010) 113.
- [32] C. Martineau, C. Legein, J.-Y. Buzaré, F. Fayon, *Phys. Chem. Chem. Phys.* 11 (2009) 950.
- [33] C. Jäger, M. Feike, Born, H.-W. Spiess, *J. Non-Cryst. Solids* 180 (1994) 91.
- [34] B. Hu, L. Delevoye, O. Lafon, J. Trébosc, J.P. Amoureux, *J. Magn. Reson.* 200 (2009) 178.
- [35] R.E. Wasylshen, Dipolar and Indirect Coupling: Basics, in: *eMagRes*, John Wiley & Sons, Ltd, 2007, <http://dx.doi.org/10.1002/9780470034590.emrstm1023>.
- [36] M. Deschamps, Ultrafast Magic Angle Spinning Nuclear Magnetic Resonance, in: *Annu. Rep. NMR Spectrosc.*, pp. 109–144, <http://dx.doi.org/10.1016/B978-0-12-800185-1.00003-6>.
- [37] S. Laage, J.R. Sachleben, S. Steuernagel, R. Pierattelli, G. Pintacuda, L. Emsley, *J. Magn. Reson.* 196 (2009) 133.
- [38] T. Karlsson, A. Brinkmann, P.J.E. Verdegem, J. Lugtenburg, M.H. Levitt, *Solid State Nucl. Magn. Reson.* 14 (1999) 43.
- [39] M. Edén, M.H. Levitt, *J. Chem. Phys.* 111 (1999) 1511.
- [40] I. Marin-Montesinos, D.H. Brouwer, G. Antonoli, W.C. Lai, A. Brinkmann, M.H. Levitt, *J. Magn. Reson.* 177 (2005) 307.
- [41] C.E. Hughes, S. Luca, M. Balducci, *Chem. Phys. Lett.* 385 (2004) 435.
- [42] M. Weingarth, G. Bodenhausen, P. Tekely, *Chem. Phys. Lett.* 502 (2011) 259.
- [43] M. Ernst, A. Samoson, B.H. Meier, *J. Magn. Reson.* 163 (2003) 332.
- [44] A.E. Bennett, C.M. Rienstra, M. Auger, K.V. Lakshmi, R.G. Griffin, *J. Chem. Phys.* 103 (1995) 6951.
- [45] B.M. Fung, A.K. Khitrin, K. Ermolaev, *J. Magn. Reson.* 142 (2000) 97.
- [46] K.O. Tan, I. Scholz, J.D. van Beek, B.H. Meier, M. Ernst, *J. Magn. Reson.* 239 (2014) 61.
- [47] Y. Ishii, J. Ashida, T. Terao, *Chem. Phys. Lett.* 246 (1995) 439.
- [48] C.M. Rienstra, M.E. Hatcher, L.J. Mueller, Sun, S.W. Fesik, R.G. Griffin, *J. Am. Chem. Soc.* 120, 199810602.
- [49] P.E. Kristiansen, D.J. Mitchell, J.N.S. Evans, *J. Magn. Reson.* 157 (2002) 253.
- [50] S.A. Carss, R.K. Harris, P. Holstein, B.J. Say, R.A. Fletton, *J. Chem. Soc., Chem. Commun.* (1994) 2407.
- [51] S.A. Carss, U. Scheler, R.K. Harris, P. Holstein, R.A. Fletton, *Magn. Reson. Chem.* 34 (1996) 63.
- [52] R.K. Harris, S.A. Carss, R.D. Chambers, P. Holstein, A.P. Minoja, U. Scheler, *Bull. Magn. Reson.* 17 (1995) 37.
- [53] E.W. Hagaman, *J. Magn. Reson.* 104A (1993) 125.
- [54] P.E. Kristiansen, M. Carravetta, W.C. Lai, M.H. Levitt, *Chem. Phys. Lett.* 390 (2004) 1.
- [55] The MathWorks, Inc., MATLAB 2014a, Natick, Massachusetts, United States, 2014.
- [56] M. Bak, J.T. Rasmussen, N.C. Nielsen, *J. Magn. Reson.* 147 (2000) 296.
- [57] Z. Tošner, R. Andersen, B. Stevansson, M. Edén, Nielsen, Niels Chr. T. Vosegaard, *J. Magn. Reson.* 246 (2014) 79.
- [58] V.B. Cheng, *J. Chem. Phys.* 59 (1973) 3992.
- [59] H. Conroy, *J. Chem. Phys.* 47 (1967) 5307.
- [60] S.K. Zaremba, *Annali di Matematica Pura ed Applicata* 73 (1966) 293.
- [61] K. Sälwächter, *Chem. Phys. Chem.* 14 (2013) 3000.
- [62] V.E. Zorin, S.P. Brown, P. Hodgkinson, *Mol. Phys.* 104 (2006) 293.

Electronic Supplementary Information

to

Influence of Proton Coupling on Symmetry-Based Homonuclear ^{19}F Dipolar Recoupling Experiments

Christoph Zehe,^[a] Renée Siegel^[a] and Jürgen Senker^{*[a]}

[a] Inorganic Chemistry III and Bayreuth Center for Colloids and Interfaces, University of Bayreuth, 95447, Bayreuth, Germany; E-mail: juergen.senker@uni-bayreuth.de; Tel: (+49) 921-55-2788;

Input files for simulations with SIMPSON

In the following, the input file used for simulations of build-up curves are given. Hereby, the selection of double-quantum coherences after excitation and before reconversion is facilitated by an appropriate filter. Due to the absence of relaxation in these simulations, the curves can be normalised by dividing through a factor $0.25 \cdot (2^N)$, where N is the number of spins in the spin system.

Par and main section for R and SR sequences with cw decoupling during recoupling:

```

par {
    variable N          [N].
    variable n          [n]
    variable nu         [nu]
    start_operator      Inz
    detect_operator     I1p
    spin_rate           [MAS spinning frequency]
    gamma_angles        40
    crystal_file        zcw232
    np                  80
    proton_frequency    600e6
    verbose             11110
    variable l1         np-1
    variable cw         [cw nutation frequency]
}

proc main {} {
    global par
    set f [fsimpson]
    fexpr $f {$re} {$sim}
    fsave $f $par(name).dat -xreim
}

```

pulseq section for R sequences with cw decoupling during recoupling:

```

proc pulseq {} {
    global par
    maxdt 1.0
    set rf [expr $par(spin_rate)*$par(N)/$par(n)]
    set p90 [expr 0.25e6/$rf]
    set p270 [expr 0.75e6/$rf]
    set ph90R [expr 180.00*$par(nu)/$par(N)]
    set ph270R [expr 180.00*$par(nu)/$par(N)+180.00]
    set ph90Rs [expr (-1)*180.00/$par(N)*$par(nu)+360]
    set ph270Rs [expr (-1)*180.00/$par(N)*$par(nu)+180.00]

    reset
    for {set m 1} {$m<= [expr $par(N)/2]} {incr m 1} {
        pulse $p90 $rf $ph90R $par(cw) 0
    }
}

```

4 Publications

```
        pulse $p270 $rf $ph270R $par(cw) 0
        pulse $p90 $rf $ph90Rs $par(cw) 0
        pulse $p270 $rf $ph270Rs $par(cw) 0
    }
    store 1

    reset
    acq
    reset

    for {set n 1} {$n<=$par(11)} {incr n 1} {
        prop 1
        store 9
        matrix set 1 totalcoherence {-2 2}
        filter 1
        prop 9
        matrix set 2 totalcoherence {0}
        filter 2
        pulseid 1 250000 -y 0 0
        acq
        reset
        prop 9
    }
}
```

pulseq section for SR sequences with cw decoupling during recoupling:

```

proc pulseq {} {
  global par
  maxdt 1.0
  set rf [expr $par(spin_rate)*$par(N)/$par(n)]
  set p90 [expr 0.25e6/$rf]
  set p270 [expr 0.75e6/$rf]
  set ph10 [expr 180.00*$par(nu)/$par(N)]
  set ph11 [expr 180.00*$par(nu)/$par(N)+180.00]
  set ph12 [expr (-1)*180.00/$par(N)*$par(nu)+360]
  set ph13 [expr (-1)*180.00/$par(N)*$par(nu)+180.00]

  reset
  for {set n 0} {$n < [expr $par(N)/2]} {incr n} {
    pulse $p90 $rf $ph10 $par(cw) 0
    pulse $p270 $rf $ph11 $par(cw) 0
    pulse $p90 $rf $ph12 $par(cw) 0
    pulse $p270 $rf $ph13 $par(cw) 0
  }
  for {set n 0} {$n < [expr $par(N)/2]} {incr n} {
    pulse $p90 $rf $ph12 $par(cw) 0
    pulse $p270 $rf $ph13 $par(cw) 0
    pulse $p90 $rf $ph10 $par(cw) 0
    pulse $p270 $rf $ph11 $par(cw) 0
  }
  store 2

  reset
  for {set n 0} {$n < [expr $par(N)/2]} {incr n} {
    pulse $p90 $rf $ph13 $par(cw) 0
    pulse $p270 $rf $ph12 $par(cw) 0
    pulse $p90 $rf $ph11 $par(cw) 0
    pulse $p270 $rf $ph10 $par(cw) 0
  }
  for {set n 0} {$n < [expr $par(N)/2]} {incr n} {
    pulse $p90 $rf $ph11 $par(cw) 0
    pulse $p270 $rf $ph10 $par(cw) 0
    pulse $p90 $rf $ph13 $par(cw) 0
    pulse $p270 $rf $ph12 $par(cw) 0
  }
  store 1

  reset
  acq
  reset

```

4 Publications

```
for {set n 1} {$n<=$par(11)} {incr n 1} {  
  prop [expr $n % 2 + 1]  
  store 9  
  matrix set 1 totalcoherence {-2 2}  
  filter 1  
  prop 9  
  matrix set 2 totalcoherence {0}  
  filter 2  
  pulseid 1 250000 -y 0 0  
  acq  
  reset  
  prop 9  
}  
}
```

Spinsys section for model a):

```

spinsys {
  nuclei 19F 19F 1H 1H 1H 1H
  channels 19F 1H
  shift 1 0.0p -25.0p 0.45 0.0 0.0 0.0
  shift 2 0.0p -25.0p 0.45 0.0 0.0 0.0
  dipole 1 2 -1750.14958968 180.0 34.4066476848 -60.9200471646
  dipole 1 3 -12209.0 180.0 78.5327174345 53.0044794181
  dipole 1 4 -10619.0 180.0 106.57999128 9.79527094101
  dipole 1 5 -6433.2 180.0 137.698605112 42.1263749075
  dipole 1 6 -6433.2 180.0 108.693316564 -39.2195461318
  dipole 2 3 -12209.0 180.0 108.830830522 71.4357131042
  dipole 2 4 -12971.0 180.0 124.99295002 24.3821383787
  dipole 2 5 -6433.2 180.0 146.979105514 68.6292668668
  dipole 2 6 -6433.2 180.0 144.661100591 -26.2059834011
  dipole 3 4 -15015.0 180.0 106.359751429 -21.4063752612
  dipole 3 5 -24450.0 180.0 163.15118707 -79.9892043967
  dipole 3 6 -12971.0 180.0 110.752061711 -80.9376205172
  dipole 4 5 -15015.0 180.0 107.94746913 11.8377271408
  dipole 4 6 -12971.0 180.0 91.8378533948 -25.0148346963
  dipole 5 6 -12971.0 180.0 69.8316169166 -76.1946301762
}

```

4 Publications

Spinsys section for model b):

```
spinsys {
  channels 19F
  nuclei 19F 19F 1H 1H 1H 1H 1H 1H 1H
  shift 1 0.0p -25.0p 0.45 0.0 0.0 0.0
  shift 2 0.0p -25.0p 0.45 0.0 0.0 0.0
  dipole 1 2 -1725.92189436 180.0 146.24188899 -61.0457462218
  dipole 1 3 -10000.25820482 180.0 29.0524696541 -65.2639938593
  dipole 1 4 -2000.13052535 180.0 19.4406926277 -4.77823733223
  dipole 1 5 -14000.656535 180.0 114.067701712 -46.8401500407
  dipole 1 6 -6156.39006723 180.0 110.997907447 -21.6138925407
  dipole 1 7 -10066.87583963 180.0 79.4456632114 3.35810169796
  dipole 1 8 -12000.87583963 180.0 20 8
  dipole 1 9 -5000.87583963 180.0 10 90
  dipole 2 3 -1000.143915852 180.0 17.5709023213 25.4137204028
  dipole 2 4 -13380.167733207 180.0 17.8464655679 84.1658968022
  dipole 2 5 -12000.91547557 180.0 44.8459992086 12.7468909108
  dipole 2 6 -4995.91125146 180.0 34.2407828541 39.537587422
  dipole 2 7 -12120.79453235 180.0 34.0541714082 54.5790462354
  dipole 2 8 -5000 180.0 79.4456632114 3.35810169796
  dipole 2 9 -11000.8 180.0 50 44
  dipole 3 4 -20974.1275948 180.0 84.1537732501 37.6871472125
  dipole 3 5 -5000.1618314 180.0 165.803463256 -16.3723275989
  dipole 3 6 -14990.67213802 180.0 138.863902851 5.13974263228
  dipole 3 7 -21810.2888571 180.0 118.725346194 23.1152789434
  dipole 3 8 -15000.87583963 180.0 29 32
  dipole 3 9 -17000.87583963 180.0 33 49
  dipole 4 5 -16340.08381063 180.0 142.696039213 -31.1360566754
  dipole 4 6 -2185.27839342 180.0 154.39377027 -30.5018199722
  dipole 4 7 -10000.38451712 180.0 140.209581296 7.6064987325
  dipole 4 8 -11000.87583963 180.0 88.434 34.543
  dipole 4 9 -9439.87583963 180.0 79.4456632114 3.35810169796
  dipole 5 6 -25280.11007628 180.0 91.5297404383 7.59676392396
  dipole 5 7 -15000.5243361 180.0 72.2532430878 21.8167917474
  dipole 5 8 -12000.87583963 180.0 66.32114 16.9796
  dipole 5 9 -13435.87583963 180.0 44.56632114 45
  dipole 6 7 -21132.3063092 180.0 37.3853389611 76.9797553063
  dipole 6 8 -19000.87583963 180.0 79.4456632114 3.35810169796
  dipole 6 9 -15000.87583963 180.0 79.4456632114 3.35810169796
  dipole 7 8 -16340.08381063 180.0 142.696039213 -31.1360566754
  dipole 7 9 -5000.1618314 180.0 165.803463256 -16.3723275989
  dipole 8 9 -12000.91547557 180.0 44.8459992086 12.7468909108
}
```

Spinsys section for model c):

```

spinsys {
  channels 19F
  nuclei 19F 19F 1H 1H 1H 1H 1H 1H 1H
  shift 1 0.0p -25.0p 0.45 0.0 0.0 0.0
  shift 2 0.0p -25.0p 0.45 0.0 0.0 0.0
  dipole 1 2 -1725.92189436 180.0 146.24188899 -61.0457462218
  dipole 1 3 -10000.25820482 180.0 29.0524696541 -65.2639938593
  dipole 1 4 -2000.13052535 180.0 19.4406926277 -4.77823733223
  dipole 1 5 -14000.656535 180.0 114.067701712 -46.8401500407
  dipole 1 6 -6156.39006723 180.0 110.997907447 -21.6138925407
  dipole 1 7 -10066.87583963 180.0 79.4456632114 3.35810169796
  dipole 1 8 -12000.87583963 180.0 20 8
  dipole 1 9 -5000.87583963 180.0 10 90
  dipole 2 3 -1000.143915852 180.0 17.5709023213 25.4137204028
  dipole 2 4 -13380.167733207 180.0 17.8464655679 84.1658968022
  dipole 2 5 -12000.91547557 180.0 44.8459992086 12.7468909108
  dipole 2 6 -4995.91125146 180.0 34.2407828541 39.537587422
  dipole 2 7 -12120.79453235 180.0 34.0541714082 54.5790462354
  dipole 2 8 -5000 180.0 79.4456632114 3.35810169796
  dipole 2 9 -11000.8 180.0 50 44
  dipole 3 4 -204.1275948 180.0 84.1537732501 37.6871472125
  dipole 3 5 -500.1618314 180.0 165.803463256 -16.3723275989
  dipole 3 6 -140.67213802 180.0 138.863902851 5.13974263228
  dipole 3 7 -2110.2888571 180.0 118.725346194 23.1152789434
  dipole 3 8 -100.87583963 180.0 29 32
  dipole 3 9 -1700.87583963 180.0 33 49
  dipole 4 5 -163.08381063 180.0 142.696039213 -31.1360566754
  dipole 4 6 -218.27839342 180.0 154.39377027 -30.5018199722
  dipole 4 7 -1000.38451712 180.0 140.209581296 7.6064987325
  dipole 4 8 -110.87583963 180.0 88.434 34.543
  dipole 4 9 -943.87583963 180.0 79.4456632114 3.35810169796
  dipole 5 6 -252.11007628 180.0 91.5297404383 7.59676392396
  dipole 5 7 -150.5243361 180.0 72.2532430878 21.8167917474
  dipole 5 8 -1200.87583963 180.0 66.32114 16.9796
  dipole 5 9 -134.87583963 180.0 44.56632114 45
  dipole 6 7 -211.3063092 180.0 37.3853389611 76.9797553063
  dipole 6 8 -1900.87583963 180.0 79.4456632114 3.35810169796
  dipole 6 9 -1500.87583963 180.0 79.4456632114 3.35810169796
  dipole 7 8 -163.08381063 180.0 142.696039213 -31.1360566754
  dipole 7 9 -500.1618314 180.0 165.803463256 -16.3723275989
  dipole 8 9 -120.91547557 180.0 44.8459992086 12.7468909108
}

```

4 Publications

Spinsys section for model d):

```
spinsys {
  channels 19F
  nuclei 19F 19F 1H 1H 1H 1H 1H 1H 1H
  shift 1 0.0p -25.0p 0.45 0.0 0.0 0.0
  shift 2 0.0p -25.0p 0.45 0.0 0.0 0.0
  dipole 1 2 -1725.92201793 180.0 33.7581053402 -61.0457490548
  dipole 1 3 -12544.7669222 180.0 65.9322315967 -46.8403977357
  dipole 1 4 -6156.3891049 180.0 69.0021066146 -21.6138961658
  dipole 1 5 -5384.93780157 180.0 15.1224865905 46.5536656041
  dipole 1 6 -3386.15800378 180.0 19.5644942498 -18.573983311
  dipole 1 7 -8179.83691168 180.0 78.4901688885 63.1266199373
  dipole 1 8 -939.902671562 180.0 31.9240821113 0.351703218058
  dipole 1 9 -6184.12922175 180.0 160.559314107 -4.7782750003
  dipole 2 3 -2790.93321611 180.0 135.154132698 12.7469214406
  dipole 2 4 -4995.90798843 180.0 145.759223805 39.5375592821
  dipole 2 5 -6555.48499346 180.0 103.896504795 76.9201209527
  dipole 2 6 -6244.78382567 180.0 95.4531956298 37.1063547762
  dipole 2 7 -741.917350223 180.0 121.676317254 62.1220797615
  dipole 2 8 -6148.87817823 180.0 69.9234282303 51.3655554353
  dipole 2 9 -508.167697363 180.0 162.153543096 84.1658941902
  dipole 3 4 -20974.1275948 180.0 84.1537732501 37.6871472125
  dipole 3 5 -5000.1618314 180.0 165.803463256 -16.3723275989
  dipole 3 6 -14990.67213802 180.0 138.863902851 5.13974263228
  dipole 3 7 -21810.2888571 180.0 118.725346194 23.1152789434
  dipole 3 8 -15000.87583963 180.0 29 32
  dipole 3 9 -17000.87583963 180.0 33 49
  dipole 4 5 -16340.08381063 180.0 142.696039213 -31.1360566754
  dipole 4 6 -2185.27839342 180.0 154.39377027 -30.5018199722
  dipole 4 7 -10000.38451712 180.0 140.209581296 7.6064987325
  dipole 4 8 -11000.87583963 180.0 88.434 34.543
  dipole 4 9 -9439.87583963 180.0 79.4456632114 3.35810169796
  dipole 5 6 -25280.11007628 180.0 91.5297404383 7.59676392396
  dipole 5 7 -15000.5243361 180.0 72.2532430878 21.8167917474
  dipole 5 8 -12000.87583963 180.0 66.32114 16.9796
  dipole 5 9 -13435.87583963 180.0 44.56632114 45
  dipole 6 7 -21132.3063092 180.0 37.3853389611 76.9797553063
  dipole 6 8 -19000.87583963 180.0 79.4456632114 3.35810169796
  dipole 6 9 -15000.87583963 180.0 79.4456632114 3.35810169796
  dipole 7 8 -16340.08381063 180.0 142.696039213 -31.1360566754
  dipole 7 9 -5000.1618314 180.0 165.803463256 -16.3723275989
  dipole 8 9 -12000.91547557 180.0 44.8459992086 12.7468909108
}
```

Spinsys section for model e):

```

spinsys {
  channels 19F
  nuclei 19F 19F 1H 1H 1H 1H 1H 1H 1H
  shift 1 0.0p -25.0p 0.45 0.0 0.0 0.0
  shift 2 0.0p -25.0p 0.45 0.0 0.0 0.0
  dipole 1 2 -1725.92201793 180.0 33.7581053402 -61.0457490548
  dipole 1 3 -12544.7669222 180.0 65.9322315967 -46.8403977357
  dipole 1 4 -6156.3891049 180.0 69.0021066146 -21.6138961658
  dipole 1 5 -5384.93780157 180.0 15.1224865905 46.5536656041
  dipole 1 6 -3386.15800378 180.0 19.5644942498 -18.573983311
  dipole 1 7 -8179.83691168 180.0 78.4901688885 63.1266199373
  dipole 1 8 -939.902671562 180.0 31.9240821113 0.351703218058
  dipole 1 9 -6184.12922175 180.0 160.559314107 -4.7782750003
  dipole 2 3 -2790.93321611 180.0 135.154132698 12.7469214406
  dipole 2 4 -4995.90798843 180.0 145.759223805 39.5375592821
  dipole 2 5 -6555.48499346 180.0 103.896504795 76.9201209527
  dipole 2 6 -6244.78382567 180.0 95.4531956298 37.1063547762
  dipole 2 7 -741.917350223 180.0 121.676317254 62.1220797615
  dipole 2 8 -6148.87817823 180.0 69.9234282303 51.3655554353
  dipole 2 9 -508.167697363 180.0 162.153543096 84.1658941902
  dipole 3 4 -2528.13110248 180.0 88.4702597121 7.59679397064
  dipole 3 5 -3713.95299692 180.0 55.2932834952 46.7616283599
  dipole 3 6 -8302.22825859 180.0 26.2741719395 75.0894828019
  dipole 3 7 -2776.66490372 180.0 96.0458994499 86.1117945201
  dipole 3 8 -793.510383419 180.0 51.1890292384 19.7269985454
  dipole 3 9 -1634.09023792 180.0 142.696137808 31.1361875474
  dipole 4 5 -5103.04143829 180.0 53.183680386 38.5390562695
  dipole 4 6 -1941.41701865 180.0 58.1302995511 9.66096160087
  dipole 4 7 -1296.06214833 180.0 95.9158563051 41.867364972
  dipole 4 8 -3089.94620422 180.0 16.7640984068 70.8651809525
  dipole 4 9 -2185.27857356 180.0 154.393763877 30.5018018098
  dipole 5 6 -21107.0716985 180.0 78.0101829493 -29.7192270238
  dipole 5 7 -3991.56502512 180.0 134.595164849 45.3151624859
  dipole 5 8 -6405.57352358 180.0 54.9382688827 -13.4652870757
  dipole 5 9 -857.088138372 180.0 172.192017418 -57.540036333
  dipole 6 7 -2723.0407603 180.0 136.305175404 89.0415450929
  dipole 6 8 -2141.69474508 180.0 72.4331443369 5.65204397481
  dipole 6 9 -603.128717865 180.0 160.861255877 8.11801069642
  dipole 7 8 -676.790561506 180.0 48.6870332656 -29.5401728467
  dipole 7 9 -1678.88452276 180.0 135.526319022 -48.2601245167
  dipole 8 9 -366.42889448 180.0 165.396885527 -2.93592222313
}

```

4 Publications

Spinsys section for model f):

```
spinsys {
  channels 19F
  nuclei 19F 19F 1H 1H 1H 1H 1H 1H 1H
  shift 1 0.0p -25.0p 0.45 0.0 0.0 0.0
  shift 2 0.0p -25.0p 0.45 0.0 0.0 0.0
  dipole 1 2 -3000 180.0 146.24188899 -61.0457462218
  dipole 1 3 -10000.25820482 180.0 29.0524696541 -65.2639938593
  dipole 1 4 -2000.13052535 180.0 19.4406926277 -4.77823733223
  dipole 1 5 -14000.656535 180.0 114.067701712 -46.8401500407
  dipole 1 6 -6156.39006723 180.0 110.997907447 -21.6138925407
  dipole 1 7 -10066.87583963 180.0 79.4456632114 3.35810169796
  dipole 1 8 -12000.87583963 180.0 20 8
  dipole 1 9 -5000.87583963 180.0 10 90
  dipole 2 3 -1000.143915852 180.0 17.5709023213 25.4137204028
  dipole 2 4 -13380.167733207 180.0 17.8464655679 84.1658968022
  dipole 2 5 -12000.91547557 180.0 44.8459992086 12.7468909108
  dipole 2 6 -4995.91125146 180.0 34.2407828541 39.537587422
  dipole 2 7 -12120.79453235 180.0 34.0541714082 54.5790462354
  dipole 2 8 -5000 180.0 79.4456632114 3.35810169796
  dipole 2 9 -11000.8 180.0 50 44
  dipole 3 4 -20974.1275948 180.0 84.1537732501 37.6871472125
  dipole 3 5 -5000.1618314 180.0 165.803463256 -16.3723275989
  dipole 3 6 -14990.67213802 180.0 138.863902851 5.13974263228
  dipole 3 7 -21810.2888571 180.0 118.725346194 23.1152789434
  dipole 3 8 -15000.87583963 180.0 29 32
  dipole 3 9 -17000.87583963 180.0 33 49
  dipole 4 5 -16340.08381063 180.0 142.696039213 -31.1360566754
  dipole 4 6 -2185.27839342 180.0 154.39377027 -30.5018199722
  dipole 4 7 -10000.38451712 180.0 140.209581296 7.6064987325
  dipole 4 8 -11000.87583963 180.0 88.434 34.543
  dipole 4 9 -9439.87583963 180.0 79.4456632114 3.35810169796
  dipole 5 6 -25280.11007628 180.0 91.5297404383 7.59676392396
  dipole 5 7 -15000.5243361 180.0 72.2532430878 21.8167917474
  dipole 5 8 -12000.87583963 180.0 66.32114 16.9796
  dipole 5 9 -13435.87583963 180.0 44.56632114 45
  dipole 6 7 -21132.3063092 180.0 37.3853389611 76.9797553063
  dipole 6 8 -19000.87583963 180.0 79.4456632114 3.35810169796
  dipole 6 9 -15000.87583963 180.0 79.4456632114 3.35810169796
  dipole 7 8 -16340.08381063 180.0 142.696039213 -31.1360566754
  dipole 7 9 -5000.1618314 180.0 165.803463256 -16.3723275989
  dipole 8 9 -12000.91547557 180.0 44.8459992086 12.7468909108
}
```

Spinsys section for model g):

```

spinsys {
  channels 19F
  nuclei 19F 19F 1H 1H 1H 1H 1H 1H 1H
  shift 1 0.0p -25.0p 0.45 0.0 0.0 0.0
  shift 2 0.0p -25.0p 0.45 0.0 0.0 0.0
  dipole 1 2 -1000 180.0 146.24188899 -61.0457462218
  dipole 1 3 -10000.25820482 180.0 29.0524696541 -65.2639938593
  dipole 1 4 -2000.13052535 180.0 19.4406926277 -4.77823733223
  dipole 1 5 -14000.656535 180.0 114.067701712 -46.8401500407
  dipole 1 6 -6156.39006723 180.0 110.997907447 -21.6138925407
  dipole 1 7 -10066.87583963 180.0 79.4456632114 3.35810169796
  dipole 1 8 -12000.87583963 180.0 20 8
  dipole 1 9 -5000.87583963 180.0 10 90
  dipole 2 3 -1000.143915852 180.0 17.5709023213 25.4137204028
  dipole 2 4 -13380.167733207 180.0 17.8464655679 84.1658968022
  dipole 2 5 -12000.91547557 180.0 44.8459992086 12.7468909108
  dipole 2 6 -4995.91125146 180.0 34.2407828541 39.537587422
  dipole 2 7 -12120.79453235 180.0 34.0541714082 54.5790462354
  dipole 2 8 -5000 180.0 79.4456632114 3.35810169796
  dipole 2 9 -11000.8 180.0 50 44
  dipole 3 4 -20974.1275948 180.0 84.1537732501 37.6871472125
  dipole 3 5 -5000.1618314 180.0 165.803463256 -16.3723275989
  dipole 3 6 -14990.67213802 180.0 138.863902851 5.13974263228
  dipole 3 7 -21810.2888571 180.0 118.725346194 23.1152789434
  dipole 3 8 -15000.87583963 180.0 29 32
  dipole 3 9 -17000.87583963 180.0 33 49
  dipole 4 5 -16340.08381063 180.0 142.696039213 -31.1360566754
  dipole 4 6 -2185.27839342 180.0 154.39377027 -30.5018199722
  dipole 4 7 -10000.38451712 180.0 140.209581296 7.6064987325
  dipole 4 8 -11000.87583963 180.0 88.434 34.543
  dipole 4 9 -9439.87583963 180.0 79.4456632114 3.35810169796
  dipole 5 6 -25280.11007628 180.0 91.5297404383 7.59676392396
  dipole 5 7 -15000.5243361 180.0 72.2532430878 21.8167917474
  dipole 5 8 -12000.87583963 180.0 66.32114 16.9796
  dipole 5 9 -13435.87583963 180.0 44.56632114 45
  dipole 6 7 -21132.3063092 180.0 37.3853389611 76.9797553063
  dipole 6 8 -19000.87583963 180.0 79.4456632114 3.35810169796
  dipole 6 9 -15000.87583963 180.0 79.4456632114 3.35810169796
  dipole 7 8 -16340.08381063 180.0 142.696039213 -31.1360566754
  dipole 7 9 -5000.1618314 180.0 165.803463256 -16.3723275989
  dipole 8 9 -12000.91547557 180.0 44.8459992086 12.7468909108
}

```


4.4 Mesoscale Polarisation *via* Geometric Frustration in Supramolecular Crystals

This work is the result of a cooperation between the Inorganic Chemistry III and the Macromolecular Chemistry I of the University of Bayreuth and the Inorganic Chemistry Laboratory of the University of Oxford. My contributions are:

- conception and main authorship of the article
- preparation of single-crystals
- conduction of all X-ray diffraction experiments and simulations
- conduction of all single-crystal structure solutions and refinements
- development of FORTRAN code for Monte-Carlo simulation of Ising models
- conduction of all quantum-chemical calculations

The contributions of all other authors are:

- conception and co-authorship of the study
- synthesis and characterisation of all chemical compounds
- support of diffraction experiments and simulations
- support of structure solutions and refinements
- support of evaluation of all data

**Mesoscale Polarisation *via* Geometric Frustration in
Columnar Supramolecular Crystals**

Christoph S. Zehe¹, Joshua A. Hill², Nicholas P. Funnell^{2,3},
Klaus Kreger⁴, Kasper P. van der Zwan¹, Andrew L. Goodwin^{2*},
Hans-Werner Schmidt^{4*}, Jürgen Senker^{1*}

¹Inorganic Chemistry III, Universitätsstrasse 30, University of Bayreuth, 95447, Bayreuth,
Germany,

²Department of Chemistry, University of Oxford, Inorganic Chemistry Laboratory, South
Parks Road, Oxford OX1 3QR, UK,

³Current address: ISIS, Rutherford Appleton Laboratory, Chilton, Didcot OX11 0QX, UK,

⁴Macromolecular Chemistry I, Universitätsstrasse 30, University of Bayreuth, 95447,
Bayreuth, Germany.

*To whom correspondence should be addressed;

Email: juergen.senker@uni-bayreuth.de, andrew.goodwin@chem.ox.ac.uk, hans-
werner.schmidt@uni-bayreuth.de.

Columnar supramolecular phases with polarisation along the columnar axis have potential for the development of ultrahigh density memories, since every single column might function as a memory element. By investigating structure and disorder for four columnar benzene-1,3,5-trisamides by total X-ray scattering and DFT calculations, we demonstrate that the column orientation and thus the columnar dipole moment is receptive to geometric frustration if the columns aggregate in a hexagonal rod packing. The frustration suppresses conventional antiferroelectric order and heightens the sensitivity towards collective intercolumnar packing effects. The latter finding allows for building-up mesoscale domains with spontaneous polarisation. Our results suggest how the complex interplay between steric and electrostatic interactions is influenced by a straightforward chemical design of the molecular synthons, in order to create spontaneous polarisation and to adjust the mesoscale domain sizes.

Organic materials featuring ferroelectric polarisation^[1] are attractive candidates for easily processible and low-cost electric sensors,^[2] electro-optics^[3] as well as non-volatile memory devices.^[4] The fundamental requirements for these materials is spontaneous and switchable polarisation. In supramolecular solids^[1,3] and liquid crystalline (LC) phases^[5] the latter is generally induced by ordering either permanent molecular dipoles or supramolecular dipole moments that are generated or enhanced by the assembly.^[6] In particular materials with polarisation along the columnar axis (referred to as axially polar) have gained increasing interest due to their potential applicability for ultrahigh density memories, where individual columns might ultimately constitute as memory elements.^[7,8]

Recently, the first example of an intrinsically ferroelectric, axially polar LC with remnant polarisation of $1.7 \mu\text{C}/\text{cm}^2$ was obtained by columnar stackings of a phthalonitrile derivative.^[9] Kemerink and Sijbesma et al. reported similar polarisation of up to $2 \mu\text{C}/\text{cm}^2$ for thin films of oriented LCs^[10] consisting of benzene-1,3,5-trisamides (BTAs)^[11] with long aliphatic side groups. Although the polarisation could be induced and switched by electric fields, its stabilisation was possible by freezing the LC state only.^[10,11] Therefore, one of the biggest challenges for axially polar materials still is the creation and the control of spontaneous polarisation without applying external stimuli. The latter requires a counterbalance of the electrostatic interaction between the dipoles of neighbouring columns in a side by side arrangement, which inevitably favours anti-alignment of the columnar polarisation, resulting in non-polar phases.^[3] Hence, suitable columnar materials with spontaneous and stable polarisation are rare up to now, and for the few observed cases^[8] its emergence remains unexplained.^[7-9,12-14]

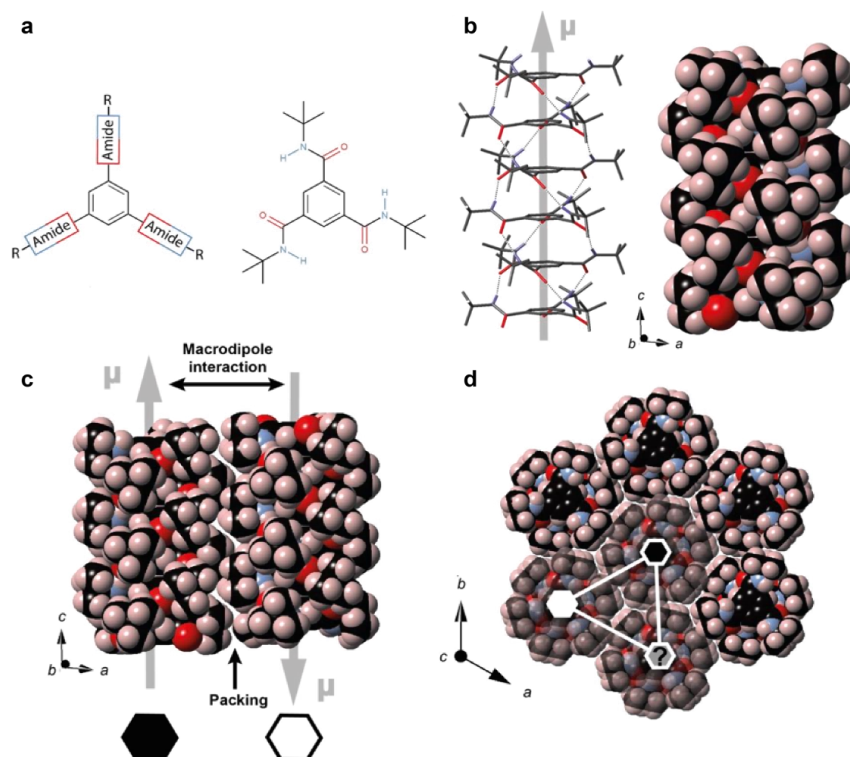


Figure 1. a) Basic design scheme of BTAs consisting of a benzene core linked by amide bonds in 1,3,5-position to peripheral groups (denoted as R), e.g. *tert*-butyl. b) Side-view of a columnar stack of six BTA molecules (left) where the hydrogen bonds are indicated as dotted lines (all non-NH protons are omitted for clarity). The macrodipole is highlighted as grey arrow. A space-filling model of the same stack is depicted on the right. c) Side view on two columns in antiparallel orientation, where the direction of the macrodipole is symbolised by a black and a white hexagon. d) Top view on an ensemble of seven stacks in a hexagonal rod packing indicating possible geometric frustration.

Here, we present a structural study of four purposely synthesised BTAs with the aim to investigate the origin of spontaneous polarisation for axially polar systems in their solid state, which offers the unique possibility to study dipole order solely governed by intrinsic interactions. In general, BTAs are based on a benzene core, which is linked to peripheral groups *via* three amide bonds in 1,3,5-positions (Figure 1a). The formation of threefold intermolecular hydrogen bonds in a helical arrangement drives the molecular self-assembly into well-ordered columns (Figure 1b, left), which aligns all carbonyl bonds in the same direction along the columnar axis. The individual dipole moments of these bonds sum up to macrodipoles^[10] along the columnar axis (Figure 1b, left). In a side by side arrangement of two

columns, the electrostatic interaction prefers anti-alignment of the macrodipoles (Figure 1c). Simultaneously, the peripheral groups give rise to a corrugated surface topography of the supramolecular aggregates (Figure 1b, right), imposing steric restraints (Figure 1c), which may favour parallel or antiparallel arrangements depending on subtle structural details of the peripheral groups. As van der Waals forces impose neighbouring columns to pack as densely as possible, often hexagonal rod packings^[14] are induced (Figure 1d). In those, however, the macrodipole interaction between neighbouring columns becomes frustrated, as it is not possible to simultaneously align all dipoles antiparallel relative to their nearest neighbours (Figure 1d). This frustration reduces the contribution of macrodipole interactions to the lattice energy and thus amplifies the influence of steric restraints. If the latter favours parallel alignments of neighbouring columns, stable ferroelectric domains should be feasible for axially polar materials.

Based on this model, compounds **1** – **4** (Figure 2a) were selected, for which we expect a varying ratio of macrodipole and steric interactions. Single crystals were grown either by solvent evaporation or by sublimation and analysed by single-crystal X-ray diffraction (crystallographic details are given in section 2 of the Supporting Information). All four BTAs crystallise in hexagonal rod packings (Figure 2b), which is in agreement with previous studies on **1**^[15] and **2**^[16]. While **1**, **2** and **4** exhibit similar intercolumnar distances d_{cc} of 14.1 Å, 14.5 Å and 13.9 Å, the longer peripheral groups of **3** increase d_{cc} to 17.1 Å. The C=O centred linkages of **1** and **3** feature higher torsional flexibility of the amide groups with mean side chain torsions $\Phi(\text{C}_{ar}\text{C}_{ar}\text{C}_{o}\text{O})$ of 39.5° (**1**) and 34.6° (**3**) compared to the N centred systems with $\Phi(\text{C}_{ar}\text{C}_{ar}\text{C}_{o}\text{O})$ of about 35.1° (**2**) and 23.7° (**4**). Larger torsion angles cause a steeper inclination of the C=O bonds towards the columnar axis and will thus lead to larger macrodipoles.

To derive a more quantitative picture of the macrodipole strengths, we estimated the average molecular dipole moments p representative for the columnar dipole for the smaller molecules **1**, **2** and **4** by quantum chemical calculations on finite clusters taken from the single-crystal structure solutions (section 3 of Supporting Information). In line with the structural considerations, p amounts to 12 D and 11 D for **1** and **2** and to 6.5 D for **4**. For the latter, p is reduced further due to anti-alignment of the C-F and C=O bonds induced by intramolecular NH...F hydrogen bonds (Figures 2a,b and S4b).^[17] In case of **3**, we expect a value close to the one derived for **2**, since their mean torsion angles are similar. As a consequence, the strongest macrodipole interactions arise for **1** ($p = 12$ D; $d_{cc} = 14.1$ Å), closely followed by **2** (11 D; 14.5 Å) and a significant reduction for **3** (11 D; 17.1 Å) due to the larger d_{cc} and **4** (6.5 D; 13.9 Å) based on the smaller p .

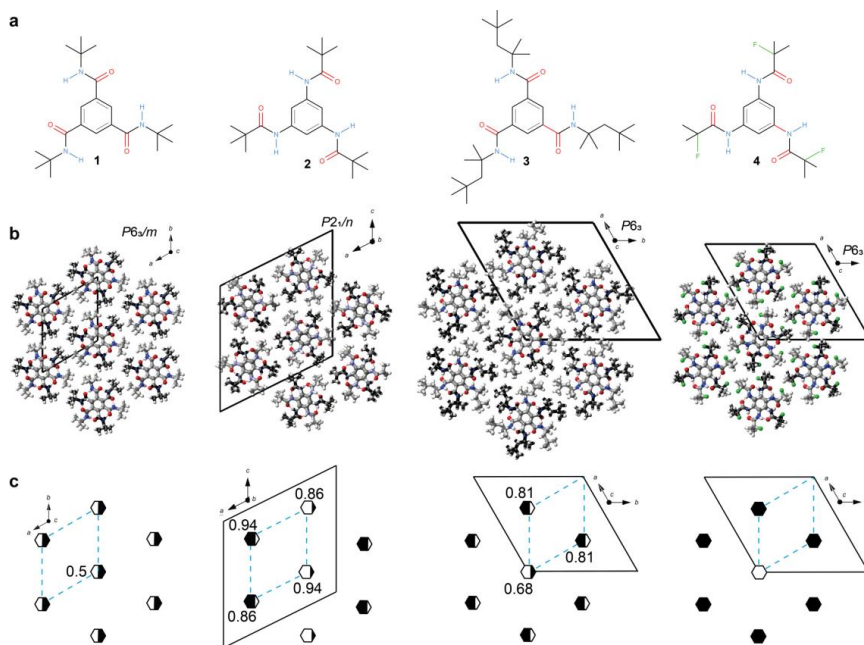


Figure 2. a) Sketches of the BTA molecules **1** – **4**. b) Bragg structure solutions viewed along the direction of molecular stacks, coinciding with the direction of the polar axis of the indicated space groups. c) Schematic representation of b) with the probabilities of up- and down-oriented columns within one stack (major components is displayed), which are additionally symbolised by the amount of black and white in each hexagon. The dashed blue line indicates the unit cell corresponding to the underlying hexagonal or pseudo-hexagonal (in case of **2**) lattice, whereas the black solid lines demark the unit cells found by single-crystal X-ray diffraction.

Remarkably, for **1** (ref. [15]), **2** and **3** each stack appears as a superposition of two columns with opposite macrodipole orientations in the conventional structure solution (Figure 2c). As Bragg diffraction arises from spatially averaged electron density within the coherence length of the X-ray beam (≈ 100 nm), this reflects disorder of the macrodipole orientations in individual unit cells.^[18] For **1**, both orientations are equally present (Figure 2c) and hence on average each stack bears a 50% probability to be either in the up or the down state. In contrast, we observed superstructures with a stripe-type macrodipole arrangement for **2** and with a honeycomb pattern for **3** and **4** (Figure 2c). For the latter BTAs, in each stack one column orientation is more likely as indicated by the colour code presented in Figure 2c. Nevertheless, the unit cells of **1** and **2** contain no net macrodipole moment since an equal part of up- and down-oriented columns are present. For **3** and **4**, the unit cells contain an excess of one orientation leading to a net polarisation along the direction of the columnar axis.

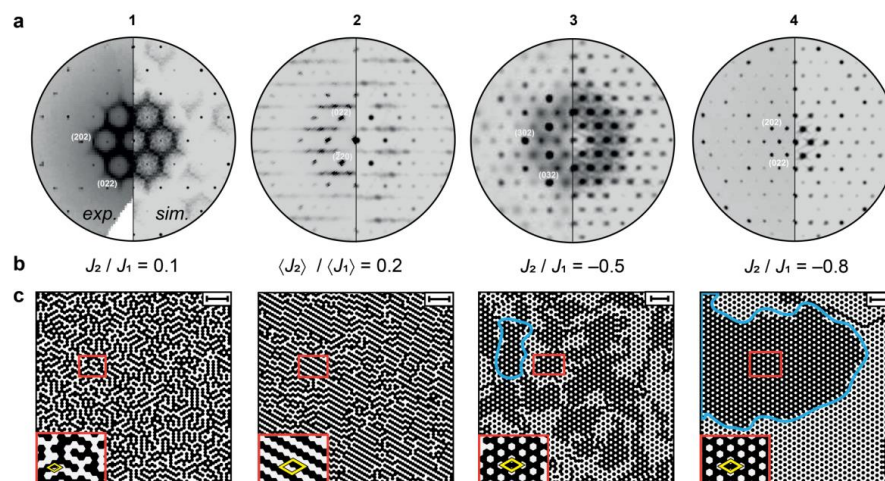


Figure 3. a) The $hk2$ planes for **1**, **3** and **4** and $h2k$ plane for **2** of the reciprocal space, together with simulations (experimental picture of **1** taken from ref. [15]). These planes are perpendicular to the stacking direction. b) Ratios for the refined coupling constants J_1 and J_2 of the Ising model simulations for **1** – **4**. Due to the reduced crystallographic symmetry in case of **2**, average values are given (Figure S1, SI). All constants are normalised according to $J_1/kT = 1$ with T being the simulation temperature. c) Resulting arrangement of up- and down-oriented macrodipoles over approximately 70×70 columns. The red boxes contain magnifications of local features, where the crystallographic unit cells (Figure 2b) are indicated in yellow. The blue lines emphasise domains exhibiting net polarisation for **3** and **4** and the scale bars in the top left corners correspond to a distance of 10 nm.

Additionally to the sharp Bragg reflections, selected layers of the reciprocal space exhibit intense structured diffuse scattering for compounds **1**, **2** and **3** (Figure 3a).^[18] In all cases, the diffuse intensities are confined to layers perpendicular to the stacking direction (Figure S2, SI). The diffuse scattering explains the disorder for up- and down-oriented columns as described above and depicted in Figure 2c and suggests deviations from the average structures for neighbouring columns within a coherence length smaller than 100 nm. In contrast, the columns are rather well ordered along the stacking direction on significantly larger length scales. To develop models reproducing the observed diffuse scattering pattern, we found it sufficient to position supramolecular columns in a hexagonal rod packing, with only the up- and down orientation of the macrodipoles subject to disorder, while the packing along the stacking direction is ordered over the whole column. We then predict ferroelectric and antiferroelectric alignments of neighbouring macrodipoles based on a 2D Ising model.^[19] Here, the energy of the system is defined based on two effective coupling constants J_1 and J_2 describing the sum of both the electrostatic and steric interactions between nearest neighbour (n.n.) and next-

4 Publications

nearest neighbour (n.n.n.) columns.^[19] J_1 and J_2 are subsequently varied until the best match between simulated and experimental diffraction patterns (Figures 3a and 3b) is reached. For a description of the technical procedure see section 1.4 of the Supporting Information.

The resulting arrangements of up and down oriented macrodipoles (Figure 3c) reproduce the diffuse scattering pattern (Figure 3a) in an almost perfect agreement. **1** and **2** both exhibit disorder on a local scale with preferential stripe-type antiferroelectric arrangements between neighbouring columns. In contrast, for **3** and **4**, mesoscale domains with a honeycomb structure carrying spontaneous polarisation are formed. While the average domain size is on the order of 20 – 30 nm for **3**, the domains become significantly larger (50 – 70 nm) for **4**. The excellent match between observed and simulated X-ray powder diffraction data (Figure S5-S8, SI), furthermore, demonstrates that both the disorder and the mesoscale domain formation are inherent properties of the bulk materials. Although domains with spontaneous polarisation have been suggested for axially polar phases before,^[7-9,12,20] our data provide the first experimental evidence for their existence. For such small domains other common methods, such as the second harmonic generation effect, are inconclusive^[21] or change the domain structure as for pyroelectric measurements. In our case, total scattering proves to be the method of choice for probing small domains without affecting the spontaneous polarisation.

For the two compounds with the largest macrodipole interactions (**1** and **2**), both J_1 and J_2 are positive, indicating that the electrostatic interaction and thus an antiferroelectric alignment between n.n. and n.n.n. columns dominates. This inevitably leads to disorder for up and down oriented columns on local length scales and non-polar unit cells as shown in Figures 2c and 3c. In contrast, for **3** and **4**, where the electrostatic interaction is significantly reduced, J_1 and J_2 bear opposite signs with $J_1 > 0$ and $J_2 < 0$. Consequently, only n.n. columns tend to be antialigned, while n.n.n. stacks favour a parallel alignment. The latter occurs only, when the steric interaction and collective packing effects^[22] get stronger than the electrostatic forces. The tendency for an opposite alignment for n.n. and n.n.n. columns in turn is the origin for the formation of mesoscale domains with spontaneous polarisation and polar unit cells (Figures 2c and 3c). Based on the calculated molecular dipole moments, the polarisation within these domain reaches values of 1.6 $\mu\text{C}/\text{cm}^2$ and 1.4 $\mu\text{C}/\text{cm}^2$ for **3** and **4**, which are among the largest values obtained for axially polar phases so far.^[9-13,23]

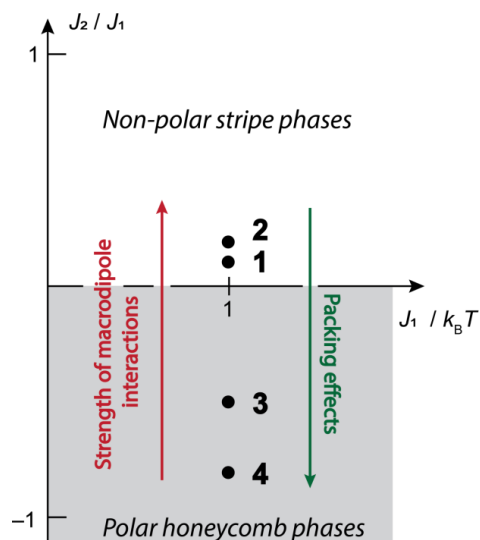


Figure 4. The ground state phase diagram^[19] of the simple two-dimensional Ising model exhibiting antiferroelectric nearest ($J_1 > 0$) and varying next-nearest neighbour interactions.

Common approaches to create ferroelectric order make use of supramolecular interactions between individual molecules to compete the electrostatic interaction.^[3] In contrast we show, that for axially polar phases polarisation emerges from weak steric interactions between self-assembled supramolecular columns if the systems are prone to geometric frustration. Since these interactions are encoded in the molecular structure, the latter drives the dipole ordering and the length scale of domain formation. As such, it is possible to move between non-polar stripe-type and polar honeycomb phases in a 2D Ising phase diagram (Figure 4).^[19] Our finding illustrates emerging complexity^[24] and is an intriguing example of introducing hierarchical order in supramolecular systems.^[25] With small but systematic chemical modifications of the molecular synthons, a broad range of antiferroelectric and ferroelectric domain structures are accessible. Counterintuitively, mesoscale domains are maximised for systems where dipolar interactions are reduced. Following this idea for other columnar materials may lead to the development of a wide variety of new axially polar columnar ferroelectric materials, both solid and liquid crystalline.

Acknowledgments

C.S.Z., K.P.Z., H.W.S. and J.S. gratefully acknowledge financial support from the German Research Foundation (SFB840). Furthermore, we thank the Hanns-Seidel-Foundation (C.S.Z.) and the Elite Network Bavaria (C.S.Z. and K.P.Z.) for financial and other support. All authors thank Thomas Weber (ETH Zürich) for the crystal structure data of **1** and Sandra Ganzleben for her support with the syntheses

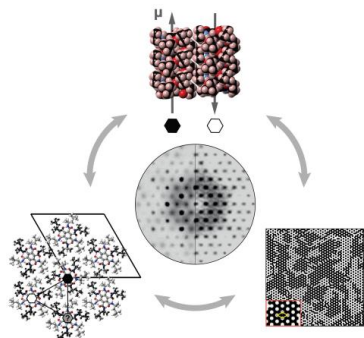
4 Publications

of the compounds. A.L.G., J.A.H., and N.P.F. gratefully acknowledge financial support from the ERC (Grant 279705) and the EPSRC (Grant EP/G004528/2).

- [1] S. Horiuchi, Y. Tokura, *Nature Mater.* **2008**, *7*, 357–366.
- [2] J. F. Scott, *Science* **2007**, *315*, 954–959.
- [3] A. S. Tayi, A. Kaeser, M. Matsumoto, T. Aida, S. I. Stupp, *Nature Chem.* **2015**, *7*, 281–294.
- [4] K. Asadi, D. M. de Leeuw, B. de Boer, P. W. M. Blom, *Nature Mater.* **2008**, *7*, 547–550.
- [5] S. T. Lagerwall, *Ferroelectrics* **2004**, *301*, 15–45.
- [6] a) S. Horiuchi, F. Ishii, R. Kumai, Y. Okimoto, H. Tachibana, N. Nagaosa, Y. Tokura, *Nature Mater.* **2005**, *4*, 163–166; b) D.-W. Fu, H.-L. Cai, Y. Liu, Q. Ye, W. Zhang, Y. Zhang, X.-Y. Chen, G. Giovannetti, M. Capone, J. Li et al., *Science* **2013**, *339*, 425–428; c) S. Horiuchi, Y. Tokunaga, G. Giovannetti, S. Picozzi, H. Itoh, R. Shimano, R. Kumai, Y. Tokura, *Nature* **2010**, *463*, 789–792; d) S. Horiuchi, Y. Okimoto, R. Kumai, Y. Tokura, *Science* **2003**, *299*, 229–232; e) E. Collet, M.-H. Lemée-Cailleau, M. Buron-Le Cointe, H. Cailleau, M. Wulff, T. Luty, S.-Y. Koshihara, M. Meyer, L. Toupet, P. Rabiller et al., *Science* **2003**, *300*, 612–615; f) A. S. Tayi, A. K. Shveyd, A. C.-H. Sue, J. M. Szarko, B. S. Rolczynski, D. Cao, T. J. Kennedy, A. A. Sarjeant, C. L. Stern, W. F. Paxton et al., *Nature* **2012**, *488*, 485–489.
- [7] K. Kishikawa, S. Nakahara, Y. Nishikawa, S. Kohmoto, M. Yamamoto, *J. Am. Chem. Soc.* **2005**, *127*, 2565–2571.
- [8] H. Takezoe, K. Kishikawa, E. Gorecka, *J. Mater. Chem.* **2006**, *16*, 2412–2416.
- [9] D. Miyajima, F. Araoka, H. Takezoe, J. Kim, K. Kato, M. Takata, T. Aida, *Science* **2012**, *336*, 209–213.
- [10] C. F. C. Fitié, W. S. C. Roelofs, M. Kemerink, R. P. Sijbesma, *J. Am. Chem. Soc.* **2010**, *132*, 6892–6893.
- [11] S. Cantekin, T. F. A. de Greef, A. R. A. Palmans, *Chem. Soc. Rev.* **2012**, *41*, 6125–6137.
- [12] H. Zimmermann, R. Poupko, Z. Luz, J. Billard, *Z. Naturforsch.* **1985**, *40*, 149–160.
- [13] C. Tschierske, *Nature* **2002**, *419*, 681–683.
- [14] M. O’Keeffe, S. Andersson, *Acta Crystallogr. A* **1977**, *33*, 914–923.
- [15] M. Kristiansen, P. Smith, H. Chanzy, C. Baerlocher, V. Gramlich, L. McCusk, T. Weber, P. Pattison, M. Blomenhofer, H.-W. Schmidt, *Cryst. Growth Des.* **2009**, *9*, 2556–2558.
- [16] M. Schmidt, J. Wittmann, R. Kress, D. Schneider, S. Steuernagel, H.-W. Schmidt, J. Senker, *Cryst. Growth Des.* **2012**, *12*, 2543–2551.
- [17] C. Zehe, M. Schmidt, R. Siegel, K. Kreger, V. Daebel, S. Ganzleben, H.-W. Schmidt, J. Senker, *CrystEngComm* **2014**, *16*, 9273–9283.
- [18] D. A. Keen, A. L. Goodwin, *Nature* **2015**, *521*, 303–309.
- [19] U. Brandt, J. Stolze, *Z. Phys. B Con. Mat.* **1986**, *64*, 481–490.
- [20] E. Gorecka, D. Pocięcha, J. Mieczkowski, J. Matraszek, D. Guillon, B. Donnio, *J. Am. Chem. Soc.* **2004**, *126*, 15946–15947.

4 Publications

- [21] J. Breu, P. Stössel, S. Schrader, A. Starukhin, W. J. Finkenzeller, H. Yersin, *Chem. Mater.* **2005**, *17*, 1745–1752.
- [22] T. R. Welberry, A. P. Heerdegen, D. C. Goldstone, I. A. Taylor, *Acta Crystallogr. B* **2011**, *67*, 516–524.
- [23] a) A. Sugita, K. Suzuki, S. Tasaka, *Chem. Phys. Lett.* **2004**, *396*, 131–135; b) H. Pleiner, H. R. Brand, P. E. Cladis, *Mol. Cryst. Liq. Cryst.* **2003**, *396*, 169–176.
- [24] A. B. Cairns, M. J. Cliffe, J. A. M. Paddison, D. Daisenberger, M. G. Tucker, F.-X. Coudert, A. L. Goodwin, *Nature Chem.* **2016**, *8*, 442–447.
- [25] T. Aida, E. W. Meijer, S. I. Stupp, *Science* **2012**, *335*, 813–817.

Graphical Abstract

Supramolecular Chemistry meets Geometric Frustration in axially polar bulk phases of benzene-1,3,5-trisamides (BTAs). The macrodipole moments generated by forming supramolecular stacks frustrate during progressive aggregation in hexagonal rod packings. Here we show with total X-ray scattering, that the frustration can be utilised to induce spontaneous polarisation on the mesoscale with domain sizes guided by chemical design of the molecular synthons.

Keywords: organic ferroelectrics, supramolecular chemistry, self-assembly, total X-ray scattering, Ising model

Supporting Information

for

Mesoscale Polarisation *via* Geometric Frustration in Columnar Supramolecular Crystals

Christoph S. Zehe¹, Joshua A. Hill², Nicholas P. Funnell^{2,3},
Klaus Kreger⁴, Kasper P. van der Zwan¹, Andrew L. Goodwin^{2*},
Hans-Werner Schmidt^{4*}, Jürgen Senker^{1*}

¹Inorganic Chemistry III, Universitätsstrasse 30, University of Bayreuth, 95447,
Bayreuth, Germany,

²Department of Chemistry, University of Oxford, Inorganic Chemistry Laboratory,
South Parks Road, Oxford OX1 3QR, UK,

³Current address: ISIS, Rutherford Appleton Laboratory, Chilton, Didcot OX11 0QX,
UK,

⁴Macromolecular Chemistry I, Universitätsstrasse 30, University of Bayreuth, 95447,
Bayreuth, Germany.

*To whom correspondence should be addressed;

Email: juergen.senker@uni-bayreuth.de, andrew.goodwin@chem.ox.ac.uk, hans-
werner.schmidt@uni-bayreuth.de.

Contents

1	Materials and Methods	Fehler! Textmarke nicht definiert.
1.1	Synthesis	3
1.2	X-Ray Diffraction Experiments	3
1.3	Quantum Chemical Calculations	3
1.4	Model Generation	4
1.5	Simulation of X-Ray Diffraction Patterns	5
2	Analysis of Single-Crystal X-Ray Diffraction Data	6
2.1	Data Collection and Refinement Details	6
2.2	Discussion of Diffuse Scattering and Twinning	10
3	Estimation of Molecular Dipole Moments	12
4	Comparison of Powder X-Ray Diffraction Data with Simulations Based on Ising Models	13

1 Experimental Details

1.1 Synthesis

All compounds were synthesised according to the procedures reported in the literature.^[1] Single crystals of **1**, **2** and **3** were obtained by slow solvent evaporation of a saturated solution using N,N-dimethylformamide under ambient conditions. Single crystals of **4** were grown through sublimation and re-condensation by keeping a small amount (~0.5 g) of sample in a closed glass vessel at 160° C for 3 days.

1.2 X-Ray Diffraction Experiments

Single crystal X-ray diffraction experiments were carried out on a STOE IPDS II instrument (Mo-K α radiation) equipped with a Ge(111) monochromator under ambient conditions for **2**. The crystal with an approximate size of 0.2 mm \times 0.2 mm \times 1.5 mm was mounted on a glass tip with glue. Data collection, indexing, space group determination, data reduction and reconstruction of reciprocal space layers were performed with the software package X-Area (Stoe). For **3** and **4**, an Oxford Diffraction (Agilent) Supernova diffractometer (CuK α_1 radiation, graphite monochromator) with an Oxford Cryosystems 700 Plus open-flow nitrogen cryostream^[2] at 150 K was used. Single crystals with a size of approximately 0.06 mm \times 0.06 mm \times 0.63 mm and 0.03 mm \times 0.03 mm \times 0.28 mm, respectively, were mounted using perfluoropolyether oil. Data collection, indexing, space group determination, data reduction and reconstruction of reciprocal space layers were performed with the software package CrysAlis Pro (Agilent). A face-based analytic absorption correction was applied to the integrated Bragg diffraction intensities.^[3]

For structure solution and refinement the software package CRYSTALS^[4] was used in all cases. Structure solution using direct methods was performed by the SIR92 package^[5] and refinement was done against F^2 as implemented in CRYSTALS. All non-hydrogen atoms were refined with anisotropic displacement parameters, all hydrogen atoms with isotropic displacement parameters. For **2** and **3**, all protons were added geometrically and riding constraints were applied. For **4**, all non-NH hydrogen atoms were added geometrically and riding constraints were applied, while all NH atoms were located by difference Fourier electron density maps and refined using riding constraints as implemented in CRYSTALS. Difference Fourier electron density maps were used to locate split sites and visualised by the MCE interface^[6] of CRYSTALS. See section 2.1 for detailed results.

Powder X-ray diffraction measurements were carried out on a STOE STADI P diffractometer equipped with a Ge(111) monochromator using CuK α_1 radiation. Experiments on powders obtained from finely ground single crystals filled in 0.5 mm capillary tubes were conducted in Debye-Scherrer geometry under ambient conditions.

1.3 Quantum Chemical Calculations

The structures obtained from single crystal refinement were geometry optimised on DFT level with the software package CASTEP^[7] using the PBE functional and the

Tkatchenko-Scheffler dispersion correction scheme.^[8] An electronic cut off energy of 900 eV and a Monkhorst k point grid spacing of 0.07 \AA^{-1} was used. Dipole moments were calculated for clusters of molecules extracted from the geometry optimised crystal structures while keeping the geometry fixed with the software package GAUSSIAN09^[9] using either the PBE1PBE functional on DFT level and a 6-311++G** basis set and the AM1 method, respectively. The dipole moments $\bar{d}_{AM1}(n_{mol})$ obtained for the semiempirical AM1 method as a function of the stack size n_{mol} were first fitted to those of the PBE functional $\bar{d}_{PBE}(n_{mol})$ for stacks consisting of up to six molecules ($n_{mol} \leq 6$) by least-squares refinement of the coefficients c_1 and c_2 in the equation $c_1 \cdot \bar{d}_{AM1}(n_{mol}) + c_2$. Subsequently, the obtained coefficients were used to correct the AM1 results $\bar{d}_{AM1}(n_{mol})$ of stacks containing more than six molecules ($n_{mol} > 6$).

1.4 Model Generation

Two-dimensional Ising models were generated with a custom Monte Carlo code. The energy was defined by

$$E = J_1 \sum_{\langle i,j \rangle} \sigma_i \sigma_j + J_2 \sum_{\langle\langle i,j \rangle\rangle} \sigma_i \sigma_j, \quad (S1)$$

where single brackets denote a sum over nearest neighbours and double brackets a sum over next nearest neighbours. $\sigma_i = 1 / -1$ represent up and down oriented columns. The energy was equilibrated for systems containing 100×100 spins with periodic boundary conditions using the Metropolis algorithm^[10] with $J_1/kT = 1$, where k denotes the Boltzmann constant and T the simulation temperature. We chose the simplest Ising model being capable of explaining the observed superstructures, which includes two effective coupling constants J_1 and J_2 .^[11] The entire code is available upon request. For the Ising model for **1**, **3** and **4**, where J_1 and J_2 are equal for all six n.n. and n.n.n., respectively, and where J_1 is positive, only three different ground states exist^[11]: i) for $J_2 > 0$ a totally ordered stripe-like pattern; ii) for $J_2 < 0$ a honeycomb phase with only one single domain; iii) for $J_2 = 0$ a degenerated manifold of disordered states result at $T = 0$.

For compound **2**, where the underlying rod packing is pseudo-hexagonal, the coupling constants were allowed to differ in the different crystallographic directions of the two-dimensional lattice (Figure S1c). After testing various combinations, the general requirement of all coupling constants being non-negative was established. To reduce the configuration space the coupling constants J_{01} , J_{11} , J_{10} (interpreted as J_1 in eqn. S1) and J_{12} , J_{21} and J_{11} (interpreted as J_2 in eqn. S1), respectively, were restrained to be as similar as possible and the best possible match between simulation and observed diffuse scattering possible was identified (Figure S1c). For these constants, a totally ordered stripe-like pattern results at $T = 0$.

Tab. S1 summarises the energies of the equilibrated models as well as the energies of the corresponding Ising ground states. Since $T \neq 0$, all equilibrium energies are larger than the ground state energies, leading to domains instead of ordered ground state structures.

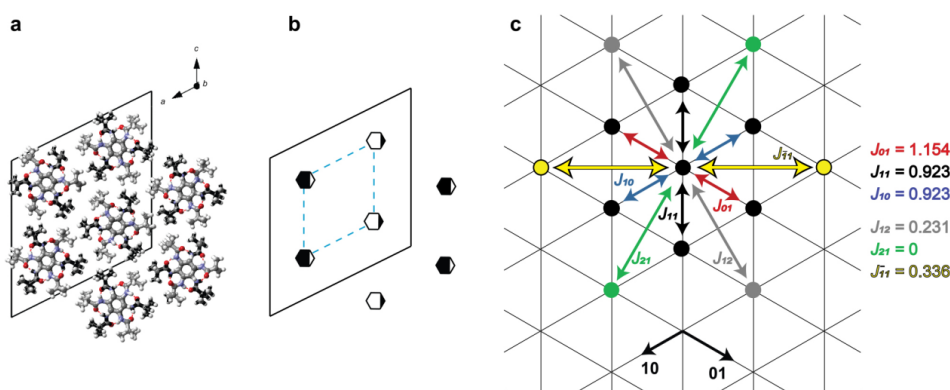


Figure S1: **a**, The pseudo-hexagonal packing of **2** and **b**, the macrodipole orientations obtained from single-crystal structure solution (cf. Figure 2). **c**, Due to the pseudo-hexagonal rod packing in **2**, an anisotropic Ising model using different coupling constants for different directions is used.

Table S1: Equilibrium energies E_{eq} per atom obtained in the MC simulations of the different Ising models as well as corresponding ground state energies E_{gr} per atom.

Compound	J_1, J_2	$E_{\text{eq}} / \text{a.u.}$	$E_{\text{gr}} / \text{a.u.}$
1	1, 0.1	-0.808	-1.1
2	1, 0.2 (average)	-1.035	-1.049
3	1, -0.5	-2.130	-4.5
4	1, -0.8	-3.387	-5.4

1.5 Simulation of X-Ray Diffraction Patterns

The calculation of powder and single crystal diffraction intensities was facilitated with the programs CrystalDiffract^[12] and SingleCrystal^[13] respectively. For all models, the basic shape of diffuse scattering was first inspected using test models being generated by populating the 100 x 100 models with carbon in case of $\sigma_i = 1$ and voids otherwise. The diffuse scattering showed sensitivity towards changes of about 5% of the coupling constants, in particular in the region around $J_{1/2} = 0$. Subsequently, 36 x 36 subensembles were randomly chosen from the 100 x 100 models and populated with stacks obtained from the single-crystal structure solutions, where every possible subensembles gave the same diffraction pattern. Scattering from these models is identical to that of the test models up to a scale factor. Comparisons of the simulations of powder diffraction patterns using those models with experimental data obtained from ground single crystals are in excellent agreement (see Supplementary Figure S9-S12).

2 Analysis of Single-Crystal X-Ray Diffraction Data

2.1 Data Collection and Refinement Details

Crystallographic information files (.cif) of a) the refinement of the initial structure solution, b) the refinement after adding atoms from difference Fourier electron density maps and c) the result of the geometry optimisation of a) are available in the online version of the paper (Tab. S2) for **2** and **3**. For **4**, the .cif files of the full refinement and of the geometry optimised structure are available.

Key crystallographic details and refinement parameters for the full refinements are given for the compounds **2-4** in Tables S3-S5 (for details of data handling and refinement procedures compare section 1.2; for compound **1** see ref. [14]).

For compound **2**, a pseudo-merohedral twin with a twin matrix $\begin{pmatrix} 0 & 0 & 1 \\ 0 & -1 & 0 \\ 1 & 0 & 0 \end{pmatrix}$, swapping the crystallographic *a* and *c* axes, and almost equal twin fractions was detected during refinement. See section 2.2 for a detailed discussion of this twin law and of twinning in general for compounds **2-4**.

The diffuse scattering surrounding certain Bragg reflections for **2** and **3** causes errors during integration of the Bragg intensities and leads to large R values, uncommonly large and anisotropic thermal displacement parameters and distorted molecular geometries for these compounds. However, the split sites appear as well-defined residual electron density peaks in Fourier difference maps and the structured diffuse scattering strongly supports our models so that our analyses are meaningful.

Table S2: Summary of the crystallographic information files available in the online version of the paper.

Comp.	File no.	Content	Name of file/data set
1		Results of refinement may be obtained from Steurer et al. ^[14]	-
1	1	Geometry optimisation of results from ref [14]	1.cif
2	2	Initial refinement	2a.cif
2	3	Full refinement including split sites	2b.cif
2	4	Geometry optimisation of file no. 2	2c.cif
3	5	Initial refinement	3a.cif
3	6	Full refinement including split sites	3b.cif
3	7	Geometry optimisation of file no. 5	3c.cif
4	8	Full refinement	4b.cif
4	9	Geometry optimisation of file no. 8	4c.cif

4 Publications

Table S3: Representative single-crystal X-ray diffraction data and refinement results including split sites for **2** (for complete cif file see online version of the paper).

Radiation	Mo-K α
Formula	C ₂₁ H ₃₃ N ₃ O ₃
<i>M</i> (g/mol)	375.51
<i>Z</i> , calculated density (g/cm ³)	8, 1.060
Crystal Size (mm)	0.2 × 0.2 × 1.5
No. of Reflections	12716
No. of Reflections (<i>I</i> / σ > 2.0)	7826
<i>T</i> / K	293
θ range (°)	1.627-29.358
Completeness (%) / <i>h</i> , <i>k</i> , <i>l</i> range	98.4 / ± 38 , ± 9 , ± 38
Crystal System	Monoclinic
Space Group	<i>P</i> 2 ₁ / <i>n</i>
<i>a</i> (Å)	27.948(6)
<i>b</i> (Å)	6.7270(13)
<i>c</i> (Å)	27.953(6)
β (°)	116.43(3)
Goodness of Fit	1.9685
<i>R</i> _p	0.1635
<i>R</i> _p (<i>I</i> / σ > 2.0)	0.1401
<i>wR</i> _p	0.5152
<i>wR</i> _p (<i>I</i> / σ > 2.0)	0.3650
Restraints/parameters	0/ 571
Twin law matrix, twin fractions	(0 0 1, 0 -1 0, 1 0 0), 0.524(4) / 0.476(4)

Table S4: Representative single-crystal X-ray diffraction data and refinement results including split sites for **3** (for complete cif file see online version of the paper).

Radiation	Cu-K α
Formula	C ₃₃ H ₅₇ N ₃ O ₃
<i>M</i> (g/mol)	543.83
<i>Z</i> , calculated density (g/cm ³)	6, 1.055
Crystal Size (mm)	0.061 × 0.061 × 0.634
No. of Reflections	7099
No. of Reflections (<i>I</i> / σ > 2.0)	5664
<i>T</i> / K	150
θ range (°)	3.466-76.126
Completeness (%) / <i>h</i> , <i>k</i> , <i>l</i> range	99.4 / -31/+36, -36/+37, \pm 8
Crystal System	Hexagonal
Space Group	<i>P</i> 6 ₃
<i>a</i> (Å)	29.4501(9)
<i>c</i> (Å)	6.8393(2)
Goodness of Fit	1.1565
<i>R</i> _p	0.1175
<i>R</i> _p (<i>I</i> / σ > 2.0)	0.1026
<i>wR</i> _p	0.2751
<i>wR</i> _p (<i>I</i> / σ > 2.0)	0.2574
Restraints/parameters	0 / 705

4 Publications

Table S5: Representative single-crystal X-ray diffraction data and refinement results including split sites for **4** (for complete cif file see online version of the paper).

Radiation	Cu-K α
Formula	C ₁₈ H ₂₄ F ₃ N ₃ O ₃
<i>M</i> (g/mol)	387.4
<i>Z</i> , calculated density (g/cm ³)	6, 1.242
Crystal Size (mm)	0.026 × 0.026 × 0.284
No. of Reflections	2278
No. of Reflections (<i>I</i> / σ > 2.0)	2171
<i>T</i> / K	150
θ range (°)	3.802-51.535
Completeness (%) / <i>h</i> , <i>k</i> , <i>l</i> range	99.9 / ± 23 , ± 23 , ± 6
Crystal System	Hexagonal
Space Group	<i>P</i> 6 ₃
<i>a</i> (Å)	23.2502(4)
<i>c</i> (Å)	6.63730(10)
Goodness of Fit	1.0069
<i>R</i> _p	0.0324
<i>R</i> _p (<i>I</i> / σ > 2.0)	0.0305
<i>wR</i> _p	0.0798
<i>wR</i> _p (<i>I</i> / σ > 2.0)	0.0780
Restraints/parameters	9 (N-H hydrogen restraints) / 253

2.2 Discussion of Diffuse Scattering and Twinning

First, we note that the diffuse scattering for compounds **2** and **3** is confined to reciprocal lattice planes perpendicular to the stacking direction (Figure S2; **4** does not exhibit any diffuse scattering). This implies that the columns are not disordered along the stacking direction within the coherence length of the beam. Hence, only macroscopic twinning may occur along the column axis, which cannot be the origin of split positions. We will discuss the possible twin operations for compounds **2-4** in the following and show that the only possible origin of the split positions and the diffuse scattering is microscopic disorder.

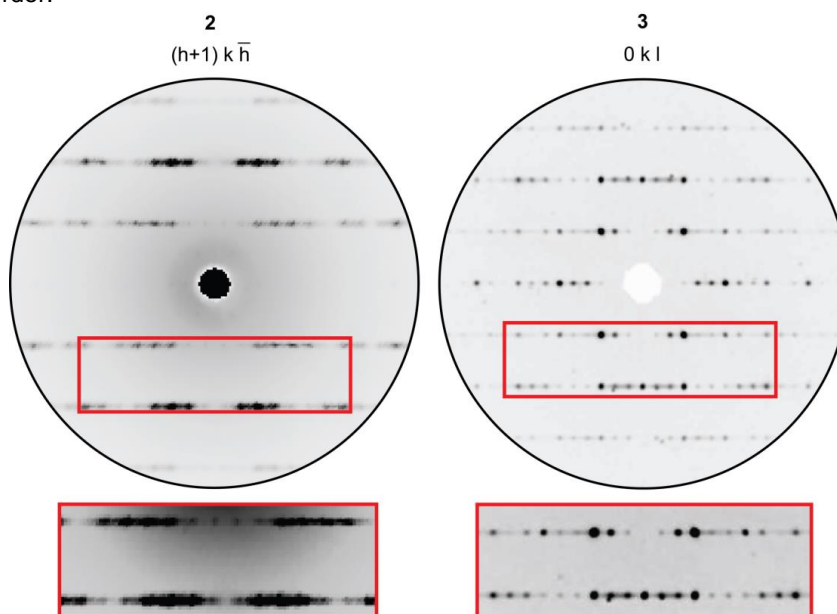


Figure S2: Planes of the reciprocal space reconstruction perpendicular to those presented in Figure 3 of the main paper for compounds **2** and **3**. The red boxes show magnifications of selected regions.

For compounds **3** and **4**, the non-centrosymmetric space group $P6_3$ was determined. In the case of twinning by merohedry, the two twin components are related by a symmetry operation, which belongs to the point group of the lattice (holohedry) but not to the point group of the crystal. This may be separated in class I and class II merohedral twinning. In class I twins by merohedry (inversion twins), the twin symmetry operation is part of the Laue group $6/m$ but not of the point group 6 of the crystal. This means that the m plane of the Laue group (or, equivalently, the inversion centre) is the twin symmetry operation. Since the diffraction patterns exhibit intrinsic inversion symmetry (i.e. Friedel pairs are equivalent since anomalous scattering was not detectable / refinement of Flack parameter was indifferent since heavy atoms are absent) this kind of twinning does not affect the observed diffraction intensities. It thus

cannot be the cause of the split positions for **3**. Moreover, since such a twinning would require a break in the hydrogen bond network of each stack, it seems energetically unfavourable.

In case of class II twinning by merohedry, the twin symmetry operation is not part of the Laue group but part of the holohedry. In this case, the diffraction intensities are affected by exact coincidence of non-identical diffraction patterns. Such a twinning, however, cannot lead to an apparent space group $P6_3$ (see ref. [15]) and hence it can be excluded for **3** and **4** (moreover, such a twinning would also retain the macrodipole directions and may not cause the well-defined split positions).

For compound **2**, the centrosymmetric space group $P2_1/n$ was determined. For this space group, twinning by merohedry is not possible. However, since the a and c axis are basically identical in length, the lattice exhibits approximately a higher point group symmetry of $2/m\ 2/m\ 2/m$ (orthorhombic) compared to the point group symmetry $2/m$ of the space group $P2_1/n$ and hence twinning by pseudomerohedry is likely. Indeed, it was found during refinement that consideration of a twin matrix $(0\ 0\ 1, 0\ -1\ 0, 1\ 0\ 0)$, swapping the crystallographic a and c axes (Figure S3a,b), leads to a significant drop of more than 10 % of the crystallographic R value. This, however, means that the twinning occurs on macroscopic length scales, which does not influence the shape of the diffuse scattering, since it is mapped on itself (Figure S3c).

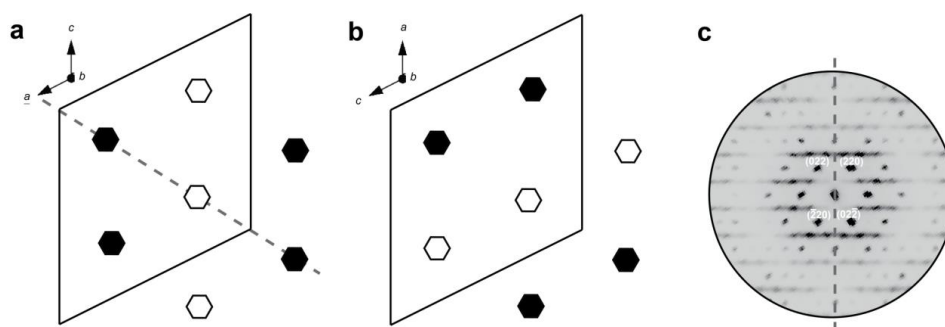


Figure S3: **a**, The twin operation $(0\ 0\ 1, 0\ -1\ 0, 1\ 0\ 0)$, swapping the crystallographic a and c axes in the structure of **2**, means a reflection of the structure on a mirror plane containing the b axis and running through the corners of the unit cell (grey dashed line). **b**, The twin component produces by this twinning operation shows the same stripe-like macrodipole pattern, but with a different orientation. The minor parts of the split positions are omitted for clarity. **c**, The diffuse scattering observed maps onto itself by this twinning operation.

Twinning by pseudo-merohedry through a 120° rotation about the b axis was not detected during refinement; in addition, such a twinning would not map the diffuse scattering onto itself but create a checked pattern, which can obviously be excluded. As a consequence, the only possible origin of the split sites for **2** and **3** is macrodipole disorder on a length scale similar to that of the coherence length of the beam.

3 Estimation of Molecular Dipole Moments

We estimate the average molecular dipole moments of an infinite stack for compounds **1**, **2** and **4** by quantum chemical calculations. First, the crystal structures obtained from structure solutions (where only the major part of the split positions were taken into account) were geometry optimised by DFT methods using the PBE functional to correct the distorted molecular geometries caused by the diffuse scattering during refinement. Next, accurate dipole moments were calculated by DFT methods using the PBE1PBE functional for stacks containing up to six molecules (Figure S4a), which constitutes the computational limit. The average dipole moment per molecule increases steadily with increasing number of molecules per stack (n_{mol}) due to cooperative effects.^[16] Convergence can be reached only using semiempirical AM1 calculations for up to twenty molecules; however, the magnitude of the dipole moments differs markedly for both techniques. Therefore, we fitted the less precise AM1 results $\bar{\delta}_{\text{AM1}}(n_{\text{mol}})$ to the more accurate PBE1PBE calculations $\bar{\delta}_{\text{PBE}}(n_{\text{mol}})$ (Figure S4a) by refining a the coefficients c_1 and c_2 of equation $\bar{\delta}_{\text{PBE}}(n_{\text{mol}}) = c_1 \cdot \bar{\delta}_{\text{AM1}}(n_{\text{mol}}) + c_2$. Subsequently, the obtained coefficients were used to correct the AM1 results $\bar{\delta}_{\text{AM1}}(n_{\text{mol}})$ of stacks containing more than six molecules ($n_{\text{mol}} > 6$). By this, we can estimate the average molecular contribution to the macrodipole to 12.2 D, 10.8 D and 6.6 D for **1**, **2** and **4**, respectively.

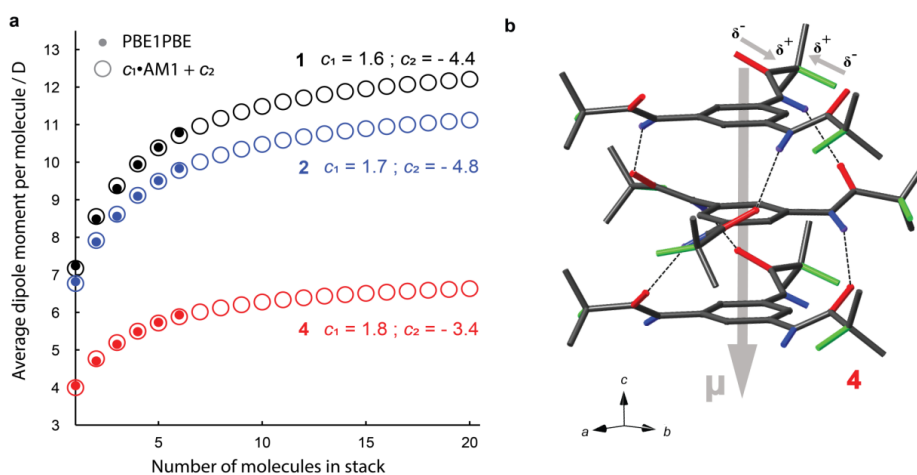


Figure S4. a, Average dipole moment per molecule for stacks of varying sizes isolated from the crystal structure without geometry optimisation. The filled circles correspond to calculations $\bar{\delta}_{\text{PBE}}(n_{\text{mol}})$ using the PBE1PBE functional and are limited to six molecules due to calculation time. The open circles are values $\bar{\delta}_{\text{AM1}}(n_{\text{mol}})$ obtained by the semiempirical AM1 method and are scaled by the equation $\bar{\delta}_{\text{PBE}}(n_{\text{mol}}) = c_1 \cdot \bar{\delta}_{\text{AM1}}(n_{\text{mol}}) + c_2$ (open circles), where the displayed c_1 and c_2 values are constants for each compound and n_{mol} demarks the number of molecules in the stack. **b**, Detail of the crystal structure of **4** where the N-H, C-F and C=O bonds are blue, green and red, respectively. The

polarities of the C=O and C-F bonds are indicated. All non-NH protons are omitted for clarity.

4 Comparison of Powder X-Ray Diffraction Data with Simulations Based on Ising Models

Figures S9-S12 show experimental powder X-ray diffraction data from ground single-crystals in comparison to simulated powder patterns based on the same models used for simulation of the single-crystal X-ray diffraction patterns (Figure 3a). They indicate that the basic underlying structure, the (pseudo-)hexagonal rod packing, is correct for all crystals of the samples and not only for the selected ones chosen for single-crystal diffraction experiments.

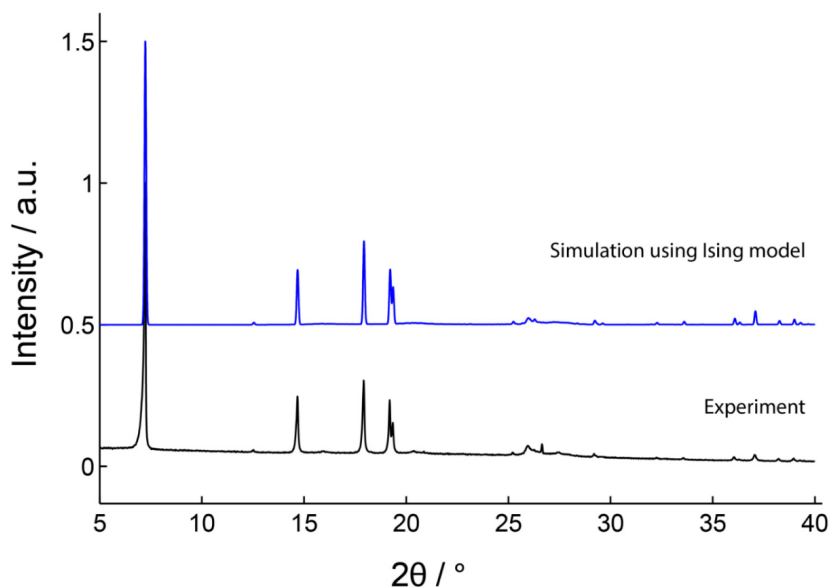


Figure S5: Comparison of powder X-ray diffraction experiment (black, bottom) of **1** with simulations of powder X-ray diffraction patterns based on the Ising models for **1** (blue, top).

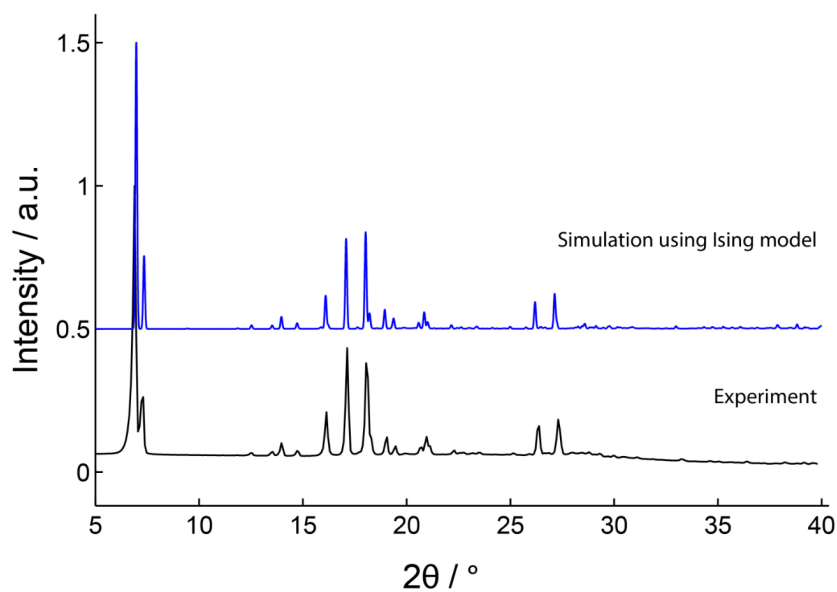


Figure S6: Comparison of powder X-ray diffraction experiment (black, bottom) of **2** with simulations of powder X-ray diffraction patterns based on the Ising models for **2** (blue, top).

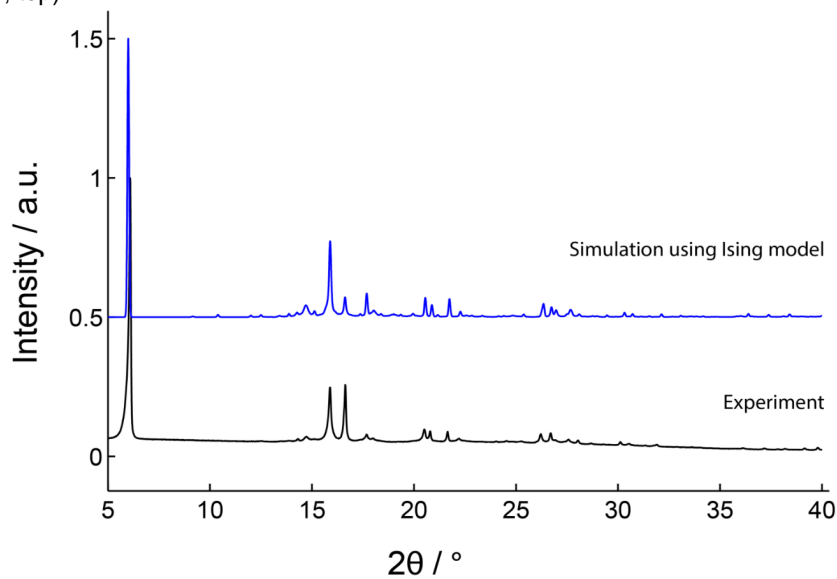


Figure S7: Comparison of powder X-ray diffraction experiment (black, bottom) of **3** with simulations of powder X-ray diffraction patterns based on the Ising models for **3** (blue, top).

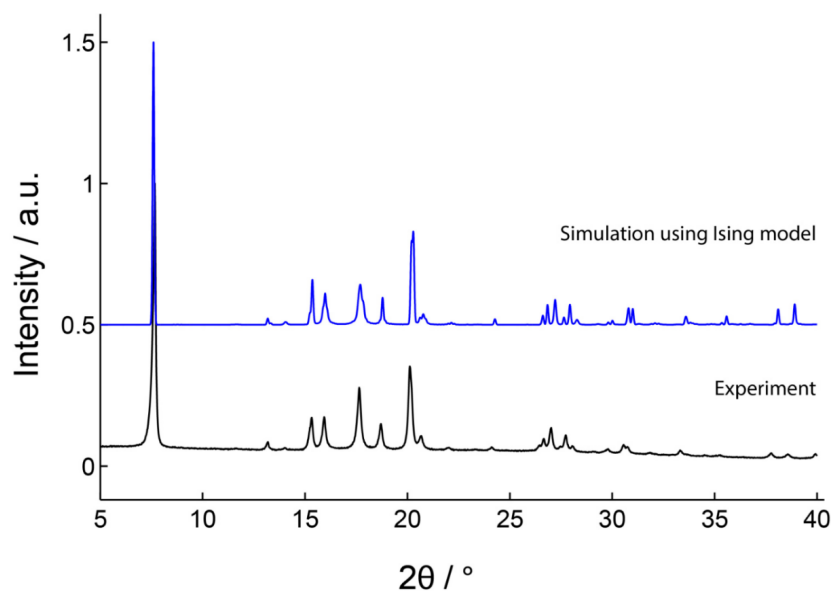


Figure S8: Comparison of powder X-ray diffraction experiment (black, bottom) of **4** with simulations of powder X-ray diffraction patterns based on the Ising models for **4** (blue, top).

References

- [1] a) C. Zehe, M. Schmidt, R. Siegel, K. Kreger, V. Daebel, S. Ganzleben, H.-W. Schmidt, J. Senker, *CrystEngComm* **2014**, *16*, 9273–9283; b) F. Abraham, S. Ganzleben, D. Hanft, P. Smith, H.-W. Schmidt, *Macromol. Chem. Phys.* **2010**, *211*, 171–181.
- [2] J. Cosier, A. M. Glazer, *J. Appl. Crystallogr.* **1986**, *19*, 105–107.
- [3] R. C. Clark, J. S. Reid, *Acta Crystallogr. A* **1995**, *51*, 887–897.
- [4] P. W. Betteridge, J. R. Carruthers, R. I. Cooper, K. Prout, D. J. Watkin, *J. Appl. Crystallogr.* **2003**, *36*, 1487.
- [5] A. Altomare, G. Cascarano, C. Giacovazzo, A. Guagliardi, M. C. Burla, G. Polidori, M. Camalli, *J. Appl. Crystallogr.* **1994**, *27*, 435.
- [6] J. Rohlíček, M. Hušák, *J. Appl. Crystallogr.* **2007**, *40*, 600–601.
- [7] S. J. Clark, M. D. Segall, C. J. Pickard, P. J. Hasnip, M. I. J. Probert, K. Refson, M. C. Payne, *Z. Kristallogr.* **2005**, *220*, 567–570.
- [8] E. R. McNellis, J. Meyer, K. Reuter, *Phys. Rev. B* **2009**, *80*, 205414.
- [9] M. J. Frisch, G. W. Trucks, H. B. Schlegel, G. E. Scuseria, M. A. Robb, J. R. Cheeseman, G. Scalmani, V. Barone, B. Mennucci, G. A. Petersson et al., *Gaussian09; Revision C.01*, Gaussian Inc., Wallingford, Connecticut, US, **2010**.
- [10] N. Metropolis, A. W. Rosenbluth, M. N. Rosenbluth, A. H. Teller, E. Teller, *J. Chem. Phys.* **1953**, *21*, 1087–1092.
- [11] U. Brandt, J. Stolze, *Z. Phys. B Con. Mat.* **1986**, *64*, 481–490.
- [12] D. C. Palmer, *CrystalDiffra* 6, CrystalMaker Software Ltd, Begbroke, Oxfordshire, England, **2013**.
- [13] D. C. Palmer, *SingleCrystal 2*, CrystalMaker Software Ltd, Begbroke, Oxfordshire, England, **2010**.
- [14] A. Simonov, T. Weber, W. Steurer, *J. Appl. Crystallogr.* **2014**, *47*, 2011–2018.
- [15] C. Giacovazzo, *Fundamentals of crystallography*, Oxford University Press, Oxford, New York, **2011**.
- [16] I. A. W. Pilot, A. R. A. Palmans, P. A. J. Hilbers, R. A. van Santen, E. A. Pidko, T. F. A. de Greef, *J. Phys. Chem. B* **2010**, *114*, 13667–13674.

4.5 Solid State NMR Spectroscopy

This work has entirely originated from the Inorganic Chemistry III of the University of Bayreuth and will be reproduced with permission from Wiley-VCH Verlag GmbH & Co. KGaA. My contributions are:

- conception of the article and authorship of Theory and Recoupling sections

The contributions of all other authors are:

- authorship of the remaining sections and conception of the article (authorship of all other sections except Theory and Recoupling)

Solid-State NMR Spectroscopy - Introduction for Solid-State Chemists

Christoph S. Zehe*, Renée Siegel*, Jürgen Senker*

Solid-state nuclear magnetic resonance spectroscopy (ssNMR) is a powerful and flexible tool for deriving structural and dynamical information for a broad variety of material classes ranging from metals, intermetallics and ceramics over organic, inorganic and metal-organic frameworks up to molecular crystals and polymers. The combination of relaxation experiments, lineshape analyses and 2D exchange techniques spans a dynamical window of about 14 decades with correlation times ranging from 10^{-12} s for fast ion conduction, up to 100 s for the α relaxation close to the glass transition. ssNMR is element selective and thus is able to identify chemical building units and simultaneously probes their homo- and heteronuclear through-bond and through-space connectivities, orientation correlations as well as distances up to a few nanometres. Thus ssNMR is ideally suited and often used to complement diffraction studies and quantum chemical calculations. It does not suffer from a loss of long range order and may equally be applied to crystalline, disordered and amorphous samples, to make progress on the structure elucidation of complex compounds. This chapter provides an overview about fundamental aspects of ssNMR including the most important nuclear spin interactions and their typical spectral lineshapes for both wide-line and high-resolution experiments. Based on this, we describe the development and application of various 1D and 2D NMR techniques, for both structural and dynamical aspects, on selected examples taken from the recent literature. In particular, we focus on strengths, weaknesses and the expressiveness of the individual methods.

*Inorganic Chemistry III, Universitätsstrasse 30, University of Bayreuth, 95447, Bayreuth, Germany;
Email: juergen.senker@uni-bayreuth.de

1 Introduction

Since the earliest days of NMR spectroscopy, this technique was used to determine materials properties in solids with one of the first examples being the determination of the proton-proton distance for water in gypsum $\text{CaSO}_4 \cdot 2\text{H}_2\text{O}$ by Pake in 1948¹. In spite of those early successes, the lack in resolution and sensitivity prevented a broad application in chemistry, material sciences, geology and biology. This was changed fundamentally by introducing *magic-angle spinning* (MAS)², *Fourier transform* NMR spectroscopy^{3,4} and *multiple-pulse*^{5,6} methods. While MAS improves the spectral resolution by imprinting a “liquid-like” motion on the sample based on spatial averaging², the latter two techniques made NMR spectroscopy much more flexible and versatile. Indeed, the combination of MAS with *multiple-pulse* methods like proton decoupling⁷ to gain even more resolution, recoupling techniques for selectively reintroducing desired nuclear spin interactions^{8,9} and with signal enhancing techniques like cross polarisation⁷ matured solid-state NMR spectroscopy (ssNMR) into one of the most expressive techniques to solve structural problems and derive information about dynamical processes.

Meanwhile, ultrafast MAS, with spinning speeds up to more than 100 kHz, allows to almost cancel even the strongest dipole couplings, as a consequence approaching liquid like resolution. A large battery of individual NMR techniques is now at the disposal of experimentalists enabling to separate and correlate nuclear spin interactions like the chemical shift and dipole as well as quadrupolar couplings, in order to answer questions concerning both structure and dynamics¹⁰. In particular, the anisotropic part of those interactions, directly measurable only in solids, provides an additional wealth of information which can be exploited for deriving connectivities, and distances on local and intermediate length scales and for studying motional mechanisms^{6,11}.

ssNMR has proven to be at its best for systems for which conventional analytic techniques like single crystal diffraction alone fail. An increasing number of *ab initio* structure solutions was reported for microcrystalline powders based on the combination of ssNMR, powder diffraction and computational modelling - often referred to as NMR crystallography¹². Since ssNMR does not depend on long range order, disordered materials like nanoscopic photocatalysts¹³ and porous frameworks¹⁴, but also amorphous systems like glasses¹⁵ and polymers⁶ and even inhomogeneous materials like bone tissue can be probed¹⁰.

Nevertheless, ssNMR is still a complex technique with many individual facets. Therefore, this chapter intends to provide the necessary background and a brief overview over the most important techniques for chemists and

material scientists who wish to use ssNMR to unravel structural properties and dynamical processes.

2 Theory and Methods

2.1 Important Interactions for NMR Spectroscopy

The nuclear spin interactions ($\hat{\mathcal{H}}_{int}$) include the Zeeman ($\hat{\mathcal{H}}_0$), the chemical shift ($\hat{\mathcal{H}}_{CS}$), the quadrupolar ($\hat{\mathcal{H}}_Q$) and the spin rotation ($\hat{\mathcal{H}}_{SR}$) interactions as well as the direct dipole-dipole ($\hat{\mathcal{H}}_{DD}$), the J ($\hat{\mathcal{H}}_J$) and for paramagnetic materials also the hyperfine ($\hat{\mathcal{H}}_{HF}$) couplings.¹⁶ Additionally, external radio-frequency (rf) fields ($\hat{\mathcal{H}}_{RF}$) allow to manipulate spin states. $\hat{\mathcal{H}}_0$ describes the interaction between nuclear spins and static external magnetic fields \vec{B}_0 , which is nowadays on the order of several Tesla, and is often the largest interaction for NMR spectroscopy. Therefore, all other interactions are treated as perturbation of $\hat{\mathcal{H}}_0$. $\hat{\mathcal{H}}_{CS}$ and $\hat{\mathcal{H}}_{HF}$ both originate from couplings of nuclei with magnetic fields generated by surrounding paired and unpaired electrons, respectively. Dipole-dipole interactions between spins may take place directly (through-space, $\hat{\mathcal{H}}_{DD}$) or indirectly *via* electrons in covalent bonds (through-bond, $\hat{\mathcal{H}}_J$). $\hat{\mathcal{H}}_Q$ describes the interaction of nuclear spins with the electric field gradient of the chemical environment, while $\hat{\mathcal{H}}_{SR}$ refers to nuclear spins coupled to angular momenta of molecular rotations. Compared to the other interactions, $\hat{\mathcal{H}}_J$ and $\hat{\mathcal{H}}_{SR}$ are both relatively small and are thus less frequently exploited in ssNMR. Therefore, we will not discuss the latter two in this chapter (for further information see refs. 11 and 17).

Tensors and Rotations. $\hat{\mathcal{H}}_{int}$ is usually anisotropic and may be described via a second rank tensor \mathbf{V} , which decodes its orientation dependent magnitude. $\hat{\mathcal{H}}_{int}$ is then expressed in the form⁵

$$\hat{\mathcal{H}}_{int} = \vec{I} \cdot \mathbf{V} \cdot \vec{J}, \quad (2.1)$$

where \mathbf{V} couples two vectors \vec{I} and \vec{J} . \vec{J} may be a magnetic field vector or a spin vector, whereas \vec{I} is always a spin vector. The interaction tensor \mathbf{V} may be decomposed into a symmetric $\mathbf{V}_{sym} = (\mathbf{V} + \mathbf{V}^\dagger)/2$ and an antisymmetric part $\mathbf{V}_{asym} = (\mathbf{V} - \mathbf{V}^\dagger)/2$ so that $\mathbf{V} = \mathbf{V}_{sym} + \mathbf{V}_{asym}$, with $\mathbf{V}_{sym} = \mathbf{V}_{sym}^\dagger$ and $\mathbf{V}_{asym} = -\mathbf{V}_{asym}^\dagger$. Since only \mathbf{V}_{sym} influences the shape of NMR spectra in first-order perturbation¹⁰, we neglect \mathbf{V}_{asym} for the following discussion. For simplicity we thus identify \mathbf{V} with \mathbf{V}_{sym} . It should be noted, however, that \mathbf{V}_{asym} plays an important role for the quantitative treatment of relaxation processes^{18,19}. Under these circumstances, a coordinate system may be chosen for which the matrix representation of \mathbf{V} is diagonal. This coordinate system is called the principal axis system (PAS) and the diagonal elements V_{XX} , V_{YY}

2.1. IMPORTANT INTERACTIONS FOR NMR SPECTROSCOPY 5

and V_{ZZ} are called the principal axis values. Tensors are often specified¹⁰ using the isotropic value σ_{iso} , the anisotropy σ_{aniso} and the asymmetry η :

$$\sigma_{iso} = \frac{V_{XX} + V_{YY} + V_{ZZ}}{3}, \quad \sigma_{aniso} = V_{ZZ} - \sigma_{iso}, \quad \eta = \frac{V_{YY} - V_{XX}}{\sigma_{aniso}} \quad (2.2)$$

Hereby, the convention $|V_{ZZ} - \sigma_{iso}| \geq |V_{XX} - \sigma_{iso}| \geq |V_{YY} - \sigma_{iso}|$ is used, which leads to $0 \leq \eta \leq 1$. σ_{aniso} reflects the maximal anisotropic interaction, whereas η is determined by the deviation of the interaction strength in the two remaining directions.

The Free Induction Decay (FID) is detected in the laboratory axis system (LAS), where commonly \vec{B}_0 is chosen to point along the z -axis. In contrast, the interaction tensor \mathbf{V} depends on the chemical structure which defines the PAS and its orientation with respect to the LAS. Since both coordinate systems are orthonormal, they are linked by the so-called Euler transformations¹¹. The graphical interpretation of \mathbf{V} is hereby often given by drawing \mathbf{V} as an ellipsoid in its PAS (Fig. 1a) and the orientation of \vec{B}_0 with respect to the PAS may then be described⁶ by the two polar angles θ and ϕ .

If, however, several reference frames are needed, a more general approach^{6,20} is advantageous: the relative orientation of two coordinate frames A (e.g. PAS) and B (e.g. LAS) may be specified by three Euler angles α , β and γ (Fig. 1b). These angles determine an overall Euler transformation $\hat{\mathcal{R}}(\alpha, \beta, \gamma)$ of the initial frame into the final one by three subsequent rotations (Fig. 1c). If the Euler transformation of frame A into frame B is given by $\hat{\mathcal{R}}(\alpha, \beta, \gamma)$ any tensor \mathbf{V}^A defined in frame A might be expressed by \mathbf{V}^B in frame B through the similarity transformation $\mathbf{V}^B = \hat{\mathcal{R}}(\alpha, \beta, \gamma) \cdot \mathbf{V}^A \cdot \hat{\mathcal{R}}(\alpha, \beta, \gamma)^\dagger$. In this notation, the orientation of \vec{B}_0 (frame B with $z_B = z_{LAS}$) in the PAS (frame A) is given by $\alpha = \phi$, $\beta = \theta$ and γ is arbitrary, since the x and y axis of the LAS may be freely chosen. Note that for axially symmetric tensors ($\eta = 0$) $\alpha = \phi$ becomes arbitrary. The actual calculation of rotations might be performed expressing $\hat{\mathcal{H}}$ in either cartesian or, which is more commonly used, in spherical coordinates⁶. The latter simplifies the outcome of rotations since they allow to decompose the tensors in parts with different rotational rank, i.e. with distinct rotational behaviours (section 3.3).

The Euler transformation for consecutive frame transformations is then simply given by the product of the rotation matrices²⁰. If e.g. the transformation of the PAS with respect to a common reference frame for all spins within the same crystallite (the crystal axis system CAS) is given by $\hat{\mathcal{R}}(\alpha_{PC}, \beta_{PC}, \gamma_{PC})$ and the orientation of the CAS with respect to the LAS is represented by $\hat{\mathcal{R}}(\alpha_{CL}, \beta_{CL}, \gamma_{CL})$, the overall Euler transformation from the PAS into LAS

6

CHAPTER 2. THEORY AND METHODS

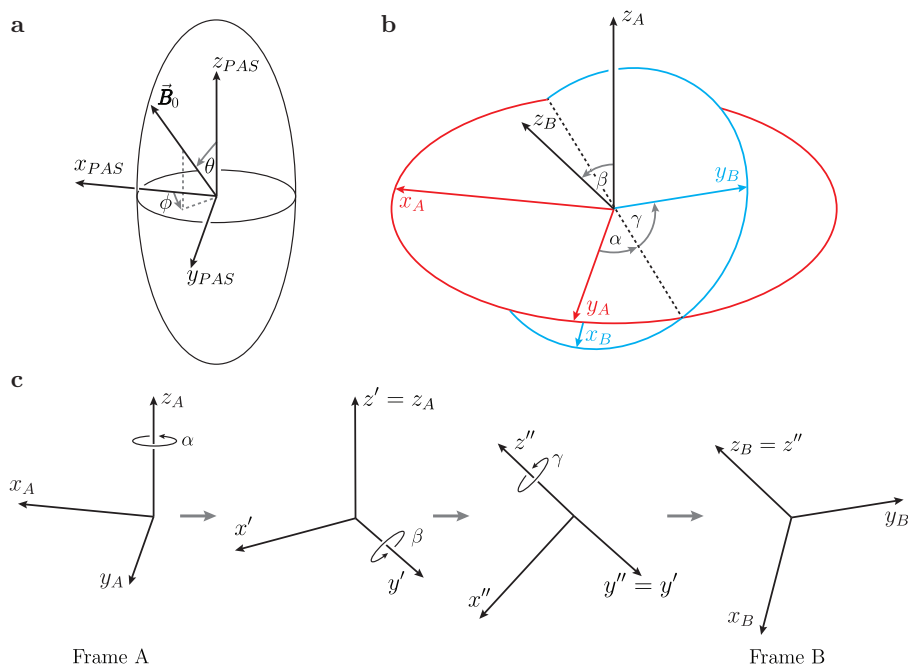


Figure 1: **a**: The tensor \mathbf{V} is represented graphically by an ellipsoid (flattened into a disc-like shape if $\eta \neq 0$), with a PAS $\{x_{PAS}, y_{PAS}, z_{PAS}\}$. The orientation of an external field \vec{B}_0 in the PAS is specified⁶ by the two polar angles θ and ϕ . **b**: The relative orientation of two coordinate frames $\{x_A, y_A, z_A\}$ and $\{x_B, y_B, z_B\}$ may be described⁶ by the Euler angles α , β and γ . α appears graphically between the the y_A axis and the node line (dashed line; intersection of the red $x_A y_A$ plane with the blue $x_B y_B$ plane); a similar consideration applies for γ . $\beta = \theta$ is the angle between z_A and z_B . **c**: The Euler angles may also be regarded²⁰ as the angles for three subsequent rotations about i) the z_A axis of the initial frame A, ii) the y' axis and iii) the z'' axis of the intermediate frames, yielding an overall transformation $\hat{\mathcal{R}}(\alpha, \beta, \gamma)$ of frame A into frame B.

is determined by $\hat{\mathcal{R}}(\alpha_{PL}, \beta_{PL}, \gamma_{PL}) = \hat{\mathcal{R}}(\alpha_{PC}, \beta_{PC}, \gamma_{PC}) \cdot \hat{\mathcal{R}}(\alpha_{CL}, \beta_{CL}, \gamma_{CL})$. This is extensively used for numerical simulations²¹, where not only the orientational average of a powdered sample but also the quantum mechanical time evolution of spin systems require such rotations.

Zeeman interaction. The quantum mechanical treatment of angular

2.1. IMPORTANT INTERACTIONS FOR NMR SPECTROSCOPY 7

momentum leads to energy quantisation¹⁶. For spins with a quantum number I , $2I+1$ energetically degenerate wave functions $|\Psi_m\rangle$ with magnetic quantum numbers $m = -I, -I+1, \dots, I-1, I$ exist. Within a static magnetic field $\vec{B}_0 = (0, 0, B_0)$ this degeneracy is broken¹⁸ according to

$$\hat{\mathcal{H}}_0 = -\gamma \vec{I} \cdot \vec{B}_0 = -\gamma B_0 \hat{\mathcal{I}}_z, \quad (2.3)$$

with $\vec{I} = (\hat{\mathcal{I}}_x, \hat{\mathcal{I}}_y, \hat{\mathcal{I}}_z)$ (please note that all $\hat{\mathcal{H}}_{int}$ are given in units of \hbar). $\hat{\mathcal{H}}_0$ is called *Zeeman interaction* and is as mentioned before usually significantly larger than the other nuclear spin interactions. To simulate NMR spectra thus the high-field (or secular) approximation⁶ is applied to discard all terms of $\hat{\mathcal{H}}_{int}$, which do not commute with $\hat{\mathcal{H}}_0$. Moreover, a transformation of $\hat{\mathcal{H}}_{int}$ into a frame rotating with ω_0 around the z axis, where $\hat{\mathcal{H}}_0$ disappears²², is usually applied for calculating the time evolution of spin systems (section 2.2).

Chemical Shift. The local magnetic field \vec{B} at the site of a nucleus is composed of two terms, the external field \vec{B}_0 and an induced magnetic field \vec{B}_{ind} shielding the nucleus⁵. The latter is caused by movements of surrounding electrons in response to \vec{B}_0 , resulting in $\vec{B} = \vec{B}_0 - \vec{B}_{ind}$. Based on eqn. 2.1, the chemical shift interaction $\hat{\mathcal{H}}_{CS}$ is given by

$$\hat{\mathcal{H}}_{CS} = \gamma \vec{I} \cdot \vec{B}_{ind} = \gamma \vec{I} \sigma \vec{B}_0 \quad (2.4)$$

with σ being the chemical shielding tensor¹⁸, which describes strength and orientation of \vec{B}_{ind} with respect to \vec{B}_0 . σ is determined by the chemical environment and may be extracted from quantum mechanical calculations^{23,24}. It should be noted, that the description of the hyperfine interaction $\hat{\mathcal{H}}_{HF}$ for paramagnetic materials is analogous to eqn. 2.4, with σ representing the hyperfine coupling tensor¹⁸. Another common convention is the use of the *Chemical Shift* tensor²² $\delta = -\sigma$, reverting the sign of eqn. 2.4; this is more common for practical applications and will hence be used in the following. The high-field approximated chemical shift interaction²²

$$\hat{\mathcal{H}}_{CS} = \gamma \sigma_{zz} B_0 \hat{\mathcal{I}}_z = -\gamma \delta_{zz} B_0 \hat{\mathcal{I}}_z = \omega_{cs} \hat{\mathcal{I}}_z \quad (2.5)$$

when combined with eqn. 2.3 results in⁶

$$\hat{\mathcal{H}}_0 + \hat{\mathcal{H}}_{CS} = (\omega_0 + \omega_{cs}) \hat{\mathcal{I}}_z = \omega_0 (1 + \delta_{zz}) \hat{\mathcal{I}}_z, \quad (2.6)$$

where $\omega_0 = -\gamma B_0$ represents the Larmor frequency of an unshielded nucleus and $\omega_{cs} = -\omega_0 \sigma_{zz} = \omega_0 \delta_{zz}$ the chemical shift frequency. The latter may be

expressed⁶ in the LAS as

$$\omega_{CS} = -\gamma B_0 \delta_{iso} - \frac{1}{2} \gamma B_0 \delta_{aniso} (3 \cos^2 \theta - 1 - \eta \sin^2 \theta \cos 2\phi) \quad (2.7)$$

where θ and ϕ are given in Fig. 1 and the three parameters $\delta_{iso} = -\sigma_{iso}$, $\delta_{aniso} = -\sigma_{aniso}$ and η are defined by the Haeberlen-Mehring-Spiess convention⁵ according to eqn. 2.2.

Dipolar interactions. Nuclear spins are not only perturbed by external magnetic fields, but also by each other through magnetic dipole-dipole interactions¹⁸. This coupling may take place directly between spins in spatial proximity, referred to as direct dipole-dipole interaction $\hat{\mathcal{H}}_{DD}$ ¹⁷. $\hat{\mathcal{H}}_{DD}$ may be derived from classic magnetic dipole-dipole interactions using the canonical quantisation leading to^{5,10}

$$\hat{\mathcal{H}}_{DD} = - \left(\frac{\mu_0 \gamma_I \gamma_S \hbar}{4\pi r^3} \right) \left(\vec{I} \cdot \vec{S} - 3 \frac{(\vec{I} \cdot \vec{r})(\vec{S} \cdot \vec{r})}{r^2} \right) = -2\vec{I} \cdot \mathbf{D} \cdot \vec{S} \quad (2.8)$$

where μ_0 is the magnetic field constant, γ_I and γ_S are the gyromagnetic ratios of the coupled spins I and S with an internuclear vector \vec{r} having the modulus r representing the distance between I and S and the dipole coupling tensor \mathbf{D} . The latter is often given using the dipolar coupling constant $d = (\mu_0 \gamma_I \gamma_S \hbar)/(4\pi r^3)$, with $D_{XX} = -\frac{d}{2}$, $D_{YY} = -\frac{d}{2}$ and $D_{ZZ} = d$ in its principal axis representation¹⁰. Thus \mathbf{D} is traceless ($\sigma_{iso} = 0$) and axially symmetric ($\eta = 0$) according to eqn. 2.2. The high-field approximation leads to

$$\hat{\mathcal{H}}_{DD}^{homo} = -d \left\{ \underbrace{\hat{\mathcal{I}}_z \hat{\mathcal{S}}_z (3 \cos^2 \theta - 1)}_A - \frac{1}{4} \underbrace{[\hat{\mathcal{I}}^+ \hat{\mathcal{S}}^- + \hat{\mathcal{I}}^- \hat{\mathcal{S}}^+]}_B (3 \cos^2 \theta - 1) \right\} \quad (2.9)$$

for the homonuclear dipole-dipole interaction⁶, where the polar angle θ is the angle between \vec{B}_0 and \vec{r} (i.e. \vec{r} points along z_{PAS} in Fig. 1) and $\hat{\mathcal{I}}^\pm = \hat{\mathcal{I}}_x \pm i\hat{\mathcal{I}}_y$. The first term is commonly called the A term, the second one the B term¹⁰. For the heteronuclear interaction only the A term remains, due to the large difference between the resonance frequencies of the I and S spins⁶ resulting in

$$\hat{\mathcal{H}}_{DD}^{hetero} = -d \hat{\mathcal{I}}_z \hat{\mathcal{S}}_z (3 \cos^2 \theta - 1). \quad (2.10)$$

2.1. IMPORTANT INTERACTIONS FOR NMR SPECTROSCOPY 9

Quadrupole interaction. Nuclei with $I > 1/2$ exhibit electric multipole moments due to non-spherical charge distributions within the nuclei with the quadrupolar moment Q being by far the largest one. Q couples to the electric field gradient (EFG) arising from the nuclear environment²⁰ leading to $\hat{\mathcal{H}}_Q$ given by^{5,18}:

$$\hat{\mathcal{H}}_Q = \frac{eQ}{2I(2I-1)\hbar} \vec{\mathcal{I}} \cdot \mathbf{V} \cdot \vec{\mathcal{I}}. \quad (2.11)$$

e is the elementary charge and \mathbf{V} is the traceless EFG tensor. \mathbf{V} exhibits the three principal axis values V_{XX} , V_{YY} , and V_{ZZ} and is most commonly characterised using the quadrupole coupling constant C_Q and the biaxiality parameter η_Q defined⁶ as

$$C_Q = \frac{eV_{ZZ}Q}{h}, \quad \eta_Q = \frac{V_{YY} - V_{XX}}{V_{ZZ}}. \quad (2.12)$$

Since the quadrupolar coupling strength is often quite strong, treating $\hat{\mathcal{H}}_Q$ as perturbation of $\hat{\mathcal{H}}_0$ usually requires two correction terms^{16,25} added to the Zeeman splitting: the first-order $\hat{\mathcal{H}}_Q^{(1)}$ and the second-order $\hat{\mathcal{H}}_Q^{(2)}$ quadrupole coupling

$$\hat{\mathcal{H}}_Q^{(1)} = -\frac{2\pi C_Q}{8I(2I-1)} (\hat{\mathcal{I}}^2 - 3\hat{\mathcal{I}}_z^2) [3 \cos^2 \theta - 1 - \eta_Q \cos 2\phi \sin^2 \theta] \quad (2.13)$$

$$\begin{aligned} \hat{\mathcal{H}}_Q^{(2)} = \frac{1}{2\omega_0} \left[\frac{2\pi C_Q}{2I(2I-1)} \right]^2 \hat{\mathcal{I}}_z \left\{ -\frac{1}{5} (\hat{\mathcal{I}}^2 - 3\hat{\mathcal{I}}_z^2) (3 + \eta_Q^2) \right. \\ + \frac{1}{28} (8\hat{\mathcal{I}}^2 - 12\hat{\mathcal{I}}_z^2 - 3) \left[(\eta_Q^2 - 3) (3 \cos^2 \theta - 1) - 6\eta_Q \sin^2 \theta \cos 2\phi \right] \\ + \frac{1}{8} (18\hat{\mathcal{I}}^2 - 34\hat{\mathcal{I}}_z^2 - 5) \left[\frac{1}{140} (18 + \eta_Q^2) (35 \cos^4 \theta - 30 \cos^2 \theta + 3) \right. \\ \left. \left. - \frac{3}{7} \eta_Q \sin^2 \theta (7 \cos^2 \theta - 1) \cos 2\phi + \frac{1}{4} \eta_Q^2 \sin^4 \theta \cos 4\phi \right] \right\}, \end{aligned}$$

where θ and ϕ denote the polar angles as given in Fig. 1.

Radio-frequency pulses. In modern Fourier-transform NMR, additional pulsed magnetic rf fields are used to manipulate the spin states. Hereby, the

nuclei are subjected to an oscillating magnetic field^{18,20}

$$\vec{B}_1(t) = B_1(\vec{e}_z \cos \theta_{rf} + \vec{e}_x \sin \theta_{rf}) \cos(\omega t + \phi_{rf}) \quad (2.14)$$

where ϕ_{rf} is the phase of the pulse, ω the frequency and θ_{rf} the angle created between \vec{B}_1 and \vec{B}_0 by the tilt of the rf coil. Within the secular approximation the corresponding Hamiltonian $\hat{\mathcal{H}}_{rf}$ reads for an on-resonance pulse (i.e. $\omega = \omega_0 + \omega_{CS}$) in the rotating frame²⁰

$$\hat{\mathcal{H}}_{rf} = -\omega_{nut}(\hat{\mathcal{I}}_x \cos \phi_{rf} + \hat{\mathcal{I}}_y \sin \phi_{rf}), \quad (2.15)$$

where $\omega_{nut} = |\frac{1}{2}\gamma B_1 \sin(\theta_{rf})|$. In contrast to the secular parts of all other nuclear spin interactions we encountered so far (with the exception of homonuclear dipolar couplings), $\hat{\mathcal{H}}_{rf}$ is dominated by $\hat{\mathcal{I}}_{x/y}$ and hence $\hat{\mathcal{I}}_{\pm}$ operators, which allow to mix different spin states and to create superpositions thereof. Thus, pulses are crucial building blocks for every modern NMR experiment.

2.2 Time Evolution of Spins Systems

To observe and to separate the nuclear interactions, sophisticated experiments are performed in ssNMR⁴. The interpretation of those often requires to simulate the time evolution of spin systems under specific interactions, which is derived by the time-dependent Schrödinger equation¹⁶

$$\frac{d}{dt} |\psi\rangle(t) = -i\hat{\mathcal{H}}(t) |\psi\rangle(t), \quad (2.16)$$

where both the wave function $|\psi\rangle(t)$ and $\hat{\mathcal{H}}(t)$ are in general time-dependent. The time-dependence of $|\psi\rangle$ is caused by rf pulses and the quantum mechanical evolution of non-eigenstates and is described using the spin-density formalism. Time dependence in the Hamiltonian is mostly imposed by a physical sample rotation, the magic-angle spinning (MAS), which alters the orientation of the interaction tensor \mathbf{V} (eqn. 2.1) periodically (section 2.3).

Spin density formalism. Since a macroscopic sample always contains a large number of spins, a quantum statistical density formalism¹⁸ is used to describe interactions and time evolution. The spin density matrix²⁰ $\hat{\rho}$ is defined as the ensemble average of the ket-bra products of the wavefunctions $|\psi_i\rangle = (c_1^i, c_2^i, \dots, c_n^i)$ of the N individual spin systems

$$\hat{\rho} = \frac{1}{N} \sum_{i=1}^N |\psi_i\rangle \otimes \langle \psi_i| = \overline{|\psi_i\rangle \otimes \langle \psi_i|} \quad (2.17)$$

and consists of N^2 elements $c_i c_j^*$ with $i, j \in \{1, \dots, N\}$. The diagonal elements $\rho_{jj} = \overline{c_j c_j^*}$ are the probabilities of finding an individual spin system in the state $|\psi_j\rangle$ and are therefore commonly called populations²⁰. The off-diagonal elements $\rho_{ij} = \overline{c_i c_j^*}$ ($i \neq j$) are called $\pm\Delta m$ coherences²⁰ (e.g. $\pm 1, \pm 2, \dots$), according to the difference $\Delta m = m_j - m_k$. Since the existence of coherences imply that different spins systems are coherently in a superposition state, they cannot exist in thermal equilibrium due to the maximisation of entropy²⁰.

In a static external magnetic field, the Zeeman interaction leads to $\hat{\rho} \sim \hat{\mathcal{I}}_z$ in thermal equilibrium, i.e. only populations exist weighted by the Boltzmann distribution. The time evolution of $\hat{\rho}$, subjected to a Hamiltonian $\hat{\mathcal{H}}$, is described by the von-Neumann equation⁴

$$\frac{\partial}{\partial t} \hat{\rho} = [\hat{\rho}, \hat{\mathcal{H}}]. \quad (2.18)$$

The density matrix $\hat{\rho}(t)$ at a time t is then derived from the density matrix at a time t_0 by⁴

$$\hat{\rho}(t) = \hat{\mathcal{U}}(t_0 \rightarrow t) \hat{\rho}(t_0) \hat{\mathcal{U}}^\dagger(t_0 \rightarrow t) \quad (2.19)$$

with a propagator $\hat{\mathcal{U}}(t_0 \rightarrow t)$

$$\hat{\mathcal{U}}(t_0 \rightarrow t) = e^{-i \int_{t_0}^t \hat{\mathcal{H}}(t') dt'}. \quad (2.20)$$

The result of a measurement using quadrature detection may be derived⁴ by

$$s(t) \propto \text{Tr}\{\hat{\mathcal{I}}^+ \hat{\rho}(t)\}. \quad (2.21)$$

In addition to this quantum-mechanical time evolution, relaxation also leads to a time-dependence of the nuclear spin states⁴. Hereby, two types of relaxation are macroscopically differentiated. First, the longitudinal or spin-lattice relaxation, characterised by a time constant T_1 , transfers magnetisation $M_z(t)$ parallel to the external static B_0 field into the thermal equilibrium state according to $M_z(t) \propto 1 - e^{-t/T_1}$. This requires a change of the populations of the spin-density matrix and, therefore, energy exchange with the environment. Second, the transversal or spin-spin-relaxation, characterised by a constant T_2 , relaxes magnetisation perpendicular to B_0 by $M_{trans}(t) \propto e^{-t/T_2}$. This type of relaxation implies a decay of coherences, which is driven purely by the entropy maximisation and does not lead to energy exchange.

Simulation of NMR experiments. If the Hamiltonian can be regarded as time independent between t_0 and t , equation 2.20 simplifies to

$$\hat{\mathcal{U}}(t_0 \rightarrow t) = e^{-i\hat{\mathcal{H}}\Delta t}, \quad (2.22)$$

with $\Delta t = t - t_0$. Dividing the course of a pulse sequence in such Δt intervals - usually on the order of microseconds or less - allows to iteratively apply equation 2.22 to simulate numerically the evolution of a complex spin system with selected interactions and pulses²¹.

The large amount of uniformly distributed crystallite orientations in a powdered sample is taken into account by various averaging schemes described in the literature²⁶. The most common ones are the Lebedev²⁷, the Zaremba-Conroy-Wolfsberg²⁸⁻³⁰ and the REPULSION²⁶ method. The orientations provided by these methods are given as sets of weighted Euler angles, where each set describes one orientation of the CAS with respect to the LAS, and simulations are carried out for each set. Various simulation packages exist, such as SIMPSON²¹, SPINEVOLUTION³¹, GAMMA³² to name only the most common ones, and the progress in computing possibilities has greatly enhanced their capabilities during recent years³³. However, the size of the spin density matrix grows exponentially with the number of spins (eqn. 2.17) which still limits the tractable size of spin systems.

2.3 Lineshapes in solid-state NMR Spectroscopy

magic-angle spinning. All nuclear spin interactions $\hat{\mathcal{H}}_{int}$ are anisotropic in the solid state and thus depend on the orientation of the interaction tensor \mathbf{V} (eqn. 2.1) with respect to $\vec{\mathbf{B}}_0$. Since \mathbf{V} is defined by the chemical structure of a given material, mechanical rotation of the sample alters the interaction strength and thus the resonance frequency. If the rotation is sufficiently fast and the rotation axis is inclined by the so-called magic angle ($\theta_{MAS} = 54.74^\circ$) with respect to $\vec{\mathbf{B}}_0$, the time average of $\hat{\mathcal{H}}_{int}$ over a full rotor period reduces to the isotropic value σ_{iso} (eqn. 2.2) within first-order perturbation. σ_{iso} is non-zero in case of the chemical shift and the J coupling and zero for the first-order quadrupole and the direct dipole-dipole interactions, which allows to derive the isotropic chemical shift directly from high-resolution solid-state NMR spectra. This setup is called magic-angle spinning² (MAS) and is extensively used in modern NMR spectroscopy.

The effect of the uniaxial rotation is easier to understand by invoking the rotor axis system (RAS), in which the macroscopic sample rotates around

the magic-angle spinning axis. The interaction tensors \mathbf{V} of the individual nuclei are then rotated from their PAS first into a joint crystal axis system (CAS) and from there into the RAS. The latter is then rotated into the LAS, whereby this rotation becomes periodically time-dependent due to MAS^{5,21}. These successive transformations introduce a dependence on the second Legendre polynomial $P_2(\cos\theta) = \frac{1}{2} \cdot (3\cos^2\theta - 1)$ for first order perturbations of $\hat{\mathcal{H}}_{int}$ as seen e.g. in eqns. 2.7, 2.9 and 2.10. The average Hamiltonian over full rotor periods thus scales with $P_2(\cos\theta_{RL})$ where θ_{RL} represents the angle between the rotation axis and $\vec{\mathbf{B}}_0$ ⁶. When $\theta_{RL} = \theta_{MAS}$ this term and thus the average Hamiltonian becomes zero. Thus signal sampling at every rotor period leads to liquid-like spectra without anisotropic lineshapes. Sampling at non-integer multiples of the rotor period, however, leads to spinning sidebands⁵, if the spinning speed is slow enough, which will be discussed in the next section. Note that the second-order quadrupolar interaction (eqn. 2.13) also contains other terms as function of θ , which do not average under MAS, leading to anisotropic lineshapes at all spinning rates²⁵.

Lineshapes. The difference between static and MAS spectra are illustrated by numerical simulations of NMR experiments for various interactions (Fig. 2). These lead to shifts of the energy eigenstates and hence influence position and splitting of the NMR signals⁶ (Fig. 2, first column). In a single crystal all translation-related spins have the same chemical surrounding and thus the same interaction tensor \mathbf{V} as well as the same polar angles θ and ϕ for the orientation of the external field in the PAS. Hence, they give rise to the same signal and the shift of this signal depends on the orientation of the single-crystal with respect to $\vec{\mathbf{B}}_0$ (Fig. 2, second column), where the constants σ_{aniso} and η determine the frequency range (cf. eqns. 2.7, 2.9/2.10, and 2.13). Since a dipolar coupled spin pair as well as a single quadrupolar nucleus exhibit more than two energy levels with unequal energy differences, they give rise to several signals, which are affected differently by first- and second-order perturbation²⁵. For the case of non-integer I , the central transition between the $+1/2$ and $-1/2$ energy levels is only affected by the second-order coupling, whereas the satellite transitions are affected by both first and second-order shifts. Additionally, every transition exhibits a different excitation behaviour (see literature³⁴ for details).

In a static powder sample, uniform orientation distribution of the crystallites causes the whole range of possible frequencies to be present at the same time. The signal is thus the superposition of all these individual signals^{4,5}, which leads to a distinct shape of the NMR signal, the so-called powder pat-

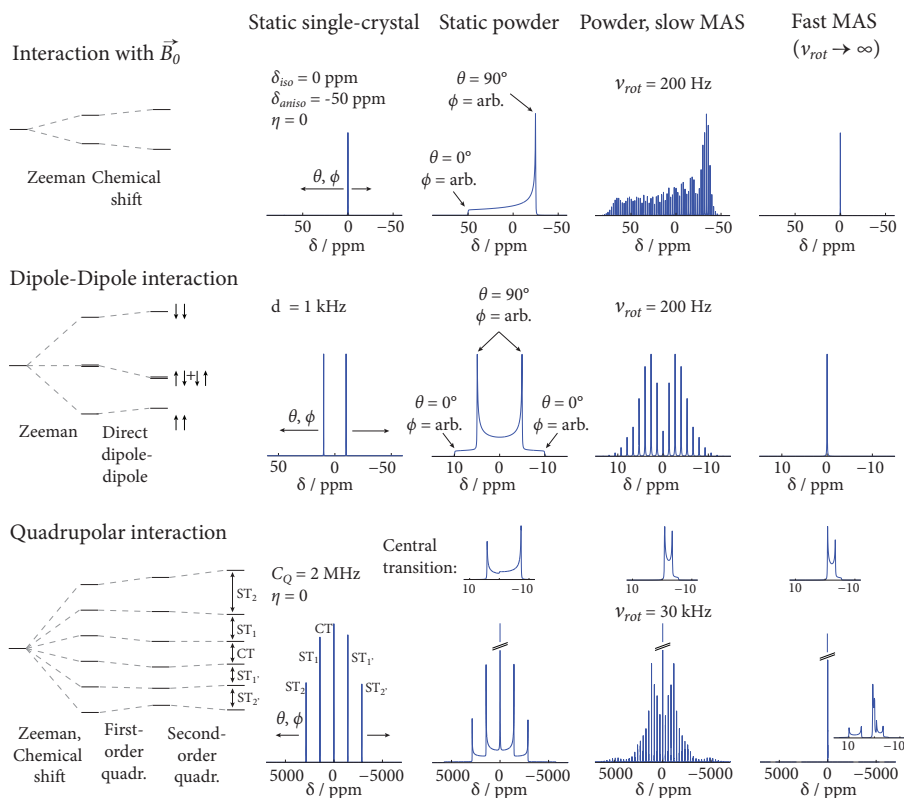


Figure 2: Influence of the spin interactions on the energy levels of $I=1/2$ nuclei (first row, left), a spin- $1/2$ pair (second row, left) and a spin- $5/2$ nucleus (third row, left) in a static \vec{B}_0 field. The energy shifts are orientation dependent and lead to a variation in the peak positions for single crystals (second column). In a powdered sample, the overlap of the signals from all orientations leads to characteristic lineshapes (third column). magic-angle spinning decomposes these into sidebands patterns, where the distance between two neighbouring lines is the spinning speed (fourth column). If the spinning is significantly faster than the interactions strength ($\omega_{rot} > 10 \cdot \sigma_{aniso}$), only the isotropic parts of the interactions remain visible (last column). For non-integer quadrupolar spins the central transition is depicted as insets above the full spectrum. For the quadrupolar coupling a magnification of the full spectrum at $\nu_{rot} \rightarrow \infty$ illustrates the difference in linewidth to the static case.

tern (Fig. 2, third column). The CSA-type powder shape changes its width with δ_{aniso} , whereas η affects the shape³⁵. For a spin-1/2 pair coupled by the direct dipolar interaction (illustrated for the homonuclear case), a so-called Pake doublet³⁶ is formed, which is the superposition of two CSA-type powder shapes with $\eta = 0$, where both pattern are reflected at the isotropic chemical shift position. For quadrupolar nuclei, the patterns arising from the different possible transitions overlap²⁵; their shapes are mostly affected by first- and second-order quadrupolar coupling as explained above. However, in some rare cases, higher order of perturbation may have a visible effect on the lineshapes.

Slow MAS leads to (partial) averaging of the different interactions and causes spinning sidebands⁵. They appear in multiples of the spinning frequency from the isotropic resonance and resemble the shape of the static powder spectrum for $\nu_{MAS} \rightarrow 0$ (Fig. 2, fourth column). Since the intensities distributed in a powder pattern are now concentrated on a finite set of signals, the intensities of such sidebands patterns are significantly higher than in a static spectrum. This is used to extract the interaction constants using e.g. the Herzfeld-Berger method³⁷ or numerical simulations with e.g. SIMPSON²¹. Sufficiently fast spinning eventually leads to full averaging of the interactions, so that only the isotropic influences on the NMR lines remain (Fig. 2, last column). For quadrupolar nuclei, this regime is often not reachable due to the high interaction strength.

3 Applications

3.1 Wideline Experiments

Since the discovery of MAS,² most of the ssNMR experiments are done with spinning. However, MAS is not always possible as for *in situ* experiments. E.g. Grey et al.³⁸ investigated silicium based lithium ion batteries *in situ* using a homemade modified static probe with a flexible plastic battery design. They observed local structural changes for the silicon electrode by following the ⁷Li NMR signal during charging and discharging the battery (Fig. 3). Compared to *ex situ* experiments,³⁸ an additional peak at -10 ppm was observed and ascribed to a reaction between the very reactive, metastable, “Li₁₅Si₄” phase with the electrolyte, via a “self-charge” mechanism.

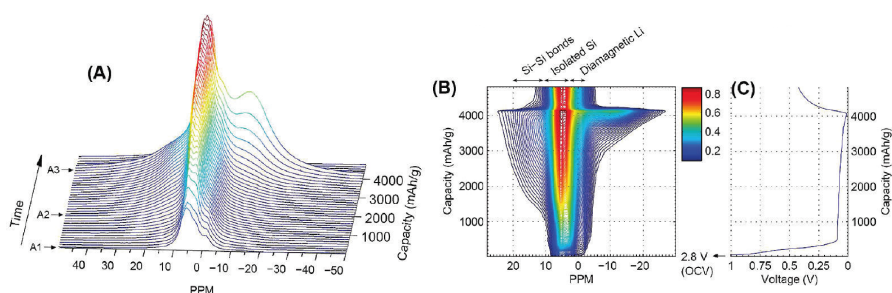


Figure 3: Stacked (A) and contour (B) plots of *in situ* ⁷Li static NMR spectra and electrochemical profile of the first discharge (C) of an actual crystalline Si // Li/Li+ battery (adapted from reference 38).

In some cases, static experiments have proven to be more useful than MAS, providing more information (e.g. via shape analysis)¹⁹. The chemical shift anisotropy and, for spin $> 1/2$, the quadrupolar interaction can be determined very precisely using static experiments. However, due to the broadness of the signal and hence the short FID, spin or quadrupolar echo experiments^{6,39} are required to compensate for the dead time of the probe (often due to acoustic ringing) which can be relatively long compared to the total length of the FID^{40,41}. In the case of ¹⁹⁵Pt NMR spectra of Pt electrocatalysts, the lineshape became so broad because of the Knight shift that even a point-by-point acquisition was necessary⁴². Nevertheless, lineshape analyses can still provide information about the surrounding geometry of the observed nuclei as shown for Ga containing intermetallic phases. In particular, the ⁶⁹Ga

and ^{71}Ga quadrupolar (and thus EFG) tensor turned out to be an excellent probe for the local electronic environment around the Ga atoms⁴³.

To enhance the usually low sensitivity of static spectra, several groups demonstrated the usefulness of the Carr-Purcell-Meiboom-Gill⁴⁴⁻⁴⁷ (CPMG or QCPMG for quadrupolar nuclei) experiment which consists of acquiring a train of echos. The Fourier transform of such an echo train resembles a spikelet spectrum with the overall shape of the regular static one and thus allows to separate the inhomogenous (e.g. CSA and quadrupolar coupling) from the homogenous (e.g. homonuclear dipolar coupling) interactions⁴⁸. The latter being represented in the width of each individual spikelet. Broad spectra can be obtained in less time with, however, the drawback of losing some precision in determining the *Chemical Shift* and the quadrupolar interaction, respectively. (Q)CPMG experiments were successfully applied on several nuclei too insensitive to be observed, even if acquired with MAS. Examples are ^{207}Pb ^{49,50}, ^{199}Hg ^{49,50}, ^{195}Pt ⁵⁰, ^{95}Mo ⁵¹, ^{14}N ⁵²....

Pines et al. developed a technique called cross-polarisation⁵³⁻⁵⁵ (CP) which enables a polarisation transfer from abundant spins I with a large γ and hence high polarisation (e.g. ^1H) to dilute spins S with low γ (e.g. ^{13}C , ^{15}N) via the heteronuclear dipolar interaction. Hereby, continuous rf irradiation on both I and S spins leads to a match of the pseudo-energy level difference in a doubly rotating frame, if the rf amplitudes are chosen in a way that the Hartmann-Hahn condition $\gamma(I)B_1(I) = \gamma(S)B_1(S)$ is fulfilled. CP has several advantages: it enhances the signal of the S spin up to a factor of $\gamma(I)/\gamma(S)$ and only requires to wait for the relaxation of the I spins which is very often much shorter than the one from the S spins making the overall experimental time much shorter.⁵³⁻⁵⁵ However, CP is not quantitative, as its signal intensities rely on several aspects including the nuclei distances ($\propto 1/r^6$) and their spin-lattice relaxation times in the rotating frame, $T_{1\rho}$. Nonetheless, CP is so powerful that it is now routinely used to observe less abundant nuclei such as ^{13}C or ^{15}N but also abundant spins like ^{31}P since the ^{31}P T_1 are often very long.^{6,56} CP can also be applied to quadrupolar nuclei, but it is more troublesome due to the presence of several possible transitions in those cases⁵⁷⁻⁵⁹.

A crucial wideline NMR application concerns the study of dynamics. Motional processes can be investigated covering more than 14 decades for the jump rates κ by analysing both spin-spin and spin-lattice relaxation ($10^{-7}\text{s}^{-1} \leq \kappa \leq 10^{-3}\text{s}^{-1}$), following lineshape changes ($10^{-12}\text{s}^{-1} \leq \kappa \leq 10^{-4}\text{s}^{-1}$) and performing 2D exchange as well as stimulated echo experiments ($10^{-4}\text{s}^{-1} \leq \kappa \leq 10^2\text{s}^{-1}$)^{6,11,60-62}. For example, Spiess et al.⁶³ used temperature dependent T_1 relaxation measurements and lineshape analyses to identify large angle jumps

as well as their rates about all 2- and 3-fold rotation axes of the tetrahedral P_4 units within the β -phase of white phosphorous at low temperatures.

Similarly, Reimer et al.⁶⁴ studied the absorption of CO_2 in the $Mg_2(dobdc)$ metal-organic framework (MOF) using ^{13}C lineshapes and the corresponding T_1 data, providing insight into the active CO_2 adsorption sites and the remaining rotational degrees of freedom for CO_2 . More importantly, 2H ($I = 1$) is ideal to investigate rotational molecular dynamics as its quadrupolar interaction mostly depends on the type of the covalent bond (e.g. CD, ND CD₃) and thus gives distinct lineshape depending on the rotational processes.⁶² In this way the anisotropic dynamics of liquid crystalline phases was characterised⁶². Also Hologne et al.⁶⁵ have identified two-site flip motions of dimethyl sulfone in the *p*-tert-butylcalix[4]arene-nitrobenzene inclusion compounds. Such studies might also be performed under MAS condition⁶⁵ or using a CPMG-like echo train to enhance the sensitivity.⁶⁶

By making additionally use of the anisotropy within relaxation processes (T_{1Z} and T_{1Q}) even for fast motional processes different jump models might be distinguished. This was done e.g. to link the reorientational dynamics of the amide ions within KND_2 salts to the macroscopic phase transitions.⁶⁷ In all phases the amide ion dynamics has to be described as a superposition of thermally activated large angle jumps and anisotropic librations with characteristic jump geometries within the monoclinic, tetragonal and cubic phases. In contrast, 2D exchange techniques allow for tracing extremely slow motional processes. In this way, the local dynamics of small molecules like benzene- d_6 or hexamethyl benzene- d_{18} within a rigid polymer matrix could be successfully studied based on 2H NMR data.⁶⁸

2D exchange experiments can also provide information about the proximity and interconnectivity of domains. For instance, the formation of two aluminophosphates frameworks, $AlPO_4-5$ and $AlPO_4-18$, has been monitored using hyperpolarised ^{129}Xe gas as a probe demonstrating an intimate contact on mesoscopic length scales between both frameworks.⁶⁹ ^{129}Xe NMR spectra⁷⁰ are also used to study pore sizes and geometry for a wide variety of porous materials such as zeolites⁷¹, nanotubes⁷² or MOFs¹⁴. Indeed, the ^{129}Xe chemical shift is very sensitive to its surroundings and, following, for example, the Fraissard model,⁷¹ one can directly relate the ^{129}Xe isotropic chemical shift with the pore sizes of zeolites.

Finally, 2D exchange wideline spectra can be used to derive connectivities and orientation correlations between neighbouring building units if the exchange is driven by spin-diffusion. The transfer rates might be enhanced and controlled by applying specific pulse sequences, such as WALTZ17^{73,74} or

BLEW12⁷⁵, during the mixing time, where one component of the transverse magnetization is spin-locked in the rotating frame. For the nucleated but still amorphous phase of the molecular glass former triphenyl phosphite, ³¹P and ¹³C (Fig. 4) rf-driven spin-diffusion spectra were measured as function of the mixing time to derive average intermolecular molecular distances, the packing density and the preferred molecular conformer^{56,76-78}.

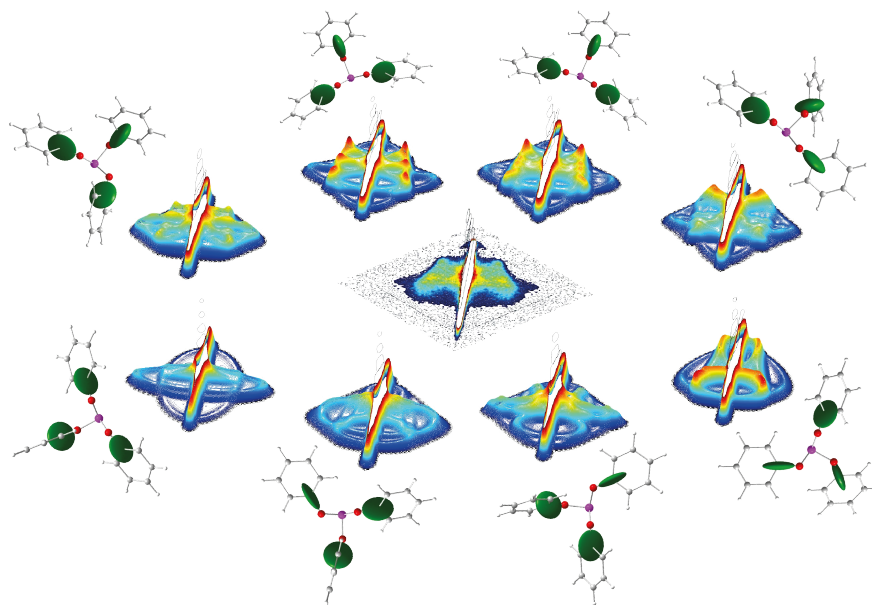


Figure 4: 2D ¹³C rf-driven spin-diffusion exchange spectra for phase aII of triphenyl phosphite. The experimental spectrum ($t_m = 10$ ms) in the centre is compared to simulated ones for possible conformers (adapted from ref. 78).

3.2 High Resolution Experiments

MAS (Section 2.3) drastically improves the spectral resolution and usually allows to distinguish different chemical environments in a sample. A prominent example is the study of zeolites, where MAS enables to resolve up to five signals in a ²⁹Si NMR spectrum⁷⁹. These signals correspond to the silicon atoms having Q⁰, Q¹, Q², Q³, and Q⁴ environments, allowing the structures

of aluminosilicate networks to be determined. Similarly, ^{31}P MAS NMR spectroscopy has been used to obtain information about the chemical bonding around PO_4 units in various phosphate glasses⁸⁰ and the isotropic ^{27}Al NMR *Chemical Shift* strongly depends on the Al coordination and nature of bonded atoms. Since ^{27}Al is very easy to observe, it has been used to study a plethora of materials¹⁵ and was for instance applied to study hydration processes of alumina cement, where the Al environment changes from tetrahedral in the dry state to octahedral when hydrated⁸¹.

Many other quadrupolar nuclei exhibit, however, broad lineshapes and have a low natural abundance, sometimes coupled with low gyromagnetic ratios, which makes them much harder to measure. Therefore, techniques were developed to increase the sensitivity. Again, QCPMG improves the signal to noise ratio^{46,47} and population transfer techniques⁸² such as RAPT⁸³, DFS⁸⁴ or HS⁵⁰ can either saturate or invert the population of the different energy levels in order to achieve the highest possible population differences for the central transition (Fig. 5). These techniques result in a theoretical signal gain of $2I$, making the experiment up to $(2I)^2$ times faster.

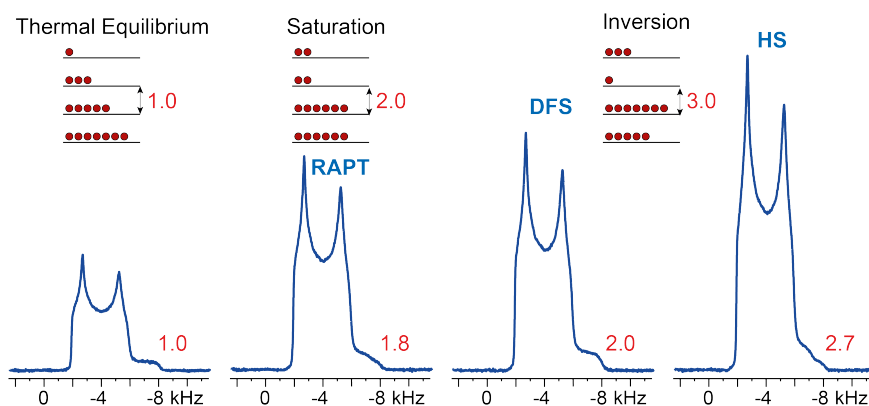


Figure 5: Top: Schematic representation of the population distribution for spin 3/2 nuclei before and after applying population transfer techniques. Bottom, left to right: Comparison of the ^{87}Rb MAS NMR signal intensity of RbClO_4 obtained with a Hahn-echo, RAPT, DFS and HS. The experimental enhancement is shown next to the spectra (adapted from ref. 50).

When the spinning speed of MAS is slower than the latitude of the nuclear

spin interactions, spinning sidebands arises, which mimics the static powder pattern (Fig. 2). Fitting those gives access to magnitude and asymmetry of the corresponding interaction and thus provide additional structural information. For example, the analysis of ^{59}Co and $^{6,7}\text{Li}$ MAS spectra of LiCoO_2 battery materials allowed to determine the quadrupolar coupling constant which was then correlated to the partial charge of the nuclei using a simple point charge model⁸⁵. The $^{6,7}\text{Li}$ chemical shift anisotropy was shown to arise from the paramagnetism of the sample. Similarly, for dehydrated and water-loaded $\text{Cu}_3(\text{BTC})_2$ MOFs differences in the ^1H - $^{63/65}\text{Cu}$ hyperfine coupling, manifesting themselves in changes of the ^1H NMR spinning side band intensities, allowed to identify the active binding sites for water⁸⁶.

Many MAS NMR experiments, in particular for low- γ nuclei in a low natural abundance, would still be very difficult to acquire without the use of CP to enhance spectral intensities. For MAS experiments, the CP Hartmann-Hahn condition differs slightly from the one for non-rotating samples to adopt the additional time dependence due to sample spinning: $\gamma(I)B_1(I) = \gamma(S)B_1(S) \pm n \cdot \nu_{\text{MAS}}$ with ($n = 1, 2, \dots$)⁸⁷. Only then, ^{15}N CP MAS NMR spectroscopy made it possible to identify the chemical building units for various semi-crystalline and amorphous carbon nitride materials, which are promising photocatalysts for water splitting⁸⁸⁻⁹⁰.

With the increased resolution of MAS, the need for even better resolution arises. For mainly two reasons, interactions might not be averaged out completely using only MAS¹⁰. First, the spinning speed may not be fast enough, which is often the case for dipolar couplings involving ^1H and ^{19}F ^{6,91-93}. Second, the interaction cannot be cancelled by spinning at the magic-angle only, which is the case e.g. for second order quadrupolar interactions^{25,94}. These problems were addressed using a variety of solutions.

When observing nuclei close to protons, ^1H heteronuclear decoupling^{95,96} needs to be applied during acquisition. While continuous wave (cw) irradiation is sufficient for non-rotating samples⁹⁷, cw appeared to be insufficient in combination with MAS and more refined multiple-pulse schemes for ^1H decoupling such as TPPM⁹⁸, SPINAL⁹⁹, XiX¹⁰⁰ and SW_f -TPPM¹⁰¹ evolved. Their common point is the application of series of pulses with flip angles close to 180° with varying phases, which introduces additional time dependencies, in turn allowing for more efficient averaging of the heteronuclear dipolar interaction. In spite of this, the gain in resolution strongly depends on the magnitude of the dipolar coupling and the internal mobility within the sample^{95,96}. The more recent decoupling sequences,¹⁰¹ usually, provide narrower resonances, with the drawback, however, of more experimental parameters needing optimisation.

Note, that when using a recoupling sequence, which simultaneously requires heteronuclear decoupling, one should only apply cw decoupling to avoid possible interferences with the recoupling¹⁰². Heteronuclear decoupling is also beneficial for other abundant $I = 1/2$ nuclei with large γ such as ^{31}P and ^{19}F and allowed for instance to distinguish pharmaceutical polymorphs with only small differences in the isotropic *Chemical Shifts*¹⁰³. For quadrupolar nuclei specific heteronuclear decoupling sequences were developed^{104,105}. Combining ^1H and ^{27}Al decoupling, for instance, greatly improved the resolution of ^{31}P NMR spectra for AlPO_4 -14.¹⁰⁶

To improve the resolution for spin systems with dominant homonuclear dipole interactions, like ^1H and ^{19}F , is more challenging since detection and decoupling has to be managed on the same channel. To circumvent this problem, homonuclear decoupling was initially used in a 2D fashion with the decoupling sequence being applied in the indirect dimension (t_1 domain) of a 2D separation experiment¹⁰⁷. The first scheme developed is the Lee-Goldburg (LG) sequence¹⁰⁸. It relies on an off-resonance cw pulse with a frequency offset $\Delta\omega = \omega_1/\sqrt{2}$ with ω_1 being the rf field strength. This causes the spins to rotate around an effective field $\omega_{eff} = \sqrt{\omega_1^2 + \Delta\omega^2}$ tilted away from the static field direction by the magic angle. The zero-order average of the dipolar Hamiltonian vanishes in such a case, resulting in an enhanced line narrowing.

When combined with MAS, so-called CRAMPS (combined rotation and multiple-pulse sequences) experiments arise⁵. The earliest sequence with windows, to enable detection on the same channel, is WHH-4¹⁰⁹. It is based on a repetitive cycle of four 90° pulses applied in different directions of the rotating frame by adapting the pulse phases and having two different inter-pulse delays, which allow to average the homonuclear interaction while retaining but scaling the chemical shift⁵. Based on this idea, more stable sequences such as MREV-8^{110,111}, BR-24¹¹², BLEW12⁷⁵, MSHOT-3¹¹³, FSLG¹¹⁴, symmetry-based R and C sequences^{115,116}, PMLG¹¹⁷ and DUMBO¹¹⁸ (a numerically optimized continuous phase modulation) were developed. They all have their effective field tilted away from the static field direction by a certain angle α , which reduces shift interactions by the so-called scaling factor. When α is equal to the magic-angle (e.g for LG, WHH-4, PMLG, DUMBO), the theoretical scaling factor is $1/\sqrt{3}$. Other sequences, with different α , lead to other scaling factors such as $\sqrt{2}/3$ for MREV-8¹⁹. For further details please refer to the following reviews^{107,119,120}. Homonuclear techniques have been broadly applied to organic molecules^{121,122}, drugs¹²³⁻¹²⁵, inorganic-organic hybrid materials¹²⁶ and inorganic compounds¹²⁷ where they are often used in combination with 2D recoupling sequences.

The 2nd order quadrupolar interaction might also significantly broaden the NMR spectrum⁹⁴. However, it is inversely proportional to B_0 and thus is diminished by going to higher fields, as shown by Gan et al.¹²⁸. Nevertheless, in most cases B_0 is not large enough and additional techniques have to be applied to reach narrow lines. The 2nd order effect cannot be averaged solely by MAS since it also depends on the 4th rank Legendre polynom (line 4 in eq. 2.13) which requires spinning at angles of 70.12° or 30.56°. The obvious solution is to rotate the sample at two angles at the same time. This is done by DOR¹²⁹, which consists of two rotors: an outer one inclined at the magic-angle and an inner one inclined at 70.12° or 30.56°. Another solution, DAS,¹³⁰ uses only one rotor, which toggles between two angles (37.38° and 79.19°) for two equal period of times with a z-filter inbetween. Using ²³Na DOR experiments, the structures of two sodium diphosphates ($\text{Na}_4\text{P}_2\text{O}_7$ and $\text{Na}_3\text{HP}_2\text{O}_7 \cdot \text{H}_2\text{O}$) could be refined based on 2D ²³Na spin-diffusion correlation spectra as function of the mixing time¹³¹.

In 1995, Frydman et al.^{132,133} showed that, by manipulating the spin part of the Hamiltonian during MAS, one can obtain high-resolution in a so-called 2D MQMAS experiment by correlating a multiple-quantum transition such as 3Q ($-3/2 \leftrightarrow +3/2$) and 5Q ($-5/2 \leftrightarrow +5/2$)¹³⁴ with the single-quantum coherence. Later, Gan¹³⁵ introduced the STMAS method, which correlates single-quantum satellite transitions with the central one. STMAS has been shown to often have an improved signal-to-noise ratio over MQMAS.¹³⁶ However, it is very sensitive to setting the magic-angle precisely and is more sensitive to dynamical processes.¹³⁶ Both MQMAS and STMAS have been improved over the years and several variants are now available, such as z-filter¹³⁷ or SPAM-MQMAS¹³⁸, DQF STMAS,¹³⁹ using shearing⁴ or split-t1¹⁴⁰ schemes. More detailed are found in refs. 136,141 and 142. Both techniques are meanwhile indispensable for a wide range of materials containing quadrupolar nuclei^{15,94}. For example, ¹⁷O MAS and MQMAS experiments allowed to distinguish the six polymorphs of MgSiO_3 demonstrating the sensitivity of the ¹⁷O quadrupole interaction towards its local environment¹⁴³. For orthoenstatite, all six ¹⁷O sites could be resolved (Fig. 6) revealing dependencies between the ¹⁷O chemical shift, the quadrupolar coupling constant and the coordination environment as well as the Si-O bond-length.

As mentioned previously, the analysis of spinning sideband patterns (ssbps) provides additional valuable information about structural and dynamical aspects. To derive proper parameters becomes difficult, however, if the ssbps of several signals overlap to heavily for an unambiguous deconvolution of 1D spectra as is often the case for ¹³C NMR spectra of organic molecules and

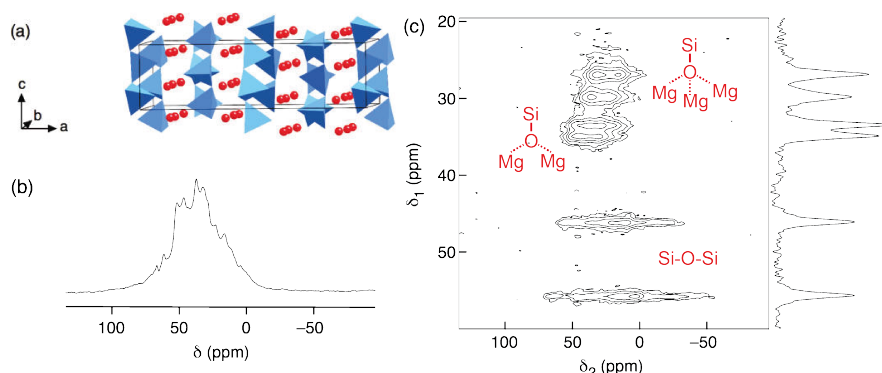


Figure 6: (a) Structure of orthoenstatite (MgSiO_3) with its corresponding (b) ^{17}O MAS and (c) ^{17}O MQMAS spectra (adapted from ref. 143).

drugs^{103,144,145}. For quadrupolar nuclei with strong 2nd order effects, additionally, the signal of the central transition becomes too broad and overlaps with the ssbbs of the satellites^{146,147}. In those cases, spinning sidebands separation techniques are helpful. E.g. the 2D PASS experiment¹⁴⁸ separates the CSA from isotropic chemical shifts. It is based on a row of π pulses with varying interpulse distances. Changing the timing between the pulses allows for the isotropic part of the chemical shift to evolve and the ssbbs are sorted according to their order in 1D slices. A similar sequence, QPASS¹⁴⁶, has been developed for quadrupolar nuclei and was used for example on ^{71}Ga of GaPO_4 quartz¹⁴⁷.

The CSA can also be recoupled when using fast MAS and two classes of pulse schemes may be differentiated. The first one recouples CSA during the indirect dimension of a 2D MAS experiment, while recording high-resolution MAS spectra in the direct dimension. The earliest sequences in this respect used rotor-synchronized pulses^{149,150}. Subsequently, CODEX^{151,152} was developed, which is particularly valuable for probing dynamical processes^{151,153}. Similar recoupling schemes^{154–156} differ mainly in the type of the recoupling pulses. Rotary resonance¹⁵⁷, phase-shifted FSLG¹⁵⁸ and symmetry-based recoupling^{159–161} might also be used to recouple the CSA with the advantage that also the homonuclear interaction can be suppressed. The second class also records 2D MAS spectra with high resolution in the direct dimension, but creates ssbbs in the indirect dimension with an apparent sample spinning

$\nu_{app} = \nu_{MAS}/s$ reduced by an adjustable factor s compared to the actual spinning speed ν_{MAS} . These might alternatively be viewed as an magnification of the CSA in the indirect dimension^{162–170}.

3.3 Dipolar Recoupling Experiments

The gain in resolution obtained through MAS is accompanied by an undesired loss of information, since MAS reduces or cancels the anisotropic parts of interactions, containing valuable information about molecular orientations, distances and connectivities^{12,144}. Extensive efforts were, therefore, made to selectively reintroduce desired interactions by preventing their averaging, while others remain suppressed⁹. This concept is called recoupling and utilises the fact, that the time-dependence of \mathbf{V} (eqn. 2.1) may be accompanied by a periodically time-dependent spin manipulation or interaction which interferes with MAS. Additionally, spin interactions behave differently under spin or space rotations, as characterised by their space and spin rank¹¹⁵. For instance, if the space-part averaging by MAS is accompanied by a rotation of the spin parts $\vec{\mathbf{I}}$ and/or $\vec{\mathbf{J}}$ by precisely timed, periodically repeated pulses, both rotations interfere. For defined time intervals the effective Hamiltonian might then be calculated using Average Hamiltonian Theory^{171,172} and Floquet theory¹⁷³, respectively, allowing to tune pulse sequences so that only desired interactions are recoupled^{22,174}.

The majority of recoupling sequences focus on the reintroduction of homo- and heteronuclear dipole-dipole interactions for $I = 1/2$ nuclei. They allow to measure distances in case of small clusters as well as isolated spin pairs and probe distance sums for dense extended spins systems, respectively. Additionally, "through-space" or "through-bond" connectivities might be derived from 2D correlation spectra^{12,175}, depending on whether the direct dipole interaction or the J coupling is recoupled¹². Although the principles of recoupling also apply to quadrupolar interactions, its magnitude causes severe perturbations¹⁷⁶ (since already the averaging of it by MAS is incomplete) and hence many sequences may only provide qualitative results^{176,177}.

Homonuclear dipolar recoupling. Homonuclear dipolar recoupling (HomDR) experiments¹⁷⁸ are frequently used for structural investigations. They may be applied either to abundant nuclei (such as ^1H , ^{31}P and ^{19}F)^{102,126,179} or rare spins (like ^{13}C , ^{15}N and ^{29}Si)^{181,182}. Due to usually strong signal intensities, the former are easier to record with the drawback, that dense arrangements of NMR-active nuclei require large spin systems for proper simulations

with the potential to give access to quantitative structural data^{102,180}. In contrast, if the sensitivity issue can be overcome, HomDR measurements on rare spins are particularly powerful, since they allow to derive individual distances based on simple two spin system simulations¹⁸²⁻¹⁸⁴.

The simplest HomDR method is rotational resonance^{185,186} (R^2). For MAS experiments, the B-terms within eqn. 2.9 is reintroduced even in the absence of rf fields, when the chemical shift difference between two spins, coupled by the direct homonuclear dipolar interaction, matches a multiple of the spinning speed, which manifests in broadening the resonance lines¹⁸⁵. The accompanied magnetisation exchange between spins by energy conserving flip-flop processes - also referred to as zero-quantum (ZQ) transfer or spin-diffusion - was used to determine intramolecular ^{13}C - ^{13}C distances as in zinc acetate¹⁸⁶. The rotational resonance condition may also be reintroduced by spin echos as for radio-frequency driven dipolar recoupling^{187,188} (RFDR) and variants like the finite pulse RFDR (fpRFDR)¹⁸⁹. In particular, working with finite real pulses has proven to be significantly more robust and broad-banded than the basic R^2 scheme. As such RFDR was used to obtain spatial proximities e.g. in the metal-organic framework MIL-121¹⁹⁰ and phosphate glasses¹⁹¹. Usually, when simulating ZQ recoupling schemes, spins within a distance of several tens of angstrom around a central probe nucleus have to be taken into account¹⁹². This makes density matrix simulations of NMR observables quite demanding and is only possible for special cases exhibiting isolated small clusters as for ^{13}C labelled p-Xylene/Dianin inclusion compounds¹⁹³. Alternatively, a phenomenological rate matrix approach¹⁹⁴, treating the spin exchange as classic diffusion problem, is commonly employed, as e.g. for SrP_2N_4 , where ^{31}P fpRFDR exchange spectra measured as function of the mixing time allowed to confirm the network topology of corner sharing PO_4 tetrahedra¹⁹².

Instead of rf-pulses, strong heteronuclear dipole interactions like ^1H -X may be used to broaden the X resonance and thus counterbalance chemical shift differences and MAS leading to proton-driven spin-diffusion variants of rotational resonance¹⁹⁵⁻¹⁹⁷ (PDSD). Quantitative evaluation of such experiments are difficult^{198,199} since the exchange kinetics now depends on both the efficiency of the energy match and the distance sums. For the detection of connectivities PDSD is a valuable tool and was, for instance, used as restraints in the structure solution of proteins²⁰⁰, as a cost function for *ab initio* structure solution in combination with quantum chemical modelling²⁰¹, and to investigate local order in polymers¹⁹⁴. Additionally, ^1H -X couplings are actively reintroduced by rf fields dipolar-assisted rotational resonance²⁰² (DARR) to adjust to higher MAS spinning speeds. This sequence is often used for proteins²⁰³ to detect

through-space connectivities⁹ up to 10 Å.

Alternatively to ZQ recoupling, the use of double-quantum (DQ) schemes were developed^{10,179}. While the former allows to treat large spin systems with weak dipolar couplings using kinetic matrices, the latter is advantageous and more accurate for small spin clusters and shorter distances. Most DQ sequences truncate small dipolar interactions in the presence of strong dipole ones, and may not be detected under these circumstances any more²⁰⁴. DQ recoupling was first used in dipolar recovery at the magic angle²⁰⁵ (DRAMA), where the interference of rf pulses synchronised with the periodic manipulation of the interaction tensor reintroduces DQ homonuclear dipolar interaction terms. This sequence is sensitive to CSA and thus more robust schemes like homonuclear rotary resonance²⁰⁶ (HORROR), its adiabatic version dipolar recoupling enhanced by amplitude modulation²⁰⁷ (DREAM) and the dipolar recoupling with a windowless sequence²⁰⁸ (DRAWS) were developed. Here, continuous rf irradiation is used to cause interferences when the rf nutation frequency matches the spinning speed. These sequences were very successfully employed for determination of torsion angles²⁰⁹ and distances²¹⁰ in biological macromolecules, for distance measurements in crystalline organic solids such as nucleic acids²¹¹ and cytidines²¹², or to detect Li-Li proximities in lithium overstoichiometric ($x > 1$) Li_xCoO_2 battery materials²¹³.

The back-to-back (BABA) sequence^{214,215} uses short 90° pulses instead of a continuous irradiation to achieve HomDR. Therefore, it is well-suited for fast MAS and long recoupling times, where high power during continuous irradiation may not be feasible. It was applied to probe through-space proton connectivities in $\text{Ba}(\text{ClO}_3)_2 \cdot \text{H}_2\text{O}$ salts²¹⁶, the local connectivities of PO_4 polyhedra in phosphate glasses²¹⁷ or to investigate ^{31}P - ^{31}P distances in magnesiumultraphosphate²¹⁵ $\text{MgP}_4\text{O}_{11}$. Various other sequences employing DQ and ZQ recoupling were identified by applying symmetry arguments^{22,183,184,218,219}. This resulted in a variety²²⁰ of R and C sequences, which allowed to specifically recouple selected terms of arbitrary spin interactions, including robust pulse schemes for HomDR. The POST-C7, R14₂⁶ and SR26₄¹¹ sequences proved valuable tools for structure elucidation in inorganic CN materials²²¹, zeolites^{182,222}, fluorinated organic materials¹⁰² or phosphate glasses²²³. In particular, the compensation for CSA and pulse imperfections due to supercycling²²⁴ allows to measure weak dipolar couplings on the order of a few tens of Hertz, which was essential for the structure elucidation of supramolecular nano-objects consisting of 1,3,5-tris(2,2-dimethylpropionyl amino)benzene (BTA) additives within the bulk and *i*PP/BTA composites (Fig. 7)^{181,225}.

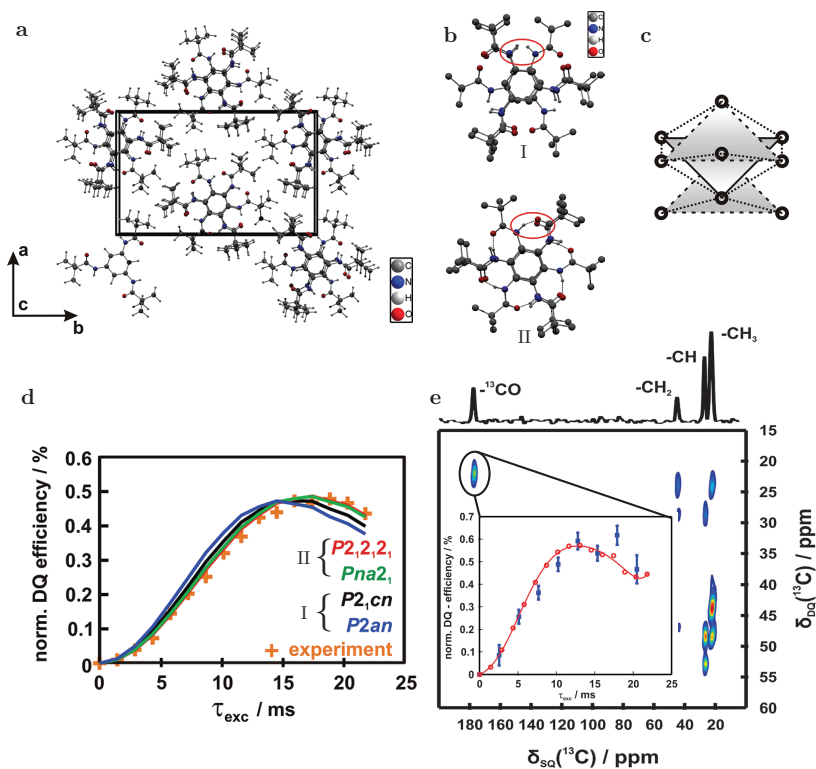


Figure 7: **a:** Potential structure models derived from powder X-ray diffraction for neat BTA. **b:** In all cases columnar stacks of molecules are formed either without (I) or with (II) intermolecular hydrogen bonds. **c:** From these models, nine-spin systems (black circles) were extracted by selecting three subsequent molecules (grey triangles) within each stack for simulating ^{13}C DQ build-up curves. **d:** Comparison between the experimental and simulated DQ build-ups strongly favour stacks with a helical hydrogen bond network (topology II). **e:** Build-up curve for the autocorrelation signal of the additives in the polymer composite at a concentration of 0.1 wt-% (blue markers, inset) confirms the existence of similar stacks. Red circles (inset) depict the neat additive for comparison. The BTA was ^{13}C enriched at the $\text{C}=\text{O}$ position for these NMR experiments (We acknowledge the SFB 840 for funding).

Heteronuclear dipolar recoupling. Heteronuclear dipolar recoupling (HetDR) covers a range of powerful methods for polarisation enhancement and structural investigations. The aforementioned CP technique may be used to

detect through-space connectivities and for spectral editing for inorganic and organic materials^{12,144,226}. The Lee-Goldburg CP²²⁷ (LG-CP) adds homonuclear decoupling on the *I* channel to suppress spin-diffusion, which enables to determine heteronuclear *I-S* distances more accurately²²⁸. Additionally, it might be used in a spectral-editing fashion by selectively transferring polarisation to nearest neighbouring spins e.g. to improve the assignment of small organic molecules²²⁹. Rotary resonance recoupling^{230,231} (R^3) and improved versions using amplitude and phase modulations²³²⁻²³⁴ recouple the heteronuclear dipolar interaction by matching the sample rotation with the nutation frequency of the spin-locked nuclei of one of the two targeted spin species. This, for instance, allowed to measure heteronuclear ^1H - ^{13}C distances of directly bonded pairs in adamantane, ferrocene and hexamethylbenzene²³⁵.

Echo double-resonance schemes, such as spin-echo double resonance^{236,237} (SEDOR) for static samples and the MAS experiments rotational-echo double resonance^{238,239} (REDOR) as well as transferred-echo double resonance²⁴⁰ (TEDOR) apply cleverly timed rf pulses to avoid averaging *I-S* dipolar couplings. They can be used to determine *I-S* spin pair distances in selectively enriched materials and provide heteronuclear connectivities, distance sums and other geometric information for extended spin systems. For instance, ^{23}Na - ^7Li SEDOR was used to investigate the cation clustering in mixed-alkali disilicate glasses²⁴¹ by analysing second moments. For MAS, REDOR allowed to analyse the heterogeneous mesoscale spatial apportionment of functional groups in mixed linker MOFs by comparing the experimental dephasing to spin pair simulations for structural models with ordered and disordered linker arrangements²⁴². Furthermore, it is frequently used to derive distance and other geometric restraints in a variety of organic natural products²⁴³. TEDOR with its better background suppression was, employed to unravel the lithium ion coordination sites in a lithium-glycine-water complex by extracting Li-C distances from 2D experiments²⁴⁴ and to demonstrate the influence of side-group functionalisation of poly(arylene vinylene) copolymers on the molecular packing and hence on the hole mobility in organic thin-film transistors²⁴⁵.

The aforementioned symmetry-based R and C sequences^{22,183,184,218,219} also allow to recouple the heteronuclear dipolar interaction. The PRESTO scheme²⁴⁶, like LG-CP, uses transfer of heteronuclear polarisation to estimate distances and connectivities, while suppressing undesired homonuclear dipole-dipole couplings and in particular strong CSA interactions. E.g. PRESTO was used to assign chemical groups in supramolecular assemblies²⁴⁷ and in functionalised MOFs¹²⁶. The supercycled symmetry-based SR_1^2 sequence^{219,248} was applied to measure three-dimensional ^{13}C - ^{14}N HETCOR experiments²⁴⁹

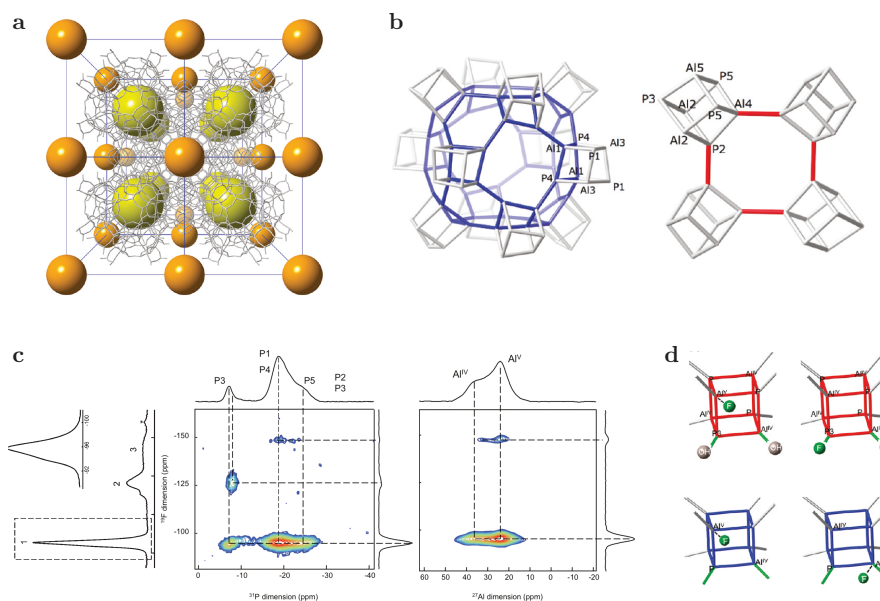


Figure 8: **a:** The framework of fluorinated aluminophosphate cloverite¹⁸⁰ exhibits pores (yellow spheres) and channels (filled with orange spheres). **b:** The basic building units in this structure are double 4-rings (D_4R), which form cubic cages. Two different D_4R types exist due to the two different ways of connecting them. **c:** The 1D ^{19}F MAS as well as the 2D ^{19}F - ^{31}P and ^{19}F - ^{27}Al HETCOR spectra (from left to right) reveal three distinct ^{19}F signals. The ^{19}F assigned to peak 1 are in close proximity with both the Al and the P atoms, whereas the ones for resonances 2 and 3 are either connected to Al or to P. This indicates that F_1 is trapped in the D_4R cages while F_2 and F_3 are covalently bonded to either Al or P thus interrupting the framework. **d:** Possible configurations for the two types of D_4R units (red, blue) with terminal OH and F outside of the cages.

in a HMQC-like way^{250,251}, in spite of the low γ and large C_Q of ^{14}N . In a fluorinated Al-cloverite¹⁸⁰ (Fig. 8a) ^{31}P - ^{27}Al , ^1H - ^{31}P , ^{19}F - ^{31}P and ^{19}F - ^{27}Al CP HETCOR experiments allowed to link the periodic framework to a nonperiodic subnetwork of fluorine. Two kinds of fluorine atoms have to be distinguished: F^- ions trapped in D_4R units (F_1) and F atoms (F_2 and F_3) covalently bonded to terminal Al or P atoms and which interrupt the AlPO network.

Bibliography

- [1] G. E. Pake, *J. Chem. Phys.*, **16**, 327 (1948).
- [2] E. R. Andrew, A. Bradbury, R. G. Eades, *Nature*, **182**, 1659 (1958).
- [3] R. R. Ernst, W. A. Anderson, *Rev. Sci. Instrum.*, **37**, 93 (1966).
- [4] R. R. Ernst, G. Bodenhausen, A. Wokaun, *Principles of nuclear magnetic resonance in one and two dimensions*, Clarendon Press, Oxford (1991).
- [5] U. Haeberlen, *High resolution NMR in solids: selective averaging*, Academic Press, New York and London (1976).
- [6] K. Schmidt-Rohr, H. W. Spiess, *Multidimensional solid-state NMR and polymers*, Academic Press, London and San Diego (1994).
- [7] J. Schaefer, E. O. Stejskal, *J. Am. Chem. Soc.*, **98**, 1031 (1976).
- [8] A. E. Bennett, R. G. Griffin, S. Vega, in P. Diehl, E. Fluck, H. Günther, R. Kosfeld, J. Seelig, editors, *NMR Basic Principles and Progress*, volume 33, 1–77, Springer Berlin Heidelberg (1994).
- [9] G. de Paepe, *Annu. Rev. Phys. Chem.*, **63**, 661 (2012).
- [10] M. J. Duer, *Introduction to solid-state NMR spectroscopy*, Blackwell, Oxford and Malden (2004).
- [11] H. W. Spiess, in P. Diehl, E. Fluck, R. Kosfeld, editors, *NMR Basic Principles and Progress*, volume 15, 55–214, Springer Berlin Heidelberg (1978).
- [12] C. Martineau, J. Senker, F. Taulelle, *Annu. Rep. NMR Spectrosc.*, **82**, 1 (2015).
- [13] M. B. Mesch, K. Bärwinkel, Y. Krysiak, C. Martineau, F. Taulelle, R. B. Neder, U. Kolb, J. Senker, *Chem. Eur. J.*, **22** (2016).
- [14] H. Hoffmann, M. Debowski, P. Müller, S. Paasch, I. Senkovska, S. Kaskel, E. Brunner, *Materials*, **5**, 2537 (2012).
- [15] K. J. D. MacKenzie, M. E. Smith, *Multinuclear solid-state NMR of inorganic materials*, Pergamon (2002).

- [16] A. Abragam, *The principles of nuclear magnetism*, Clarendon Press, Oxford (1994).
- [17] R. E. Wasylshen, *Dipolar and Indirect Coupling: Basics*, eMagRes, John Wiley & Sons, Ltd. (2009).
- [18] C. P. Slichter, *Principles of magnetic resonance*, Springer, Berlin and Heidelberg (1990).
- [19] M. Mehring, *Principles of High Resolution NMR in Solids*, Springer-Verlag, Berlin (1983).
- [20] M. H. Levitt, *Spin dynamics - Basics of nuclear magnetic resonance*, Wiley, Chichester (2008).
- [21] M. Bak, J. T. Rasmussen, N. C. Nielsen, *J. Magn. Reson.*, **147**, 296 (2000).
- [22] M. H. Levitt, *J. Chem. Phys.*, **128**, 52205 (2008).
- [23] J. C. Facelli, *Shielding Calculations*, eMagRes, John Wiley & Sons, Ltd. (2007).
- [24] L. B. Casabianca, A. C. de Dios, *J. Chem. Phys.*, **128**, 052201 (2008).
- [25] P. P. Man, *Quadrupolar interactions*, eMagRes, John Wiley & Sons, Ltd. (2007).
- [26] M. Bak, N. C. Nielsen, *J. Magn. Reson.*, **125**, 132 (1997).
- [27] Eden, Levitt, *J. Magn. Reson.*, **132**, 220 (1998).
- [28] S. K. Zaremba, *Ann. Mat. Pur. Appl.*, **73**, 293 (1966).
- [29] H. Conroy, *J. Chem. Phys.*, **47**, 5307 (1967).
- [30] V. B. Cheng, *J. Chem. Phys.*, **59**, 3992 (1973).
- [31] M. Veshtort, R. G. Griffin, *J. Magn. Reson.*, **178**, 248 (2006).
- [32] S. A. Smith, T. O. Levante, B. H. Meier, R. R. Ernst, *J. Magn. Reson. A*, **106**, 75 (1994).

- [33] Z. Tošner, R. Andersen, B. Stevansson, M. Edén, Nielsen, Niels Chr., T. Vosegaard, *J. Magn. Reson.*, **246**, 79 (2014).
- [34] R. Hajjar, Y. Millot, P. P. Man, *Prog. Nucl. Magn. Res. Sp.*, **57**, 306 (2010).
- [35] D. M. Grant, *Chemical Shift Tensors*, eMagRes, John Wiley & Sons, Ltd. (2007).
- [36] R. E. Wasylshen, *Dipolar and Indirect Coupling Tensors in Solids*, eMagRes, John Wiley & Sons, Ltd. (2007).
- [37] J. Herzfeld, A. E. Berger, *J. Chem. Phys.*, **73**, 6021 (1980).
- [38] B. Key, R. Bhattacharyya, M. Morcrette, V. Seznec, J.-m. Tarascon, C. P. Grey, *J. Am. Chem. Soc.*, **131**, 9239 (2009).
- [39] E. L. Hahn, *Phys. Rev.*, **80**, 580 (1950).
- [40] M. L. Buess, G. L. Petersen, *Rev. Sci. Instrum.*, **49**, 1151 (1978).
- [41] C. Jaeger, F. Hemmann, *Solid State Nucl. Mag.*, **63**, 13 (2014).
- [42] Y. Tong, C. Belrose, A. Wieckowski, E. Oldfield, *J. Am. Chem. Soc.*, **119**, 11709 (1997).
- [43] F. Haarmann, K. Koch, P. Jeglič, O. Pecher, H. Rosner, Y. Grin, *Chem. Eur. J.*, **17**, 7560 (2011).
- [44] H. Y. Carr, E. M. Purcell, *Phys. Rev.*, **94**, 630 (1954).
- [45] S. Meiboom, D. Gill, *Rev. Sci. Instrum.*, **29**, 688 (1958).
- [46] F. H. Larsen, H. J. Jakobsen, P. D. Ellis, N. C. Nielsen, *J. Chem. Phys. A*, **101**, 8597 (1997).
- [47] R. Siegel, T. T. Nakashima, R. E. Wasylshen, *Concept Magn. Reson. A*, **26A**, 62 (2005).
- [48] M. M. Maricq, J. S. Waugh, *J. Chem. Phys.*, **70**, 3300 (1979).
- [49] I. Hung, A. J. Rossini, R. W. Schurko, *J. Chem. Phys. A*, **108**, 7112 (2004).

- [50] R. Siegel, T. T. Nakashima, R. E. Wasylshen, *J. Phys. Chem. B*, **108**, 2218 (2004).
- [51] M. M. Forgeron, R. E. Wasylshen, *Phys. Chem. Chem. Phys.*, **10**, 574 (2008).
- [52] L. A. O'Dell, R. W. Schurko, *Chem. Phys. Lett.*, **464**, 97 (2008).
- [53] R. S. Hartmann, E. L. Hahn, *Phys. Rev.*, **128**, 2042 (1962).
- [54] A. Pines, M. G. Gibby, J. S. Waugh, *J. Chem. Phys.*, **56**, 1776 (1972).
- [55] A. Pines, M. Gibby, J. S. Waugh, *J. Chem. Phys.*, **59**, 569 (1973).
- [56] J. Senker, E. Rössler, *Chem. Geol.*, **174**, 143 (2001).
- [57] S. E. Ashbrook, M. J. Duer, *Concept Magn. Reson. A*, **28A**, 183 (2006).
- [58] A. J. Vega, *J. Magn. Reson.*, **96**, 50 (1992).
- [59] S. Vega, *Phys. Rev. A*, **23**, 3152 (1981).
- [60] K. Saalwaechter, *Prog. Nucl. Mag. Res. Sp.*, **51**, 1 (2007).
- [61] M. Vogel, P. Medick, E. Rössler, in G. Webb, editor, *Ann. R. NMR. S.*, volume 56, 231–299, Academic Press (2005).
- [62] G. L. Hoatson, R. L. Vold, in *NMR Basic Principles and Progress*, volume 32, 1–67, Springer Berlin Heidelberg, Berlin, Heidelberg (1994).
- [63] H. W. Spiess, R. Groseanu, H. Haeberlen, *Chem. Phys.*, **6**, 226 (1974).
- [64] X. Kong, E. Scott, W. Ding, J. A. Mason, J. R. Long, J. A. Reimer, *J. Am. Chem. Soc.*, **134**, 14341 (2012).
- [65] M. Hologne, J. Hirschinger, *Solid State Nucl. Mag.*, **26**, 1 (2004).
- [66] F. H. Larsen, H. J. Jakobsen, P. D. Ellis, N. C. Nielsen, *Chem. Phys. Lett.*, **292**, 467 (1998).
- [67] J. Senker, *Solid State Nucl. Mag.*, **26**, 22 (2004).
- [68] R. Böhmer, G. Diezemann, G. Hinze, E. A. Rössler, *Prog. Nucl. Mag. Res. Sp.*, **39**, 191 (2001).

- [69] D. N. Sears, B. A. Demko, K. J. Ooms, R. E. Wasylshen, Y. Huang, *Chem. Mater.*, **17**, 5481 (2005).
- [70] C. J. Jameson, *Xe NMR*, eMagRes, John Wiley & Sons, Ltd. (2009).
- [71] J. Fraissard, *Microporous Materials and Xenon-129 NMR*, eMagRes, John Wiley & Sons, Ltd. (2007).
- [72] K. Romanenko, A. Fonseca, S. Dumonteil, J. Nagy, J.-B. d'Espinose de Lacaillerie, O. Lapina, J. Fraissard, *Solid State Nucl. Mag.*, **28**, 135 (2005).
- [73] P. Robyr, B. Meier, R. Ernst, *Chem. Phys. Lett.*, **162**, 417 (1989).
- [74] P. Robyr, M. Tomaselli, J. Straka, C. Grob-Pisano, U. Suter, B. Meier, R. Ernst, *Mol. Phys.*, **84**, 995 (1995).
- [75] D. Burum, M. Linder, R. Ernst, *J. Magn. Reson.*, **44**, 173 (1981).
- [76] J. Senker, L. Seyfarth, J. Voll, *Solid State Sci.*, **6**, 1039 (2004).
- [77] J. Senker, J. Sehnert, S. Correll, *J. Am. Chem. Soc.*, **127**, 337 (2005).
- [78] J. Sehnert, J. Senker, *Chem. Eur. J.*, **13**, 6339 (2007).
- [79] J. Klinowski, S. Ramdas, J. M. Thomas, C. A. Fyfe, J. S. Hartman, *J. Chem. Soc. Farad. T. 2*, **78**, 1025 (1982).
- [80] R. Kirkpatrick, R. K. Brow, *Solid State Nucl. Mag.*, **5**, 9 (1995).
- [81] T. Luong, H. Mayer, H. Eckert, T. I. Novinson, *J. Am. Ceram. Soc.*, **72**, 2136 (1989).
- [82] R. Siegel, T. T. Nakashima, R. E. Wasylshen, *Concept Magn. Reson. A*, **26A**, 47 (2005).
- [83] Z. Yao, H.-T. Kwak, D. Sakellariou, L. Emsley, P. J. Grandinetti, *Chem. Phys. Lett.*, **327**, 85 (2000).
- [84] A. Kentgens, R. Verhagen, *Chem. Phys. Lett.*, **300**, 435 (1999).
- [85] R. Siegel, J. Hirschinger, D. Carlier, S. Matar, M. Ménétrier, C. Delmas, *J. Chem. Phys. B*, **105**, 4166 (2001).

- [86] F. Gul-E-Noor, B. Jee, A. Pöppl, M. Hartmann, D. Himsl, M. Bertmer, *Phys. Chem. Chem. Phys.*, **13**, 7783 (2011).
- [87] E. Stejskal, J. Schaefer, J. Waugh, *J. Magn. Reson.*, **28**, 105 (1977).
- [88] L. Seyfarth, J. Senker, *Phys. Chem. Chem. Phys.*, **11**, 3522 (2009).
- [89] L. Seyfarth, J. Seyfarth, B. V. Lotsch, W. Schnick, J. Senker, *Phys. Chem. Chem. Phys.*, **12**, 2227 (2010).
- [90] E. Wirnhier, M. B. Mesch, J. Senker, W. Schnick, *Chem. Eur. J.*, **19**, 2041 (2013).
- [91] C. S. Zehe, R. Siegel, J. Senker, *Solid State Nucl. Mag.*, **65**, 122 (2015).
- [92] C. Vinod Chandran, P. K. Madhu, P. Wormald, T. Bräuniger, *J. Magn. Res.*, **206**, 255 (2010).
- [93] S. A. Carss, U. Scheler, R. K. Harris, P. Holstein, R. A. Fletton, *Magn. Reson. Chem.*, **34**, 63 (1996).
- [94] R. E. Wasylshen, S. E. Ashbrook, S. Wimperis, *NMR of Quadrupolar Nuclei in Solid Materials*, WILEY-VCH Verlag (2012).
- [95] M. Ernst, *J. Magn. Reson.*, **162**, 1 (2003).
- [96] P. Hodgkinson, *Prog. Nucl. Mag. Res. Sp.*, **46**, 197 (2005).
- [97] A. L. Bloom, J. N. Shoolery, *Phys. Rev.*, **97**, 1261 (1955).
- [98] A. E. Bennett, C. M. Rienstra, M. Auger, K. V. Lakshmi, R. G. Griffin, *J. Chem. Phys.*, **103**, 6951 (1995).
- [99] B. Fung, A. Khitrin, K. Ermolaev, *J. Magn. Reson.*, **142**, 97 (2000).
- [100] A. Detken, E. H. Hardy, M. Ernst, B. H. Meier, *Chem. Phys. Lett.*, **356**, 298 (2002).
- [101] R. S. Thakur, N. D. Kurur, P. K. Madhu, *Chem. Phys. Lett.*, **426**, 459 (2006).
- [102] C. Zehe, M. Schmidt, R. Siegel, K. Kreger, V. Daebel, S. Ganzleben, H.-W. Schmidt, J. Senker, *CrystEngComm*, **16**, 9273 (2014).

- [103] R. K. Harris, *The Analyst*, **131**, 351 (2006).
- [104] R. M. Orr, M. J. Duer, *Solid State Nucl. Mag.*, **30**, 130 (2006).
- [105] L. Delevoye, J. Trébosc, Z. Gan, L. Montagne, J.-P. Amoureux, *J. Magn. Reson.*, **186**, 94 (2007).
- [106] L. Delevoye, C. Fernandez, C. M. Morais, J.-P. Amoureux, V. Montouillout, J. Rocha, *Solid State Nucl. Mag.*, **22**, 501 (2002).
- [107] S. P. Brown, H. W. Spiess, *Chem. Rev.*, **101**, 4125 (2001).
- [108] M. Lee, W. I. Goldberg, *Phys. Rev.*, **140**, A1261 (1965).
- [109] J. S. Waugh, L. M. Huber, U. Haeberlen, *Phys. Rev. Lett.*, **20**, 180 (1968).
- [110] P. Mansfield, *J. Phys. C Solid State*, **4**, 1444 (1971).
- [111] W.-K. Rhim, *J. Chem. Phys.*, **59**, 3740 (1973).
- [112] D. P. Burum, W. K. Rhim, *J. Chem. Phys.*, **71**, 944 (1979).
- [113] M. Hohwy, P. V. Bower, H. J. Jakobsen, N. C. Nielsen, *Chem. Phys. Lett.*, **273**, 297 (1997).
- [114] A. Bielecki, A. Kolbert, M. Levitt, *Chem. Phys. Lett.*, **155**, 341 (1989).
- [115] M. H. Levitt, *Symmetry-based pulse sequences in Magic-Angle spinning solid-state NMR*, eMagRes, John Wiley & Sons, Ltd. (2007).
- [116] P. Madhu, X. Zhao, M. H. Levitt, *Chem. Phys. Lett.*, **346**, 142 (2001).
- [117] E. Vinogradov, P. Madhu, S. Vega, *Chem. Phys. Lett.*, **314**, 443 (1999).
- [118] D. Sakellariou, A. Lesage, P. Hodgkinson, L. Emsley, *Chem. Phys. Lett.*, **319**, 253 (2000).
- [119] C. Coelho, J. Rocha, P. Madhu, L. Mafra, *J. Magn. Reson.*, **194**, 264 (2008).
- [120] K. R. Mote, V. Agarwal, P. K. Madhu, *Prog. Nucl. Mag. Res. Sp.* (2016).
- [121] S. P. Brown, *Solid State Nucl. Mag.*, **41**, 1 (2012).

- [122] B. Elena, L. Emsley, *J. Am. Chem. Soc.*, **127**, 9140 (2005).
- [123] J. M. Griffin, D. R. Martin, S. P. Brown, *Angew. Chem. Int. Edit.*, **46**, 8036 (2007).
- [124] L. Mafra, S. M. Santos, R. Siegel, I. Alves, F. A. Almeida Paz, D. Dudenko, H. W. Spiess, *J. Am. Chem. Soc.*, **134**, 71 (2012).
- [125] J. P. Bradley, S. P. Velaga, O. N. Antzutkin, S. P. Brown, *Cryst. Growth Des.*, **11**, 3463 (2011).
- [126] J. Wack, R. Siegel, T. Ahnfeldt, N. Stock, L. Mafra, J. Senker, *J. Chem. Phys. C*, **117**, 19991 (2013).
- [127] J. Trebosc, J. W. Wiench, S. Huh, V. S.-Y. Lin, M. Pruski, *J. Am. Chem. Soc.*, **127**, 7587 (2005).
- [128] Z. Gan, P. Gor'kov, T. A. Cross, A. Samoson, D. Massiot, *J. Am. Chem. Soc.*, **124**, 5634 (2002).
- [129] A. Samoson, E. Lippmaa, A. Pines, *Mol. Phys.*, **65**, 1013 (1988).
- [130] A. Llor, J. Virlet, *Chem. Phys. Lett.*, **152**, 248 (1988).
- [131] F. a. Perras, I. Korobkov, D. L. Bryce, *CrystEngComm*, **15**, 8727 (2013).
- [132] L. Frydman, J. S. Harwood, *J. Am. Chem. Soc.*, **117**, 5367 (1995).
- [133] A. Medek, J. S. Harwood, L. Frydman, *J. Am. Chem. Soc.*, **117**, 12779 (1995).
- [134] C. Fernandez, J. Amoureux, *Chem. Phys. Lett.*, **242**, 449 (1995).
- [135] Z. Gan, *J. Am. Chem. Soc.*, **122**, 3242 (2000).
- [136] S. E. Ashbrook, S. Wimperis, *Prog. Nucl. Mag. Res. Sp.*, **45**, 53 (2004).
- [137] J.-P. Amoureux, C. Fernandez, S. Steuernagel, *J. Magn. Reson. A*, **123**, 116 (1996).
- [138] Z. Gan, H.-T. Kwak, *J. Magn. Reson.*, **168**, 346 (2004).
- [139] H.-T. Kwak, Z. Gan, *J. Magn. Reson.*, **164**, 369 (2003).

- [140] S. P. Brown, S. J. Heyes, S. Wimperis, *J. Magn. Reson. A*, **119**, 280 (1996).
- [141] A. Goldbourn, P. K. Madhu, *Monatsh. Chem.*, **133**, 1497 (2002).
- [142] C. Fernandez, M. Pruski, in *Top. Curr. Chem.*, volume 306, 119–188, Springer Berlin Heidelberg (2011).
- [143] S. E. Ashbrook, A. J. Berry, D. J. Frost, A. Gregorovic, C. J. Pickard, J. E. Readman, S. Wimperis, *J. Am. Chem. Soc.*, **129**, 13213 (2007).
- [144] R. K. Harris, R. E. Wasylishen, M. J. Duer, editors, *NMR Crystallography*, Wiley (2009).
- [145] R. K. Harris, *Solid State Sci.*, **6**, 1025 (2004).
- [146] D. Massiot, V. Montouillout, F. Fayon, P. Florian, C. Bessada, *Chem. Phys. Lett.*, **272**, 295 (1997).
- [147] D. Massiot, T. Vosegaard, N. Magneron, D. Trumeau, V. Montouillout, P. Berthet, T. Loiseau, B. Bujoli, *Solid State Nucl. Mag.*, **15**, 159 (1999).
- [148] O. Antzutkin, S. Shekar, M. Levitt, *J. Magn. Reson. A*, **115**, 7 (1995).
- [149] M. A. Alla, E. I. Kundla, E. T. Lippmaa, *JETP Lett.*, **27**, 194 (1978).
- [150] Y. Yarim-Agaev, P. N. Tutunjian, J. S. Waugh, *J. Magn. Reson.*, **47**, 51 (1982).
- [151] E. R. DeAzevedo, W.-G. Hu, T. J. Bonagamba, K. Schmidt-Rohr, *J. Am. Chem. Soc.*, **121**, 8411 (1999).
- [152] M. Hong, *J. Am. Chem. Soc.*, **122**, 3762 (2000).
- [153] W. Li, A. McDermott, *J. Magn. Reson.*, **222**, 74 (2012).
- [154] R. Tycko, G. Dabbagh, P. A. Mirau, *J. Magn. Reson.*, **85**, 265 (1989).
- [155] R. M. Orr, M. J. Duer, *J. Magn. Reson.*, **181**, 1 (2006).
- [156] S.-F. Liu, J.-D. Mao, K. Schmidt-Rohr, *J. Magn. Reson.*, **155**, 15 (2002).
- [157] Z. Gan, D. M. Grant, R. Ernst, *Chem. Phys. Lett.*, **254**, 349 (1996).

- [158] J. D. Gross, P. R. Costa, R. G. Griffin, *J. Chem. Phys.*, **108**, 7286 (1998).
- [159] J. C. C. Chan, R. Tycko, *J. Chem. Phys.*, **118**, 8378 (2003).
- [160] Y. Nishiyama, T. Yamazaki, T. Terao, *J. Chem. Phys.*, **124**, 064304 (2006).
- [161] G. Hou, I.-J. L. Byeon, J. Ahn, A. M. Gronenborn, T. Polenova, *J. Chem. Phys.*, **137**, 134201 (2012).
- [162] D. P. Raleigh, A. C. Kolbert, T. G. Oas, M. H. Levitt, R. G. Griffin, *J. Chem. Soc. Farad. T. 1*, **84**, 3691 (1988).
- [163] T. Gullion, *J. Magn. Reson.*, **85**, 614 (1989).
- [164] A. Kolbert, R. Griffin, *Chem. Phys. Lett.*, **166**, 87 (1990).
- [165] C. Crockford, H. Geen, J. J. Titman, *Chem. Phys. Lett.*, **344**, 367 (2001).
- [166] B. Eléna, S. Hediger, L. Emsley, *J. Magn. Reson.*, **160**, 40 (2003).
- [167] L. Shao, C. Crockford, H. Geen, G. Grasso, J. J. Titman, *J. Magn. Reson.*, **167**, 75 (2004).
- [168] M. Strohmeier, D. M. Grant, *J. Magn. Reson.*, **168**, 296 (2004).
- [169] R. M. Orr, M. J. Duer, S. E. Ashbrook, *J. Magn. Reson.*, **174**, 301 (2005).
- [170] I. Hung, Z. Gan, *J. Magn. Reson.*, **213**, 196 (2011).
- [171] U. Haeberlen, J. S. Waugh, *Phys. Rev.*, **175**, 453 (1968).
- [172] M. M. Maricq, *Phys. Rev. B*, **25**, 6622 (1982).
- [173] O. Weintraub, S. Vega, *J. Magn. Reson. A*, **105**, 245 (1993).
- [174] R. Tycko, S. O. Smith, *J. Chem. Phys.*, **98**, 932 (1993).
- [175] T. T. Nakashima, R. E. D. McClung, *Heteronuclear Shift Correlation Spectroscopy*, eMagRes, John Wiley & Sons, Ltd. (2007).
- [176] M. Eden, H. Annersten, A. Zazzi, *Chem. Phys. Lett.*, **410**, 24 (2005).

- [177] J. Amoureux, J. Trébosc, L. Delevoye, O. Lafon, B. Hu, Q. Wang, *Solid State Nucl. Mag.*, **35**, 12 (2009).
- [178] R. Tycko, *Dipolar recoupling: homonuclear experiments*, eMagRes, John Wiley & Sons, Ltd. (2009).
- [179] C. Jäger, M. Feike, Born, H.-W. Spiess, *J. Non-Cryst. Solids*, **180**, 91 (1994).
- [180] C. Martineau, B. Bouchevreau, Z. Tian, S.-J. Lohmeier, P. Behrens, F. Taulelle, *Chem. Mater.*, **23**, 4799 (2011).
- [181] M. Schmidt, J. Wittmann, R. Kress, D. Schneider, S. Steuernagel, H.-W. Schmidt, J. Senker, *Cryst. Growth Des.*, **12**, 2543 (2012).
- [182] D. H. Brouwer, P. E. Kristiansen, C. A. Fyfe, M. H. Levitt, *J. Am. Chem. Soc.*, **127**, 542 (2005).
- [183] M. Carravetta, M. Eden, O. G. Johannessen, H. Luthman, P. J. E. Verdegem, J. Lugtenburg, A. Sebald, M. H. Levitt, *J. Am. Chem. Soc.*, **123**, 10628 (2001).
- [184] P. E. Kristiansen, M. Carravetta, W. C. Lai, M. H. Levitt, *Chem. Phys. Lett.*, **390**, 1 (2004).
- [185] E. R. Andrew, S. Clough, L. F. Farnell, T. D. Gledhill, I. Roberts, *Phys. Lett.*, **21**, 505 (1966).
- [186] D. P. Raleigh, M. H. Levitt, R. G. Griffin, *Chem. Phys. Lett.*, **146**, 71 (1988).
- [187] A. E. Bennett, R. G. Griffin, J. H. Ok, S. Vega, *J. Chem. Phys.*, **96**, 8624 (1992).
- [188] D. K. Sodickson, M. H. Levitt, S. Vega, R. G. Griffin, *J. Chem. Phys.*, **98**, 6742 (1993).
- [189] Y. Ishii, *J. Chem. Phys.*, **114**, 8473 (2001).
- [190] C. Volkringer, T. Loiseau, N. Guillou, G. Férey, M. Haouas, F. Taulelle, E. Elkaim, N. Stock, *Inorg. Chem.*, **49**, 9852 (2010).
- [191] T. M. Alam, R. K. Brow, *J. Non-Cryst. Solids*, **223**, 1 (1998).

- [192] F. W. Karau, L. Seyfarth, O. Oeckler, J. Senker, K. Landskron, W. Schnick, *Chem. Eur. J.*, **13**, 6841 (2007).
- [193] Eduardo Zaborowski, Herbert Zimmermann, Shimon Vega, *J. Magn. Reson.*, **136**, 47 (1999).
- [194] P. Robyr, M. Tomaselli, J. Straka, C. Grob-Pisano, U. W. Suter, B. H. Meier, R. R. Ernst, *Mol. Phys.*, **84**, 995 (1995).
- [195] N. Bloembergen, *Physica*, **15**, 386 (1949).
- [196] D. Suter, R. R. Ernst, *Phys. Rev. B*, **25**, 6038 (1982).
- [197] N. M. Szeverenyi, M. J. Sullivan, G. E. Maciel, *J. Magn. Reson.*, **47**, 462 (1982).
- [198] A. Grommek, B. H. Meier, M. Ernst, *Chem. Phys. Lett.*, **427**, 404 (2006).
- [199] M. Veshtort, R. G. Griffin, *J. Chem. Phys.*, **135** (2011).
- [200] F. Castellani, B. van Rossum, A. Diehl, M. Schubert, K. Rehbein, H. Oschkinat, *Nature*, **420**, 98 (2002).
- [201] E. Salager, R. S. Stein, C. J. Pickard, B. Elena, L. Emsley, *Phys. Chem. Chem. Phys.*, **11**, 2610 (2009).
- [202] K. Takegoshi, S. Nakamura, T. Terao, *Chem. Phys. Lett.*, **344**, 631 (2001).
- [203] E. Crocker, A. B. Patel, M. Eilers, S. Jayaraman, E. Getmanova, P. J. Reeves, M. Ziliox, H. G. Khorana, M. Sheves, S. O. Smith, *J. Biomol. NMR*, **29**, 11 (2004).
- [204] M. J. Bayro, M. Huber, R. Ramachandran, T. C. Davenport, B. H. Meier, M. Ernst, R. G. Griffin, *J. Chem. Phys.*, **130**, 114506 (2009).
- [205] R. Tycko, G. Dabbagh, *Chem. Phys. Lett.*, **173**, 461 (1990).
- [206] N. C. Nielsen, H. Bildsoe, H. J. Jakobsen, M. H. Levitt, *J. Chem. Phys.*, **101**, 1805 (1994).
- [207] R. Verel, M. Ernst, B. H. Meier, *J. Magn. Reson.*, **150**, 81 (2001).

- [208] D. M. Gregory, D. J. Mitchell, J. A. Stringer, S. Kiihne, J. C. Shiels, J. Callahan, M. A. Mehta, G. P. Drobny, *Chem. Phys. Lett.*, **246**, 654 (1995).
- [209] P. V. Bower, N. Oyler, M. A. Mehta, J. R. Long, P. S. Stayton, G. P. Drobny, *J. Am. Chem. Soc.*, **121**, 8373 (1999).
- [210] M. A. Caporini, V. S. Bajaj, M. Veshtort, A. Fitzpatrick, C. E. MacPhee, M. Vendruscolo, C. M. Dobson, R. G. Griffin, *J. Phys. Chem. B*, **114**, 13555 (2010).
- [211] M. A. Mehta, D. M. Gregory, S. Kiihne, D. J. Mitchell, M. E. Hatcher, J. C. Shiels, G. P. Drobny, *Solid State Nucl. Mag.*, **7**, 211 (1996).
- [212] S. R. Kiihne, K. B. Geahigan, N. A. Oyler, H. Zebroski, M. A. Mehta, G. P. Drobny, *J. Phys. Chem. A*, **103**, 3890 (1999).
- [213] M. Murakami, Y. Noda, Y. Koyama, K. Takegoshi, H. Arai, Y. Uchi-moto, Z. Ogumi, *J. Phys. Chem. C*, **118**, 15375 (2014).
- [214] R. Graf, D. E. Demco, J. Gottwald, S. Hafner, H. W. Spiess, *J. Chem. Phys.*, **106**, 885 (1997).
- [215] K. Saalwächter, F. Lange, K. Matyjaszewski, C.-F. Huang, R. Graf, *J. Magn. Reson.*, **212**, 204 (2011).
- [216] J. Gottwald, D. E. Demco, R. Graf, H. W. Spiess, *Chem. Phys. Lett.*, **243**, 314 (1995).
- [217] M. Feike, D. E. Demco, R. Graf, J. Gottwald, S. Hafner, H. W. Spiess, *J. Magn. Reson.*, **122**, 214 (1996).
- [218] Y. K. Lee, N. D. Kurur, M. Helmle, O. G. Johannessen, N. C. Nielsen, M. H. Levitt, *Chem. Phys. Lett.*, **242**, 304 (1995).
- [219] A. Brinkmann, M. H. Levitt, *J. Chem. Phys.*, **115**, 357 (2001).
- [220] P. E. Kristiansen, D. J. Mitchell, J. N. S. Evans, *J. Magn. Reson.*, **157**, 253 (2002).
- [221] L. Seyfarth, J. Seyfarth, B. Lotsch, W. Schnick, J. Senker, *Phys. Chem. Chem. Phys.*, **12**, 2227 (2010).

- [222] D. H. Brouwer, R. J. Darton, R. E. Morris, M. H. Levitt, *J. Am. Chem. Soc.*, **127**, 10365 (2005).
- [223] J. Ren, H. Eckert, *Angew. Chem. Int. Ed.*, **51**, 12888 (2012).
- [224] P. E. Kristiansen, M. Carravetta, J. D. van Beek, W. C. Lai, M. H. Levitt, *J. Chem. Phys.*, **124**, 234510 (2006).
- [225] M. Schmidt, J. Wittmann, R. Kress, H.-W. Schmidt, J. Senker, *Chem. Commun.*, **49**, 267 (2013).
- [226] B. Lotsch, M. Döblinger, J. Sehnert, L. Seyfarth, J. Senker, O. Oeckler, W. Schnick, *Chem. Eur. J.*, **13**, 4969 (2007).
- [227] V. Ladizhansky, S. Vega, *J. Am. Chem. Soc.*, **122**, 3465 (2000).
- [228] L. Seyfarth, J. Sehnert, N. El-Gamel, W. Milius, E. Kroke, J. Breu, J. Senker, *J. Mol. Struct.*, **889**, 217 (2008).
- [229] C. M. Widdifield, H. Robson, P. Hodgkinson, *Chem. Commun.*, **52**, 6685 (2016).
- [230] T. G. Oas, R. G. Griffin, M. H. Levitt, *J. Chem. Phys.*, **89**, 692 (1988).
- [231] M. H. Levitt, T. G. Oas, R. G. Griffin, *Isr. J. Chem.*, **28**, 271 (1988).
- [232] P. R. Costa, J. D. Gross, M. Hong, R. G. Griffin, *Chem. Phys. Lett.*, **280**, 95 (1997).
- [233] R. Fu, S. A. Smith, G. Bodenhausen, *Chem. Phys. Lett.*, **272**, 361 (1997).
- [234] K. Takegoshi, K. Takeda, T. Terao, *Chem. Phys. Lett.*, **260**, 331 (1996).
- [235] S. J. Kitchin, K. D. Harris, A. E. Aliev, D. C. Apperley, *Chem. Phys. Lett.*, **323**, 490 (2000).
- [236] D. E. Kaplan, E. L. Hahn, *J. Phys. Radium*, **19**, 821 (1958).
- [237] S. E. Shore, J.-P. Ansermet, C. P. Slichter, J. H. Sinfelt, *Phys. Rev. Lett.*, **58**, 953 (1987).
- [238] T. Gullion, J. Schaefer, *Adv. Magn. Reson.*, **13**, 57 (1989).
- [239] T. Gullion, J. Schaefer, *J. Magn. Reson.*, **81**, 196 (1989).

- [240] A. W. Hing, S. Vega, J. Schaefer, *J. Magn. Reson.*, **96**, 205 (1992).
- [241] A. T.-W. Yap, H. Förster, S. R. Elliott, *Phys. Rev. Lett.*, **75**, 3946 (1995).
- [242] X. Kong, H. Deng, F. Yan, J. Kim, J. A. Swisher, B. Smit, O. M. Yaghi, J. A. Reimer, *Science*, **341**, 882 (2013).
- [243] S. Matsuoka, M. Inoue, *Chem. Commun.*, 5664 (2009).
- [244] A. Haimovich, A. Goldbourn, *J. Magn. Reson.*, **254**, 131 (2015).
- [245] I.-S. Jung, Y. J. Lee, D. Jeong, R. Graf, T.-L. Choi, W.-J. Son, X. Bulliard, H. W. Spiess, *Macromolecules*, **49**, 3061 (2016).
- [246] X. Zhao, W. Hoffbauer, J. Schmedt auf der Günne, M. H. Levitt, *Solid State Nucl. Mag.*, **26**, 57 (2004).
- [247] M. Schmidt, C. S. Zehe, R. Siegel, J. U. Heigl, C. Steinlein, H.-W. Schmidt, J. Senker, *CrystEngComm*, **15**, 8784 (2013).
- [248] A. Brinkmann, A. P. M. Kentgens, *J. Am. Chem. Soc.*, **128**, 14758 (2006).
- [249] Renée Siegel, Julien Trébosc, Jean-Paul Amoureux, Zhehong Gan, *J. Magn. Reson.*, **193**, 321 (2008).
- [250] S. Cavadini, A. Lupulescu, S. Antonijevic, G. Bodenhausen, *J. Am. Chem. Soc.*, **128**, 7706 (2006).
- [251] Z. Gan, *J. Am. Chem. Soc.*, **128**, 6040 (2006).

Erklärung

Hiermit erkläre ich mich damit einverstanden, dass die elektronische Version meiner Dissertation unter Wahrung meiner Urheberrechte und des Datenschutzes einer gesonderten Überprüfung hinsichtlich der eigenständigen Anfertigung der Arbeit unterzogen werden kann.

Hiermit erkläre ich eidesstattlich, dass ich die vorliegende Dissertation selbstständig verfasst und keine anderen als die angegebenen Hilfsmittel und Quellen benutzt habe.

Weiterhin versichere ich, die Arbeit in gleicher oder ähnlicher Form noch keiner Prüfungsbehörde zur Erlangung eines akademischen Grades vorgelegt und diese oder eine gleichartige Doktorprüfung engültig nicht bestanden zu haben.

Ich habe keine Hilfe von gewerblichen Promotionsberatern/-vermittlern in Anspruch genommen und werde dies auch künftig nicht tun.

Christoph Zehe